CZECH TECHNICAL UNIVERSITY IN PRAGUE

Faculty of Electrical Engineering

Department of Cybernetics

Advanced Analysis of MRI Data in Patients with Central Nervous System Disease

Analýza pokročilých MRI dat u pacientů s postižením centrální nervové soustavy

Master´s Thesis

Study program: Biomedical Engineering and Informatics

Branch of study: Biomedical Engineering

Supervisor: Mgr. Ing. Marek Dostál, Ph.D.

Bc. Adam Rytina

Prague, May 2020

MASTER‘S THESIS ASSIGNMENT

I. Personal and study details

Student's name: **Rytina Adam** Personal ID number: **435023**

Faculty / Institute: **Faculty of Electrical Engineering**

Department / Institute: **Department of Cybernetics**

Study program: **Biomedical Engineering and Informatics**

Branch of study: **Biomedical Engineering**

II. Master’s thesis details

Master’s thesis title in English:

Advanced Analysis of MRI Data in Patients with Central Nervous System Disease

Master’s thesis title in Czech:

Analýza pokročilých MRI dat u pacientů s postižením centrální nervové soustavy

Guidelines:

1. Get acquainted with MR imaging basic principles and techniques. Focus on brain tissue and its surrounding tissues imaging.
2. Study MR diffusion-weighted imaging (DWI) method and analyse a usage of this approach.
3. Propose the proper procedure of the image analysis (segmentation of brain tissue and its surrounding tissues, correction of artifacts, image registration). Use and compare available software tools for each step of the analysis.
4. Measure IVIM (Intravoxel Incoherent Motion) parameters in different types of tissue and perform a statistical analysis of acquired data.

Bibliography / sources:

[1] Brown, R.W., Cheng, Y.-C.N., Haacke, E.M., Thompson, M.R., Venkatesan, R., 2014. Classical Response of a Single Nucleus to a Magnetic Field, in: Magnetic Resonance Imaging. John Wiley & Sons, Ltd, pp. 19–36. https://doi.org/10.1002/9781118633953.ch2

[2] Gurney-Champion, O.J., Klaassen, R., Froeling, M., Barbieri, S., Stoker, J., Engelbrecht, M.R.W., Wilmink, J.W., Besselink, M.G., Bel, A., van Laarhoven, H.W.M., Nederveen, A.J., 2018. Comparison of six fit algorithms for the intra-voxel incoherent motion model of diffusion-weighted magnetic resonance imaging data of pancreatic cancer patients. PLoS One 13. https://doi.org/10.1371/journal.pone.0194590

[3] Jesper L.R. Andersson, Stefan Skare, John Ashburner, How to correct susceptibility distortions in spin-echo echo-planar images: application to diffusion tensor imaging, NeuroImage, Volume 20, Issue 2, 2003, Pages 870-888, ISSN 1053-8119, https://doi.org/10.1016/S1053-8119(03)00336-7

[4] Kingsley, P.B., 2006a. Introduction to diffusion tensor imaging mathematics: Part I. Tensors, rotations, and eigenvectors. Concepts in Magnetic Resonance Part A 28A, 101–122. https://doi.org/10.1002/cmr.a.20048

[5] Kingsley, P.B., 2006b. Introduction to diffusion tensor imaging mathematics: Part II. Anisotropy, diffusion□weighting factors, and gradient encoding schemes. Concepts in Magnetic Resonance Part A 28A, 123–154. https://doi.org/10.1002/cmr.a.20049

[6] Kingsley, P.B., 2006c. Introduction to diffusion tensor imaging mathematics: Part III. Tensor calculation, noise, simulations, and optimization. Concepts in Magnetic Resonance Part A 28A, 155–179. https://doi.org/10.1002/cmr.a.20050

[7] Le Bihan, D., 2017. What can we see with IVIM MRI? NeuroImage. https://doi.org/10.1016/j.neuroimage.2017.12.062

[8] Yang, A., Wang Ai-ling and Jincai Chang, "The research on parallel least squares curve fitting algorithm," 2009 International Conference on Test and Measurement, Hong Kong, 2009, pp. 201-204. doi: 10.1109/ICTM.2009.5413074

Name and workplace of master's thesis supervisor:

Mgr. Ing. Marek Dostál, University Hospital Brno

Name and workplace of second master's thesis supervisor or consultant:

doc. Ing. Lenka Lhotská, CSc., Department of Natural Sciences, FBME

Date of master's thesis assignment: **30.09.2019** Deadline for master's thesis submission: **22.05.2020**

Assignment valid until: **30.09.2021**

Mgr. Ing. Marek Dostál Supervisor's signature	doc. Ing. Tomáš Svoboda, Ph.D. Head of department's signature	prof. Mgr. Petr Páta, Ph.D. Dean's signature

III. Assignment receipt

The student acknowledges that the master's thesis is an individual work. The student must produce his thesis without the assistance of others, with the exception of provided consultations. Within the master's thesis, the author must state the names of consultants and include a list of references.

.	
Date of assignment receipt	Student's signature

Declaration

„I declare that the presented work was developed independently and that I have listed all sources of information used within it in accordance with the methodical instructions for observing the ethical principles in the preparation of university theses.“

Prague, May 20, 2020 Adam Rytina

Acknowledgement

I would like to thank my supervisor Mgr. Ing. Marek Dostál, Ph.D. for his guidance, very helpful approach and especially for the opportunity to work on this exciting topic.

I would also like to acknowledge doc. Ing. Lenka Lhotská, CSc. for her important advice.

I sincerely thanks Mgr. Tomáš Sieger, Ph.D. for the help with the statistical analysis.

My appreciation goes to MUDr. Tereza Kopřivová from the University Hospital Brno for performing image segmentation that was a necessary step for my further image processing and data analysis.

I would also like to extend my thanks to the University Hospital Brno (Department of Radiology and Nuclear Medicine) for providing me with patient data.

I also want to pay my regards to my colleagues from the company GE Healthcare for giving advice from the clinical praxis.

Abstract

Distinguishing between brain tumors and the healthy tissue in brain and differentiation of individual brain tumor types is mainstay of the magnetic resonance exam. This thesis deals with a special diffusion magnetic resonance method *intravoxel incoherent motion* (IVIM). It incorporates an overview of basic magnetic resonance sequences used in brain imaging. The emphasis is on diffusion imaging. The study is focused on the image analysis using various methods and software tools. Part of this analysis is to minimize distortions in diffusion images. The main aim of this work is to measure IVIM parameters f, D a $D*$ in tumor brain tissue and surrounding tissues and to subject them to statistical analysis. The work aims to verify the suitability of this method in distinguishing individual types of brain tumors and individual brain tissues. Parameters for twenty patients with three types of brain tumors (gliomas, metastasis and meningiomas) are evaluated. Image analysis is performed in several programs using several procedures whose influence on the final IVIM parameters is analyzed. A statistically significant difference is confirmed for some brain tissue pairs in different brain tumors. This work verifies that the concept of *intravoxel incoherent motion* may be a suitable method for accurate differentiation of brain tumor types.

Key words

diffusion magnetic resonance, diffusion weighted imaging (DWI), intravoxel incoherent motion (IVIM), distortion correction in DWI, MR neuroimaging

Abstrakt

Odlišení nádorové hmoty v mozku od zdravé nervové tkáně a odlišení jednotlivých typů mozkových nádorů patří mezi stěžejní výzvy při vyšetření pomocí magnetické rezonance. Tato diplomová práce se zabývá speciální metodou difúzní magnetické rezonance *intravoxel incoherent motion* (IVIM). Obsahuje přehled základních sekvencí magnetické rezonance sloužící pro zobrazení mozku. Důraz je kladen na zobrazení difúze. Práce je zaměřena na provedení jednotlivých kroků analýzy obrazu pomocí odlišných metod a pomocí jednotlivých programových nástrojů. Součástí této analýzy je minimalizace distorzí v difúzních obrazech. Hlavním cílem práce je proměření IVIM parametrů f, D a $D*$ v nádorové mozkové tkáni a okolních tkáních a jejich podrobení statistické analýze. Práce si klade za cíl ověřit vhodnotst této metody při odlišení jednotlivých typů mozkových tumorů a jednotlivých mozkových tkání. Jsou vyhodoceny parametry pro dvacet pacientů se třemi typy mozkových nádorů (gliomy, metastázy a meningiomy). Analýza obrazu je provedena v několika programech pomocí několika postupů, jejichž vliv na výsledné IVIM parametry je rozebrán. Statisticky významný rozdíl je potvrzen pro některé dvojice mozkových tkání v různých mozkových nádorech. Tato práce ověřuje, že koncept *intravoxel incoherent motion* může být vhodnou metodou pro přesné odlišení jednotlivých typů mozkových nádorů.

Klíčová slova

difúzní magnetická rezonance, difúzí vážené zobrazení (DWI), intravoxel incoherent motion (IVIM), korekce distorzí v difúzi váženém zobrazení, zobrazení mozku pomocí magnetické rezonance

Contents

1. Introduction

Nervous system cancer is worldwide one of the common causes of death. Brain tumors can occur in both children and adults. There are many types of brain tumors that are assigned to four grades representing the rate of the tumor´s growth. Brain tumors are typically treated with radiation therapy, chemotherapy and surgery. The early brain tumor detection enables to choose between several treatment options. Moreover, when tumors in brain are identified early, the disease is more likely to be effective to the treatment and the probability of surviving is increased. In addition, it means less expensive treatment. For early tumors detection diagnostic imaging methods are irreplaceable. In the case of brain tumors detection magnetic resonance plays a vital role. A challenging task in magnetic resonance is to distinguish the tumor from its surrounding area and moreover, to effectively distinguish individual brain tumor types.

Magnetic resonance diffusion imaging has been proven to be one of major methods to characterize brain tumors. At present, a new concept of diffusion magnetic resonance imaging, *intravoxel incoherent mo*tion, is under investigation to determine its clinical significance.

In this thesis, I aim to analyze the magnetic resonance diffusion method in neuroimaging and to shed some light on the concept of *intravoxel incoherent motion*. I will conduct image analysis that is a necessary step before measuring the *intravoxel incoherent motion* parameters. The parameters will be measured in patients suffering from different brain tumor types. I will perform statistical analysis of acquired data.

2. Introduction to Magnetic Resonance

The magnetic resonance (MR) phenomenon is based on the interaction between an external magnetic field and nuclei in the human body[1]. The main static magnetic field B_0 is produced by a powerful magnet.

In order to provide an exact spatial MR signals location in three dimensions, three sets of spatial encoding coils to produce the magnetic field in *x*, *y* and *z* direction are implemented. These gradient fields are not constant but are intended to produce a magnetic gradient. In comparison with the main magnetic field B_0, gradient fields are much weaker and ideally vary linearly in all three axes. *„Gradient coils for MRI must have high current efficiency, short switching time, gradient linearity over a large volume, low power consumption, and minimal interaction with any other equipment, which would otherwise result in eddy currents."* [1] A first applied gradient is the slice selective gradient G_Z (in this work a direction of the slice selective gradient refers to the z-axis) during the radiofrequency (RF) excitation pulse[2]. All slices have afterwards different precession frequency[3] throughout the z-axis. To visualize the slice, the RF pulse with the particular Larmor frequency of this slice is applied. The range of frequencies Δf that can excite a slice can be calculated according to the formula 2.1; thus, it is directly proportional to the slice thickness Δz, the gradient strength G_Z and the gyromagnetic ratio γ[4]. The stronger gradients applied, the thinner slice selected. The change of the RF pulse frequency makes possible to select an upper or a lower slice.

$$\Delta \mathrm{f} = \gamma \cdot G_Z \cdot \Delta \mathrm{z} \qquad (2.1)$$

After the slice selection in 2D imaging, it is important to encode the spatial position within a slice. Therefore, frequency and phase encoding gradients are applied. The phase encoding gradient G_Y, which generates spins dephasing along one axis of the x-y plane (in this work a direction of the phase encoding gradient refers to the y-axis), is applied immediately after the excitation

---

[1] In this work MR refers to an investigation of $^1\mathrm{H}$ Hydrogen nuclei so terms nuclei, spins and protons are equivalent.

[2] A radiofrequency excitation pulse is intended to excite the protons ensemble from a lower energy state to a higher energy state.

[3] The precession frequency, the so-called Larmor frequency, represents a rate of the precession movement (rotation around the z- axis) of the spinning ensemble under the influence of the external magnetic field.

[4] The gyromagnetic ratio is a constant that is nuclei dependent. It includes particles´ size, a mass and nuclear spin values. The unit is $\frac{MHz}{T}$.

pulse. Thereby, each pixel along the y-axis has a different phase shift. At the time the G_Y gradient is active, there is a change in a frequency and a phase causing that some protons move faster than the adjacent protons. When the gradient is off, all the protons start to move with the original frequency, but they have accumulated a phase shift. According to the phase shift varying in the y-axis, the position in y-axis can be specified. The phase shift $d\Phi$ is proportional to the time t, the gyromagnetic coefficient γ and the strength of the gradient G_Y. Finally, all pixels in the *Field of View* (FOV)[5] have their unique phase and frequency within a slice.

$$\Phi = \gamma \cdot G_Y \cdot t \qquad (2.2)$$

The last step is the use of the frequency encoding gradient G_X determining one axis of the x-y plane of the selected slice (in this work a direction of the frequency encoding gradient refers to the x-axis) by producing the gradient of the Larmor frequencies along this direction. Individual spins will move with a slightly different Larmor frequency value in the linear scale along this axis. A frequency encoding gradient is applied when the signal is received.

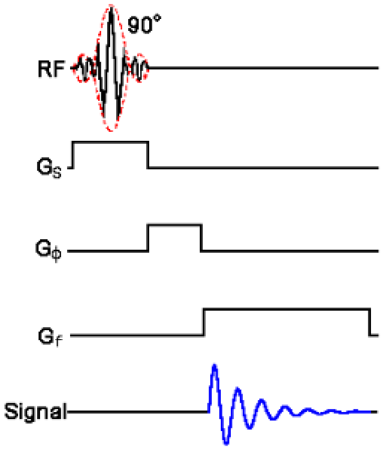

Figure 2.1: Timing of three gradients application. The slice selective gradient in the z-axis G_Z (in this figure G_S) is applied during the RF pulse application, the phase encoding gradient in the y-axis G_Y (in this figure G_Φ) is applied right after the end of the RF pulse, the frequency encoding gradient in the x-axis G_X (in this figure G_f) is active during the signal is being read out.

---

[5] FOV is the image area containing the examined part of the body.

3. Basic sequences in Magnetic Resonance

An essential step to perform optimal MR exams is to choose a MR sequence which optimally displays pathologic lesions. It means to display a region with requested image contrast[6] (a different type of image weighting), with desired image quality and in as short time as possible. The sequence choice is highly influenced by the system technical specifications and the anatomical structures to be visualized or which structures to be suppressed. Nowadays, in a time of fast technical development, MR protocols with appropriate parameters values are already preset and can be eventually adjusted by an operator.

In this chapter the description of fundamental non-diffusion MR sequences T_1 and T_2 is given. Moreover, the suppression technique FLAIR, which is crucial in MR neuroimaging, is mentioned. Last but not least, fast MR Echo-planar imaging (EPI) sequences, which are key sequences for diffusion MR imaging (MRI), are covered. The MR data I am processing in my practical task were acquired with these techniques.

3.1. MR signal weighting

MR images depend on magnetic properties and a number of hydrogen nuclei in the area being examined. Basic MR sequences T_1 and T_2 weighted sequences[7] are part of almost all MR protocols. By running a different weighting sequence, different contrast of the image will be acquired. *„In T_2 weighted images, tissues with long T_2 give the highest signal intensities, producing a bright appearance. T_1 weighted images are completely different; long T_1 tissues give the weakest signal, i.e. bright pixels on T_1 are associated with short T_1."* [2, p. 32] The particular sequence might be acquired by specifying primary parameters; the repetition time T_R[8] and the echo time T_E[9]. By setting different values of T_R and T_E, MR is able to acquire images that are

---

[6] The image contrast represents an ability to distinguish surrounding tissues A from B with similar signal intensities S_A and S_B.

[7] T_1 and T_2 sequences refer to the T_1 and T_2 relaxation time. After the RF pulse application, the spins tend to return to their equilibrium. T_1 relaxation time interval corresponds to the return of the longitudinal magnetization (in the z-axis), whereas T_2 relaxation time interval corresponds to the decay of the transverse magnetization (in the x-y plane).

[8] The repetition time T_R represents the time interval from the application of the RF pulse to the application of the next pulse.

[9] The echo time T_E represents the time interval from the application of the RF pulse and the peak of the induced signal in a coil.

weighted with parameters according to the T_1 relaxation time or with the T_2 relaxation time. In praxis, though, a mixed contribution of both parameters is always present.

T_1 weighted images are acquired with short T_E and T_R times, whereas the setting of longer T_E an T_R times determines T_2 weighted images. If the T_R time is proportional to the T_1 relaxation time and T_E much lower than T_2, it is an example of T_1 weighting. In T_1 weighting the contribution of T_2 relaxation rate is suppressed. Whereas in the case of T_2 weighting, T_R is much longer than T_1 and T_E proportional to T_2. In T_2 weighting the T_1 relaxation rate is suppressed. When the repetition time is very short, the relaxation time of tissues cannot be optimally measured. By setting greatly long T_R, the whole examination time is prolonged, thus it is more susceptible to image distortions.

MR image	T_R **[ms]**	T_E **[ms]**
T_1 **weighting**	400 - 700	10 - 20
T_2 **weighting**	at least 2000	80 - 120

Table 3.1: A choice of the repetition time T_R *and the echo time* T_E *determines a degree of MR weighting.* T_2 *images are acquired with longer* T_R *and* T_E *times than* T_1 *images. [3, p. 7]*

Tissue	T_1 **weighting**	T_2 **weighting**
Water, CSF[10]	dark	bright
White brain matter (WM)[11]	bright	dark gray
Gray brain matter (GM)[12]	gray	gray
Muscle	gray	dark gray
Fat	bright	less bright
Inflammation	dark	Bright

Table 3.2: T_1 *weighting sequences use short* T_R *so the signal from water is low, thus appearing dark.* T_2 *weighting sequences implement long* T_E *time, thus water signal is high appearing with a bright color. Even if in* T_1 *sequence* T_R *is short, the signal coming from fat is intensive, thus appears bright.* T_2 *for fat is also short and with long* T_E *the signal from fat is less bright (darker than water). The color representation of other structures with different weighting sequences are seen in this table.*

---

[10] CSF refers to *Cerebrospinal fluid*. The explanation is given in the section 5.1.

[11] A description of WM is given in the section 5.1.

[12] A description of GM is given in the section 5.1.

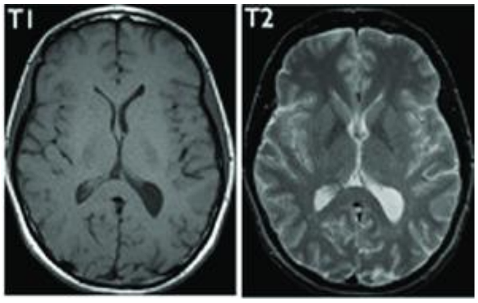

Figure 3.1: A brain MR image sample in the axial plane, on the left: T_1 *weighting, on the right:* T_2 *weighting. [4]*

3.2. Suppression methods in MR imaging

One of a major achievement in MR imaging is a possibility to suppress tissue with concrete T_1 relaxation time. Hence, the signal level and the contrast in a *region of interest* (ROI) may be enhanced. Besides aforesaid parameters T_R and T_E, the inversion time T_I[13] can be specified to null out the tissue signal. In suppression *Inversion Recovery* (IR) sequences an additional 180° pulse at the beginning of the sequence preceding a 90° excitation pulse is applied. By setting the T_I time, which depends on the T_1 tissue relaxation time, the signal coming from the tissue with T_1 is suppressed. The signal coming from fat tissue and hydrophilic tissue composing of water (eventually *Cerebrospinal fluid*) can be separated due to their significantly different T_1 relaxation time. The fat and water suppression are the most often suppression methods.

FLAIR (*Fluid Attenuated Inversion Recovery*) is a key sequence whose aim is to scan brain tissue in which the CSF[14] signal is suppressed. The FLAIR sequence generates T_2 weighting images with the only difference of CSF signal nulling. The CSF is attenuated and visualized dark, whereas some abnormalities and fat are made bright. *„The technique has proved to be an invaluable and sensitive technique for imaging disease processes characterized by abnormal* T_2 *signal in close proximity to the cerebral ventricles and other cerebrospinal fluid spaces in the brain; it is now routinely used for brain imaging in many centers.“* [5]

---

[13] The inversion time T_I represents the time interval between the inversion 180° pulse (a tilt of the magnetization into the longitudinal plane) and the excitation 90° pulse (a tilt of the magnetization into the transverse plane).

[14] Water content of CSF is roughly 99%, thus it is assumed the water and CSF suppression are the same.

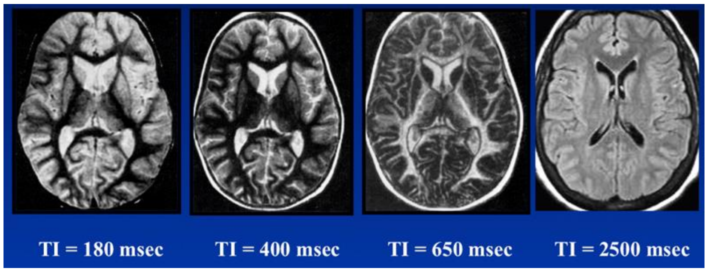

Figure 3.2: A choice of the inversion time T_I[15] *to suppress a concrete tissue type.* $T_I = 180\ ms$*: a sequence for fat nulling,* $T_I = 400\ ms$*: a sequence for white matter nulling,* $T_I = 650\ ms$*: a sequence for gray matter nulling,* $T_I = 2500\ ms$*: the FLAIR sequence for CSF nulling. The longest inversion time is required to remove the signal coming from CSF. [6]*

3.3. Fast MR imaging sequences

Fast MR imaging has been rapidly maturing. An initial purpose of fast sequences was to shorten the total acquisition time and to display fast processes. Today its impact is growing since fast imaging techniques might reduce motion artefacts, enable 3D imaging, flow and cine imaging. [7] Not only do fast MRI methods reduce the total acquisition time but also improve the temporal resolution[16].

The fastest MR sequence is called the echo-planar imaging (EPI)[17] that enables a single image acquisition in tens of ms. [8] A whole k-space[18] is obtained within one repetition. EPI sequence is a basis of MR applications, such as perfusion, functional and diffusion imaging. All spatial encoding information is acquired with even only a single RF excitation pulse, whilst conventional MR techniques require to apply multiple RF pulses. *„The major advantages of echo-planar imaging over conventional imaging are (a) reduced imaging time with the potential for improved patient throughout, (b) reduced motion artifact, and (c) the ability to image rapid physiologic and kinetic processes."* [9] On the other hand, limited spatial resolution, low signal and high sensitivity to magnetic susceptibility changes is followed. To perform EPI sequences, the

---

[15] The inversion time also depends on the main magnetic field strength B_0.

[16] The temporal resolution; the shortest time for acquisition of single frames of a dynamic process, is related to the total acquisition time.

[17] It refers to the single-shot EPI; forming of a whole k-space within one excitation sequence.

[18] k-space is a grid representing spatial frequency (x-axis of k-space) and phase (y-axis of k-space) information in the MR image.

demands on MR hardware and software are placed. Large gradient amplitudes are necessary. The speed of the EPI sequence is limited by the gradient switching.

Diffusion Weighted Imaging (DWI) EPI sequence is extremely prone to image artefacts. EPI sequences are very sensitive to non-zero resonance fields that are caused by magnetic susceptibility and eddy current effects. A more detailed explanation of distortions that are present in EPI sequences is given in the chapter 6.3.2. EPI images show a low bandwidth[19] in the phase encoding direction; thus, image distortions are typical along the phase encoding direction.

---

[19] The bandwidth means a range of frequencies of a signal reception.

4. Diffusion Magnetic Resonance methods

Water molecules in living tissue are not fixed in place but still move in the tissue. Diffusion magnetic resonance is a unique technique measuring mobility of water molecules in tissue. Diffusion (*Brownian* movement); the microscopic spontaneous, incessant movement of particles in random directions, can influence the MR signal intensity. Whereas in the conventional MR method, the signal intensity attenuation depends on the tissue type and its relaxation time, the diffusion MR is sensitive to water diffusion processes in tissue by applying an additional gradient magnetic field. Water molecules driven by a thermal energy are still moving and are colliding. Because of their unordered movement and their initial location changes, the signal attenuation comes into effect. The longer diffusion distance, the greater signal attenuation. The diffusion direction can be arbitrary in all directions or can be enhanced only in concrete directions in the case the omnidirectional diffusion is hindered by some obstacles (membranes and macromolecules[20]).

Diffusion MR has become a pillar in neuroimaging for an assessment of some brain pathologic disorders. Changes in the material construction will subsequently influence how fast the diffusion occurs. This method is therefore excellent for evaluation of the chemical molecules' movement restriction. If so, it might represent some inflammatory processes. Moreover, diffusion MR might be a useful technique for distinguishing between chronic and acute ischemia[21]. In addition, this method is used in a field of oncology that is a primary part of my master´s thesis. *„Tumor cells are known to have many more membranes that both restrict motion and displace structures like axons that tend to have higher anisotropy. For that reason, there is great interest in using diffusion imaging in brain tumors."* [10] *„Diffusion MR approach is complementary to fluorodeoxyglucose (FDG) positron emission tomography (PET), which seems to be more sensitive in lungs and perhaps in lymph nodes, but diffusion MR imaging, which does not use ionizing radiation and any tracer and affords better spatial resolution, appears promising for the management of breast, prostate, liver, and thyroid cancers, as well as lymphomas.*

---

[20] Fibrous structures of muscles and white brain matter.

[21] Brain ischemia means an insufficient blood flow to a brain. Acute brain ischemia happens abruptly and demands an immediate health care. While, chronic brain ischemia means progressive narrowing of arteriae caused by ageing and wrong lifestyle.

Furthermore, diffusion MR imaging gives access to tissue obscured by sites of physiologic FDG accumulation, such as in the pelvis around the bladder.“ [11]

Diffusion is mostly isotropic, so does not depend on the direction, thus the diffusion probability is the same in all directions. The diffusion might be also anisotropic (highly influenced by the direction of the diffusion gradient) in some tissues, such as white brain matter and muscles. The result of the diffusion MR imaging is either a gray map representing the diffusion scale (DWI) or a color scale map (Diffusion Tensor Imaging (DTI)). Isotropic diffusion can be represented by the DWI method, whereas the DTI method is a great tool for visualization of anisotropic diffusion. In my thesis the emphasis is put on diffusion weighted imaging method.

Gray brain matter shows isotropic diffusion, whereas white brain matter shows its direction dependency, thus DTI is the right method to investigate the white matter. In the structures of gray matter there is no coherence between internal structures, thus gray matter is isotropic. *„Water diffusion is anisotropic in brain white matter, because axon membranes limit molecular movement perpendicular to the fibers.“* [15] *„It was found that the diffusivity in white matter structures is much slower when the diffusion is measured perpendicular to the neuronal fiber orientation, than in parallel.”* [17] While diffusion in the isotropic media can be described by a single number, the diffusion in the anisotropic media can be calculated via 3x3 matrix, so-called the diffusion tensor, representing diffusion along three axes.

4.1. The mathematics of diffusion

Diffusion processes in general can be described by two Fick´s laws. According to the Fick´s first law 4.1, flux of particles J is directly proportional to the concentration gradient ∇C related by the diffusion coefficient D. The Fick´s first law determines the density and the direction of flux. The flux depends on the material microstructure as determined by the diffusion coefficient. The negative sign in the equation indicates the particles flow from higher to lower concentration. The fact that particles´ concentration gradient decreases with an increase in time is not considered while using the Fick´s first equation.

$$J = -D\frac{dC}{dx} \qquad (4.1)$$

- J: diffusion flux $[\frac{1}{m^2 \cdot s}]$

- D: the diffusion coefficient $[\frac{m^2}{s}]$
- $\frac{dC}{dx}$: the concentration gradient at the position x $[\frac{1}{m^4}]$

The Fick´s second law (4.2) indicates the concentration change over time t is equal to the change in the diffusion flux.

$$\frac{\partial C}{\partial t} = D \frac{\partial^2 C}{\partial x^2} \qquad (4.2)$$

Both Fick´s laws describe the macroscopic mutual diffusion in which particles drift to lower concentration.

4.1.1. Diffusion parameters

The diffusion coefficient D (the diffusivity) gets increased proportionally to the absolute temperature T and is inversely proportional to the viscosity of the medium η and the size of diffusing particles, as highlighted in the Stokes-Einstein equation[22] 4.3. The diffusivity expresses how fast one material can go through another material. The higher diffusivity, the faster diffusion process. The D of pure water at room temperature is $2.2 \cdot 10^{-3}\ mm^2 \cdot s^{-1}$.

$$D = \frac{k \cdot T}{6\pi \cdot \eta \cdot \mathrm{R}} \qquad (4.3)$$

- k: the Boltzmann constant[23], $k = 1.38 \cdot 10^{-23}$ $[m^2 \cdot kg \cdot s^{-2} \cdot K^{-1}]$
- T: the thermodynamic temperature $[T]$
- η: solvent viscosity of a medium η $[kg \cdot m^{-1} \cdot s^{-1}]$
- R: a particle radius R $[m]$

The susceptibility to diffusion, thus a range of diffusion weighting, is described with the *b* value including the strength and time duration of diffusion gradients (so the area under the gradient pulse amplitude vs. time curve). The higher *b* value, the stronger diffusion effect. The consequence of using higher *b* values is the contrast improvement, but it means low *Signal*

---

[22] The Stokes-Einstein equation can be applied for particles in a viscous fluid.

[23] The Boltzmann constant expresses the relation between the energy and the temperature of the gas in thermodynamics.

to Noise Ratio (SNR)[24]. While applying higher *b* values longer acquisition time usually follows[25], thus some motion artefacts can be present. A number of *b* values and their numerical values are selected prior the examination. The MR signal attenuation is high for large *b* values and in the case of fast diffusion. The unit of *b* value is $[\frac{s}{mm^2}]$. Greater diffusion weighting, thus a larger *b* value, is accomplished by increasing the gradient amplitude G, duration δ and by making wider the interval between gradient pulses Δ. Thus, *b* value is calculated according to the formula 4.4.

$$b = \gamma^2 \cdot G^2 \cdot \delta^2 \cdot \left(\Delta - \frac{\delta}{3}\right) \qquad (4.4)$$

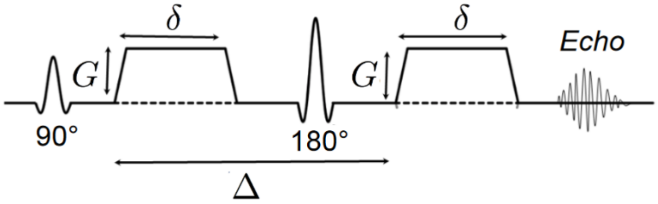

Figure 4.2: The pulsed MR gradient diffusion method within the EPI sequence, two diffusion gradient lobes are inserted along both sides of the 180° RF pulse. [12]

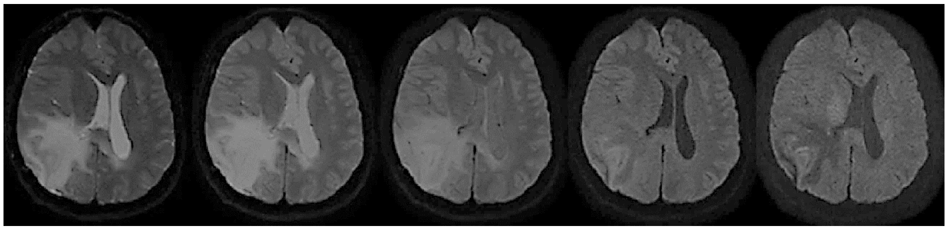

Figure 4.3: DWI axial brain images for 5 b values from left to right, $b = 0, b = 200, b = 500, b = 1000, b = 2000$ $[\frac{s}{mm^2}]$.

The ADC (*Apparent Diffusion Coefficient*) represents a degree of diffusion within tissue. Its unit is $[\frac{mm^2}{s}]$. The importance of this parameter is its reproducibility in the clinical practice. The study [13] revealed the reproducibility of the ADC measurement of malignant hepatic tumors. Today´s MR scanners enable to automatically obtain the ADC parametric map (a graphical representation

---

[24] SNR measure is intended to compare the level of signal to the background noise level.

[25] The higher *b* value, the longer duration of diffusion gradient pulse application. The echo T_E and repetition T_R time get increased; thus, the acquisition time is longer. Moreover, at higher *b* values, lower signal level is reached. The compensation technique lies in several repetitions of excitation sequences; determined with the *Number of Excitations* (NEX).

of ADC values) by acquiring of the DWI set of images at two *b* values, $b = 0$ and a non-zero *b* value. The ADC parameter might be calculated according to the formula 4.5. The structures with low ADC values are displayed with a dark color, whilst a bright color represents high ADC values. *„ADC maps can provide additional information for tumor grading and assessing the effects of therapy in cases where T_1- and T_2-weighted images alone provide insufficient diagnostic information."* [10]

$$ADC = -\frac{\ln\left(\frac{S}{S_0}\right)}{b} \qquad (4.5)$$

- S_0: a signal intensity of no diffusion gradients [-]
- S: a signal intensity for *b* value [-]
- b: a non-zero *b* value used for ADC calculation [$\frac{s}{mm^2}$]

Brain tissue	**ADC [x 10^{-3} $mm^2 \cdot s^{-1}$]**	**Relative signal (at $b = 1000$) [$\frac{s}{mm^2}$]**
CSF	2.94	0.05
Gray matter	0.76	0.47
White matter perpendicular to fibers	0.45	0.63
White matter parallel to fibers	0.95	0.39

Table 4.1: Typical ADC values for human brain tissue. [2, p. 331] The diffusion in a fluidic CSF is not hindered, thus ADC value of CSF is the highest and it means the lowest measured signal level. Water diffusion is less restricted in the CSF than in gray and white brain matter. The difference of calculated ADC values and measured signal in gray and white matter is due to their composition. White matter is composed of myelinated[26] axons, while gray matter mostly of unmyelinated axons. The water composition of GM (80%) is higher than in WM (70%) [14], thus the diffusion in gray matter is faster. The rate of diffusion is lower for white matter measured perpendicular to the neuronal fibers than in parallel to fibers, thereby the ADC in the perpendicular direction is lower than in the parallel direction.

4.1.2. Diffusion in human tissue

The utterly homogenous material shows isotropic diffusion. Water molecules in a human body, which is not homogenous material, are located in intracellular and extracellular environments.

---

[26] Myelin is a lipid-rich insulating layer that forms around nerve cell axons.

„Water molecules in extracellular environments experience relatively free diffusion while intracellular molecules show relatively "restricted diffusion". Different tissue of the human body has a characteristic cellular architecture and proportions of intra and extracellular compartments; and hence have characteristic diffusion properties. The relative proportion of the water distribution between these compartments is affected by the pathologic processes." [15] Water molecules are located between the intracellular and extracellular space approximately in a ratio 3:1 depending on the exact tissue and the organ. Water molecules diffusion is more hindered in the intracellular space, due to the presence of macromolecules and membranes with higher viscosity, than in the extracellular space. Water diffusion in tissue with high cellular density is more restricted than in tissue with low cellularity. *„Also the cellularity (ratio of volume occupied by the cells to the volume of the extracellular space) has a large impact on the diffusion in biological tissues. When the number of cells increases, as in cancer, there is less extracellular space to allow diffusion, thus the diffusion drops."* [16]

In living tissue, the diffusion is not free, the diffuse water molecules are hindered by cell membranes and fibers. It follows, the diffusion in tissue deviates from the Gaussian law, unlike pure liquids, for instance. In the diffusion coefficient D calculation, there is a deviation due to the interaction of water molecules with some obstacles, thus D is not the free diffusion coefficient, hence, ADC coefficient was released. No single D value fully describes the diffusion process in living tissue. The stronger diffusion effect, the more significant non-Gaussian behavior.

According to the Gaussian model, the graphical representation of the signal attenuation against the *b* values is a straight line with its slope ADC value. The signal intensity S from the tissue with the Gaussian model can be calculated according to the formula 4.6 with the traditional mono-exponential model. The assumption of this model is that all water molecules follow the Gaussian law. It is a simple model widely implemented in most MR scanners.

$$S = S_0 \cdot e^{-b \cdot ADC} \qquad (4.6)$$

To model the non-Gaussian behavior, several models can be implemented. For instance, it is the Kurtosis model, the Stretched Exponential model and the Statistical model. Moreover, *Intravoxel incoherent motion* (IVM) (a biexponential model) can be present as well, in detail explained in the chapter 4.3. The non-Gaussian behavior is considerably visible at high *b* values. The behavior departing from the mono-exponential function can be recognized by applying a large *b* value.

- **Diffusion Kurtosis Imaging**

An example of non-Gaussian diffusion effect is the *Diffusion Kurtosis Imaging* (DKI). The Kurtosis effect is likely to be observable at higher *b* values (roughly higher than 1500 $\frac{s}{mm^2}$). The diffusion effect is stronger when gradient pulses are applied along the axons of cells. The signal attenuation level at these larger *b* values is lower than expected (see the figure 4.6) At lower *b* values the signal attenuation is almost straight just as with the Gaussian diffusion. „*Whole-body diffusion kurtosis imaging has the potential to extract more microstructural information than the ADC, as a high-degree diffusion weighting (high b values) increases the effect on the signal of obstacles to free diffusion present in tissue, notably cell membranes.*“ [11]

The non-Gaussian diffusion in the Kurtosis model includes an additional term to calculate the measured signal level. K parameter represents a degree of a deviation from the mono-exponential model, it means when Gaussian diffusion is taken into account. DKI tool requires to use at least three *b* values ($b = 0$ and two non-zero *b* values) to acquire model parameters D and K. The Kurtosis fitting model can be unstable when reaching high *b* values.

$$S = S_0 \cdot e^{-b \cdot \mathrm{D} + \frac{b^2 \cdot \mathrm{D} \cdot \mathrm{K}}{6}} \qquad (4.7)$$

- ○ K: the Kurtosis parameter $[\frac{mm^2}{s}]$[27]

- **Stretched Exponential model (SEM)**

The Stretched Exponential model is modification of the mono-exponential model. Unlike the mono-exponential model, this model does not consider any shape of distribution of diffuse molecules. The parameters DDC and α were acquired by fitting the SEM to the DWI data according to the equation 4.8. It is necessary to utilize at least three b values ($b = 0$ and two non-zero b values) to optimally fit the model and obtain the parameters DDC and α. The DDC parameter has the same properties as the ADC coefficient. α values range between 0 and 1 and represent the heterogeneity of the diffusion signal. If $\alpha = 1$ all water molecules diffuse in tissue follow the Gaussian distribution.

---

[27] The Kurtosis parameter for the Gaussian diffusion is zero, for non-Gaussian diffusion K is usually positive.

$$S = S_0 \cdot e^{[-(b \cdot \mathrm{DDC})^{\alpha}]} \qquad (4.8)$$

- DDC: a distributed diffusion coefficient $[\frac{mm^2}{s}]$
- α: a heterogeneity index [-]

- **Statistical Diffusion model (SDM)**

The signal attenuation rate of the SDM is influenced by parameters of the Gaussian distribution; a center of the Gaussian distribution D_g and the width of the Gaussian distribution σ. In the case of unrestricted diffusion, the width of the Gaussian distribution tends to zero. The SDM for small *b* values reduces to the mono-exponential model.

$$S = S_0 \cdot \frac{1 + \Phi \cdot (\frac{D}{\sigma \cdot \sqrt{2}} - \frac{b \cdot \sigma}{\sqrt{2}})}{1 + \Phi \cdot (\frac{D}{\sigma \cdot \sqrt{2}})} \cdot e^{-(b \cdot \mathrm{D} + \frac{1}{2} \cdot b^2 \cdot \sigma^2)} \qquad (4.9)$$

where Φ is the error function.

$$\Phi(\mathrm{x}) = \frac{2}{\sqrt{\pi}} \int_0^x e^{-t^2}\, dt \qquad (4.10)$$

4.2. Diffusion weighted imaging

Diffusion weighted imaging is characterized by measuring the random diffusion movement of water molecules within tissue voxels in various directions. DWI is an indispensable tool for examining the central nervous system (CNS). DWI MR method is a key technique for stroke patients and can detect early brain injuries during an infarct, too. It is a right method to pinpoint brain tumors. *„ADC values have been shown to be decreased in highly cellular tumors such as CNS lymphoma, medulloblastoma, and high-grade glioma. Lower ADC values have been reported to be associated with higher-grades and poorer prognosis.“* [15]

When spatial encoding gradients are on, stationary spins along the gradient magnetic field direction will feature with a lower phase shift, whereas phases of moving diffusing spins will be more affected, thus it follows a greater loss of signal. The amount of loss signal is proportional to the diffusion rate.

In order to obtain absolutely DWI weighted image, the repetition time is long to minimize T_1 effects. In order to avoid T_2 effects, the T_E echo time should be as low as possible, however, to apply both diffusion gradients, longer T_E is required. Hence, each DWI image is also T_2 weighted image. The idea of DWI stems from the T_2 signal attenuation that determines a degree of diffusion. If molecules can diffuse through the material more easily, the higher signal attenuation is followed. In the structures with the free diffusion the low signal level is measured, thus this structure is highlighted with a dark color. In contrast, structures that hinder the diffusion are highlighted with a light color, because there is not significant signal attenuation. DWI images might be misinterpreted due to the T_2 *shine through effect*. If T_2 relaxation time of some pathologic tissue is long, it might cause the signal increase in the isotropic DWI image that can be subsequently wrongly assessed as diffusion restrictions. In contrast, ADC maps eliminate this effect and can objectively asses the diffusion rate. Higher *b* values eliminate this effect, too.

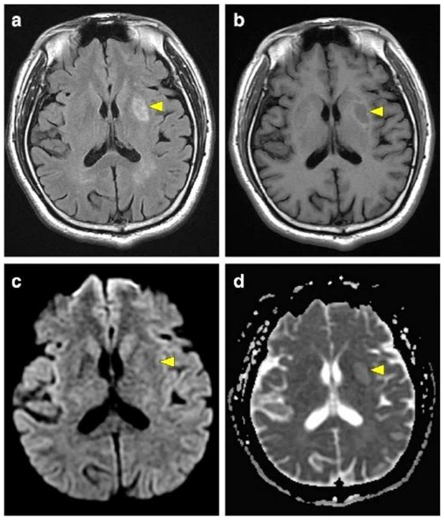

Figure 4.4: MR axial brain scans showing the presence of a subacute to chronic infarct in the left putamen, a: FLAIR image, b: T_1 weighted image, c: DWI image, d: ADC map. [18]

4.2.1. DWI Pulse sequence

DWI images, which are commonly acquired with EPI sequences, are significantly prone to image distortions. Moreover, the DWI protocol is often quite long[28], thus the DWI sequence is sensitive

---

[28] The DWI exam itself does not take too long time, but the whole DWI protocol usually includes applying several *b* values, thus the exam prolongs.

to motion distortions[29]. The origin of the distortions and the following correction algorithms are explained in the section 6.3.2.

A degree of diffusion is determined by the b value. DWI pulse sequences often begin with the acquisition of T_2 image with no diffusion weighting, which means a baseline $b = 0$ image. During the DWI MR scan additional diffusion encoding gradients are applied in all three directions simultaneously with imaging gradients. The diffusion gradients are active right before and right after the 180-degree pulse. The diffusion gradients make the sequence susceptible to diffusion. Both gradients cause a residual phase shift in diffusion spins, thus subsequent further signal attenuation. The readout process starts immediately after the second gradient ceases. Unlike conventional MR imaging methods, DWI requires a higher performance of gradient coils, since the diffusion gradients must be rapidly switched on and off.

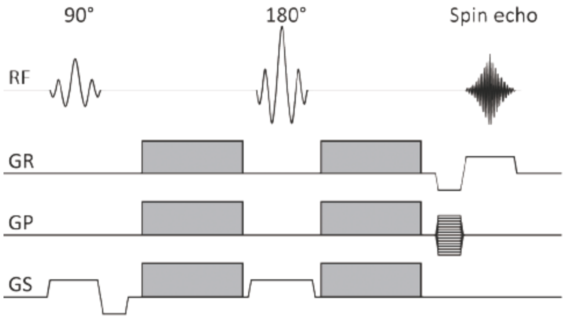

Figure 4.5: DWI sequence, GR is a read-out (a frequency encoding gradient in x-axis), GP is a phase encoding gradient in y-axis, GS is a slice selective gradient in z-axis. Diffusion gradients (gray rectangles) are applied in all axes on both sides of the 180° pulse. [19]

4.3. Intravoxel incoherent motion

As discussed in the section 4.1.2., diffusion in biologic tissue does not follow the Gaussian distribution. The induced signal loss is due to the water molecules random movement. IVIM concept provides an extra view on MR diffusion methods. The perfusion imaging technique IVIM, the powerful addition to the diffusion MRI, incorporates two effects causing non-exponential signal loss whose decay velocity depends on b values. Not only is the microscopic water molecules movement caused by diffusion (true diffusion) but also by the blood flow in capillaries,

---

[29] Head motion is not very susceptible to the origin of this kind of artefacts. Motion distortions are commonly distinct in abdominal examination, for instance.

the so-called capillary perfusion. Both effects play an important role on a subvoxel scale. Microcirculation in the bloodstream, the so-called pseudo-diffusion, represents water molecules movement from one capillary to the next one. The blood stream in capillaries mimic diffusion processes. This effect influences the DWI signal primarily at low *b* values. Above this low *b* value threshold in the case there are no perfusion effects, the ADC is equal to the diffusion coefficient in tissue. If the perfusion is given in voxels, the ADC is higher than the diffusivity D. *„IVIM-DWI thereby provides the opportunity not only to compute an ADC value but rather to measure the respective influence of true molecular diffusion and microcirculation within a voxel.“* [20] The signal attenuation highly depends on a blood velocity and a structure of the bloodstream. Due to the fact the pseudo-diffusion effect vanishes 10 times faster than diffusion, both effects can be separated. [21] To separate both effects, the high SNR must be present. However, there is not an exact value of the *b* parameter to determine a threshold where both effects can be separated. This threshold is chosen according to the SNR parameter values and the expected perfusion rate depending on an examined part of the body. Both effects themselves contribute to the mono-exponential MR signal decay. IVIM allows to simultaneously make use of both diffusion and perfusion imaging concepts. The importance of IVIM method is the ADC calculation and especially determining of diffusion and perfusion contributions within voxels.

The final DWI IVIM signal is acquired by scanning with several *b* values. At low *b* values (lower than 300 – 500 $\frac{s}{mm^2}$) there is larger MR signal attenuation due to capillary perfusion. In the case strong diffusion gradients are applied, the diffusion effect prevails over the perfusion effect, whilst with weaker diffusion gradients the IVIM capillary perfusion effect contributes significantly to signal attenuation. The choice of *b* values depends on the examined organ.

IVIM effect is very different in other vessel types due to their different structure. Large vessels might experience the IVIM flow since the laminar or turbulent flow cause the spatial distribution of blood velocities in vessels resulting in the IVIM effect. A signal from large vessels with the rapid flow acquired with low *b* values decay very fast, whereas a signal from small vessels with a slower flow might contribute to the IVIM effect.

4.3.1. The use of IVIM

Diffusion and perfusion MRI are becoming more relevant in the clinical use since both methods can provide information about the tissue properties, such as cellularity and vascularity. The IVIM effect is not only related to the blood flow, it is also susceptible to any flow if there is the IVIM distribution. The CSF flow, which might be a right example, can be altered in several pathological conditions, such as hydrocephalus[30] and syringomyelia[31]. The flow from a pancreas, salivary glands and breast ducts can be right examples as well. In addition, the tubular flow and the vascular perfusion in kidneys can be described by the IVIM technique, too.

MR diffusion sequences are part of today´s MR scanners protocols, thus IVIM images can be easily obtained simultaneously with DWI images. Furthermore, IVIM exams do not require the contrast agents[32] administration. Hence, this technique is relevant in patients with renal failure[33] and in patients with adverse reactions to contrast agents.[34] IVIM techniques might be implemented due to substantial technical MR hardware progress, especially due to large MR gradients and MR sequences development.

According to my information, IVIM methods have never been put into practice yet. Its practical significance is still being investigated. *„IVIM is a niche in clinical practice because it is not implemented in commercially available software, and depends on off-line analysis in custom software."* [16] On the other hand, IVIM has successfully showed its significance in various organs, often related to oncological applications. IVIM method could be used in a field of oncology for differentiation of brain tumors as my master´s thesis is focused on. *„Brain imaging with IVIM is particularly challenging due to the low blood volume fractions of cerebral tissue and CSF partial volume contamination."* [22] The study [22] investigated patients

---

[30] Hydrocephalus is a condition featuring with an abnormal build-up of the CSF. It causes the increased pressure inside the skull.

[31] Syringomyelia is a genetic condition in which a cyst or a cavity form within the spinal cord.

[32] Contrast agents have become a vital part of MR imaging used to better visualize inner organs since they improve the tissue contrast. In general, contrast media adjusts the relaxation rates in tissues where they accumulate.

[33] Gadolinium based contrast agents might increase risks of disease nephrogenic systemic fibrosis in people with severe kidney failure.

[34] There are other MR techniques measuring perfusion. *Arterial Spin Labeling* (ASL) does not demand the administration of gadolinium contrast medium but its drawback is limited spatial resolution. The study [108] revealed the correlation between some IVIM and ASL parameters in brain tumors. Other perfusion methods, *Dynamic Susceptibility Contrast* (DSC) and *Dynamic Contrast Enhancement* (DCE), require the contrast agents administration.

with brain tumors and acute strokes: „*Recent work in neuro-oncology has shown the potential for IVIM in differentiating tumor recurrence from posttreatment effects in the preoperative evaluation of tumor grade and in differentiating primary CNS lymphoma from glioblastoma. IVIM has also been applied in the setting of acute stroke.“* The studies [23] [24] showed the potential of IVIM to assess the liver cirrhosis and to characterize liver lesions. Moreover, renal dysfunction might be detected by this technique, too. [25] The potential of IVIM concept is rapidly extending.

IVIM concept might be also an optimal approach for non-perfusion aspects. IVIM could be also used in the future in MR IVIM virtual elastography for assessing mechanical properties of soft tissue, which means for detecting liver fibrosis, for example. The correlation between IVIM and MR elastography was confirmed. „*Mechanical vibrations used for MR elastography also induce phase distributions in each tissue voxel and an IVIM effect when considering the amplitude of the signal. This IVIM effect will be larger in normal tissue than in lesions, presenting higher elasticity values, and IVIM MRI could be used, potentially, to estimate those elasticity values.”* [26] In addition, supposing the flow in large vessels leads to the velocity distribution within the vessels lumen and subsequent IVIM signal attenuation, IVIM can be used for 3D angiography, too. [21] Therefore, it brings advantage for evaluating the blood vessels and identifying their abnormalities without the need of a contrast medium administration.

4.3.2. IVIM limitations

To correctly estimate IVIM parameters, handling with the noise must be taken into consideration. A high level of noise might highly impact the calculated IVIM parameters. A high SNR value is essential to overcome noise distortions. This value is limited, beside other indicators, by artefacts caused by other flow sources. Hence, it is difficult to separate the flow in the area of kidneys, salivary glands, pancreases and mammary glands. „*At high b values, when SNR becomes low, the signal reaches a “noise floor” and does not get to 0. The signal attenuation appears curved, even for mono-exponential diffusion, and fitting signals with any diffusion model will give erroneous values.“* [21] Especially the perfusion fraction parameter f is susceptible to noise distortions leading to underestimation of this parameter that can even become negative. [21] The noise can be minimized by using phase-array coils[35]. Although the higher noise

---

[35] Phased array coils are RF receiving coils consisting of multiple surface coils aligned into an array.

level is more common at high *b* values, images acquired with low *b* values can be disrupted by the noise, too.

In the case of the non-Gaussian behavior at large *b* values, the noise is more evident. The signal does not reach the zero level but is still above a threshold, the so-called the Rician noise floor. The noise can cause the discrepancy between DWI acquired data and calculated IVIM parameters. *„However, the fitting process is known to be sensitive to noise and may lead to erroneous or inaccurate parameter estimates if the number of acquired signals is not very large compared to the number of parameters to estimate.“* [21] The distortions due to noise in diffusion (IVIM) images are in detail described in the section 6.3.2.1.

Another deviation might originate from not perfectly calibrated RF pulses. This imprecision is inherent arising due to the B_0 field inhomogeneity. An important drawback of IVIM is the lack of standardization of scanning parameters and the choice of *b* values. [16]

4.3.3. IVIM model

IVIM effect of the biexponential model, today´s most common model, is represented with the equation 4.11. The parameter f (dimensionless), the flowing component, represents the perfusion fraction[36] (the area of intravascular space), so the percentage expression of voxels volume occupied by capillaries. The f parameter is high in greatly perfused tissue. While the static parameter $(1-f)$ represents the area of extravascular space where only diffusion is evident, so no perfusion processes at all. $\mathrm{D}*$ pseudo-diffusion coefficient in the blood is a rate of spins dephasing due to the pseudo-diffusion effect. $\mathrm{D}*$ is usually one order of magnitude greater than the diffusivity D in the tissue. [27] Due to this fact, the $\mathrm{D}*$ effects at *b* values higher than approximately 200 $\frac{s}{mm^2}$ on signal attenuation level can be neglected. As a result, at these higher *b* values the equation 4.11 can be adjusted to the basic form 4.6.

$$\frac{S}{S_0} = (1-f) \cdot e^{(-b\cdot\mathrm{D})} + f \cdot e^{(-b\cdot\mathrm{D}*)} \qquad (4.11)$$

---

[36] Under the assumption of the IVIM concept, protons in the blood do not leave the bloodstream. Otherwise, this fact might be another source of a mistake when estimating f parameter.

ADC parameter is calculated according to the formula 4.12. ADC coefficient gets increased at low *b* values, because perfusion contributes to ADC values more at low *b* values.

$$ADC = D + \frac{f}{b} \qquad (4.12)$$

The semilogarithmic relation of signal attenuation on the y-axis and *b* values on the x-axis without the pseudo-diffusion effect is a straight line with a slope of the D parameter. When both effects are considered, both effects contribute to the MR signal separately leading to a bi-exponential shape of the function.

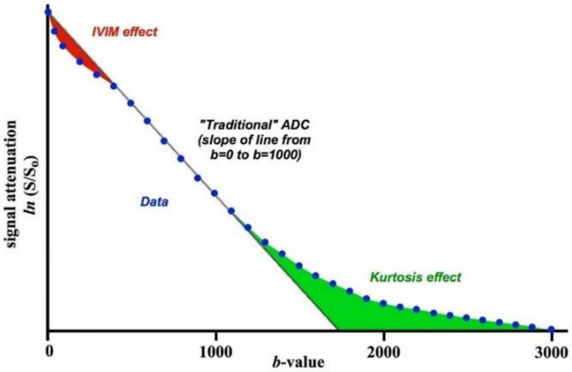

Figure 4.6: A semilogarithmic plot of signal attenuation $\ln\left(\frac{S}{S_0}\right)$ *vs b values. When only Gaussian diffusion is considered, this relation is represented by a straight line with the slope of* D *coefficient. While, when both effects, so diffusion and pseudo-diffusion are taken into account, the curve is changed to its bi-exponential shape. The IVIM effect is observable at low b values. The signal attenuation is greater at low b values than expected. The non-Gaussian Kurtosis effect is observable at higher b values. The signal attenuation is lower at high b values than expected. [28]*

By acquiring DWI images with the EPI sequence at several *b* values and subsequent fitting of MR signals values, IVIM parameters f, D and $D*$ can be extracted. Since the IVIM effect is observable at low *b* values, more low *b* values are considering. Due to the fact there are three IVIM parameters, a minimum of three *b* values must be used to describe the bi-exponential IIVM model. *„The number of b values used for extracting perfusion-sensitive information at DW-MRI varies between studies and ranges from four to more than 10."* [29] If the images are acquired with more *b* values, the more accurate IVIM parameters calculation and the total inaccuracy estimation is given. On the other hand, longer acquisition is followed. It follows, a balance between the acquisition time and the image quality must be taken into consideration. [16] The parameters estimation is influenced by physiologic processes in the tissue and by the noise. The number of implemented *b* values and their numerical values influence the final IVIM parameters calculation. IVIM fitting methods, the parameters extraction and their statistical analysis, which I implemented in my practical task, are described in the chapter 9.

As mentioned above, the bi-exponential model is the most common model type. However, there are other models fitting the IVIM parameters. Two other important models are described.

- **Sinc model**

Signal attenuation can be modeled with the $sinc$ function[37] since the blood flow is not too fast, capillary segments are long and long measurement time cannot be accomplished. [21] In this case, blood nuclear spins remain in capillary segments during the diffusion encoding. The c coefficient is the pulse gradient factor similar to the diffusion *b* value. The $D*$ can be calculated according to the formula 4.14. $D*$ does not depend on the capillary length since nuclear spins do not travel through capillary segments when the diffusion encoding is on. [21]

$$\frac{S}{S_0} = f \cdot e^{(-b \cdot \mathrm{D})} \cdot sinc(c \cdot v_{blood}) \qquad (4.13$$

$$\mathrm{D}* = \frac{{v_{blood}}^2 \cdot c^2}{6 \cdot b} \qquad (4.14)$$

- **Mono-exponential model**

In today´s clinical studies another IVIM model is present; the mono-exponential (pseudo-diffusion) model. *„The exponential pseudo-diffusion model assumes blood changes several times direction (capillary segment) during the encoding time. This condition is met when flow is fast enough, capillary segments are not too long and the encoding time is long enough to accommodate those direction changes.“* [21]

$$\frac{S}{S_0} = f \cdot e^{[-b \cdot (\mathrm{D} + \mathrm{D}*)]} \qquad (4.15)$$

---

[37] The sinc function is defined for x ≠ 0 as $sinc(x) = \frac{\sin(x)}{x}$

The pseudo-diffusion coefficient $\mathrm{D}*$ is a sum of the IVIM effect and the diffusion coefficient of water molecules in blood D.

$$D *= \frac{L \cdot v_{blood}}{6} + D \qquad (4.16)$$

- L: mean capillary segment length $[m]$
- v_{blood}: a blood velocity $[\frac{m}{s}]$

Unlike these both models; sinc and mono-exponential model, the bi-exponential model can better describe a whole IVIM concept, because this model contains contributions to IVIM signal from both areas, so from intra and extravascular space.

4.3.3.1. IVIM fitting algorithms

A major challenge of IVIM is to estimate the parameters with high accuracy and to obtain the parametric maps (distribution of IVIM parameters) with a low noise level. Therefore, the IVIM fitting model plays a vital role. IVIM parameters numerical values may depend on a chosen fitting algorithm. Errors in IVIM parameters estimation might be overcome by increasing SNR of the acquisition technique, choosing a higher number of *b* values and by application of post-processing denoising filters and other distortions correction techniques. *„Generally, more* b-*values will improve fitting stability, so at this stage we would recommend acquiring as many* b-*values as practical.“* [30]

It is possible to fit the data of both effects at the same time or to split the fitting process into two fitting steps; the first for diffusion from high *b* values and the second for perfusion at low *b* values after removing the diffusion signal part. This iterative fitting algorithm is more robust.

Acquired diffusion MR signals are fitted to a specific IVIM model. The estimation of all IVIM parameters is performed voxel by voxel. The explanation of fitting algorithms below is given for the bi-exponential model. There are two main fitting types; the first based on the least squares algorithms and the second based on the probability theory.

4.3.3.1.1. Least squares algorithms

MR IVIM parameters estimation based on least squares fitting algorithms are so far the most typical. However, it is speculated about its susceptibility to noise. The mathematical description of least squares fitting algorithms is given in the appendix in A.I.

Since the IVIM model consists of three parameters, there might be three fitting approaches.

- **One step fitting method**

Within *one step fitting* method all IVIM parameters are fitted simultaneously in a single process over all *b* values using the equation 4.11. This method is simple, but the estimated parameters are not usually accurate due to the interaction between diffusion and pseudo-diffusion components of the signal. Its drawback is the limited robustness. Hence, the parameters estimation might be improved by implementation of step by step fitting algorithms that are more robust and moreover, show substantial lower computational cost.

- **Two steps fitting method**

The D parameter is derived from the conventional mono-exponential model 4.6 since it is assumed perfusion effects are negligible at high *b* values; approximately higher than 200 $\frac{s}{mm^2}$. The f and $D*$ are after that derived from the bi-exponential fitting 4.11 over all *b* values.

- **Three steps fitting method**

Together with the *two steps fitting* method, the D is derived from the mono-exponential model. Secondly, the parameter f is calculated according to the formula 4.17. The last step is to derive the $D*$ parameter from the bi-exponential equation 4.11 over all *b* values.

$$f = \frac{S_0 - S(int)}{S_0} \qquad (4.17)$$

- $S(int)$: an intercept of the signal curve with the y-axis

At high *b* values the signal can be approximated with the mono-exponential decay and even simplified with a linear fit. Therefore, in *two* and *three steps fitting* methods, the D parameter can be obtained with a linear regression (linear least squares) algorithm using *b* values higher than roughly 200 $\frac{s}{mm^2}$. An initial value of the f parameter is given as the y-axis intersection of the linear regression based on the equation 4.17. f and $D*$ parameters are also derived from the bi-exponential fitting 4.11 with implementing the non-linear least squares method.

4.3.3.1.2. Algorithms based on probability theory

There are two significant fitting algorithms based on probability theory, namely the Bayesian method and the maximum likelihood estimation. In a nutshell, the Bayesian theorem describes the process how to update probability of an event based on prior knowledge of all conditions related to the event. Maximum likelihood estimation (MLE) is a method to estimate the parameters of given data distribution using some observed data. The detailed mathematical description is shown in the appendix A.II.

5. Magnetic resonance imaging of the central nervous system

Magnetic resonance imaging plays a vital role in neuroimaging. *„MRI of the brain is the most commonly performed examination at most institutions which reflects the enormous amount of information that MR provides about this complex organ.“* [2, p. 19] MR is able to differentiate between gray and white matter and is an indispensable tool for brain tumors and other brain abnormalities detection. There are two basic MR brain exams; with and without contrast agents administration. The contrast-free brain exam is used for general brain disorders evaluation. The exam with contrast medium administration is intended to be used in patients for inflammatory processes imaging, tumors detection, diffusion and other abnormalities detection.

This chapter incorporates a basic description of brain anatomy. It gives a description of the brain segments that are utilized in the practical task, namely brain edema, a contrast enhanced part brain lesions (tumors) and a contrast non-enhanced part of tumors. An example of the brain image with highlighted these three brain segments is introduced in the section 8.4. Three types of brain tumors the patients from this study suffered from are briefly explained here.

5.1. Brain anatomy on Magnetic Resonance Imaging

The nervous system is divided into the central and peripheral nervous system. The central nervous system includes the brain, cranial nerves and the spinal cord, whereas the peripheral nervous system encompasses the nerves outside the CNS. The description in this section is focused on the brain.

The brain is housed in a bony structure called the skull (*cranium*) that cushions the brain from injury. Between the brain and the skull there are three layers of the meninges protecting the brain and the spinal cord. *Cerebrospinal fluid* (liquor), which is clear and colorless, is found within the brain and the spinal cord. Its total volume is approximately 150 ml and its daily production is approximately 450 ml, which means it is replaced itself three times a day. [32] Liquor has mechanical and supportive functions and also protects the brain from sudden temperature and pressure changes. *„Liquor helps to maintain the correct composition of the environment surrounding nervous tissue cells (homeostasis). It also partially provides the supply of nutrients* *and disposal of the metabolic waste products and forms a medium through which a diffusion of a various signal molecules (like neurotransmitters) takes place.“* [33]

The central nervous system incorporates two fundamental tissues; gray matter and white matter. Gray matter is typical for the tissue composition of neuron cell bodies, dendrites and unmyelinated axons, whilst white matter of myelinated axons. Gray matter is located in the areas with higher concentration of cell bodies. The white matter is situated in deeper subcortical brain areas where axon tracts prevail. Brain structures dominantly composing of gray matter are responsible for sensory perception and muscular activity. Since white matter is composed of myelin, it helps to insulate axons and enables to fasten the nerve signals transportation to the spinal cord. According to studies [34] [35], the *gray-white matter ratio* (GWR) might be in the future a significant tool in clinical practice.

„By definition cerebral edema is the excess accumulation of water in the intra- and/or extracellular spaces of the brain.“ [36] The magnetic resonance is an inevitable tool for an early brain edema detection. In T_2 and FLAIR images brain edema produces increased signal (hyperintensity) while in T_1 images a decreased signal level (hypointensity).

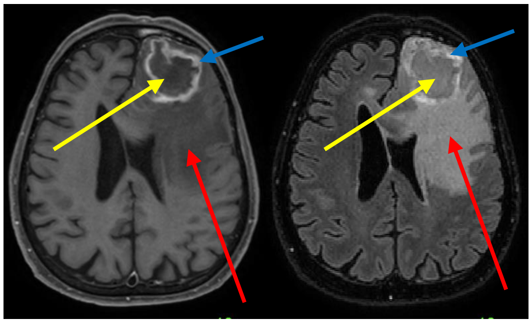

Figure 5.2: The brain image with brain edema, contrast enhanced and non-enhanced part of a brain tumor, visualized in the axial plane, marked with arrows (red arrows: brain edema, yellow arrows: not contrast enhanced part of a tumor (an inner part of bordered area), blue arrows: contrast enhanced part of a tumor (a border of the inner part)). On the left: in the T_1 image brain edema represents the signal hypointensity, thus it is visualized with a dark color. On the right: in the FLAIR image brain edema represents the signal hyperintensity, thus it is visualized with a light color. This kind of a brain tumor is more hyperintense on FLAIR image.

A brain lesion refers to an abnormality in the MR image. Lesions might be caused by trauma, inflammation within brain tissue, disease and genetic defects. Different types of brain lesions appear on brain MR images in a different way. A common type of a brain lesion is a brain tumor. Brain tumors represent a mass of abnormal cells in the brain. The study [37] gives a list of typical MR sequences used for brain tumor detection. *„Conventional structural magnetic resonance imaging (MRI) remains the standard of care imaging method for neuro-oncologic practice. Current consensus recommendations for a standardized brain tumor MRI protocol are the following: 3-dimensional (3-D) T_1, axial fluid-attenuated inversion recovery (FLAIR), axial diffusion-weighted imaging (DWI), axial gadolinium contrast-enhanced T_2, and 3-D gadolinium contrast-enhanced T_1, performed on a minimum 1.5 tesla MR system. If 3-D sequences cannot be performed due to time constraints or technical limitations, 2-D sequences can be substituted. The structural sequences (T_2-weighted, FLAIR, and pre- and postcontrast T_1-weighted) provide the primary foundation of an MRI examination.“* [37] For accurate brain tumor localization contrast agents are often administered to the patient´s body. Contrast media administration causes the contrast enhancement[38] in the tissue area where a contrast agent has leaked out of the *blood-brain-barrier* (BBB)[39][40]. [37] However, at some brain tumor types a whole area of tumor tissue cannot be visualized by the contrast enhancement. Tumor cells are also located beyond the enhancing margins of the brain tumor where BBB is still intact. [39] This represents the contrast non-enhanced tumor part as highlighted in the figure 5.2.

Brain tumors can be divided into two main types; malignant tumors containing cancer cells and benign tumors containing non-cancer cells. Several brain tumor types exist. High-grade gliomas (HGG) are highly malignant tumors. *„Among more than 100 different histological subgroups of brain tumors, high-grade gliomas (HGG) are the most frequent entities, accounting for over 50% of primary malignant brain tumors, depending on age and country. The incidence of HGG has increased in past decades and has become quite significant in the older population.”* [40] These tumors are hyperintense on T_2 images and hypointense on T_1 images. [41] Typical properties of these tumors are contrast enhancement, necrosis[41], hemorrhage[42] and edema. [41]

---

[38] In several brain tumor types, e.g. low grade astrocytomas, the contrast enhancement is not visible. [38]

[39] Blood-brain-barrier is a selective semipermeable membrane that allows only certain substances to flow from the bloodstream to the brain. Its function is to protect the brain from e.g. pathogens that could be potentially harmful to neurons.

[40] Though, some non-tumoral lesions, such as infections, infarctions and demyelinating diseases, can break the BBB as well, thus simulate the brain tumor behavior. [39]

[41] Brain necrosis refers to the death of cells in the brain living tissue.

[42] Brain hemorrhage represents bleeding in the brain.

„The association of contrast enhancement with tumor grade has been extensively studied. Although contrast enhancement is a common feature of HGG, it remains a nonspecific finding. For example, almost a third of HGG tumors do not enhance.“ [41]

Metastatic brain tumors (also called secondary brain tumors) origin is related to spreading cancer cells, so-called metastasizing process, to the brain tissue from another part of the body, such as lungs, kidneys, a colon, breasts and melanoma. Metastatic brain tumors are commonly considered malignant. *„On MRI, metastases are usually iso- or hypointense on* T_1*, hyperintense on* T_2*, and exhibit avid enhancement. Some metastases, such as melanoma, are* T_1 *hyperintense due to the paramagnetic effects of melanin. Hemorrhagic metastases may also demonstrate* T_1 *signal hyperintensity, depending on the age of hemorrhage. DWI usually demonstrates facilitated diffusion (i.e., bright on apparent diffusion coefficient (ADC) map), rather than diffusion restriction."* [42] Metastasis are often surrounded by vasogenic edema[43]. [43]

Meningioma is a brain tumor which arises from meninges. Most meningeal tumors are benign. *„The typical MRI signal intensity characteristics consist of isointensity to slight hypointensity relative to gray matter on the* T_1*-weighted sequence and isointensity to slight hyperintensity relative to gray matter on the* T_2 *sequence. After contrast administration, meningiomas typically demonstrate avid, homogeneous enhancement; however, they may occasionally have areas of central necrosis or calcification that do not enhance.“* [44] This brain tumor type is usually not associated with brain edema. [44]

---

[43] Vasogenic edema is a type of brain edema in which BBB is disrupted.

6. Image processing

Image analysis includes several steps to extract the meaningful information from acquired MR images. This chapter deals with the theoretical explanation of basic processing steps in MR images, namely the brain extraction and the image registration. In addition, the explanation of distortions correction on MR anatomical and diffusion images is given. Lastly, the image segmentation process is described.

6.1. Brain extraction

MR head images incorporate instead of brain and non-brain tissue other components, such as the skull, fat, bones, skin and eye orbits. The first step in brain image processing is the non-brain tissue removal, the so-called skull stripping. Non-brain segments might influence further processing, thus their removal at the beginning of further processing is crucial. The skull stripping quality highly influences outcomes of further processing steps. In practice, it is always better to apply a less stringent method of non-brain segments removal and thus to leave some non-brain segments than to choose an aggressive algorithm removing all non-brain tissue but simultaneously eliminating little parts of brain tissue, too.

Several skull stripping algorithms are present today. This section briefly describes mathematical morphology-based methods, intensity-based methods, atlas-based methods and deformable surface-based methods. Today´s software tools are commonly based on the automated processes. *„Skull stripping process is a sophisticated and challenging task due to the intrinsically imprecise nature of the brain images. Automated algorithms for skull stripping should be robust, efficient, reliable, and produce consistent and more accurate results on the large volume of datasets. However, the presence of noise and various imaging artifacts in MR may introduce undesired distortions to the brain images which may substantially degrade their quality.“* [45]

6.1.1. Mathematical morphology-based methods

Morphological image processing is a collection of non-linear operations based on a shape of an object. *„The key idea of morphological analysis is extracting knowledge from the relation of an image and a simple, small probe (called the structuring element), which is a predefined shape. It is checked in each pixel, how does this shape matches or misses local shapes in the image.”* [46]

Since morphological processing originally handles with binary images as an input, the first processing step is thresholding. An example of thresholding technique, which is commonly used in skull stripping, is the Otsu´s thresholding algorithm[44]. In the next steps, morphological operations, such as erosion and dilatation, are applied on the binary images. Erosion excludes pixels on the object´s boundaries resulting in the object´s shrinking and the overall structure simplification, whilst dilation adds pixels to the boundaries and thus fills small gaps resulting in the structure´s size increase. There are other morphological operations based on a combination of erosion and dilatation, such as morphological opening (erosion followed by dilatation) that is intended to remove small objects from an image and morphological closing (dilatation followed by erosion) that is used for holes filling in the image while keeping a shape and a size of larger objects in the image. These operations are applied to binary images in order to separate the skull and other non-brain tissues from brain tissue. *„The main drawbacks of these methods are that they often depend on many parameters such as size and shape of the structural element for morphological operation. These parameters are fixed by empirical experimentation; the value on these parameters directly influences the final output of these methods."* [45]

Brain Surface Extractor (BSE) is an algorithm based on this method. Its idea stems from the technique edge detection[45] which identifies the brain border. After the edge detection algorithm is used, the image is binarized and then morphological operations are used to find the boundary between the skull and the brain tissue. These operations break connections between both tissue types. To improve the brain extraction accuracy, the anisotropic diffusion filter (ADF) for noise reduction[46] is applied to MR images prior morphological operations are put into effect. [47] [48]

6.1.2. Intensity-based methods

Intensity based skull striping methods proceeds from classifying the brain and the non-brain tissue according to their intensity values of pixels in the image. These techniques are not robust

---

[44] The Otsu´s thresholding method is intended to convert a gray image onto a binary image considering two classes of the image´s pixels, which means foreground and background pixel classes. The threshold value for ideal separation between two classes is chosen if the inter-class variance is maximized, whereas the intra-class variance is minimized. The assumption of the Otsu´s thresholding method is a bimodal histogram of an input image.

[45] Edge detection is a method in digital image processing that finds pixels, in which the image intensity changes sharply. The edges might be detected by applying filters that enhance the brightness change in the image in the vertical and the horizontal direction.

[46] The anisotropic diffusion filter is an adaptive filter which removes high frequency noise preserving the sharp edges in the image.

since they depend on the MR scanner properties and the origin of image artefacts, which means for instance, on the homogeneity imperfections of the radiofrequency coils, field inhomogeneities, motion artefacts, low resolution, low contrast and high noise. [45] An example of these skull stripping methods might be thresholding whose cut value is determined from the intensity histogram.

An example of this algorithm is the *watershed* algorithm (WAT). WAT is intended to find the local minima and maxima image intensities in order to find a boundary between the skull and the brain and thus to segment the image onto brain and non-brain components. *„The basic assumption of the watershed algorithm is the connectivity of the white matter. Since darker gray matter and even darker CSF surround the connected white matter, this region can be interpreted as the top of a hill in a 3-dimensional virtual landscape."* [49] This approach suffers from over-segmentation, thus it is usually followed by post-processing steps to combine regions belonging to the same structure. [49] On the other hand, its advantage is the simplicity and fact that it usually creates complete brain boundaries. [50]

6.1.3. Atlas-based methods

These brain extraction methods utilize already defined brain template images created by experts. *„In recent years, several multi-atlas–based methods have been proposed, producing very accurate, state-of-the-art segmentations. The main premise is that multiple atlases cover much wider anatomical variations and, when registered to the target image, they can correct errors among each other, thus providing an increased accuracy and robustness."* [51] A major challenge of this method is to choose an optimal brain template from the external atlas library that best fits the data within the study. The overall skull stripping quality is proportional to a range of similarity between the brain atlas images and the brain target images.

6.1.4. Deformable surface-based methods

A basic idea of deformable surface brain extraction methods is the application of surface models that specify a degree of deformation of the brain surface. The surface deformation is conducted iteratively. The force defining the deformation of the surface is derived from image intensities calculation. The level of external deforming force depends on the surface topology and smoothness. [52] *„In general, deformable models have the potential to produce more robust* *and accurate skull stripping results than methods using edge detection and threshold classification.“* [45] This skull stripping technique has been proven to be very robust but are highly susceptible to initialization of the deformation effect location. [53] Hence, some today´s automatic skull stripping algorithms, the so-called hybrid skull stripping methods, use deformable models calculated in the pre-segmentation steps according to the histograms analysis resulting in more accurate initialization of deformable models. [53] The study [49] applies firstly the *watershed* algorithm as the pre-segmentation step that removes most of the non-brain tissue. This hybrid approach shows in total both the robustness of the *watershed* algorithm and the accuracy of deformable models.

Brain Extraction Tool (BET) applies deformable models to find the outer surface of the skull. The initial step is to roughly estimate a center of gravity in the brain image and the minimum and maximum of intensity values that determine an approximate threshold for brain/non-brain segmentation. It follows the brain image is binarized and the brain mask is created. [47] The deformation effect is initialized in the center of gravity and the deformation of the brain surface is performed in an iterative fashion. [53] The deformable model is expanded or shrunk in order reach the brain boundary.

6.2. Image registration

Image registration is a process of aligning two images with overlapping of common features located in both images and with enhancing an abnormality that is visible only in one image. *„Image registration is the process of finding the transformation that aligns or maps an object of one coordinate to an object of a different coordinate. The goal of registration is to find a corresponding anatomical or functional position in two or more images.“* [54, p. 24] Image registration is typically used to merge MR images with images acquired from other imaging modalities, to compare current image data with older image data and for distortions minimizing. The image that is deformed by geometric transformation is called a source image (also a moving image) and the second image is called a reference image (also a target image). A reference image controls the final resolution and FOV of a fused image.

There are several image registration types differing from how many *degrees of freedom* (DOF) they use. The following image registration examples are given for 3D images registration. The image registration might be divided into two main groups; linear and non-linear registration. Two main types of linear registration that were implemented in my task is rigid and affine registration.

The rigid registration transforms images by applying rotation and translation. The actual size and a shape of an object is constant. It uses 6 DOF – three DOF for rotation and three for translation. This type of registration is convenient for the registration within the same subject. The affine registration is able to utilize up to 12 DOF. Not only can the affine registration apply rotation and translation operations, but also allows to apply scaling and shearing. Three DOF are used for rotation, three for transformation, three for scaling and three for shearing. This type of image registration is used for distortions correction, especially for eddy currents correction described in the section 6.3.2.3.

The 3D affine registration is described with 12 transformation parameters usually displayed with the 4x4 transformation matrix T combining effects of translation, rotation, scaling and shearing. The affine matrix T transforms a vector (or a point) x to a vector (or point) y according to the formula 6.2. The parameters d_x, d_y, and d_z represent translation of an object in all three axes. Translation matrices slightly move an object along three axes, whereas rotation matrices are intended to rotate an object about three axes. The affine transformation is described by three rotation matrices representing a rotation of an object about each axis. Scaling matrices change a size of an initial object by shrinking or expanding an object. Last matrices, the so-called shearing matrices, tilt an object. The final 4x4 affine transformation matrix is acquired by multiplication of all the aforesaid 4x4 matrices.

$$T = \begin{matrix} a_{11} & a_{12} & a_{13} & d_x \\ a_{21} & a_{22} & a_{23} & d_y \\ a_{31} & a_{32} & a_{33} & d_z \\ 0 & 0 & 0 & 1 \end{matrix} \qquad (6.1)$$

$$y = T \cdot x \qquad (6.2)$$

The non-linear registration uses more than 12 DOF and is a right method for image registration between different subjects. It is represented by 3D deformation (displacement) field.

If the image registration includes the image resizing from one grid to another one, it is necessary to apply an interpolation method assigning values to each pixel in the output image. The interpolation algorithms might be divided into two main groups, into adaptive and non-adaptive algorithms. *„Adaptive interpolation algorithms use a pixel-by-pixel approach for interpolation and generate images of good visual quality whereas non adaptive interpolation algorithms interpolate by predetermined prototype for all pixels equally. The accuracy of output image depends on the number of pixels used in interpolation. But the computation time increases with the use of more number of pixels."* [55] In this section most frequently used adaptive interpolation algorithms are explained.

- **Nearest neighbor interpolation**

Nearest neighbor interpolation is a simple method that is the least time consuming. The effect of this algorithm is making bigger each pixel. It considers only one pixel; the unknown pixel value is calculated as the value of the closest neighbor pixel in the known original image. This interpolation method tends to produce images with lower quality.

- **Bilinear and trilinear interpolation**

The bilinear type of interpolation calculates the value of an unknown pixel according to the closest 2x2 pixels in the original image surrounding an unknown pixel. The value is calculated as a weighted average value of these 4 pixels. It results in smoother visualization which, however, takes more time. An extension of the bilinear interpolation is the trilinear interpolation taking into account 8 pixels surrounding an unknown pixel.

- **Bicubic interpolation**

The most computationally expensive interpolation technique among aforementioned methods, which gives on the other hand the most accurate results, is the bicubic interpolation. This technique uses 16 closest pixels to calculate an unknown pixel value.

There are other interpolation methods, such as the B-spline, which is a piecewise polynomial function[47]. Unknown pixel values are estimated by fitting a polynomial curve through all the known data points. The B-spline interpolation is usually an optimal choice for non-linear registration. Another similar interpolation solution uses fitting through the *sinc* function.

---

[47] The piecewise polynomial function shows a polynomial shape on each of its sub-domains but likely with a different shape at each sub-domain.

6.3. Image distortions correction

The magnetic resonance itself is a source of several image artefacts that have to be in some cases minimized before further image processing. Some artefacts are typical only for anatomical (structural) images and some only for diffusion images. Naturally, some artefacts are visible in both image structures. This chapter describes the most common artefacts enhanced in anatomical and diffusion MR images. The causes of their origin and their appearance on the images are given. The post-processing correction methods are emphasized. The minimizing of distortions on diffusion images, which is a main practical task, is highlighted.

Motion artefacts are an example of distortions that can be present in all types of images no matter which sequence parameters are chosen. A typical cause of motion artefacts is the patient´s movement resulting from involuntary physiological motion and from the subject´s movement during the data acquisition. *„The two main components of motion in brain imaging are bulk motion (translation and rotation) of the whole head and the periodic local motion of brain tissue due to cerebral spinal fluid pulsation.“* [56] These distortions are typically shown in the phase encoding direction; random motion causes a smear in a phase encoding direction. Fast sequences are useful to address these distortions. The motion artefacts reduction can be accomplished in the post-processing stage by the image registration. Diffusion images are more susceptible to motion distortions. In the section 6.3.2. common retrospective corrections in diffusion images are mentioned.

6.3.1. Distortions correction in anatomical MR images

MR anatomical images are usually prone to image artefacts caused by noise and inhomogeneities in the main magnetic field. This section describes in brief both mentioned artefacts.

6.3.1.1. Image distortions due to noise

The noise degrades the MR image quality; thus, it deteriorates the further image processing and eventually MR parameters quantification. Thereby, it might be crucial to remove (or at least to minimize) the noise, which means to apply the denoising process. *„Noises caused due to several reasons like movements of charge bodies, measurement anomalies, and pulse sequence bandwidth and device configuration like size of radio frequency coil.“* [57] Typical spatial filtering techniques[48] include using the common filters, namely median filters[49], Gaussian filters[50], Wiener filters[51], mean filters[52], anisotropic diffusion filters and non-local means (NLM) filters[53]. These filters remove a certain kind of the noise. The study [59] investigating these filters on skull-stripped MR anatomical brain images revealed the Wiener filter leads to most accurate results (the highest SNR) and non-local means filters perform the best smoothening. The filtering method choice always depends on the type and the amount of the noise in the image.

6.3.1.2. Image distortions due to field inhomogeneities

MR bias distortions[54], which are mainly caused by inhomogeneities in the static magnetic field, represent a smooth signal intensities variation in the same tissue type across the image. The signal intensities variation is expressed by an image, the so-called the bias field. The example of the bias field that was created in my practical task is shown in the section 8.3.1. The source of these distortions might be the MR machine itself that can be calibrated and thus the disturbance impact minimized. Another source may be the examined object itself and its orientation that is difficult to compensate, though. Minimizing of this artefact might be attained in a prospective fashion by a combination of using surface coils (high SNR but high bias, too) and a body coil (low SNR and low bias, too). [60]

There are also several retrospective correction techniques. *„The model of bias field in medical images is commonly based upon the assumption that bias field is a low-frequency artifact and perceived as a smooth spatially varying function alters the image intensities.“* [60] Hence, post-processing correction methods, which use low-pass filtering methods, remove these low-frequency distortions from the high-frequency image. However, this approach is limited since: *„first, many useful low-frequency structures might be mistakenly eliminated by low-pass filtering. Second, high contrast structures characterized at the low frequencies may generate filtering*

---

[48] Spatial filters adjust the pixels values in the image through a function of intensities of the pixels in the neighborhood. [58]

[49] Median filters reduce a type of the noise *salt and pepper* (random presence of light and dark pixels in the image) caused by the sudden disturbance in the MR signal.

[50] Gaussian filters reduce the Gaussian noise (noise following the normal distribution).

[51] Wiener filters are a frequency domain filters reducing the additive noise and performing the smoothness simultaneously.

[52] Mean filters smooth the image since they act as low-pass filters. It removes the grain noise.

[53] NLM filters tend to calculate a new signal intensity value in a voxel by computing a weighted average value of signal intensities in a whole image. The NLM filters reduce the spatially varying noise.

[54] Also called the intensity non-uniformity (INU) and the intensity inhomogeneity distortions.

artifacts known as edge effects, which can cause distortion of homogeneous tissues near the edges." [60] Other retrospective reduction techniques are directly based on signal intensity histograms. This is an automatic method that does not require any prior knowledge of intensity variation through the image. The last-mentioned corrections methods are segmentation-based methods. The bias correction is often considered as a necessary step for the image segmentation. [60] Several segmentation approaches are present, such as the method considering the maximum likelihood criterion to estimate the image intensity probability distribution. [61]

6.3.2. Distortions correction in diffusion MR images

As mentioned in the section 4.2.1., diffusion images might be acquired with the fast EPI sequence that is highly prone to image distortions. The EPI sequence is extremely sensitive to any inhomogeneities in the main magnetic field. *„The acquisition as well as the interpretation of diffusion imaging results are not straightforward. This is both due to the sensitivity of diffusion imaging experiments to phenomena other than diffusion, and to the fact that, like any other magnetic resonance imaging (MRI) technique, it remains subject to artifacts, numerous technical difficulties, and other sources of error. More specifically, in addition to common MRI artifacts, DWI encounters characteristic problems regarding gradient hardware, especially in terms of eddy currents and sensitivity to motion."* [62] Furthermore, a higher noise level typically present in images with higher *b* values is also a source of artefacts. In MR diffusion demands are placed on the hardware to be able to produce stable gradients with a maximal intensity that may be challenging in the whole-body exams. [63] Artefacts in diffusion MR usually result from the strong diffusion gradient pulses use.

Motion distortions are extremely important in MR diffusion methods since strong and long gradient pulses are applied. Consequently, the same voxels location in two DWI images corresponding to the same anatomical location is not guaranteed. Motion artefacts can be reduced by the affine registration of non-zero *b* value images to the zero *b* value image, so the same technique that is used for eddy currents effects minimizing described in the section 6.3.2.3. In addition, these distortions might be minimized by the registration of DWI images to the reference anatomical T_2 image. [64]

The subsections below give a description of typical artefacts highlighted in diffusion images, namely distortions caused by noise, eddy currents and susceptibility induced distortions.

6.3.2.1. Image distortions due to noise

Noise in MR images tends to, in general, increase the mean signal intensity. A higher noise level is typically seen on DWI images since diffusion gradients are applied and the echo time is prolonged. [65] A simple method to overcome these distortions is to repeat scans and average them, however, it significantly prolongs the total acquisition time that is not usually acceptable in the clinical practice. Noise in the real and imaginary part of complex images follows commonly the Gaussian distribution with the same noise variance, whereas noise in the magnitude images usually follows the Gaussian distribution and the Rician distribution[55], too. MR data are acquired as the complex data with real and imaginary part. Magnitude images, which represent the scanning outcome, are reconstructed from complex data; which simply means a combination of the real and the imaginary complex data into a single magnitude image. The denoising techniques are mostly applied on magnitude images since complex images are not commonly present on MR scanners and in addition, magnitude images are free of phase distortions. [67]

If SNR is high, the Gaussian and the Rician distribution are almost equal, whereas in the lower SNR values both distributions differ. [68] This section incorporates the post-processing denoising methods conducted on magnitude MR images. To adequately apply a denoising approach, it is substantial to determine the noise distribution in the image. To do it so, information concerning a type of parallel imaging sequence[56], a number of receiver coils and a type of filters and other factors should be known. [69] *„Estimation of signal distributions deviating from theoretical cases is challenging and oftentimes requires information such as coil sensitivities or reconstruction*

---

[55] The Rician distribution is closely related to the Gaussian distribution since the Rician distribution is basically distribution modelling the square root of the sum of squares of two independent and identically distributed Gaussian distributions with the same variance. [66] The Rician distribution is valid only for positive numbers, therefore it indicates MR magnitude images gain only positive values.

[56] MR parallel imaging is a method for MR data acquisition. The acquisition time is shortened by decreasing a number of k-space lines that have to be acquired. A measured signal is detected by several receiver coils surrounding an object in different locations. Two reconstruction methods are present. The *Sensitivity Encoding* (SENSE) method is performed in the image space right after data are acquired from each individual coil. Whilst, *Generalized Autocalibrating Partially Parallel Acquisitions* (GRAPPA) method is performed in the k-space.

In the case of parallel imaging reconstruction the noise in the DWI images follows the Rician distribution, whereas in the case of GRAPPA parallel imaging the noise follows the non-central Chi-squared distribution (the distribution modelling the square root of the sum of squares of several independent and identically distributed Gaussian distributions with the same variance. [66]

matrices. This information may not be recorded at acquisition time or is even not available from the scanner, making techniques relying on these parameters difficult to apply in practice." [69]

„The correction scheme based on the Rician distribution shows the advantages of easy calculation and ability to handle averaged magnitude images. However, this scheme is not recommended when the SNR is very low." [68] The reduction of the Rician noise can be achieved by several denoising approaches, for instance the anisotropic diffusion filtering and the non-local means filtering. The study [70] revealed the high accuracy of NLM filters adapted to the Rician distributed noise since the NLM filters still preserve sharp edges in small structures, such as vessels. The study [71] presents some significant limitations of ADF approach; it highly blurs the edges in the image at the induced noise level greater than 3%. In the study [72] the *Local Principal Component Analysis* (LPCA) approach for the noise reduction was introduced. *„The key idea of this process is the fact that image patterns can be represented as a linear combination of a small number of basis images while the noise, being not sparse will be spread over all available components."* [72] The approach is performed in three steps. Firstly, the signal in the image is divided into the local principal components. Secondly, the least relevant components are shrunk. Lastly, the signal is back reconstructed. To optimally reduce the noise in the DWI images, the Rician nature of the noise must be taken into account. This technique is intended to be used in images with spatially varying noise that is typical for MR parallel imaging methods. The LPCA filter is robust and fully automatic and moreover, it is the only filter considering the nature of 4D DWI images data set. [72]

6.3.2.2. Distortions due to magnetic susceptibility effect

Susceptibility artefacts in MR are encountered on the interface of structures with different magnetic properties. *„Dedicated experiments have demonstrated that in most of healthy brain, iron and myelin dominate tissue susceptibility variations, although their relative contribution varies substantially. Local variations in these compounds can affect both amplitude and frequency of the MRI signal. In white matter, the myelin sheath introduces an anisotropic susceptibility that has distinct effects on the water compartments inside the axons, between the myelin sheath, and the axonal space, and renders their signals dependent on the angle between the axon and the magnetic field."* [73] The susceptibility difference generates local gradient fields that influence a degree of protons dephasing resulting in the signal loss. It causes geometric distortions appearing themselves as pixel movements and intensity modulations in images. To minimize the artefacts prior the scanning, it is important to decrease a voxel size, to acquire thinner slices, to shorten the T_E time for spins dephasing less time and to increase a receiver pixel bandwidth. Susceptibility artefacts are more highlighted at larger magnetic field strength.

Susceptibility induced distortions are significant in EPI diffusion images due to its low bandwidth in the phase encoding direction. These distortions are generated by the main homogenous magnetic field disruptions caused by scanning an object; a human head. *„When a non-spherical object rotates around an axis other than that parallel with the magnetic flux (the* z*-axis) it changes the way it disrupts the field, leading to different distortions."* [74] The difference between the initial homogenous field and the current disrupted field is called the susceptibility induced off-resonance field, the so-called field map. The field map represents the pixels shift due to the field inhomogeneities and is used to correct the distortions. The field map is subsequently combined with the distorted images to generate new undistorted images. The example of the field map that was created in my practical task is shown in the section 8.3.2.1.

Susceptibility artefacts might be minimized with post-processing methods based on the field map calculation. There are two main methods; the first method is based on the phase difference between two different echoes using the double echo sequence, while the second method uses the acquisition of a pair of diffusion images acquired with both phase encoding polarities.

- **Phase difference between two echo times in double echo sequence**

This method is based on using double echo sequences. Two images at two different echo times are acquired and the field map is calculated according to the phase shift between two images. The phase difference is proportional to the time difference between two echoes and the B_0 inhomogeneity. *„This method has various limitations due to the difficulty of calculating the phase difference in areas where the field inhomogeneity is high, challenges regarding phase unwrapping, and the lack of voxel intensity information. The scan sequences required to obtain the phase map also takes several minutes to acquire, as opposed to the few seconds it takes to acquire an EPI scan of an entire brain, therefore subject motion during the former can lead to large errors in the field map and subsequent correction."* [75]

- **Reversed polarity of phase gradients**

The second method means the acquisition of a pair of diffusion images with a negative and a positive polarity in the phase encoding direction during the EPI scan. It results in the reversed distortions with respect to the pixel shift direction along the phase encoding direction. The phase encoding is commonly performed in the y-axis direction; the classical image acquisition corresponds to *anterior-posterior* AP direction (the so-called blip-up image), whereas the image acquired only for the distortions correction purposes corresponds do the *posterior-anterior* PA direction (the so-called blip down image). The displacement field is created by matching these two diffusion images. Relative to the previous method, this is much less time consuming.

Another approach of susceptibility induced distortions reduction is the use of the non-rigid registration, so the non-linear registration using tens of DOF. It does not require to obtain additional data as aforesaid methods do. It uses anatomical images as reference images without significant distortions to estimate distortions location and subsequently to correct the intensity values in diffusion images which are considered as the moving images. The study [76] revealed significant limitations of this method; different contrast of diffusion images and the reference anatomical image. The undistorted anatomical image is typically the T_1 and the T_2 image. [76]

6.3.2.3. Distortions due to eddy currents

The eddy currents origin in MR is related to the application of large diffusion gradients and radiofrequency coils. Eddy currents represent electrical currents induced within conductors by either changing the magnetic field or the motion of a conductor in the stationary magnetic field. Eddy currents generate an additive magnetic field with the opposite effect to the main magnetic field as stated in the Lenz´s law[57]. Diffusion images using fast EPI sequences are prone to the origin of distortions caused by eddy currents generated by very rapid gradient switching.

Eddy currents deteriorate gradients switching do the shift in the main magnetic field B_0 and generate an undesirable time varying gradient magnetic field. [78] *„Image distortions from eddy currents blur the interface of gray and white matter tissues, cause misregistration between individual diffusion-weighted images, produce erroneous calculations of the diffusion*

---

[57] *„The Lenz's law states that the direction of the current induced in a conductor by a changing magnetic field is such that the magnetic field created by the induced current opposes the initial changing magnetic field.“* [77]

signals.“ [79] Since diffusion images are acquired with a different degree of diffusion weighting (a different *b* value), the distortions vary between DWI images resulting in the data bias and inaccuracy. [63] *„Unlike magnetic susceptibility induced distortions, these effects vary across diffusion gradient orientations and are enhanced by the fact that higher b-values require the application of stronger diffusion gradients for longer periods.“* [80]

There are several post-processing strategies minimizing the influence of eddy currents which are described below. Moreover, selection of a right pulse sequence is important, too. *„Post-processing techniques are the most widely used, as they have several advantages: they can be applied retrospectively to already acquired data, a user can revert to the original data if the technique does not work as hoped, and they don't require additional scan-time, which is often expensive.“* [81] In this section three basic correction retrospective methods are present.

- **Correction based on pairs of images acquired with the opposite gradient polarity**

This correction technique uses inverse characteristics of induced distortions created by both polarities of diffusion gradients. Two images acquired with both diffusion gradients polarities have very similar contrast. *„Based on Maxwell's laws, voxel shifts resulting from the eddy currents induced by the diffusion gradients have the same magnitude but opposite direction if the polarity of the gradients is reversed, that is, if a gradient* $G- = -G+$ *is effective instead of* $G+$*. This enables a correction scheme that only uses diffusion-weighted images and, most importantly, images with identical contrast properties for the alignment procedure.“* [82] In this case, the acquisition of non-diffusion weighted images is not required. It is demanding to acquire an equal number of datasets with both gradient polarities. Another correction possibility, which stems from the same idea, is the use of reversed polarities of phase encoding gradients.

Other post-processing techniques are based on the affine registration approaches. Eddy currents (and motion distortions as well) cause the diffusion data misalignment that can be characterized by the 3D affine transformation. [83] It follows these distortions might be removed (or at least minimized) by the affine registration. There are two main registration approaches; pairwise and groupwise registration. Pairwise registration represents registration of a series of images with the reference image separately, whilst in groupwise registration a whole image series is registered with the reference image simultaneously. According to the study [84], *„using a groupwise approach, a bias towards the reference image is avoided and the intensity* *information of all images is taken into account simultaneously, lead into more consistent registration results*." [85] There are commonly two types of the affine transformation for eddy current corrections. The slice-wise registration ensures the misalignment correction between slice planes, whereas the whole-brain transformation corrects 3D eddy current distortions.

- **Affine registration of non-zero *b* value images to zero *b* value image**

Another possibility of aligning DWI images, and thus eddy currents distortions reduction, might be attained by the affine registration of images with non-zero *b* value to the $b = 0$ value that is considered as a reference image. This method does not require to obtain another data set, however, on the other hand, this method is less convenient for artefacts correction at high *b* values that represent the higher signal attenuation and the greater contrast difference between these high *b* values images and the reference $b = 0$ image. [80]

- **Registration of diffusion and non-diffusion weighted images**

The third possibility refers to coregister DWI images to the reference images with no diffusion weighting, which means they are considered almost without no eddy currents effects. [86]

6.4. Image segmentation

„Segmentation is one of the most important steps in medical image processing that is normally after enhancement. It extracts any clot/abnormal lesion or blood cells/blood vessels present in an image. Each region in a segmented image possesses homogenous properties with respect to features, such as gray level, texture or color, and the property is different for different regions in an image." [54, p. 24] The segmentation can be conducted on 2D or 3D images. The image segmentation might be classified into three main groups. In the automatic approach, the segmentation runs automatically without any response from the operator. The semiautomatic method represents the automatic segmentation with the segmentation´s parameters adjustment. The last approach; the manual segmentation, is fully performed by an operator that segments and labels the input image by hand. This method in 3D images segmentation, which is done in a "slice-by-slice" fashion, is very time consuming and moreover is impossible to reproduce. On the other hand, this method is believed to be very accurate.

Today, several segmentation approaches are present. In this section a brief description of the most typical algorithms is given.

- **Thresholding**

The traditional segmentation method is based on setting threshold values to group all pixels in the image into several classes. The threshold cut-off value is determined by the image intensity histogram analysis. It is a fast method that is, however, sensitive to noise and intensity inhomogeneities. [87] The example of this segmentation approach is the skull stripping method based on morphological operations described in the section 6.1.1.

- **Region growing**

In the region growing segmentation method pixels with similar intensity values are grouped, thus a segment is created and is subsequently being broadened. At first, an initial point in a segment, the so-called a seed, is set. The seeds define the area with the properties that are typical for a particular region. The seed point can be set by an operator or calculated by an automatic algorithm finding the seed points. *„Region growing is suitable for segmentation of volumetric images which are composed of large connected homogeneous regions. Thus, it is successfully used in medical image analysis to segment different tissues, organs, or lesions from MR images. For example, it is used in brain MRI analysis for segmentation of brain vessels, brain tumor segmentation, or extraction of brain surface.“* [87]

Another segmentation approach, the clustering method, represents the pixels classification into several groups (clusters) based on the calculation of intensities in each pixel. The edge detection and the watershed segmentation algorithms are already mentioned in the sections 6.1.1. and 6.1.2. as the skull stripping methods.

7. Data and software tools description

This chapter names used software tools in the image processing practical task, gives their brief description and describes the acquired MR data.

7.1. Acquired data description

Data were acquired at the University Hospital Brno in 2019 using the MR system *Achieva* with the magnetic field strength 1.5 T manufactured by the company *Philips Healthcare*.

The MR data represent brain images in patients with brain tumors. The contrast agents[58] were applied during an examination. The DWI IVIM method at the University Hospital Brno is used as a pre-surgical planning tool. It is conducted in patients with suspicion of brain tumors that can be surgically removed. The MR exam consists of following MR sequences.

- **3D navigation**

3D navigation is a sequence with an isotropic voxel[59] after the contrast agent is administered. This sequence is crucial for the medical stuff for localization and segmentation of anatomical structures and pathologic lesions. Due to the tumor enhancement by contrast agents, which means the signal intensity increase compared to the T_1 weighting signal, 3D navigation enables more detailed evaluation of lesions in images. When referring to the T_1 sequence in the practical task, it means this 3D navigation sequence. This sequence takes roughly 3.5 minutes.

- **FLAIR**

3D FLAIR sequence is a right sequence for pinpointing brain edema and T_2 brain hyperintensities. Moreover, this sequence is used for detecting brain tumors and verifying health brain tissue. The FLAIR sequence takes circa 5 minutes.

- **T_1 weighting**

2D T_1 weighting images are native, so before contrast media application. Medical stuff looks at these images to compare them with the images acquired by the 3D navigation sequence. The

---

[58] In these exams the contrast agents ProHance and Dotarem were used.

[59] Isotropic voxels of a cubic shape are uniform in all directions.

comparison reveals which brain parts are enhanced after contrast agents administration. A degree of enhancement represents a degree of blood flow and the brain tumor activity. These images are not optimal for image analysis purposes. Its duration is about 2 minutes.

- **T_2 weighting**

2D T_2 native weighting sequence is a basic sequence for the medical stuff for determining the primary diagnosis. It takes approximately 2 minutes.

- **DWI b0 – b1000**

It is a diffusion sequence acquired with two *b* values, $b = 0$ and $b = 1000$ $[\frac{s}{mm^2}]$. It is used to calculate ADC values according to the formula 4.7. The duration is approximately 60 seconds.

- **dADC b0 – b1000**

These images represent calculated ADC values; it means values in all voxels correspond to the ADC values. These values are calculated by using the values from the *DWI b0-b1000 sequence*.

- **DWI IVIM**

The DWI IVIM is a diffusion sequence. Unlike the *DWI b0-b1000 sequence*, these images are acquired with more *b* values. There are 10 *b* values: 0, 10, 20, 30, 50, 100, 200, 500, 1000, 2000 $[\frac{s}{mm^2}]$. For *b* values: 0, 10, 20, 30 and 50 $[\frac{s}{mm^2}]$ one NEX value was implemented. For *b* values: 100 and 200 $[\frac{s}{mm^2}]$ two NEX values were applied, for *b* values: 500 and 1000 $[\frac{s}{mm^2}]$ three NEX values were used and 6 NEX values were applied for *b* value 2000 $[\frac{s}{mm^2}]$. Unlike other implemented sequences, this sequence might not cover a whole head area since this sequence is intended to pinpoint mainly the area of a brain lesion. This sequence takes circa 6 minutes.

Other data necessary for my practical task are binary masks of brain segments; edema, contrast enhanced part of brain lesions (tumors) and not contrast enhanced part of brain tumors. The example of these masks highlighted in colors is given in the section 8.4.

$b = 0$ DWI images were acquired with both polarities of a phase encoding gradient. Both images (images in the AP and PA direction) are used for distortions correction.

Clinical MR images were collected from 20 patients at the University Hospital Brno. 10 subjects were female with a mean age of 61.7 ± 10.9 and 10 subjects were male with a mean age of 58.9 ± 10.6. After the brain surgery, the histology[60] of brain tissue was performed in order to determine the concrete brain tumor type. 10 subjects suffer from the high-grade gliomas, 6 patients from the meningeal tumors and 4 patients from metastatic brain tumors. The brain lesions (tumors) were segmented for each patient. For all patients suffering from HGG tumors and metastatic brain tumors, brain edema and contrast non-enhanced part of the tumor were segmented, too. For 5 from 6 patients with a diagnosis of meningeal tumors, brain edema and the contrast non-enhanced part of brain tumors did not surround the brain tumor, thus these brain masks were not created.

7.2. Used software tools

In the practical task of my master´s thesis I used several programs for MR images processing. Here is a list of the programs I used.

The software ITK-SNAP [88] [89] (version 3.6.0) is based on ITK (*Insight Tool Kit*) libraries with open sources. I used this tool especially as a medical image viewer, a convertor to other medical image formats and for image registration. Moreover, this tool was used for image segmentation.

Software FSL [90] [91] (version 6.0.1) is a complex library for overall image data analysis acquired from magnetic resonance and its methods (functional and diffusion MR). Overall MR image analysis was performed in the FSL tool.

Software package FreeSurfer [92] [93] (version 6.0) is an extensive tool for evaluating the parameters of MR brain images.

Program interface and programming language MATLAB [94] (version R2019.a) includes already implemented algorithms. In my practical task I utilized the *Image Processing Toolbox*.

---

[60] During the histology microscopic structure of cells are examined.

Neuroscientific toolbox SPM [95] (*Statistical Parametric Mapping*) (version SPM12) is primarily utilized for statistical analyses acquired from functional magnetic resonance. This toolbox is run through the MATLAB interface. Whole MR image processing was performed in this software tool.

BrainSuite [96] [97] (version 19a) software toolbox enables the magnetic resonance data processing. This tool serves for all the image processing steps.

ANTs [98] (*Advanced Normalization Tools*) is an open-source software package without a graphical interface. I used this tool for brain extraction and image registration.

IVIM model fitting and producing parametric maps of IVIM parameters was performed in the MITK *Diffusion* application. [106]

8. Image analysis implementation

This chapter provides the explanation of all the steps that were performed in the practical task during the image processing stage. In a nutshell, below is a list of all consecutive steps performed. The steps 1., 2. and 3. were not conducted by me. The steps 1. and 2. were performed by my supervisor Mgr. Ing. Marek Dostál, Ph.D. The step 3. was done by MUDr. Tereza Kopřivová from the University Hospital Brno. The segmentation step requires a professional medical approach. Image analysis was run in different software tools whose time duration is roughly measured and results are shown in Appendix B and briefly described in the chapter 10.3. The duration of automated image analysis algorithms is a significant factor in praxis in order to choose an optimal technique.

1. Skull stripping of anatomical T_1 and FLAIR images
2. Rigid registration of T_1 and FLAIR images (T_1 a reference image, FLAIR a moving image)
3. Segmentation of brain components from the registered image T_1 and FLAIR
4. Skull stripping of 4D DWI diffusion images acquired at 10 *b* values
5. Distortions correction of 4D DWI diffusion images acquired at 10 *b* values
6. Rigid registration of T_1 and DWI $b = 0$ image
7. Transformation of segmented binary masks from the anatomical space to the diffusion space determined by the transformation matrix acquired with the rigid registration of T_1 and DWI $b = 0$ image

8.1. Skull stripping

In my practical task I performed skull stripping of MR head images in the following six software tools. More detailed description of skull stripping methods these software tools are based on is given in the section 6.1. This section covers the use of concrete algorithms. The skull stripping was conducted in MR anatomical head images of the T_1 and FLAIR sequences and on diffusion DWI images acquired at 10 *b* values. Brain extraction of anatomical images was conducted by my supervisor in FSL. After skull stripping is performed, it is essential to display the segmented brain mask overlaid into the original head image. Some inconsistency in the brain tissue removal are likely to be revealed in a sagittal plane. If little brain tissue is removed or non-brain tissue is left, it is crucial to repeat the process with adjusted skull stripping parameters. The assessment of skull stripping quality is not a part of my thesis.

The skull stripping using mathematical morphological operations I realized in MATLAB. I utilized already built functions performing the morphological operations. The figure 8.1 shows a process of removing non-brain tissue from 2D slices. This method is convenient for brain extraction of 2D slices but is not a right method for automated skull stripping. Its benefit is running of already implemented functions which offer a variety of morphological operations.

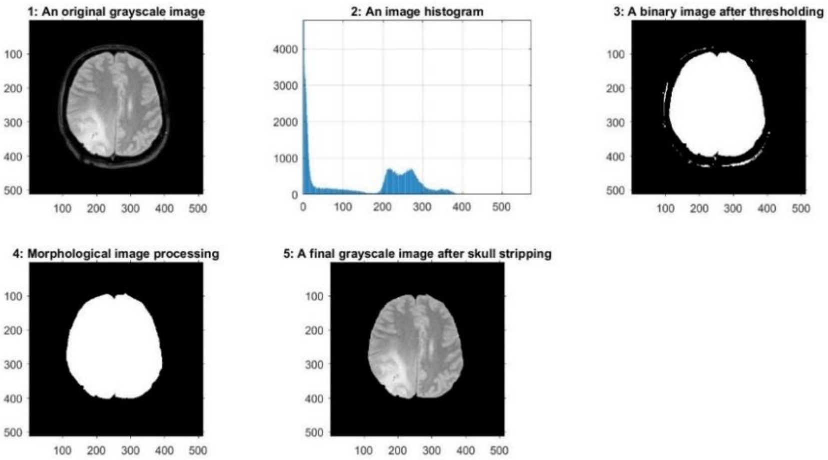

Figure 8.1: The skull stripping of a 2D brain T_1 axial image based on morphological operations implemented in MATLAB. 2: The image histogram with the approximate bimodal gray level distribution, x-axis: the intensity range of pixel values in the image of 16-bits (brightness values ranging from 0 to 65535[61]), y-axis: the count of pixels for each brightness level, 3: The binary image acquired after applying the Otsu´s thresholding method , 4: The skull-stripped binary image by applying morphological operations (erosion, holes filling and opening), 5: The final grayscale image produced by superimposing of the binary image with the input image.

The BSE brain extraction algorithm is built in the software BrainSuite. To optimally perform the skull stripping, several parameters might be adjusted. It is possible to set a number of *diffusion iterations* (usually up to 6 iterations) determining how many times the diffusion filter is applied to the image. A higher number of diffusion iterations might cause the blurring in the region of low edges. The *edge constant* parameter determines a number of edges in the image. Decreasing the *edge constant* (typically in the range 0.5 – 1) ensures less stringent skull stripping (more brain

---

[61] In the image the whole range of brightness values is not displayed.

tissue included). The parameter *erosion size* (ranging from 1 to 4) defines how much small brain components will be removed.

The software package FreeSurfer utilizes the *watershed* algorithm as the intensity-based skull stripping method. The skull stripping is conducted in the *recon-all* (*autorecon1*) stage. The degree of skull stripping might be determined by adjusting the *watershed* parameter *wsthresh* whose values are in the range of 0 to 50 percent (the default value is 25 percent). The lower this value, the skull stripping more aggressive, thereby more brain tissue is removed and vice versa.

SPM tool does not explicitly use one of four skull stripping methods explained in the chapter 6.1. The extracted brain tissue may be generated by the probabilistic brain tissue segmentation method. Firstly, tissue segmentation of MR images is performed resulting in the creation of probability maps of brain compartments GM, WM and CSF. Final brain images are acquired by multiplying of the sum of probability maps of brain compartments and the initial head image[62]. Final skull stripping quality in my data was poor. Little part of brain usually was removed.

The atlas-based brain extraction tools were implemented in the program ANTs. ANTs software performs the brain extraction by running the script *antsBrainExtraction.sh*. The template that works the best with the data was the Kirby template. [99]

Last but not least, I executed the brain extraction in the software package FSL whose skull stripping algorithm BET is based on the deformable surface-based methods. The main brain extraction program integrated in FSL is called *bet2*. [100] It is possible to set the *fractional intensity threshold* within the range between 0 and 1 (a default value is 0.5). This value determines the threshold value separating brain and non-brain tissue. The higher value, the more stringent brain tissue removal (more brain tissue removed) and vice versa. In addition, by setting the parameter *vertical gradient in fractional intensity threshold* in the range between -1 and 1 (a default value 0), the bigger fractional intensity threshold value for the slices at the top and the lower value for the slices at the bottom, and vice versa, can be obtained. Overall, the skull stripping quality is visually on a high level; it includes just little of non-brain tissue in the

---

[62] The probability map of GM labeled with i_2, of WM with i_3 and of with CSF i_4. i_1 denotes to the initial head image. The skull stripped images were acquired by using the equation: $i1.\cdot ((i2 + i3 + i4) > 0.5)$. 0.5 is the optimal threshold value for my data. The higher threshold value, the more brain tissue removed and vice versa.

final images. Moreover, it is possible to remove the residual non-brain tissue in the neck area and furthermore, FSL enables to remove residual eye and optic nerve voxels as well.

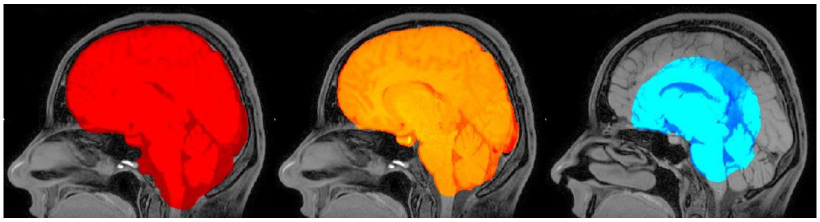

Figure 8.2: The skull stripping of 3D brain T_1 images displayed in a sagittal plane implemented in FSL BET. Background gray images are the initial head images, foreground color highlighted images are brain images after the skull stripping with applying different fractional intensity threshold values. On the left: the fractional intensity threshold value 0.1, it includes also little non-brain tissue, especially in the neck area. In the middle: the fractional intensity threshold value 0.5, it is an optimal choice including approximately only brain tissue. On the right: the fractional intensity threshold value 0.9, it removes lot of brain tissue, the result is unacceptable, thus the skull stripping must be repeated with adjusted parameters.

8.2. Image registration

In my practical task the process involves applying two different image registration steps. Firstly, the image registration of anatomical images of sequences T_1 and FLAIR was performed. Secondly, it was the image registration of the anatomical image of the sequence $T_1$and the diffusion DWI image acquired at $b = 0$. The image registration of T_1 and FLAIR images was done by my supervisor in FSL *Linear Image Registration Tool* (FLIRT) using rigid transformation. The evaluation of the image registration quality, which is based on the minimizing or maximizing the cost function[63] and using some optimization algorithms, is not included in this work. Today´s image processing software tools enable to choose a right registration method determined by a number of DOF and a type of interpolation.

Within the registration of anatomical images T_1 and FLAIR, a reference image is the T_1 image and the FLAIR image is taken as a moving image. The important characteristic of T_1 images is its high spatial resolution; thus, these images offer an accurate pinpointing of brain abnormalities.

---

[63] The cost functions determine the degree of similarity between two images. The image registration is an iterative process aiming to find the best alignment of two 3D volumes by minimizing (or maximizing) the cost function.

Hence, the T_1 images are considered as the reference images. The approximate voxel size of the T_1 image is 0.48 x 0.48 x 0.55 mm and of the FLAIR image 1.04 x 1.04 x 0.57 mm.

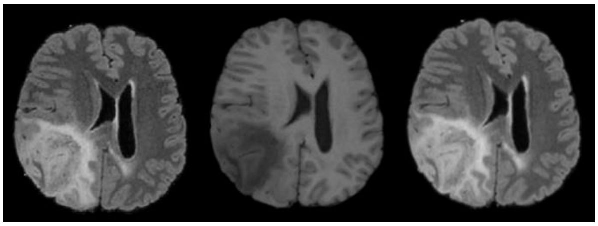

Figure 8.3: The rigid registration with 6 DOF of anatomical images of T_1 and FLAIR implemented in the MATLAB script register_files_affine [101] that is a part of BrainSuite software package (a reference image: T_1 and a moving image: FLAIR), brain images displayed in the axial plane. On the left: the skull stripped FLAIR image, in the middle: the skull stripped T_1 image, on the right: the final fused image.

The second registration step involves fusing of the anatomical T_1 image and the diffusion DWI image acquired at $b = 0$. Despite the fact that the DWI $b = 0$ image shows worse spatial resolution and thus the anatomical information description gets deteriorated, the DWI $b = 0$ image is considered as a reference image and the T_1 image as a moving image. If the T_1 image was taken as a reference image, the interpolation od DWI data would be strictly necessary (the approximate voxel size of the T_1 image is 0.48 x 0.48 x 0.55 mm and of the DWI $b = 0$ image 1.0 x 1.0 x 4.0 mm), which could result in the bias in DWI data. Since the accuracy of DWI data in further data processing is crucial, the registration was performed in this fashion.

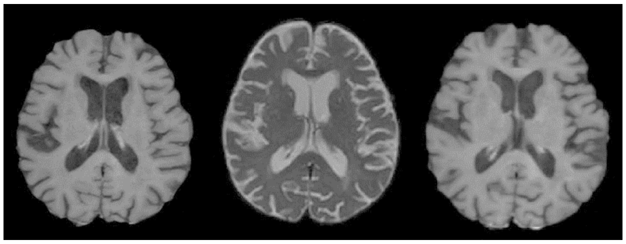

Figure 8.4: The rigid registration with 6 DOF of the anatomical image of T_1 and the diffusion DWI image acquired at $b = 0$ implemented in the software tools ITK-SNAP and ANTs (a reference image: T_1 and a moving image: DWI image), brain images displayed in the axial plane. On the left: the skull stripped T_1 image, in the middle: the skull stripped diffusion DWI image, on the right: the final fused image.

8.3. Image distortions correction

This section incorporates the procedure of distortions correction in MR images in the practical task. The emphasis is put on corrections techniques in diffusion images. Images after distortions reduction are not shown since a difference between the initial and corrected image cannot be simply visible.

8.3.1. Distortions correction in anatomical images

As stated above, the distortions correction on anatomical images was not conducted in this task since doctors in normal clinical practice do not perform these steps as well. Despite all of this, I performed the distortions correction on anatomical images as well. In this section, the denoising and bias field correction methods are present.

The image processing software tools enable to use already built filters to denoise anatomical images. The SPM denoising tool *smooth* uses the Gaussian filter that can be further specified by determining its *Full Width at Half Maximum*[64] (FWHM) in the *x*, *y* and *z* direction. The optimal FWHM choice depends on the voxels´ size of the initial image. By using great FWHM values, high frequencies from the image are removed and the image is considered to be blurred. The loss of spatial precision is followed.

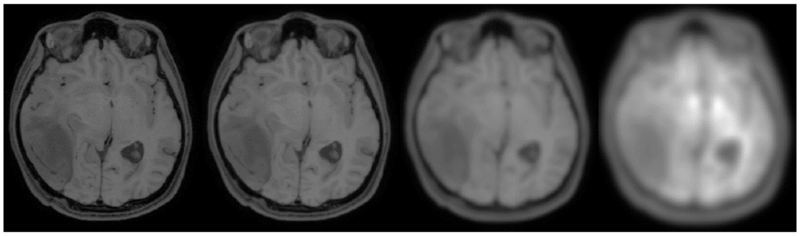

Figure 8.5: The impact of different FWHM values of the Gaussian smoothing filter on the appearance of the T_1 *anatomical image, implemented in SPM. It is the effect of a low-pass filter removing high frequencies of the signal intensities, while enhancing low frequencies. The first image on the left: the original image, the second image from the left: the application of FWHM=1 mm, the second image from the right: the application of FWHM=4 mm, the first image on the right: the application of FWHM=8 mm.*

---

[64] FWHM represents the width of the kernel at half of the maximal height of the Gaussian function.

Bias field correction approaches are in image processing software packages often built within the segmentation module. The example of the bias field correction approach is the *FMRIB's Automated Segmentation Tool* (FAST) in FSL. [102] This tool produces a bias-field corrected input image and the estimation of a bias field. This tool enables to adjust some parameters. The bias field estimation is an iterative process; thus, a number of iterations can be set. Moreover, a level of smoothness on the estimated bias field defined by the FWHM parameter can be adjusted.

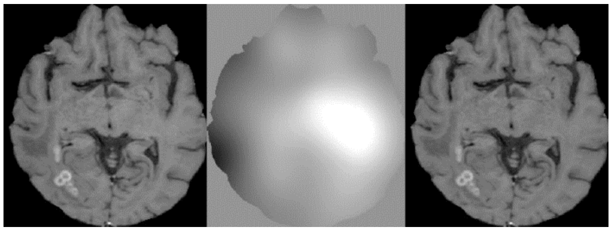

Figure 8.6: The application of the bias field correction on 3D T_1 anatomical image implemented in the FSL FAST tool; brain images displayed in the axial plane. On the left: the original corrupted 3D T_1 image, in the middle: the estimated bias field (values ranging between approximately 0.9 (a dark color) – 1.1 (a light color)), on the right: the corrected image (since there were no significant bias distortions in the initial image, the corrected image is visually the same as the initial).

8.3.2. Distortions corrections in diffusion images

The corrections of the diffusion 4D DWI image containing images acquired at 10 *b* values were conducted in three software tools; FSL, SPM and BrainSuite. This step is essential in the further IVIM analysis and these software tools´ influence on the IVIM parameters calculation is discussed in the chapters 10. and 11.. A theoretical description of all steps performed in these software tools is given in this section 6.3.2. Moreover, I performed the denoising on 4D DWI images.

The software tools for 4D DWI image correction often require specifying a text file containing a list of all *b* values applied during the data acquisition, the so-called *bvals* file and a text file of diffusion gradient directions, the so-called *bvecs* file. In my data the gradient direction in three axes for non-zero *b* value images is represented with 1 and for $b = 0$ image with 0.

8.3.2.1. Diffusion images reduction performed in FSL

The diffusion data processing in FSL includes the magnetic susceptibility distortions, eddy currents and motion reduction.

1. Magnetic susceptibility artefacts reduction

The FSL tool *topup* [103] creates a field map calculated by specifying two $b = 0$ DWI images acquired with both polarities of the phase encoding gradient. These images are optimal for the field map estimation due to reaching the highest SNR from the 4D DWI dataset and are least susceptible to eddy currents. To estimate the field map, it is essential to set the total EPI readout time (a time interval from the center of the first echo to the center of the last echo). The total EPI readout time was calculated in the data according to the formula published by BrainVoyager neuroimaging software package. [107] The value for my data is: $3.81 \cdot 10^{-5} s$.

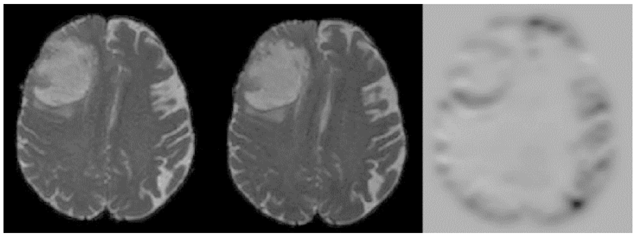

Figure 8.7: The generation of a field map based on the method using two DWI $b = 0$ images acquired with both phase encoding polarities. On the left: the AP DWI $b = 0$ image, in the middle: the PA DWI $b = 0$ image, on the right: a created field map.

Once the field map is created, the whole 4D DWI data set is corrected by running the command script *applytopup*. [103]

2. Eddy current and motion correction

After applying the magnetic susceptibility correction, I ran the command line script *eddy_correct* [81] minimizing the motion and eddy current distortions. This approach uses the affine groupwise registration with the trilinear interpolation method of the 4D DWI image containing 10 images acquired at different *b* values to the reference DWI image $b = 0$.

8.3.2.2. Diffusion images reduction performed in SPM

The diffusion images correction in SPM was performed in its sub-toolbox ACID (*Artefact Correction in Diffusion MRI*). It includes the eddy currents and motion correction followed by susceptibility induced distortions reduction.

1. Eddy current and motion correction

In the first step I applied the technique minimizing the distortions caused by eddy currents and the effects of motion by running the tool ECMOCO (*Eddy Current and Motion Correction*). [86] This algorithm runs the affine groupwise registration of 10 non-zero b images to the $b = 0$ image.

ECMOCO tool enables to generate graphical representation of motion distortions parameters. A head movement might be described in terms of three axes and three planes; a median plane (vertically from the top to the bottom), a frontal plane (vertically from side to side) and a transverse plane (horizontally through a head). The x-axis determines a movement from front to back, the y-axis a movement from side to side and the z-axis a vertical movement. A head movement is described by three parameters of translation and three parameters of rotation.

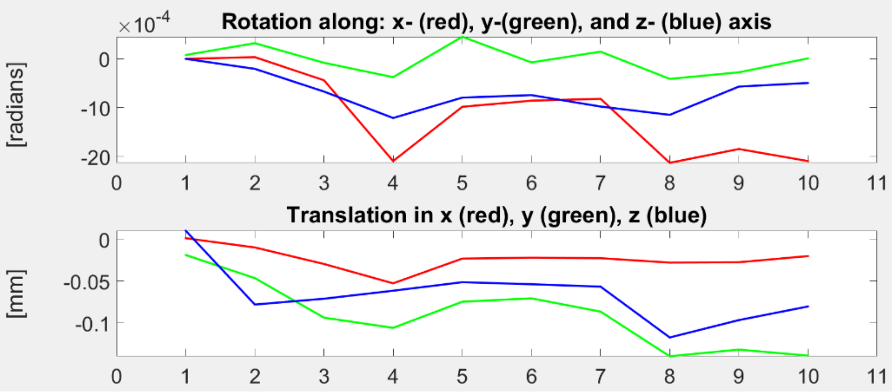

Figure 8.8: Both graphs show the movement of 10 DWI images acquired with different b values between each image. The whole DWI sequence takes roughly 6 minutes, thus the alignment of each DWI image little bit differs due to patient´s movement. The lower graph represents three components of translation of head movement, x-axis: a number of DWI images acquired at 10 different b values, y-axis: translation of the head in millimeters. Red color: the backward and forward head movement along the x-axis, green color: the head movement from side to side along the y-axis, blue color: the vertical head movement along the z-axis. The upper image represents three components of rotation of head movement, x-axis: a number of DWI images acquired at 10 different b values, y-axis: rotation of the head in radians. Red color: Rotation of the head in a frontal plane along the x-axis, green color: rotation of the head in a median plane along the y-axis, blue color: rotation of the head in a transverse plane along the z-axis.

2. Magnetic susceptibility artefacts reduction

The second correcting step involves the magnetic distortions correction conducted in the SPM software tool HYSCO 2.0 (*Hyperelastic Susceptibility Artefact Correction*). [104] The field map is estimated by the same procedure as in the FSL *topup* tool. The whole DWI dataset of 10 images is then combined with the field map in the tool *Write HYSCO Corrected Images.*

8.3.2.3. Diffusion images reduction performed in BrainSuite

The distortions in diffusion images can be reduced in the *BrainSuite Diffusion Pipeline* (BDP). For this purpose, the *Registration-based distortion correction* technique [76] implemented in BDP was used. Unlike the diffusion data correction procedures in FSL and SPM, this method does not require to add a field map for geometric distortions correction. This method uses the extracted information from the anatomical 3D T_1 image to correct some geometric misalignment in the diffusion data set.

It includes two steps; the first step is initialized by using the simple rigid transformation to register the anatomical T_1 image to the EPI $b = 0$ image followed by the correction of EPI geometric distortions in the second step. The correction of EPI geometric distortions is based on implementing the non-linear non-rigid transformation as discussed in the section 6.3.2.2. The bias field corrected anatomical T_1 image is considered as the reference template to which the whole 4D DWI data set is fused.

8.3.2.4. Diffusion images denoising

The software tools SPM, FSL and BrainSuite, in which the distortions correction on the DWI data was performed, do not include the denoising approaches that would be relevant to the DWI data. Hence, I performed the denoising approach on the 4D DWI magnitude images containing 10 images and compared the calculation of IVIM parameters with and without the denoising approach as discussed in the sections 10. and 11. The LPCA filter (explained in the section 6.3.2.1.) was implemented in MATLAB in the *DWI Denoising Software* package introduced by Pierrick Coupé and Jose Manjon. [105] This method is a convenient filtering technique for these MR data since the parallel technique SENSE is used and moreover, due to the SENSE reconstruction, the noise could become non-stationary[65]. It is assumed the noise in the DWI data follows the Rician distribution. According to the concept of these MR data, it is assumed the denoising approach does not have significant impact since only one direction of diffusion was active. Moreover, for higher *b* values images several NEX values were used, thus the random noise influence should be minimized.

8.4. Image segmentation

In the image segmentation process three different segments were created. It is a mask of brain edema, a contrast enhanced part of a brain lesion (a tumor) and a contrast non-enhanced part of a tumor. The image segmentation was performed by MUDr. Tereza Kopřivová from the University Hospital Brno in the tool ITK-SNAP in the semiautomatic fashion using the pre-segmentation method classification[66]. The segments were created on the skull-stripped fused 3D image of anatomical T_1 and FLAIR images. Any further pre-processing was not conducted on these images. The segmented parts of brain were afterwards manually corrected.

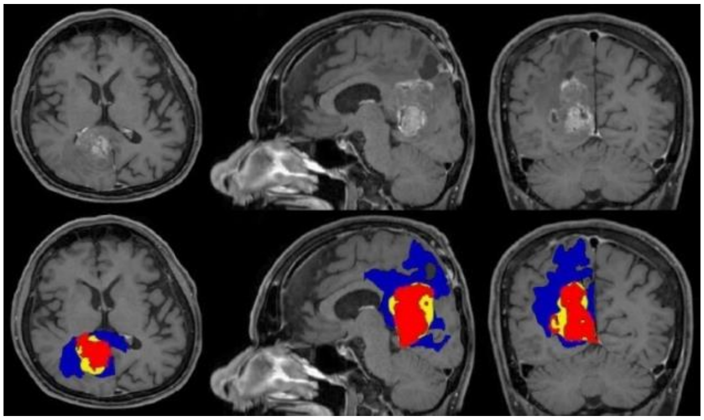

Figure 8.9: The brain 3D T_1 images with highlighted segmented binary masks, brain images visualized in three planes (on the left: an axial plane, in the middle: a sagittal plane, on the right: a coronal plane). Blue color binary masks: brain edema, red color binary masks: contrast enhanced parts of a brain lesion, yellow color binary masks: not-enhanced parts of a brain tumor. This patient suffers from the metastatic brain tumor. In this case, the tumor is little hyperintense, brain edema is hypointense.

---

[65] The non-stationary noise is modeled with a different value of the standard deviation for each voxel instead of a single value of the standard deviation for whole volume.

[66] Desired ROI is drawn by a user on a 2D slice and automatic machine learning algorithms use this segment´s example to create the 3D ROI in a whole image.

9. IVIM parameters modelling and statistical processing

The main practical task is to calculate the IVIM parameters f, D and $D*$ for each of three brain segmented masks and perform their statistical analysis. IBM SPSS (version 21.0.) [109] and MedCalc [110] statistical software tools were used to perform all statistical analysis.

This section incorporates a description of all steps conducted for the acquisition of IVIM parameters and performing the statistical analysis.

9.1. IVIM fitting methods

In the MITK tool it is required to specify a 4D DWI image and a binary mask of a brain segment. MR DWI data in each segment are fitted with the bi-exponential IVIM model. In the MITK tool three fitting algorithms can be selected. The detailed mathematical description of fitting algorithms is provided in the Appendix A.

- **Jointly fit *D*, *f* and *D****

This is the *one step fitting* method of the *Levenberg-Marquardt* algorithm.

- **Fit D and f with fixed $D*$ value**

It is the *one step fitting* method of the *Levenberg-Marquardt* algorithm, except that $D*$ is fixed and can be set in the range between 0 and 0.1 $[\frac{s}{mm^2}]$. In the practical task the $D*$ value was set to 0.07 $[\frac{s}{mm^2}]$[67].

- **Fit D and f (with high *b*), then fit $D*$**

This is the *two steps fitting* method of the *Levenberg-Marquardt* algorithm. In the MITK software this is a default method. In this algorithm it is crucial to set the option *Ignore b< (first fit)*. This algorithm takes the *b* value greater than the set threshold, performs the fitting and calculates values of D and f parameters. The $D*$ parameter values are calculated with the *b* value lower than the set threshold. In this work the *Ignore b< (first fit)* parameter was set to $b = 300$ $[\frac{s}{mm^2}]$.

---

[67] The value of $D*$ was selected according to the study [111].

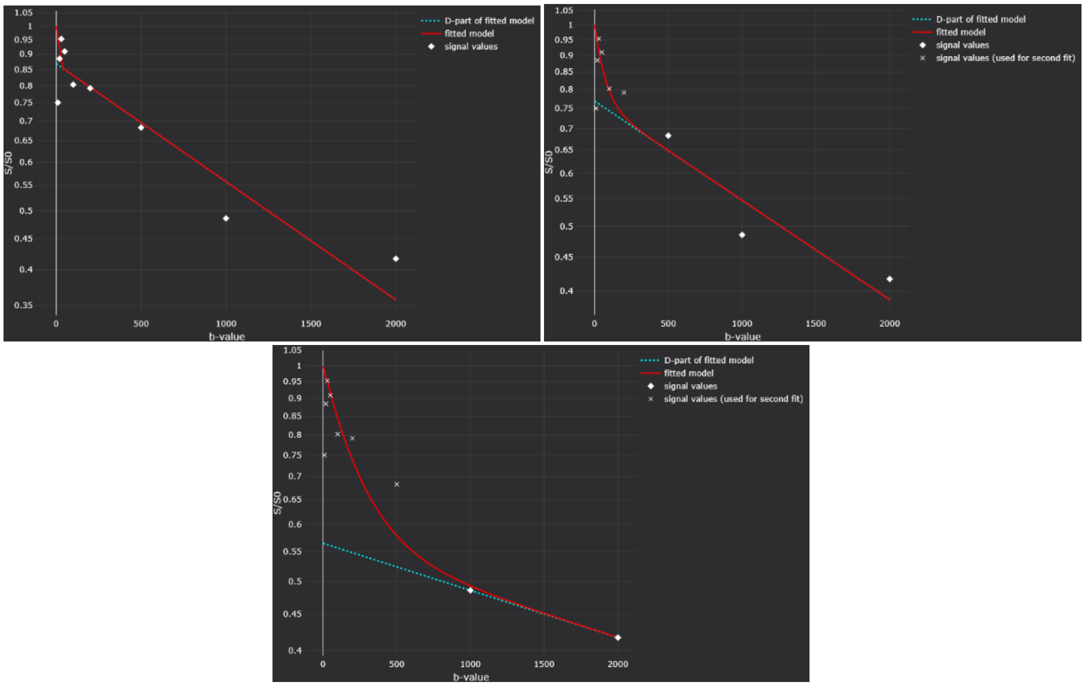

Figure 9.1: The fitting IVIM curves acquired with the fitting algorithm "Fit D and f (with high b), then fit D" with three different values of the parameter "Ignore b< (first fit)," the input is the 4D DWI image of 10 b values, implemented in the MITK tool. x-axis: b values, y-axis: the signal attenuation in the range between 0 and 1. The left image on the top: Ignore b< (first fit) = 0, the right image on the top: Ignore b< (first fit) = 300, the image at the bottom: Ignore b< (first fit) = 600. Red curve: the total IVIM fitting curve, the green dashed curve: the fitting curve with b values above the threshold. If the b-value threshold is set to a low value (e.g.* $b = 0\ [\frac{s}{mm^2}]$*) both curves are overlapped and the IVIM effect at low b values is not enhanced, the D* value calculation is underestimated. Conversely, if the b value threshold is set to a high value (e.g.* $b = 600\ [\frac{s}{mm^2}]$*) both curves are highly separated, and the D* value calculation is overestimated. The optimal threshold b value is approximately* $b = 300\ [\frac{s}{mm^2}]$ *in which both curves are separated at low b values.*

The result of the fitting process is a parametric map for each IVIM parameter, which means a value in each voxel corresponds to the value of IVIM parameter. I created the parametric map for every brain segment by multiplication of a whole brain parametric map and a binary mask of a brain segment. Values of the parameter f are in the range between 0 and 1. In MITK the parameters D and $D*$ are bounded above; D parameter with the upper bound 0.003 and $D*$ with 0.15. Greater values are physiologically not plausible and probably represent computational and fitting error.

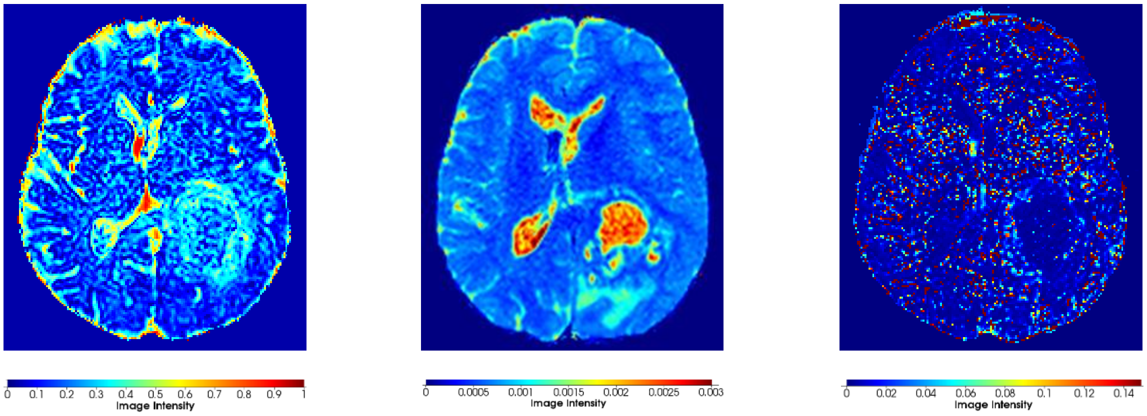

Figure 9.2: Parametric maps of IVIM parameters, visualized in the axial plane. On the left: f IVIM parameter, in the middle: D IVIM parameter, on the right: $D*$ IVIM parameter.

9.2. Statistical analysis

For optimal statistical analysis it is crucial to know the data distribution of parametric maps. A common shape of histograms for three IVIM parameters is visualized in the figure 9.3. The $D*$ data are transformed with $log\ (x)$ function in order to acquire symmetric data distribution.

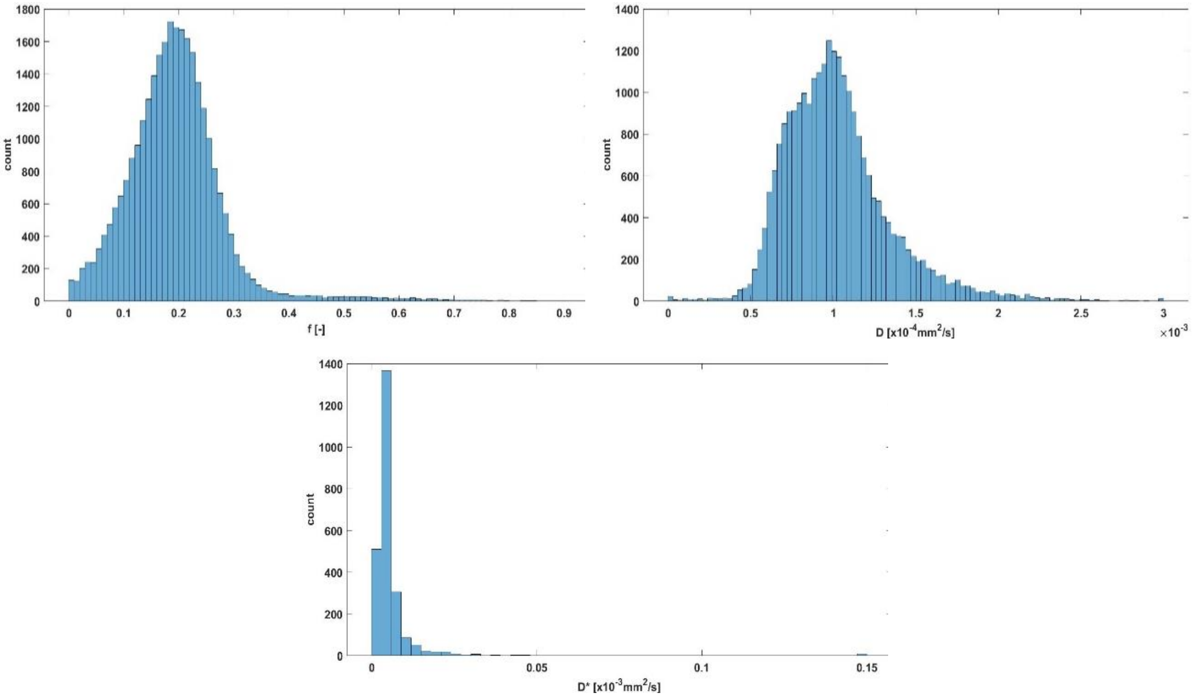

Figure 9.3: A typical histogram shape for IVIM parameters f (on the left on top), D (on the right on top) and $D*$ (in the middle at the bottom).

All numerical values in each brain segment are aggregated and expressed as a vector of statistical parameters; mean value, median, first quartile Q 25%, third quartile Q 75% and interquartile range (IQR) (difference between third quartile and first quartile). Due to the aggregation of all data together the loss of sensitivity in some brain segments might be followed. The choice of statistical method among brain segments including specific brain tumors depends on the data distribution. For further data processing I express the aggregated numerical values in parametric maps for each brain segment as IQR value. I visually verified the data distribution of IQR measure follows roughly normal distribution. Since the number of subjects is low[68] any test for determining whether a data set is modeled with a normal distribution cannot be performed, thereby the assumption of normality of data distribution is confirmed visually. The figure 9.4 represents the data distribution of three IVIM parameters in three brain segments.

---

[68] 20 subjects with contrast enhanced part of all brain tumor types, 15 subjects with brain edema of all tumor types and 15 subjects with contrast not enhanced part of all brain tumor types. There are 10 patients with contrast enhanced part of HGG tumor, 4 patients with contrast enhanced part of brain tumor metastasis and 6 patients with contrast enhanced part of brain tumor meningioma. Furthermore, 10 patients with brain edema of HGG tumor and 4 patients with brain edema of tumor metastasis. In addition, there are 10 patients with contrast not enhanced part of HGG tumor and 4 patients with contrast not enhanced part of tumor metastasis.

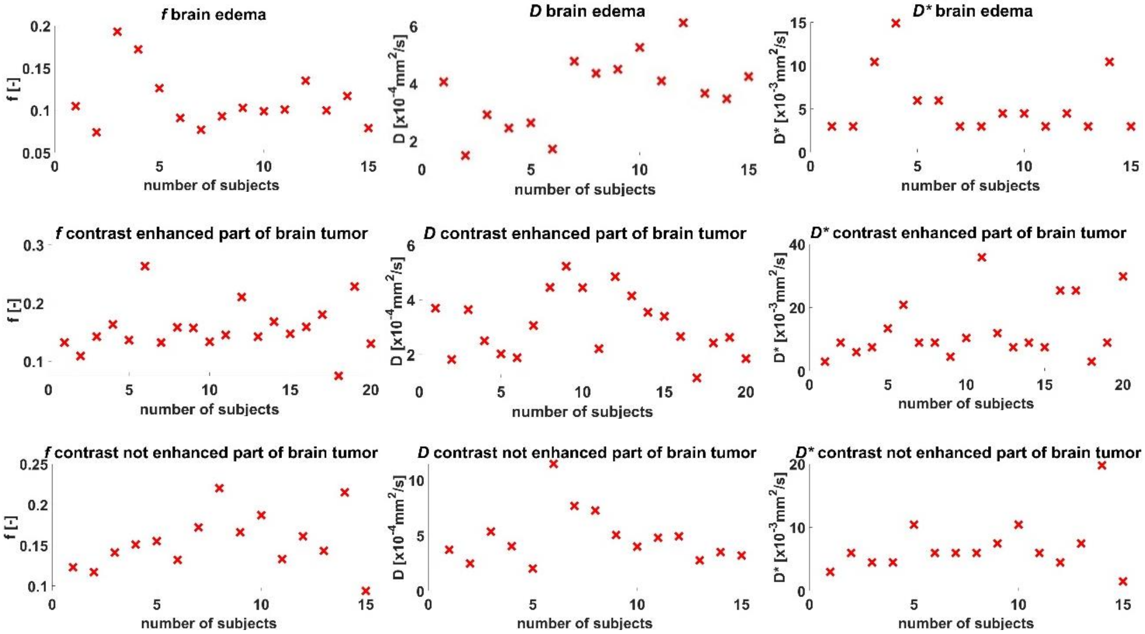

Figure 9.4[69]*: Data distribution of three IVIM parameters in three brain segments. Numerical values in all voxels of parametric maps expressed as IQR value. The red crosses represent the mean value of IQR parameter for each patient. There are 15 subjects with brain edema, 15 subjects with contrast not enhanced part of all tumor types and 20 subjects with contrast enhanced part of all tumor types. Normal distribution of data assumed. Diffusion images correction implemented in SPM, without denoising, fitting algorithm: Fit D and f (with high b), then fit D*.*

Three IVIM parameters in two corresponding following brain regions were statistically analyzed:

- Brain edema and contrast enhanced part in brain tumors
- Brain edema and contrast not enhanced part in brain tumors
- Contrast enhanced and contrast not enhanced part in brain tumors
- Contrast enhanced part in brain tumors HGG and metastasis
- Contrast enhanced part in brain tumors HGG and meningioma
- Contrast enhanced part in brain tumors metastasis and meningioma
- Brain edema in brain tumors HGG and metastasis
- Contrast not enhanced part in brain tumors HGG and metastasis

---

[69] Data distribution for other approaches in the practical task (application of diffusion images correction in other software tools, denoising technique and other fitting algorithms and for brain segments in particular brain tumors) is not visualized. Due to the low number of subjects, the test of normality cannot be practically performed, thus the normality for other data is assumed.

The data for all subjects, for each IVIM parameter and for each brain segment are presented as mean value, standard deviation (std), median, first quartile, third quartile, IQR, maximum value, minimum value and range (difference between maximum and minimum value). These statistical parameters for the data are shown in the tables and graphically represented by boxplots in Appendix C. The data for IVIM parameters in each brain segment come from the same subjects, thus the statistical independence of data cannot be presumed. Since normal distribution of data presented as IQR for each subject is assumed[70], parametric tests for a mean value were applied. A paired Student´s *t*-test was performed to determine the statistical difference between brain edema and contrast not enhanced part of brain tumors. For determining the statistical difference between other brain segments the independent *t*-test was conducted. Moreover, the statistical analysis between different DWI correction software tools (with the noise reduction, too) and different fitting algorithms within IVIM parameters in brain edema, contrast enhanced and not enhanced part of brain tumors was executed using a paired Student´s *t*-test. All *t*-tests were performed with not equal variances assumed. All tests were adopted with the level of *p*-value $p < 0.05$ indicating statistical significance.

Receiver operating characteristics (ROC) curves[71] were derived to analyze the statistical difference of IVIM parameters in different brain segments to determine the optimal cut-off value, sensitivity and specificity. ROC was implemented to compare the ability of IVIM parameters in differentiating brain edema, contrast enhanced and not enhanced part of brain tumors and moreover, in discriminating patients with different brain tumor types; HGG, metastasis and meningioma. ROC curves constructed for the data are shown in Appendix C. The *area under curve* (AUC)[72], sensitivity and specificity of each IVIM parameter for every brain segment is calculated at the threshold value maximizing the value of the Youden index[73]. Comparison of ROC curves between two regions was carried out by given *p* value at $AUC = 0.5$.

---

[70] For other statistical measures; mean, median, first and third quartile, data distribution does not visually follow roughly normal distribution. In that case, non-parametric tests would be used that could eventually result in the lack of statistical power and higher risk.

[71] ROC is a probability curve that is created by plotting *sensitivity* against *1 - specificity*.

[72] AUC represents the entire area underneath the ROC curve. It shows the accuracy of the test; a degree of separability between two classes.

[73] In this practical task it is assumed the sensitivity and specificity are diagnostically equally significant, thus Youden index is used. The Youden index is defined as the sum of sensitivity and specificity minus one.

10. Results

In this chapter the results of all the statistical tests I performed are given. The section 10.1. incorporates statistical comparison between different approaches for IVIM parameters f, D and $D*$ calculation in brain edema, contrast enhanced and not enhanced part of brain tumors. In the subsection 10.1.1. statistical analysis of four diffusion images correction methods is given. The subsection 10.1.2. provides the results acquired by analyzing the IVIM parameters obtained after the application of four different diffusion correction tools with the noise reduction. Lastly, the subsection 10.1.3. contains the comparison between three different IVIM fitting algorithms. Statistically significant difference $p < 0.05$ is highlighted with a gray color. Individual statistical tests were performed for a different number of subjects *n*. The chapter 10.2. is focused on the results derived from analyzing the ROC curves, which means on the ability of differentiation of different tissues types and different brain tumor types. 8 statistical tests between corresponding pairs were conducted. The subsection 10.2.1. incorporates results acquired from four different correction tools, the subsection 10.2.2. provides the results acquired from the statistical analysis of IVIM data after the application of diffusion data correction and denoising approach, too, and the subsection 10.2.3. gives the results obtained by using three different IVIM fitting algorithms. The results are shown for each correction approach and for each fitting algorithm. Analyzing of statistically significant differences between individual approaches and fitting algorithms is not a part of this study. In addition to statistical analysis, the part of my practical task was the comparison of time duration between individual automated software tools within the image analysis. The results are described in the section 10.3.

10.1. IVIM parameters calculation in different brain tissue types

I am investigating whether the statistical analysis of computed IVIM parameters differs from the diverse DWI data correction tools. I performed the distortions correction on 4D diffusion IVIM images in three tools; FSL, SPM and BrainSuite. Moreover, I show the results for the input image without running any correction algorithms. In this task I calculated IVIM parameters with the default fitting algorithm; *Fit D and f (with high b), then fit D**. In addition to distortions minimizing in diffusion images, I reduced the noise by the denoising approach described in the section

6.3.2.1. Distortions correction was also carried out in three software tools and the results without DWI data correction are shown, too. The fitting algorithm was the default algorithm, so *Fit D and f (with high b), then fit D**. Lastly, I´m aiming to prove how different IVIM fitting algorithms influence final IVIM parameters. The distortions correction on input 4D IVIM data was conducted in SPM without denoising.

10.1.1. Different DWI correction tools

mean value (standard deviation)		**FSL**	**SPM**	**BrainSuite**	**Without correction**
edema (n=15)	f [-]	0.12 (0.04)	0.11 (0.03)	0.12 (0.04)	0.12 (0.03)
	D [x 10^{-4} mm^2/s]	3.36 (1.12)	3.71 (1.29)	3.81 (1.27)	3.80 (1.31)
	D^* [x 10^{-3} mm^2/s]	7.25 (6.14)	5.46 (3.64)	7.13 (5.13)	6.95 (5.12)
enhanced tumor (n=20)	f [-]	0.16 (0.03)	0.16 (0.04)	0.17 (0.04)	0.16 (0.03)
	D [x 10^{-4} mm^2/s]	2.87 (1.05)	3.08 (1.15)	3.21 (1.24)	3.05 (1.15)
	D^* [x 10^{-3} mm^2/s]	13.32 (9.27)	12.81 (9.38)	17.80 (14.72)	15.25 (10.60)
non-enh. tumor (n=15)	f [-]	0.16 (0.03)	0.15 (0.04)	0.16 (0.03)	0.16 (0.04)
	D [x 10^{-4} mm^2/s]	4.51 (2.25)	4.81 (2.44)	4.84 (2.39)	4.78 (2.31)
	D^* [x 10^{-3} mm^2/s]	6.95 (4.31)	6.88 (4.29)	8.73 (4.81)	8.44 (4.93)

Table 10.1: Comparison of IVIM parameters f, D and $D*$ in brain edema, contrast enhanced and contrast not enhanced part of brain tumors. Values expressed as mean value (standard deviation). Diffusion images correction implemented in FSL, SPM, BrainSuite and without diffusion correction. Without denoising. Fitting algorithm: Fit D and f (with high b), then fit D.*

p-values		**FSL x SPM**	**FSL x BrainSuite**	**FSL x Without cor.**	**SPM x BrainSuite**	**SPM x Without cor.**	**BrainSuite x Without cor.**
edema	f	0.195	0.928	0.794	0.060	<0.001	0.858
	D	<0.001	<0.001	<0.001	0.069	<0.001	0.414
	D^*	0.021	0.470	0.424	0.010	0.004	0.671
enhanced tumor	f	0.988	0.272	0.591	0.124	0.591	0.297
	D	0.007	0.014	0.004	0.503	0.537	0.287
	D^*	0.584	0.065	0.073	0.006	0.001	0.120
non-enh. tumor	f	0.280	0.958	0.739	0.095	0.001	0.301
	D	0.008	0.160	0.005	0.653	0.628	0.716
	D^*	0.683	0.031	<0.001	0.018	<0.001	0.807

Table 10.2: The analysis between different DWI correction tools within IVIM parameters in edema, contrast enhanced and non-enhanced part of brain tumors. Statistical difference p<0.05 highlighted with gray color.

10.1.2. DWI denoising

mean value (standard deviation)		**FSL**	**SPM**	**BrainSuite**	**Without correction**
edema (n=15)	f [-]	0.09 (0.03)	0.08 (0.03)	0.08 (0.04)	0.07 (0.03)
	D [x 10^{-4} mm^2/s]	3.22 (1.23)	3.48 (1.44)	3.56 (1.43)	3.53 (1.47)
	$D*$ [x 10^{-3} mm^2/s]	3.18 (2.63)	3.11 (1.85)	3.19 (2.67)	3.08 (1.99)
enhanced tumor (n=20)	f [-]	0.13 (0.03)	0.13 (0.05)	0.14 (0.05)	0.13 (0.04)
	D [x 10^{-4} mm^2/s]	2.58 (1.02)	2.80 (1.13)	3.11 (1.45)	2.70 (1.11)
	$D*$ [x 10^{-3} mm^2/s]	6.56 (5.89)	6.41 (4.88)	9.02 (8.74)	6.93 (5.45)
non-enh. tumor (n=15)	f [-]	0.14 (0.03)	0.13 (0.04)	0.14 (0.05)	0.13 (0.05)
	D [x 10^{-4} mm^2/s]	4.32 (2.49)	4.59 (2.65)	4.74 (2.63)	4.53 (2.60)
	$D*$ [x 10^{-3} mm^2/s]	3.08 (3.00)	3.38 (2.55)	4.58 (4.58)	3.58 (2.92)

Table 10.3: Comparison of IVIM parameters f, D and $D*$ in brain edema, contrast enhanced and contrast not enhanced part of brain tumors. Values expressed as mean value (standard deviation). Diffusion images correction implemented in FSL, SPM, BrainSuite and without diffusion correction. Image denoising included. Fitting algorithm: Fit D and f (with high b), then fit D.*

p-values		**FSL x SPM**	**FSL x BrainSuite**	**FSL x Without cor.**	**SPM x BrainSuite**	**SPM x Without cor.**	**BrainSuite x Without cor.**
edema	f	0.055	0.077	0.015	0.484	0.431	0.392
	D	0.001	<0.001	<0.001	0.113	0.017	0.249
	$D*$	0.870	0.671	0.719	0.435	0.905	0.867
enhanced tumor	f	0.804	0.553	0.880	0.551	0.380	0.180
	D	0.018	0.036	0.029	0.179	0.083	0.076
	$D*$	0.772	0.075	0.460	0.030	0.049	0.059
non-enh. tumor	f	0.313	0.919	0.748	0.214	0.216	0.344
	D	0.015	0.083	0.021	0.839	0.127	0.595
	$D*$	0.189	0.026	0.019	0.096	0.164	0.120

Table 10.4: Statistical analysis between different DWI correction tools (after implementing the denoising approach) within IVIM parameters f, D and $D*$ calculation in brain edema, contrast enhanced and not enhanced part of brain tumors. Statistical difference $p<0.05$ highlighted with a gray color.

10.1.3. Different IVIM fitting algorithms

mean value (standard deviation)		**Jointly D, f, D* fitting**	**Fit D and f with fixed D* value**	**Fit D and f (with high *b*) then fit D***
edema (n=15)	f [-]	0.69 (0.13)	0.06 (0.02)	0.11 (0.03)
	D [x 10^{-4} mm^{2}/s]	7.48 (2.27)	4.84 (1.62)	3.71 (1.29)
	$D*$ [x 10^{-3} mm^{2}/s]	29.92 (24.95)		5.46 (3.64)
enhanced tumor (n=20)	f [-]	0.46 (0.16)	0.08 (0.03)	0.16 (0.04)
	D [x 10^{-4} mm^{2}/s]	4.75 (1.75)	4.68 (2.00)	3.08 (1.15)
	$D*$ [x 10^{-3} mm^{2}/s]	66.98 (35.03)		12.81 (9.38)
non-enh. tumor (n=15)	f [-]	0.66 (0.12)	0.07 (0.02)	0.15 (0.04)
	D [x 10^{-4} mm^{2}/s]	6.84 (1.83)	7.51 (4.18)	4.81 (2.44)
	$D*$ [x 10^{-3} mm^{2}/s]	37.26 (26.25)		6.88 (4.29)

Table 10.5: Comparison of IVIM parameters f, D and $D*$ in brain edema, contrast enhanced and contrast not enhanced part of brain tumors. Values expressed as mean value (standard deviation). Diffusion images correction implemented in SPM. Without denoising. Fitting algorithms: Jointly fit D, f and D, Fit D and f with fixed D* value ($0.07\ [\frac{s}{mm^2}]$) and Fit D and f (with high b), then fit D*.*

p-values		**Jointly D, f, D* fitting x Fit D and f with fixed D* value**	**Jointly D, f, D* fitting x Fit D and f (with high *b*) then fit D***	**Fit D and f with fixed D* value x Fit D and f (with high *b*) then fit D***
edema	f	<0.001	<0.001	<0.001
	D	<0.001	<0.001	<0.001
	$D*$		0.001	
enhanced tumor	f	<0.001	<0.001	<0.001
	D	0.850	<0.001	<0.001
	$D*$		<0.001	
non-enh. tumor	f	<0.001	<0.001	<0.001
	D	0.506	0.004	<0.001
	$D*$		<0.001	

Table 10.6: Statistical analysis between different IVIM fitting algorithms within IVIM parameters f, D and $D*$ calculation in brain edema, contrast enhanced and not enhanced part of brain tumors. Statistical difference p<0.05 highlighted with a gray color.

10.2. Brain tissue and brain tumor types differentiation

I am analyzing whether the IVIM method is able to differentiate diverse brain tissue types and different brain tumor types based on the patient´s data. I am finding out the impact of different correction approaches and fitting algorithms on the differentiation ability. I performed the distortions correction on diffusion images, applied the noise reduction and used three different fitting algorithms. The procedure is the same as in the section 10.1. In this chapter the results obtained from the ROC curves by applying SPM DWI correction tool (without and after applying the denoising approach) are given. The results for other correction approaches; FSL, BrainSuite and without correction (without and after applying the denoising approach) are shown in Appendix D. Moreover, this chapter contains the results acquired by implementing three fitting algorithms.

10.2.1. Different DWI correction tools

mean value (standard deviation)		**SPM**
enh. HGG (n=10)	*f* [-]	0.14 (0.03)
	D [x 10^{-4} mm^2/s]	3.23 (1.09)
	*D** [x 10^{-3} mm^2/s]	7.45 (3.37)
enh. meta (n=4)	*f* [-]	0.16 (0.03)
	D [x 10^{-4} mm^2/s]	4.21 (0.61)
	*D** [x 10^{-3} mm^2/s]	8.94 (2.11)
enh. meni. (n=6)	*f* [-]	0.18 (0.05)
	D [x 10^{-4} mm^2/s]	2.06 (0.57)
	*D** [x 10^{-3} mm^2/s]	24.34 (9.07)
edema HGG (n=10)	*f* [-]	0.12 (0.04)
	D [x 10^{-4} mm^2/s]	3.45 (1.45)
	*D** [x 10^{-3} mm^2/s]	5.81 (3.94)
edema meta. (n=4)	*f* [-]	0.09 (0.01)
	D [x 10^{-4} mm^2/s]	4.44 (0.71)
	*D** [x 10^{-3} mm^2/s]	3.35 (0.75)
non-enh HGG (n=10)	*f* [-]	0.15 (0.03)
	D [x 10^{-4} mm^2/s]	4.94 (2.75)
	*D** [x 10^{-3} mm^2/s]	5.36 (2.45)
non-enh meta (n=4)	*f* [-]	0.16 (0.03)
	D [x 10^{-4} mm^2/s]	4.80 (2.09)
	*D** [x 10^{-3} mm^2/s]	7.45 (2.11)

Table 10.7: Comparison of IVIM parameters in contrast enhanced part of tumors HGG, metastasis and meningioma, in edema of tumors HGG and metastasis, in contrast non-enhanced part of tumors HGG and metastasis. Values expressed as mean value (standard deviation). Images correction implemented in SPM. Without denoising. Fit D and f (with high b), then fit D.*

- **SPM DWI correction tool**

		p-value	AUC	*p* (AUC=0.5)	Youden index	Cut-off value	Sensit. [%]	Specific. [%]
edema × enhanced	f	0.001	0.83	<0.001	0.70	0.13 [-]	90.00	80.00
	D	0.139	0.64	0.158	0.30	3.64 [x 10^{-4} mm^2/s]	70.00	60.00
	$D*$	0.004	0.80	<0.001	0.60	5.96 [x 10^{-3} mm^2/s]	80.00	80.00
edema × non-enhan.	f	0.003	0.83	<0.001	0.60	0.11 [-]	93.33	66.67
	D	0.152	0.62	0.270	0.33	4.78 [x 10^{-4} mm^2/s]	46.67	86.67
	$D*$	0.273	0.66	0.122	0.33	2.98 [x 10^{-3} mm^2/s]	86.67	46.67
enhanced × non-enhan.	f	0.911	0.50	0.987	0.10	0.16 [-]	40.00	70.00
	D	0.020	0.75	0.003	0.42	3.69 [x 10^{-4} mm^2/s]	66.67	75.00
	$D*$	0.018	0.74	0.005	0.47	5.96 [x 10^{-3} mm^2/s]	66.67	80.00
enhan. HGG × enh. meta.	f	0.159	0.79	0.025	0.60	0.14 [-]	100.00	60.00
	D	0.061	0.78	0.048	0.55	3.69 [x 10^{-4} mm^2/s]	75.00	80.00
	$D*$	0.346	0.61	0.484	0.40	5.96 [x 10^{-3} mm^2/s]	100.00	40.00
enhan. HGG × enh. meni.	f	0.068	0.78	0.042	0.53	0.14 [-]	83.33	70.00
	D	0.013	0.80	0.009	0.60	2.66 [x 10^{-4} mm^2/s]	100.00	60.00
	$D*$	0.005	0.94	<0.001	0.83	13.41 [x 10^{-3} mm^2/s]	83.33	100.00
enh. meta × enh. meni	f	0.469	0.63	0.527	0.42	0.16 [-]	66.67	75.00
	D	0.001	1.00	<0.001	1.00	2.66 [x 10^{-4} mm^2/s]	100.00	100.00
	$D*$	0.008	0.94	<0.001	0.83	11.92 [x 10^{-3} mm^2/s]	83.33	100.00
edema HGG × edem. meta	f	0.124	0.68	0.256	0.60	0.10 [-]	100.00	60.00
	D	0.112	0.73	0.132	0.50	2.91 [x 10^{-4} mm^2/s]	100.00	50.00
	$D*$	0.087	0.73	0.066	0.40	4.47 [x 10^{-3} mm^2/s]	100.00	40.00
n.-enh. HGG × n-enh. meta	f	0.464	0.68	0.299	0.40	0.13 [-]	100.00	40.00
	D	0.921	0.50	1.000	0.25	4.80 [x 10^{-4} mm^2/s]	25.00	50.00
	$D*$	0.158	0.78	0.024	0.50	4.47 [x 10^{-3} mm^2/s]	100.00	50.00

Table 10.8: The p-value indicating the statistically significant difference, the values of AUC, p-value (AUC=0.5), Youden index, suggested cut-off, sensitivity and specificity values for IVIM parameters f, D *and* $D*$ *derived from the ROC curve in different brain tissue types and different brain tumor types. Statistical difference* $p<0.05$ *highlighted with a gray color. Diffusion images correction implemented in SPM, without denoising, fitting algorithm: Fit D and f (with high b), then fit D*.*

10.2.2. DWI denoising

mean value (standard deviation)		**SPM**
enh. HGG (n=10)	*f* [-]	0.11 (0.03)
	D [x 10^{-4} mm^2/s]	2.91 (1.12)
	*D** [x 10^{-3} mm^2/s]	3.73 (1.61)
enh. meta (n=4)	*f* [-]	0.14 (0.02)
	D [x 10^{-4} mm^2/s]	3.81 (0.67)
	*D** [x 10^{-3} mm^2/s]	4.47 (2.11)
enh. meni. (n=6)	*f* [-]	0.17 (0.08)
	D [x 10^{-4} mm^2/s]	1.96 (0.79)
	*D** [x 10^{-3} mm^2/s]	12.17 (5.11)
edema HGG (n=10)	*f* [-]	0.08 (0.04)
	D [x 10^{-4} mm^2/s]	3.18 (1.62)
	*D** [x 10^{-3} mm^2/s]	3.18 (1.54)
edema meta. (n=4)	*f* [-]	0.06 (0.01)
	D [x 10^{-4} mm^2/s]	4.30 (0.74)
	*D** [x 10^{-3} mm^2/s]	1.86 (0.75)
non-enh HGG (n=10)	*f* [-]	0.12 (0.03)
	D [x 10^{-4} mm^2/s]	4.75 (2.98)
	*D** [x 10^{-3} mm^2/s]	2.53 (1.01)
non-enh meta (n=4)	*f* [-]	0.12 (0.02)
	D [x 10^{-4} mm^2/s]	4.53 (2.31)
	*D** [x 10^{-3} mm^2/s]	3.35 (0.75)

Table 10.9: Comparison of IVIM parameters f, D and $D\ast$ in contrast enhanced part of brain tumors HGG, metastasis and meningioma, in brain edema of brain tumors HGG and metastasis, in contrast non-enhanced part of brain tumors HGG and metastasis. Values expressed as mean value (standard deviation). Diffusion images correction implemented in SPM. Denoising included. Fitting algorithm: Fit D and f (with high b), then fit D.*

- **SPM DWI correction tool**

		p-value	AUC	*p* (AUC=0.5)	Youden index	Cut-off value	Sensit. [%]	Specific. [%]
edema × enhanced	f	<0.001	0.85	<0.001	0.70	0.08 [-]	90.00	80.00
	D	0.143	0.65	0.125	0.35	3.42 [x 10^{-4} mm^2/s]	75.00	60.00
	$D*$	0.010	0.75	0.002	0.38	2.98 [x 10^{-3} mm^2/s]	65.00	73.33
edema × non-enhan.	f	0.001	0.86	<0.001	0.80	0.08 [-]	100.00	80.00
	D	0.180	0.60	0.376	0.27	4.39 [x 10^{-4} mm^2/s]	46.67	80.00
	$D*$	0.657	0.52	0.815	0.13	1.49 [x 10^{-3} mm^2/s]	73.33	40.00
enhanced × non-enhan.	f	0.783	0.54	0.694	0.25	0.14 [-]	45.00	80.00
	D	0.025	0.73	0.009	0.42	4.42 [x 10^{-4} mm^2/s]	95.00	46.67
	$D*$	0.024	0.75	0.003	0.45	2.98 [x 10^{-3} mm^2/s]	65.00	80.00
enhan. HGG × enh. meta.	f	0.074	0.85	0.002	0.70	0.12 [-]	100.00	70.00
	D	0.097	0.78	0.048	0.55	3.42 [x 10^{-4} mm^2/s]	75.00	80.00
	$D*$	0.555	0.59	0.628	0.25	5.96 [x 10^{-3} mm^2/s]	25.00	100.00
enhan. HGG × enh. meni.	f	0.111	0.76	0.051	0.40	0.10 [-]	100.00	40.00
	D	0.067	0.73	0.073	0.50	2.98 [x 10^{-4} mm^2/s]	100.00	50.00
	$D*$	0.009	1.00	<0.001	1.00	5.96 [x 10^{-3} mm^2/s]	100.00	100.00
enh. meta × enh. meni	f	0.341	0.50	1.000	0.33	0.11 [-]	66.67	0.00
	D	0.005	0.96	<0.001	0.83	2.39 [x 10^{-4} mm^2/s]	83.33	100.00
	$D*$	0.013	0.96	<0.001	0.75	4.47 [x 10^{-3} mm^2/s]	100.00	75.00
edema HGG × edem. meta	f	0.174	0.63	0.438	0.50	0.07 [-]	100.00	50.00
	D	0.103	0.73	0.132	0.50	2.53 [x 10^{-4} mm^2/s]	100.00	50.00
	$D*$	0.054	0.76	0.033	0.45	1.49 [x 10^{-3} mm^2/s]	75.00	70.00
n.-enh. HGG × n-enh. meta	f	0.846	0.68	0.300	0.40	0.10 [-]	100.00	40.00
	D	0.885	0.50	1.000	0.25	4.51 [x 10^{-4} mm^2/s]	25.00	50.00
	$D*$	0.135	0.73	0.053	0.40	1.49 [x 10^{-3} mm^2/s]	100.00	40.00

Table 10.10: The p-value indicating the statistically significant difference, the values of AUC, p-value (AUC=0.5), Youden index, suggested cut-off, sensitivity and specificity values for IVIM parameters f, D *and* $D*$ *derived from the ROC curve in different brain tissue types and different brain tumor types. Statistical difference p<0.05 highlighted with a gray color. Diffusion images correction implemented in SPM, denoising included, fitting algorithm: Fit D and f (with high b), then fit D*.*

10.2.3. Different IVIM fitting algorithms

mean value (standard deviation)		**Jointly D, f, D* fitting**	**Fit D and f with fixed D* value**	**Fit D and f (with high *b*) then fit D***
enh. HGG (n=10)	f [-]	0.56 (0.12)	0.07 (0.01)	0.14 (0.03)
	D [x 10^{-4} mm^2/s]	5.46 (1.93)	4.75 (1.66)	3.23 (1.09)
	D^* [x 10^{-3} mm^2/s]	51.54 (20.49)		7.45 (3.37)
enh. meta (n=4)	f [-]	0.47 (0.06)	0.09 (0.02)	0.16 (0.03)
	D [x 10^{-4} mm^2/s]	5.09 (1.19)	6.74 (1.61)	4.21 (0.61)
	D^* [x 10^{-3} mm^2/s]	47.93 (21.01)		8.94 (2.11)
enh. meni. (n=6)	f [-]	0.28 (0.12)	0.11 (0.04)	0.18 (0.05)
	D [x 10^{-4} mm^2/s]	3.36 (0.79)	3.19 (1.59)	2.06 (0.57)
	D^* [x 10^{-3} mm^2/s]	105.41 (33.22)		24.34 (9.07)
edema HGG (n=10)	f [-]	0.68 (0.15)	0.06 (0.03)	0.12 (0.04)
	D [x 10^{-4} mm^2/s]	7.62 (2.58)	4.43 (1.80)	3.45 (1.45)
	D^* [x 10^{-3} mm^2/s]	29.73 (24.02)		5.81 (3.94)
edema meta. (n=4)	f [-]	0.75 (0.04)	0.05 (0.01)	0.09 (0.01)
	D [x 10^{-4} mm^2/s]	7.91 (0.67)	5.76 (0.84)	4.44 (0.71)
	D^* [x 10^{-3} mm^2/s]	18.14 (13.74)		3.35 (0.75)
non-enh HGG (n=10)	f [-]	0.71 (0.07)	0.06 (0.01)	0.15 (0.03)
	D [x 10^{-4} mm^2/s]	7.38 (1.97)	7.46 (4.17)	4.94 (2.75)
	D^* [x 10^{-3} mm^2/s]	29.32 (19.60)		5.36 (2.45)
non-enh meta (n=4)	f [-]	0.61 (0.09)	0.08 (0.01)	0.16 (0.03)
	D [x 10^{-4} mm^2/s]	6.00 (0.76)	8.12 (5.27)	4.80 (2.09)
	D^* [x 10^{-3} mm^2/s]	40.58 (19.46)		7.45 (2.11)

Table 10.11: Comparison of IVIM parameters f, D and $D*$ in contrast enhanced part of brain tumors HGG, metastasis and meningioma, in brain edema of brain tumors HGG and metastasis, in contrast non-enhanced part of brain tumors HGG and metastasis. Values expressed as mean value (standard deviation). Diffusion images correction implemented in SPM. Without denoising. Fitting algorithms: Jointly fit D, f and D, Fit D and f with fixed D* value ($0.07\ [\frac{s}{mm^2}]$) and Fit D and f (with high b), then fit D*.*

- **Fitting algorithm: Jointly fit D, f and D***

		***p*-value**	**AUC**	***p* (AUC=0.5)**	**Youden index**	**Cut-off value**	**Sensit. [%]**	**Specific. [%]**
edema × enhanced	*f*	<0.001	0.88	<0.001	0.73	0.69 [-]	100.00	73.33
	D	0.001	0.82	<0.001	0.58	6.75 [x 10^{-4} mm^2/s]	85.00	73.33
	*D**	0.001	0.80	<0.001	0.53	20.47 [x 10^{-3} mm^2/s]	100.00	53.33
edema × non-enhan.	*f*	0.531	0.61	0.295	0.27	0.70 [-]	60.00	66.67
	D	0.308	0.60	0.356	0.40	6.91 [x 10^{-4} mm^2/s]	66.67	73.33
	*D**	0.287	0.63	0.238	0.33	9.91 [x 10^{-3} mm^2/s]	93.33	40.00
enhanced × non-enhan.	*f*	<0.001	0.86	<0.001	0.62	0.55 [-]	86.67	75.00
	D	0.002	0.82	<0.001	0.60	5.64 [x 10^{-4} mm^2/s]	80.00	80.00
	*D**	0.007	0.77	0.001	0.50	34.98 [x 10^{-3} mm^2/s]	60.00	90.00
enhan. HGG × enh. meta.	*f*	0.092	0.73	0.125	0.55	0.48 [-]	75.00	80.00
	D	0.672	0.50	1.000	0.30	3.90 [x 10^{-4} mm^2/s]	100.00	30.00
	*D**	0.781	0.58	0.722	0.30	36.97 [x 10^{-3} mm^2/s]	50.00	80.00
enhan. HGG × enh. meni.	*f*	0.001	0.93	<0.001	0.83	0.36 [-]	83.33	100.00
	D	0.010	0.90	<0.001	0.67	3.37 [x 10^{-4} mm^2/s]	66.67	100.00
	*D**	0.008	0.93	<0.001	0.73	73.47 [x 10^{-3} mm^2/s]	83.33	90.00
enh. meta × enh. meni	*f*	0.011	0.88	0.004	0.83	0.36 [-]	83.33	100.00
	D	0.053	0.96	<0.001	0.83	3.70 [x 10^{-4} mm^2/s]	83.33	100.00
	*D**	0.010	0.92	<0.001	0.83	72.39 [x 10^{-3} mm^2/s]	83.33	100.00
edema HGG × edem. meta	*f*	0.187	0.58	0.660	0.40	0.69 [-]	100.00	40.00
	D	0.749	0.50	1.000	0.40	8.69 [x 10^{-4} mm^2/s]	0.00	60.00
	*D**	0.284	0.60	0.527	0.40	37.46 [x 10^{-3} mm^2/s]	100.00	40.00
n.-enh. HGG × n-enh. meta	*f*	0.122	0.81	0.010	0.60	0.70 [-]	100.00	60.00
	D	0.084	0.75	0.077	0.60	6.68 [x 10^{-4} mm^2/s]	100.00	60.00
	*D**	0.384	0.68	0.300	0.40	16.10 [x 10^{-3} mm^2/s]	100.00	40.00

Table 10.12: The p-value indicating the statistically significant difference, the values of AUC, p-value (AUC=0.5), Youden index, suggested cut-off, sensitivity and specificity values for IVIM parameters f, D and $D*$ derived from the ROC curve in different brain tissue types and different brain tumor types. Statistical difference p<0.05 highlighted with a gray color. Diffusion images correction implemented in SPM, without denoising, fitting algorithm: Jointly fit D, f and D.*

- **Fitting algorithm: Fit D and f with fixed D* value ($\mathbf{0.07}$ [$\frac{\mathbf{s}}{\mathbf{mm^2}}$])**

		***p*-value**	**AUC**	***p* (AUC=0.5)**	**Youden index**	**Cut-off value**	**Sensit. [%]**	**Specific. [%]**
edema x enhanced	*f*	0.015	0.79	0.001	0.63	0.06 [-]	90.00	73.33
	D	0.793	0.52	0.818	0.22	3.59 [x 10^{-4} mm^2/s]	35.00	86.67
	*D**							
edema x non-enhan.	*f*	0.346	0.69	0.078	0.47	0.06 [-]	80.00	66.67
	D	0.038	0.71	0.038	0.47	5.57 [x 10^{-4} mm^2/s]	66.67	80.00
	*D**							
enhanced x non-enhan.	*f*	0.089	0.70	0.040	0.42	0.07 [-]	66.67	75.00
	D	0.025	0.72	0.013	0.45	6.11 [x 10^{-4} mm^2/s]	60.00	85.00
	*D**							
enhan. HGG x enh. meta.	*f*	0.088	0.86	0.001	0.60	0.07 [-]	100.00	60.00
	D	0.088	0.83	0.015	0.65	6.06 [x 10^{-4} mm^2/s]	75.00	90.00
	*D**							
enhan. HGG x enh. meni.	*f*	0.025	0.90	<0.001	0.83	0.08 [-]	83.33	100.00
	D	0.087	0.77	0.057	0.53	3.99 [x 10^{-4} mm^2/s]	83.33	70.00
	*D**							
enh. meta x enh. meni	*f*	0.223	0.69	0.312	0.42	0.09 [-]	66.67	75.00
	D	0.012	0.96	<0.001	0.83	3.99 [x 10^{-4} mm^2/s]	83.33	100.00
	*D**							
edema HGG x edem. meta	*f*	0.090	0.71	0.213	0.55	0.05 [-]	75.00	80.00
	D	0.086	0.80	0.031	0.65	5.46 [x 10^{-4} mm^2/s]	75.00	90.00
	*D**							
n.-enh. HGG x n-enh. meta	*f*	0.045	0.91	<0.001	0.70	0.06 [-]	100.00	70.00
	D	0.832	0.53	0.898	0.25	6.92 [x 10^{-4} mm^2/s]	75.00	50.00
	*D**							

Table 10.13: The p-value indicating the statistically significant difference, the values of AUC, p-value (AUC=0.5), Youden index, suggested cut-off, sensitivity and specificity values for IVIM parameters f, D *and* $D*$ *derived from the ROC curve in different brain tissue types and different brain tumor types. Statistical difference p<0.05 highlighted with a gray color. Diffusion images correction implemented in SPM, without denoising, fitting algorithm: Fit D and f with fixed D* value* (0.07 [$\frac{s}{mm^2}$]).

- **Fitting algorithm: Fit D and f (with high *b*), then fit D*** - the same as in the table 10.8., page 89.

10.3. Time duration of software tools

In this section I compare the results of time duration of different software tools within skull stripping, image registration and diffusion images correction approach. The results are introduced in the Appendix B.

According to the results, the automated algorithms perform brain extraction in greatly different time. The longest running tool ANTs executed skull stripping in more than 60 minutes, whilst the shortest running program FSL in less than one minute. Then, I compared the time duration of three different software tools (FSL FLIRT, BrainSuite and ITK SNAP + ANTs) executing image registration of T_1 and FLAIR images. The longest running tool BrainSuite registered both images in more than 25 minutes, whereas ITK SNAP + ANTS, the shortest running method, in roughly 3 minutes. I measured, furthermore, the time duration of three diffusion images correction tools. FSL tools carried out the distortions correction on 4D IVIM images in about 50 minutes, SPM in circa 9 minutes and BrainSuite in roughly 25 minutes.

11. Discussion

This chapter is divided into three parts. The first part 11.1. focuses on the description of IVIM parameters acquired with different four diffusion images correction tools; FSL, SPM, BrainSuite and without diffusion correction, with included denoising approach and last but not least, with the use of three different IVIM fitting algorithms. The comparison of the data regarding the ability to differentiate between single brain tissue types and brain tumor types is described in the section 11.2. The explanation of the results based on the theoretical background is given. In the last chapter 11.3. the main outcomes of this study are emphasized. Moreover, I suggest the optimal procedure including the use of concrete software tools and fitting algorithms. Last not least, the strengths and the limitations of the study are analyzed.

The null hypothesis in the tests I performed is the mean value in each IVIM parameter is equal in both brain segments and in both correction and fitting algorithms, respectively. The alternative hypothesis is that the mean value in each IVIM parameter is not equal in both brain segments and in both correction and fitting algorithms, respectively.

11.1. Different DWI correction tools and fitting algorithms

This chapter includes the analysis how IVIM parameters values differ from using diverse software tools for diffusion images correction (with denoising included as well) and different IVIM fitting algorithms. The statistically significant difference was investigated between different approaches within IVIM parameters in brain edema, contrast enhanced and contrast non-enhanced part of brain tumors. A remarkable finding out is there is no statistically significant difference in any IVIM parameter in any of three brain segments between the BrainSuite tool and the approach without diffusion correction. Contrarily, the statistically significant difference was confirmed between other correction approaches. Significant differences between a pair of correction tools were revealed in D and $D*$ parameter, while f parameter did not usually show any significant difference. A significant point of using three different correction software tools is their time duration. SPM tool enables to obtain the final images in much shorter time than FSL and BrainSuite, thus SPM tool is a convenient method in the clinical practice. Since I assume the use of denoising does not have substantial impact on IVIM parameters it was confirmed that the results after the noise reduction shows similar results as without denoising application. Moreover, mean $D*$ values after the application of denoising were lower than without the use of denoising. Almost all the tests confirmed the statistically significant difference between a pair of individual three fitting algorithms. Principal finding is that perfusion coefficients f and $D*$ for the fitting algorithm *Jointly fit* D*,* f *and* $D*$ are greatly higher than other two fitting algorithms; *Fit* D *and* f *with fixed* $D*$ and *Fit* D *and* f *(with high b), then fit* $D*$.

11.2. Brain tissue types and brain tumor types differentiation

In this chapter the overall comparison of results concerning differentiation of brain tissue types and brain tumor types within three diffusion correction approaches based on theory is given. At the end of this chapter, the influence of different DWI correction tools (with and without denoising) and different fitting algorithms on the ability of brain tissues and brain tumors differentiation is mentioned.

IVIM parameters f and $D*$ are physiological markers of perfusion, which means they represent the current condition of the capillary network. According to the theoretical background, the higher capillary perfusion, the higher f value. f parameter correlates with the total vessel area, vessel count differentiation degree and vascular area fraction. [112] $D*$ is proportional to the dynamic flow rate and correlates with mean vessel diameter. [112] D parameter (the pure diffusion coefficient) does not include microcirculation of blood in capillaries, while reflects the diffusion in both intra- and extra-cellular space. D parameter highly depends on cell density and extracellular space. [112]

- **Brain edema and contrast enhanced part of brain tumors**

In all the tests brain segments edema and contrast enhanced part of brain tumors could have been optimally distinguished in f and $D*$ IVIM parameter. f and $D*$ values in edema are lower than in contrast enhanced part of brain tumors. I expect f values in the contrast enhanced part of brain tumors are higher than in brain edema due to rapid tumor cells proliferation, so due to the *neovascularization* (formation of new blood vessels). $D*$ values in contrast enhanced part of brain tumors are higher than in brain edema indicating that capillary perfusion is higher due to more distinct vascular proliferation. It was concluded D parameter does not have statistically significant difference between both components. A possible explanation is that when tumor cells enter the brain tissue free movement of the fluid in the brain is restricted but these tumor cells infiltrate surrounding area as well (especially in highly invasive HGG brain tumors), thus the diffusion in brain edema would be restricted as well.

- **Brain edema and contrast not enhanced part of brain tumors**

Nearly all the approaches revealed statistical significance between edema and contrast not enhanced part of brain tumors in f parameter. The values of this parameter in edema are lower than in contrast non-enhanced part of tumors. D and $D*$ values did not detect the significant difference. The clarification for statistical significance of f IVIM parameter and non-statistical significance of D parameter is anticipated the same as for the test *brain edema and contrast enhanced part of brain tumors*.

- **Contrast enhanced and contrast not enhanced part of brain tumors**

Results in D and $D*$ are considered statistically significant between contrast enhanced and contrast non-enhanced part of brain tumors in almost all the tests I performed. D parameter values in contrast enhanced part are significantly lower than in contrast non-enhanced part, whereas $D*$ values in contrast enhanced tissue are higher than in contrast not enhanced part of brain tumors. D parameter is lower in contrast enhanced part due to limited diffusion and $D*$ parameter is higher in this brain tissue so the higher capillary perfusion in this tissue is expected. By contrast, f parameter does not have an ability to separate between both brain components. Proportion of microcirculation of both segments do not significantly differ.

- **Contrast enhanced part of brain tumors HGG and metastasis**

According to the results I assume contrast enhanced part of HGG tumor and metastasis cannot be considered as statistically significant in any IVIM parameter. This result is incompatible with the study [113] which revealed the statistical significance in f and $D*$ parameter between the HGG tumor and metastasis. It was proven $D*$ derived from HGG was significantly higher than that of metastatic tumors since HGG tumors show a wider range of vascular proliferation, thus capillary perfusion in HGG tumor is higher than in metastasis.

- **Contrast enhanced part of brain tumors HGG and meningioma**

In all the tests the $D*$ parameter revealed the statistically significant difference between contrast enhanced part of brain tumors HGG and meningioma. $D*$ in contrast enhanced part of HGG tumor was significantly lower than in meningioma. In comparison with HGG, meningioma is considered less invasive tumor [114], thereby it is assumed $D*$ in HGG is higher than in metastasis that was not, however, confirmed by the test analysis. Moreover, f and D parameters are also considered to have an ability to distinguish between both brain segments. f parameter in contrast enhanced part of HGG tumor is supposed to be statistically lower than in contrast enhanced part of meningioma. Due to the invasion of HGG tumors, the capillary perfusion in HGG is lower than in less invasive metastatic tumors. D values in contrast enhanced part of HGG tumor are considered statistically higher than in contrast enhanced part of meningioma tumor. This result is also in contrary to the initial assumption that free movement of fluid is especially restricted by the invasive tumor cells, so the D gets decreased as supported by the study. [112] The discrepancy might be caused by a different size of both samples.

- **Contrast enhanced part of brain tumors metastasis and meningioma**

The samples of contrast enhanced part of brain tumors metastasis and meningioma were especially statistically different in D and $D*$. D values in contrast enhanced part of metastasis were revealed significantly higher than in contrast enhanced part of meningioma, while $D*$ in contrast enhanced part of metastasis was significantly lower than in contrast enhanced part of meningioma. It might indicate the higher rate of capilary perfusion is more enhanced in meningioma than in metastatic tumors, thus $D*$ is higher in meningioma. The reason why D parameter in metastasis is significantly higher than in meningioma can be that infiltration of meningioma tumor cells cause the increased cellular density in this tissue resulting in the restriction of free diffusion. f IVIM parameter is said not to be statistically significant between both components. It follows the proportion of perfusion of microcirculation in both tumor types is not significantly different.

- **Edema in brain tumors HGG and metastasis**

According to the results, there is no statistical significance in most of the tests so I presume both brain components cannot be distinguished. This result is contrary to the study [113] that revealed the $D*$ values in brain edema of HGG tumors are significantly higher than in brain edema of metastasis due to their different pathological changes. Brain edema of metastatic tumors (vasogenic edema) represents lower capillary perfusion since metastatic tumor cells do not infiltrate brain edema, whereas HGG tumor cells grow in an invasive fashion in which tumor cells infiltrate other brain tissue, so including the brain edema.

- **Contrast not enhanced part of brain tumors HGG and metastasis**

Almost all the tests did not show the statistical significance between contrast not enhanced part of brain tumors HGG and metastasis thus I guess both brain segments cannot be distinguished.

It is not strictly proven whether there is some difference between three correction software tools and which algorithm performs the correction resulting in the most accurate differentiation ability. Moreover, it cannot be determined whether the approach without diffusion images correction is significantly different from correction methods. On the other hand, in some IVIM parameters within a pair of brain segments the ability of differentiation was revealed in a correction tool, whilst another correction tool did not reveal the differentiation ability. Hence, I presume the individual correction tools might play an important role in the ability of differentiation, too.

According to the results acquired with the diffusion data correction methods and with the correction including denoising, the denoising does not have any significant impact on the ability of differentiation between individual brain tissue types and brain tumor types. This fact was assumed since DWI images with higher *b* values were acquired with more NEX values, thereby the influence of random noise is not significant.

Despite the fact that the statistically significant difference was revealed between several brain segments within using the fitting algorithm *Jointly fit* D, f *and* $D*$ I assume this algorithm is not a right method for different brain tissue types and different brain tumor types differentiation. This approach does not provide accurate IVIM parameters calculation since it executes simultaneous fitting of all three IVIM parameters over all *b* values. The fitting algorithm *Fit* D *and* f *with fixed* $D*$ highly depends on the choice of the fixed $D*$ value so the differentiation ability is highly influenced by the choice of this parameter. Hence, thorough analysis of data prior the fitting is crucial. I suppose the most accurate differentiation ability was obtained by applying the fitting algorithm *Fit D and f (with high b), then fit $D*$.*

11.3. Overall summary

I cannot explicitly determine which diffusion data correction tool was the best in terms of the results accuracy and the ability of differentiation. Nonetheless, a significant factor I would be considering is the time duration, thereby I assume the SPM correction tool is the best approach. The noise reduction on this dataset does not markedly influence the results and the ability of differentiation, thus the denoising approach on this dataset did not have to be applied. However, the denoising approach for other datasets may be very important. Within other studies and in the clinical practice it is essential to examine the acquired data, to find out the acquisition parameters and thus to decide whether the denoising approach is necessary. I guess the most convenient fitting method for IVIM data is the *Fit D and f (with high b), then fit $D*$.* This algorithm is able to separate perfusion effects that are negligible at high *b* values that is a key feature for IVIM concept. I would suggest using this algorithm in other studies.

Within the study it was revealed the following brain segments pairs can be significantly distinguished: brain edema and contrast enhanced part of brain tumors, brain edema and contrast non-enhanced part of brain tumors, contrast enhanced and not enhanced part of brain tumors, contrast enhanced part of brain tumors HGG and meningioma, contrast enhanced part of brain tumors metastasis and meningioma. It follows brain tumors HGG and meningioma can be distinguished by the IVIM concept. Moreover, the study showed the ability to differentiate between brain tumors metastasis and meningioma. According to the results, the brain tumors HGG and metastasis cannot be differentiated.

The strengths of this study include the use of several approaches for IVIM parameters calculation. I thoroughly tested individual software tools for diffusion data correction and investigated the impact of the noise minimizing that is often a crucial step in diffusion images analysis. Furthermore, I acquired IVIM parameters by implementing three fitting algorithms that highly influence final IVIM parameters. Moreover, I investigated the time duration of single software tools that is an important aspect of implementing in practice.

This study suffers from several limitations. Firstly, the number of all the subjects (20) was relatively small. In addition, the sample size of patients suffering from brain tumors HGG (4) and brain tumor meningioma (6) was small. Despite the fact that in some tests between these samples the final results were excellent, the fact might be misrepresented due to a low number of both subjects whose sample sizes are not equal. Secondly, the data in three IVIM parametric maps were together aggregated in all voxels and expressed as one value. This could have resulted in the loss of sensitivity in some subjects in some brain components. A possible way how to increase the power of the statistical analysis could be to perform the measurement on the 3T MR system resulting in higher SNR. Thirdly, f values depend on the echo time T_E representing the degree of signal attenuation at low b values, thus f value in some cases might not be the true perfusion fraction parameter. Furthermore, absolutely precise image segmentation of brain lesions is very challenging so it might represent a source of inaccuracies, too. Lastly, in several statistical tests three types of different tumor types with a different growth pattern and behavior were combined together that could lead to wrongly assessment.

In further studies, it is essential to include several other brain tumor types and to extend a number of subjects. This could result in more precise verification of the IVIM concept to have an ability to differentiate between individual brain tumor types.

12. Conclusion

In this thesis I analyzed a new concept of diffusion magnetic resonance *intravoxel incoherent motion*. IVIM is a promising tool having an ability to assess perfusion and diffusion in tissue without the need of any contrast medium. One of the advantages of IVIM method is that it can be integrated onto routine magnetic resonance protocols. I performed the statistical analysis of acquired IVIM parameters. Before the statistical analysis was taken, I had executed the overall image analysis in different software tools. A crucial step for statistical analysis of IVIM parameters is distortions reduction in diffusion images which I conducted within four approaches. The results acquired by different correction approaches do not greatly differ. Moreover, the noise reduction on MR images did not influence final IVIM parameters, too. I compared three fitting algorithms for IVIM data. I assume the fitting algorithm *Fit D and f (with high b), then fit $D*$* is the most accurate since its ability to model separately perfusion and diffusion effects.

The main objective proven in this thesis is the ability of the IVIM concept to distinguish between a brain tumor and its surrounding areas and to differentiate between individual brain tumor types. The study revealed a significant variability of IVIM parameters in following pairs of brain components: brain edema and contrast enhanced part of brain tumors, brain edema and contrast non-enhanced part of brain tumors, contrast enhanced and not enhanced part of brain tumors, contrast enhanced part of brain tumors HGG and meningioma, contrast enhanced part of brain tumors metastasis and meningioma. Brain tumors HGG and meningioma; and metastasis and meningioma were confirmed to have an ability to be distinguished between each other. Brain tumors HGG and metastasis were not shown to be statistically different.

In the future, it would be interesting to repeat this study on a larger data set. I performed the statistical analysis testing the mean value in each IVIM parameter. Analysis of the variation of IVIM parameters could be a right approach, too. In this study the statistical analysis was executed on segmented brain components. It could be beneficial to run the analysis on a whole brain segment which could be a less time-consuming method since image segmentation would not be required. In the study I applied the IVIM biexponential method to model the non-Gaussian behavior. The use of other models and their comparison could be advantageous for the clinical practice.

13. References

[1] HIDALGO-TOBBON, S.S. Theory of gradient coil design methods for magnetic resonance imaging. *Concepts in Magnetic Resonance Part A. Volume 36A, Number 4.* 2010. p. 223-242. ISSN: 1546-6086. Online at: https://onlinelibrary.wiley.com/doi/full/10.1002/cmr.a.20163; accessed April 17, 2020.

[2] MCROBBIE, D.W., E.A. MOORE, M.J. GRAVES and M.R. PRINCE. *MRI From Picture to Proton, second edition*. New York: Cambridge University Press, 2007. ISBN: 10-0-521-865-27-1.

[3] MECHL, M., J. TINTĚRA and J. ŽIŽKA. *Protokoly MR zobrazování*. Praha: Galén, 2014. ISBN: 978-80-7492-109-4.

[4] EL-DAHSHAN, E.A., K. REVETT, H. MOHSEN and A.B. SALEM. Computer-aided diagnosis of human brain tumor through MRI: A survey and a new algorithm. *Expert Systems with Applications*. *Volume 41, Number 11*. 2014. p. 5526-5545. ISSN: 0957-4174. Online at: https://www.researchgate.net/publication/261715655_Computer-aided_diagnosis_of_human_brain_tumor_through_MRI_A_survey_and_a_new_algorithm; accessed February 10, 2020.

[5] BRUCE, L.D., A. SHIMAKAWA, M.R. BLUM and R.J. HERFKENS. Single-shot fluid attenuated inversion recovery (FLAIR) magnetic resonance imaging of the bladder. *Journal of Magnetic Resonance Imaging (JMRI). Volume 11, Number 6.* 2000. p. 673-677. ISSN: 1053-1807. Online at: https://onlinelibrary.wiley.com/doi/full/10.1002/1522-2586%28200006%2911%3A6%3C673%3A%3AAID-JMRI14%3E3.0.CO%3B2-F; accessed February 10, 2020.

[6] QUESTIONS AND ANSWERS IN MRI. *Selecting IR Parameters*. Online at: http://mriquestions.com/choice-of-ir-parameters.html; accessed: February 13, 2020.

[7] HAACKE, E.M. and J.A. TKACH. Fast MR Imaging: Techniques and Clinical Applications. *American Journal of Roentgenology. Volume 155, Number 5.* 1990. p. 951-964. ISSN: 0361-803X. Online at: https://pubmed.ncbi.nlm.nih.gov/2120964/; accessed: January 17, 2020.

[8] POUSTCHI-AMIN, M., S.A. MIROWITZ, J.J. BROWN, R.C. MCKINSTRY and T. LI. Principles and Applications of Echo-planar Imaging: A Review for the General Radiologist. *RadioGraphics.*

Volume 21, Number 3. 2001. p. 767-780. ISSN: 0271-5333. Online at: https://pubs.rsna.org/doi/full/10.1148/radiographics.21.3.g01ma23767; accessed: January 17, 2020.

[9] DELAPAZ, R.L. Echo-planar Imaging. *RadioGraphics. Volume 14, Number 5.* 1994. p. 1045-1058. ISSN: 0271-5333. Online at: https://pubs.rsna.org/doi/pdf/10.1148/radiographics.14.5.7991813; accessed: January 17, 2020.

[10] KORFIATIS, P. and B. ERICKSON. The basics of diffusion and perfusion imaging in brain tumors. *Applied Radiology. Volume 43, Number 7.* 2014. p. 22-29. ISSN: 0160-9963. Online at: https://www.appliedradiology.com/articles/the-basics-of-diffusion-and-perfusion-imaging-in-brain-tumors; accessed: February 17, 2020.

[11] LIMA, M. and D.L. BIHAN. Clinical Intravoxel Incoherent Motion and Diffusion MR Imaging: Past, Present, and Future. *Radiology. Volume 278, Number 1.* 2015. p. 13-32. ISSN: 0033-8419. Online at: https://pubs.rsna.org/doi/full/10.1148/radiol.2015150244; accessed: February 17, 2020.

[12] STANFORD UNIVERSITY. *Diffusion MRI: Lecture 1 of 2.* Online at: http://web.stanford.edu/class/rad229/Notes/5b-Diffusion.pdf; accessed: February 25, 2020.

[13] KIM, S.Y. et al. Reproducibility of Measurement of Apparent Diffusion Coefficients of Malignant Hepatic Tumors: Effect of DWI Techniques and Calculation Methods. *Journal of Magnetic Resonance Imaging. Volume 36, Number 5.* 2012. p. 1131-1138. ISSN: 1053-1807. Online at: https://onlinelibrary.wiley.com/doi/pdf/10.1002/jmri.23744; accessed: April 16, 2020.

[14] REGENOLD, W.T. Lithium and Increased Hippocampal Volume - More Tissue or More Water. *Neuropsychopharmacology. Volume 33, Number 7*. 2008. p. 1773-1774. ISSN: 0893-133X. Online at: https://www.nature.com/articles/1301524; accessed: February 25, 2020.

[15] BALIYAN, V., C.J. DAS, R. SHARMA and A.K. GUPTA. Diffusion weighted imaging: Technique and applications. *World Journal of Radiology. Volume 8, Number 9*. 2016. p. 785-798. ISSN: 1949-8470. Online at: https://www.ncbi.nlm.nih.gov/pmc/articles/PMC5039674/; accessed February 5, 2020.

[16] HILDEBRAND, D. *Quantitative diffusion-weighted imaging in breast and liver tissue.* Groningen: Rijksuniversiteit Groningen, 2016. ISBN: 978-90-367-9096-3. Online at: https://www.rug.nl/research/portal/files/36426322/Complete_thesis.pdf; accessed April 3, 2020.

[17] ASSAF, Y and Y. COHEN. Inferring Microstructural Information of White Matter from Diffusion MRI*. Diffusion MRI*. 2014. p. 185-208. ISBN: 9780123747099. Online at: https://www.sciencedirect.com/science/article/pii/B9780123964601000093; accessed: February 24, 2020.

[18] TSAI, R., L. HSIEH, S. CHENG and C. CHEN. Secondary pallidonigral degeneration mimicking recurrent acute stroke in clinical presentation and magnetic resonance imaging: a case report. *BMC Neurology. Volume 17, Number 1*. 2017. Online at: https://www.researchgate.net/publication/321734277_Secondary_pallidonigral_degeneration_mimicking_recurrent_acute_stroke_in_clinical_presentation_and_magnetic_resonance_imaging_A_case_report; accessed February 24, 2020.

[19] WINSTON, G. The physical and biological basis of quantitative parameters derived from diffusion MRI. *Quantitative imaging in medicine and surgery. Volume 2, Number 4*. 2012. p. 254-265. ISSN: 2223-4292. Online at: http://qims.amegroups.com/article/view/1315/1771; accessed February 24, 2020.

[20] CHIARADIA, M. et al. Intravoxel incoherent motion (IVIM) MR imaging of colorectal liver metastases: Are we only looking at tumor necrosis? *Journal of magnetic resonance imaging. Volume 39, Number 2. 2013.* p. 317-325. ISSN: 1053-1807. Online at: https://onlinelibrary.wiley.com/doi/full/10.1002/jmri.24172; accessed October 22, 2019.

[21] BIHAN, D.L. What can we see with IVIM MRI? *NeuroImage. Volume 187*. 2019. p. 56-67. ISSN: 1053-8119. Online at: https://www.sciencedirect.com/science/article/pii/S1053811917310868; accessed: October 14, 2019.

[22] CONKLIN, J. et al. A Simplified Model for Intravoxel Incoherent Motion Perfusion Imaging of the Brain. *American Journal of Neuroradiology. Volume 37, Number 12*. 2016. p. 2251-2257. ISSN: 0195-6108. Online at:

http://www.ajnr.org/content/ajnr/early/2016/08/25/ajnr.A4929.full.pdf; accessed: February 04, 2020.

[23] PATEL, J. et al. Diagnosis of cirrhosis with intravoxel incoherent motion diffusion MRI and dynamic contrast-enhanced MRI alone and in combination: Preliminary experience. *Journal of Magnetic Resonance Imaging. Volume 31, Number 3*. 2010. p. 589-600. ISSN: 1053-1807. Online at: https://www.ncbi.nlm.nih.gov/pmc/articles/PMC5207803/; accessed April 13, 2020.

[24] WU, H. et al. Meta-analysis of intravoxel incoherent motion magnetic resonance imaging in differentiating focal lesions of the liver. *Medicine. Volume 97, Number 34*. 2018. ISSN: 0025-7974. Online at: https://www.ncbi.nlm.nih.gov/pmc/articles/PMC6112959/; accessed April 13, 2020.

[25] BANE, O. et al. Assessment of Renal Function Using Intravoxel Incoherent Motion Diffusion-Weighted Imaging and Dynamic Contrast-Enhanced MRI. *Journal of Magnetic Resonance Imaging. Volume 44, Number 2.* 2016. p. 317-326. ISSN: 1053-1807. Online at: https://pubmed.ncbi.nlm.nih.gov/26855407/; accessed March 04, 2020.

[26] BIHAN, D.L., M. LIMA, C. FEDERAU and E.E. SIGMUND. *Intravoxel Incoherent Motion (IVIM) MRI*. New York: Jenny Stanford Publishing, 2018. ISBN: 9780429427275.

[27] TOFTS, P. *Quantitative MRI of the Brain: Measuring Changes Caused by Disease*. New Jersey: Chichester, 2010. ISBN: 9780470869499.

[28] QUESTIONS AND ANSWERS IN MRI. *IVIM Imaging*. Online at: http://mriquestions.com/ivim.html; accessed: February 14, 2020.

[29] KOH, D., D.J. COLLINS and M.R. ORTON. Intravoxel Incoherent Motion in Body Diffusion-Weighted MRI: Reality and Challenges. *American Journal of Roentgenology. Volume 196, Number 6*. 2011. p. 1351-1361. ISSN: 0361-803X. Online at: http://mriquestions.com/uploads/3/4/5/7/34572113/koh_ivim_body_ajr.10.5515.pdf; accessed: February 27, 2020.

[30] WÁNG, Y.X.J. Living tissue intravoxel incoherent motion (IVIM) diffusion MR analysis without b=0 image: an example for liver fibrosis evaluation. *Quantitative imaging in medicine*

and surgery. Volume 9, Number 2. 2019. p. 127-133. ISSN: 2223-4292. Online at: http://qims.amegroups.com/article/view/24080/22818; accessed February 27, 2020.

[31] JALNEFJORD, O. *Intravoxel incoherent motion modeling - Optimization of acquisition, analysis and tumor tissue characterization*. Gothenburg: BrandFactory, 2018. ISBN: 978-91-7833-078-2. Online at: https://gupea.ub.gu.se/bitstream/2077/56355/2/gupea_2077_56355_2.pdf; accessed: February 27, 2020.

[32] GÖLGELI, A. and M.H. GÖLGELI. *Cerebrospinal Fluid*. Recent Researches in Health Sciences. 2018. p. 20-32. ISBN: 9781527520066.

[33] Third Faculty of Medicine, Charles University. *Cerebrospinal Fluid, Blood-Brain Barrier and Blood-CSF Barrier.* Online at: http://fblt.cz/en/skripta/regulacni-mechanismy-2-nervova-regulace/12-likvor-hematoencefalicka-a-hematolikvorova-bariera/; accessed March 15, 2020.

[34] NA, M.K. et al. Gray matter to white matter ratio for predicting neurological outcomes in patients treated with target temperature management after cardiac arrest: A systematic review and meta-analysis. *Resuscitation. Volume 132*. 2018. p. 21-18. ISSN: 0300-9572. Online at: https://www.sciencedirect.com/science/article/abs/pii/S0300957218308062; accessed March 15, 2020.

[35] MOCCIA, M. et al. Gray:white Matter Ratio at Diagnosis and the Risk of 10-year Multiple Sclerosis Progression. *European Journal of Neurology. Volume 24, Number 1*. 2017. p. 195-204. Online at: https://pubmed.ncbi.nlm.nih.gov/27801535/; accessed March 15, 2020.

[36] JHA, S.K. Cerebral Edema and its Management. *Medical journal, Armed Forces India. Volume 54, Number 4.* 2003. p. 326-331. ISSN: 0377-1237. Online at: https://www.ncbi.nlm.nih.gov/pmc/articles/PMC4923559/; accessed March April 13, 2020.

[37] VILLANUEVA-MEYER, J.E., M.C. MABRAY and S. CHA. Current Clinical Brain Tumor Imaging. *Neurosurgery. Volume 81, Number 31.* 2017. p. 397-415. ISSN: 1524-4040. Online at: https://www.ncbi.nlm.nih.gov/pmc/articles/PMC5581219/; accessed April 18, 2020.

[38] MIHARA, F. Non-enhancing supratentorial malignant astrocytomas: MR features and possible mechanisms. *Radiation Medicine. Volume 13, Number 1*. 1995. ISSN: 0288-2043.

Online at: https://www.researchgate.net/publication/15602339_Non-enhancing_supratentorial_malignant_astrocytomas_MR_features_and_possible_mechanisms; accessed April 18, 2020.

[39] RADIOLOGY ASSISTANT. *Brain Tumor - Systematic Approach*. Online at: https://radiologyassistant.nl/neuroradiology/brain-tumor-systematic-approach; accessed April 18, 2020.

[40] MIRIMANOFF, R. High-grade gliomas: reality and hopes. *Chinese journal of cancer. Volume 33, Number 1.* 2014. p. 1-3. ISSN: 1000-467X. Online at: https://www.ncbi.nlm.nih.gov/pmc/articles/PMC3905083/; accessed April 19, 2020.

[41] POPE, W.B. and G. BRANDAL. Conventional and advanced magnetic resonance imaging in patients with high-grade glioma. *Quarterly Journal of Nuclear Medicine and Molecular Imaging. Volume 62, Number 3*. 2018. p. 239-253. ISSN: 1824-4785. Online at: https://www.ncbi.nlm.nih.gov/pmc/articles/PMC6123261/; accessed April 19, 2020.

[42] FINK, K.R. and J.R. FINK. Imaging of brain metastases. *Surgical neurology international. Volume 4.* 2013. p. 209-219. ISSN: 2229-5097. Online at: https://www.ncbi.nlm.nih.gov/pmc/articles/PMC3656556/; accessed April 19, 2020.

[43] POPE, W.B. Brain metastases: neuroimaging. *Handbook of Clinical Neurology. Volume 149*. 2018. p. 89-112. ISSN: 0072-9752. Online at: https://www.ncbi.nlm.nih.gov/pmc/articles/PMC6118134/; accessed April 20, 2020.

[44] WATTS, J. et al. Magnetic resonance imaging of meningiomas: a pictorial review. *Insights into Imaging. Volume 5, Number 1.* 2014. p. 113-122. Online at: https://www.ncbi.nlm.nih.gov/pmc/articles/PMC3948902/; accessed April 20, 2020.

[45] KALAVATHI, P. and V.B.S. PRASATH. Methods on Skull Stripping of MRI Head Scan Images - a Review. *Journal of Digital Imaging. Volume 29, Number 3*. 2016. p. 2016. ISSN: 0897-1889. Online at: https://www.ncbi.nlm.nih.gov/pmc/articles/PMC4879034/; accessed April 06, 2020.

[46] HLAVÁČ, V. *Mathematical morphology*. Online at: http://people.ciirc.cvut.cz/~hlavac/TeachPresEn/11ImageProc/71-3MatMorpholBinEn.pdf; accessed April 08, 2020.

[47] NAYAK, J. Performance Evaluation of Skull Stripping Methods and Tools. *International Journal of Computer Trends and Technology. Volume 4, Number 9.* 2013. p. 3278-3281. ISSN: 2231-2803. Online at: http://ijcttjournal.org/Volume4/issue-9/IJCTT-V4I9P157.pdf; accessed April 08, 2020.

[48] KAZEMI, K. and N. NOORIZADEH. Quantitative Comparison of SPM, FSL, and BrainSuite for Brain MR Image Segmentation. *Journal of biomedical physics & engineering. Volume 4, Number 1.* 2014. p. 13-26. ISSN: 2251-7200. Online at: https://www.ncbi.nlm.nih.gov/pmc/articles/PMC4258855/; accessed April 10, 2020.

[49] SÉGONNE, F. et al. A Hybrid Approach to the Skull Stripping Problem in MRI. *NeuroImage. Volume 13, Number 6*. 2001. ISSN: 1053-8119. Online at: http://surfer.nmr.mgh.harvard.edu/ftp/articles/segonne05.pdf; accessed April 10, 2020.

[50] ROSLAN, R., R. MAHMUD and N. JAMIL. Skull stripping of MRI brain images using mathematical morphology. *Conference: Biomedical Engineering and Sciences*. 2010. ISBN: 978-1-4244-7599-5. Online at: https://www.researchgate.net/publication/224227528_Skull_stripping_of_MRI_brain_images_using_mathematical_morphology; accessed April 12, 2020.

[51] DOSHI, J. et al. Multi-Atlas Skull-Stripping. *Academic Radiology. Volume 20, Number 12.* 2013. p. 1566-1576. ISSN: 1076-6332. Online at: https://www.ncbi.nlm.nih.gov/pmc/articles/PMC3880117/; accessed April 12, 2020.

[52] TAO, X. and M.C. CHANG. A Skull Stripping Method Using Deformable Surface and Tissue Classification. *Progress in Biomedical Optics and Imaging - Proceedings of SPIE*. 2010. ISSN: 1605-7422. Online at: https://www.albany.edu/faculty/mchang2/files/2010_01_SPIE_Skull_Stripping.pdf; accessed April 13, 2020.

[53] GALDAMES, F., F. JAILLET and C.A. PEREZ. An Accurate Skull Stripping Method Based on Simplex Meshes and Histogram Analysis in Magnetic Resonance Images. *Journal of Neuroscience Methods. Volume 206, Number 2*. 2012. p. 103-119. ISSN: 0165-0270. Online at: https://liris.cnrs.fr/Documents/Liris-5295.pdf; accessed April 10, 2020.

[54] CHAIRA, T. *Medical Image Processing – Advanced Fuzzy Set Theoretic Techniques*. New York: Taylor&Francis Group, 2015. ISBN: 978-1-4987-0045-0.

[55] SHODHGANGA. *Review of Interpolation Methods*. Online at: https://shodhganga.inflibnet.ac.in/bitstream/10603/121236/9/09_chapter2.pdf; accessed: April 15, 2020.

[56] DIETRICH, O., S. HEILAND, T. BENNER and K. SARTOR. Reducing motion artefacts in diffusion-weighted MRI of the brain: Efficacy of navigator echo correction and pulse triggering. *Neuroradiology. Volume 42, Number 2*. 2000. p. 85-91. ISSN: 0028-3940. Online at: https://www.researchgate.net/publication/12650809_Reducing_motion_artefacts_in_diffusion-weighted_MRI_of_the_brain_Efficacy_of_navigator_echo_correction_and_pulse_triggering; accessed April 15, 2020.

[57] SHEELA, V.K. and S.S. BABU. Performance Analysis of Noise Reduction Technologies in Brain MRI Image. *International Journal of Circuit Theory and Applications. Volume 7, Number 1*. 2016. p. 69-74. ISSN: 2229-6093. Online at: http://www.ijcta.com/documents/volumes/vol7issue1/ijcta2016070115.pdf; accessed April 17, 2020.

[58] YANG, J. et al. Brain MR image denoising for Rician noise using pre-smooth non-local means filter. *BioMedical Engineering OnLine. Volume 14, Number 1.* 2015. ISSN: 1475-925X. Online at: https://www.ncbi.nlm.nih.gov/pmc/articles/PMC4360923/; accessed April 10, 2020.

[59] AKSHATH, M.J. and H.S. SHESHADRI. Denoising of skull stripped brain tumor MR images. *International Journal of Computer Sciences and Engineering. Volume 6, Number 11*. 2018. Online at: https://www.researchgate.net/publication/330136674_Denoising_of_skull_stripped_brain_tumor_MR_images; accessed April 10, 2020.

[60] SONG, S., Y. ZHENG and Y. HE. A Review of Methods for Bias Correction in Medical Images. *Biomedical Engineering Review. Volume 3, Number 1*. 2017. ISSN: 2375-9143. Online at: https://journals.ke-i.org/index.php/bme/article/view/1550/1255; accessed April 10, 2020.

[61] VOVK, U., F. PERNUŠ and B. LIKAR. A Review of Methods for Correction of Intensity Inhomogeneity in MRI. *IEEE Transactions on Medical Imaging. Volume 26, Number 3*. 2007. p.

405-421. Online at: https://mriquestions.com/uploads/3/4/5/7/34572113/surface_intensity_correction.pdf; accessed April 05, 2020.

[62] TSOUGOS, I. *Advanced MR Neuroimaging*: From Theory to Clinical Practice. CRC Press, 2019. ISBN: 9780367876500.

[63] BIHAN, D.L., C. POUPON, A. AMADON and F. LETHIMONNIER. Artifacts and Pitfalls in Diffusion MRI. *Journal of Magnetic Resonance Imaging. Volume 24*. 2006. p. 478-488. Online at: http://www.meteoreservice.com/PDFs/DLB06.pdf; accessed March 15, 2020.

[64] MAJUMDAR, A., R.K. WARD and K. INIEWSKI. *MRI physics, image reconstruction, and analysis*. New York: Taylor & Francis Group, 2016. ISBN: 9781482298871.

[65] DIETRICH, O., S. HEILAND and K. SARTOR. Noise correction for the exact determination of apparent diffusion coefficients at low SNR. *Magnetic Resonance in Medicine. Volume 45., Number 3*. 2001. p. 448-453. Online at: https://onlinelibrary.wiley.com/doi/full/10.1002/1522-2594%28200103%2945%3A3%3C448%3A%3AAID-MRM1059%3E3.0.CO%3B2-W; accessed March 23, 2020.

[66] FERNÁNDEZ, S.A. and G.V.S. FERERO. *Statistical Analysis of Noise in MRI*. Springer International Publishing, 2016. ISBN: 978-3-319-39933-1. Online at: https://link.springer.com/content/pdf/bbm%3A978-3-319-39934-8%2F1.pdf; accessed April 03, 2020.

[67] LAM, F. et al. Denoising Diffusion-Weighted Magnitude MR Images using Rank and Edge Constraints. *Magnetic resonance in medicine. Volume 71, Number 3*. 2014. p. 1272-1284. ISSN: 0740-3194. Online at: https://www.worldcat.org/title/denoising-diffusion-weighted-magnitude-mr-images-using-rank-and-edge-constraints/oclc/5540113342&referer=brief_results; accessed April 05, 2020.

[68] KONISHI, Y. et al. Simple noise reduction for diffusion weighted images. *Radiological Physics and Technology. Volume 9, Number 2*. 2016. p. 221-226. ISSN: 1865-0333. Online at: https://core.ac.uk/download/pdf/197208538.pdf; accessed April 05, 2020.

[69] ST-JEAN, S. et al. *Automated characterization of noise distributions in diffusion MRI data*. 2019. Online at: https://www.researchgate.net/publication/334107872_Automated_characterization_of_noise_distributions_in_diffusion_MRI_data; accessed April 04, 2020.

[70] DAESSLÉ, N.W. et al. Rician noise removal by non-Local Means filtering for low signal-to-noise ratio MRI: applications to DT-MRI. *Medical image computing and computer-assisted intervention. Volume 11, Number 2.* 2008. p. 171-179. Online at: https://www.ncbi.nlm.nih.gov/pmc/articles/PMC2665702/; accessed April 06, 2020.

[71] PALMA, C.A. et al. Anisotropic Diffusion Filtering Operation and Limitations - Magnetic Resonance Imaging Evaluation. *IFAC Proceedings Volumes. Volume 47, Number 3.* 2014. p. 3887-3892. Online at: https://www.sciencedirect.com/science/article/pii/S147466701642210X; accessed April 13, 2020.

[72] MANJÓN, J.V. et al. Diffusion Weighted Image Denoising Using Overcomplete Local PCA. *PLOS One*. 2013. Online at: https://journals.plos.org/plosone/article?id=10.1371/journal.pone.0073021; accessed April 10, 2020.

[73] DUYN, J. MR susceptibility imaging. *Journal of Magnetic Resonance. Volume 229*. 2013. p. 198-207. ISSN: 1090-7807. Online at: https://www.ncbi.nlm.nih.gov/pmc/articles/PMC3602381/; accessed April 15, 2020.

[74] ANDERSSON, J.L.R. et al. Susceptibility-induced distortion that varies due to motion: Correction in diffusion MR without acquiring additional data. *NeuroImage. Volume 171.* 2018. p. 277-295. ISSN: 1053-8119. Online at: https://www.sciencedirect.com/science/article/pii/S1053811917310601#bib4; accessed April 15, 2020.

[75] MCGINLEY, G. *Magnetic Susceptibility Artefact Correction of Spin-Echo and Gradient-Echo EPI Images.* Oslo, 2016. Master's thesis. University of Oslo, Department of Physics.

[76] BHUSHAN, C., J.P. HALDAR, A.A. JOSHI and R.M. LEAHY. Correcting Susceptibility-Induced Distortion in Diffusion-Weighted MRI using Constrained Nonrigid Registration. *Signal and*

Information Processing Association Annual Summit and Conference. 2012. Online at: https://www.ncbi.nlm.nih.gov/pmc/articles/PMC4708288/; accessed March 24, 2020.

[77] WIKIPEDIA. *Lenz's law*. Online at: https://en.wikipedia.org/wiki/Lenz%27s_law; accessed April 10, 2020.

[78] SPEES, W.M. et al. Quantification and Compensation of Eddy-Current-Induced Magnetic Field Gradients. *Journal of Magnetic Resonance. Volume 212, Number 1.* 2011. p. 116-123. ISSN: 1090-7807. Online at: https://www.ncbi.nlm.nih.gov/pmc/articles/PMC3163721/; accessed April 04, 2020.

[79] ZHUANG, J. *The eddy current distortion in the multiband diffusion images: diagnosis and correction.* 2017. Online at: https://arxiv.org/ftp/arxiv/papers/1704/1704.00494.pdf; accessed April 08, 2020.

[80] BRUN, L. et al. Diffusion MRI: Assessment of the Impact of Acquisition and Preprocessing Methods Using the BrainVISA-Diffuse Toolbox. *Frontiers in Neuroscience*. 2019. ISSN: 1662-453X. Online at: https://www.frontiersin.org/articles/10.3389/fnins.2019.00536/full; accessed April 13, 2020.

[81] GRAHAM, M.S., I. DROBNJAK and H. ZHANG. Realistic simulation of artefacts in diffusion MRI for validating post-processing correction techniques. *NeuroImage. Volume 125*. 2016. p. 1079-1094. ISSN: 1053-8119. Online at: https://www.sciencedirect.com/science/article/pii/S1053811915010289?via%3Dihub; accessed April 14, 2020.

[82] BODAMMER, N., J. KAUFMANN, M. KANOWSKI and C. TEMPELMANN. Eddy current correction in diffusion-weighted imaging using pairs of images acquired with opposite diffusion gradient polarity. *Magnetic resonance in medicine. Volume 51, Number 1*. 2003. p. 188-193. ISSN: 0740-3194. Online at: https://onlinelibrary.wiley.com/doi/full/10.1002/mrm.10690; accessed January 24, 2020.

[83] HUIZINGA, W. et al. *Groupwise Registration for Correcting Subject Motion and Eddy Current Distortions in Diffusion MRI Using a PCA Based Dissimilarity Metric*. 2013. ISSN: 1612-3786. Online at: https://www.researchgate.net/publication/284617465_Groupwise_Registration_for_Correctin

g_Subject_Motion_and_Eddy_Current_Distortions_in_Diffusion_MRI_Using_a_PCA_Based_Dissimilarity_Metric; accessed April 01, 2020.

[84] METZ, C.T. et al. Nonrigid Registration of Dynamic Medical Imaging Data Using nD + T B-splines and a Groupwise Optimization Approach. *Medical Image Analysis. Volume 15, Number 2*. 2011. p. 238-249. ISSN: 1361-8415. Online at: https://pubmed.ncbi.nlm.nih.gov/21075672/; accessed April 01, 2020.

[85] HUIZINGA, W. et al. Groupwise registration for correcting subject motion and eddy current distortions in diffusion MRI using a PCA based dissimilarity metric. *Mathematics and Visualization.* 2014. p. 163-174. ISSN: 1612-3786. Online at: https://www.researchgate.net/publication/298189917_Groupwise_Image_Registration_in_Diffusion_Weighted_MRI_using_a_PCA_based_Dissimilarity_Metric; accessed April 04, 2020.

[86] MOHAMMADI, S. et al. Correcting Eddy Current and Motion Effects by Affine Whole-Brain Registrations: Evaluation of Three-Dimensional Distortions and Comparison With Slicewise Correction. *Magnetic Resonance in Medicine. Volume 64, Number 4*. 2010. p. 1047-1056. ISSN: 0740-3194. Online at: https://www.researchgate.net/publication/44699157_Correcting_Eddy_Current_and_Motion_Effects_by_Affine_Whole-Brain_Registrations_Evaluation_of_Three-Dimensional_Distortions_and_Comparison_With_Slicewise_Correction; accessed April 04, 2020.

[87] DESPOTOVIĆ, I., B. GOOSSENS and W. PHILIPS. MRI Segmentation of the Human Brain: Challenges, Methods, and Applications. *Computational and Mathematical Methods in Medicine*. 2015. ISSN: 1748-6718. Online at: https://www.ncbi.nlm.nih.gov/pmc/articles/PMC4402572/; accessed April 10, 2020.

[88] YUSHKEVICH, P.A. et al. User-guided 3D active contour segmentation of anatomical structures: Significantly improved efficiency and reliability. *NeuroImage. Volume 31, Number 3.* 2006. p. 1116-1128. ISSN: 1053-8119. Online at: https://pubmed.ncbi.nlm.nih.gov/16545965/; accessed September 15, 2019.

[89] ITK-SNAP. *ITK-SNAP 3.6.0*. [software]. [accessed September 15, 2019]. Online at: http://www.itksnap.org.

[90] WOOLRICH, M.W. et al. Bayesian analysis of neuroimaging data in FSL. *NeuroImage. Volume 45, Number 1*. 2009. p. 173-186. ISSN: 1053-8119. Online at: https://pubmed.ncbi.nlm.nih.gov/19059349/. Accessed September 16, 2019.

[91] FMRIB Software Library. *FSL 6.0.1* [software]. [accessed September 16, 2019]. Online at: https://fsl.fmrib.ox.ac.uk/fsl/fslwiki.

[92] REUTER, M., N.J. SCHMANSKY, H.D. ROSAS and B. FISCHL. Within-subject template estimation for unbiased longitudinal image analysis. *NeuroImage. Volume 61, Number 4*. 2012. p. 1402-1418. ISSN: 1053-8119. Online at: https://pubmed.ncbi.nlm.nih.gov/22430496/. Accessed September 29, 2019.

[93] FreeSurfer. *FreeSurfer 6.0.* [software]. [accessed September 29, 2019]. Online at: https://surfer.nmr.mgh.harvard.edu/.

[94] MATLAB - MathWorks - MATLAB & Simulink. *MATLAB R2019.a*. [software]. [accessed August 29, 2019]. Online at: https://www.mathworks.com/.

[95] SPM - Statistical Parametric Mapping. *SPM 12*. [software]. [accessed September 14, 2019]. Online at: https://www.fil.ion.ucl.ac.uk/spm/software/spm12/.

[96] SHATTUCK, D.W. and R.M. LEAHY. BrainSuite: An Automated Cortical Surface Identification Tool. *Medical Image Analysis. Volume 6, Number 2*. 2002. p. 129-142. ISSN: 1361-8415. Online at: https://pubmed.ncbi.nlm.nih.gov/12045000/; accessed October 13, 2019.

[97] BrainSuite. *BrainSuite 19a.* [software]. [accessed October 13, 2019]. Online at: http://brainsuite.org/.

[98] Advanced Normalization Tools. *ANTs*. [software]. [accessed October 26, 2019]. Online at: http://stnava.github.io/ANTs/.

[99] AVANTS, B. and N. TUSTISON. *ANTs/ANTsR Brain Templates*. 2018. Online at: https://doi.org/10.6084/m9.figshare.915436.v2; accessed November 14, 2019.

[100] SMITH, S.M. Fast robust automated brain extraction. *Human Brain Mapping. Volume 17, Number 3.* 2002. p. 143-155. ISSN: 1065-9471. Online at: https://pubmed.ncbi.nlm.nih.gov/12391568/; accessed September 15, 2019.

[101] Rigid and affine registration of 3D volumes. *register_files_affine*. [software]. [accessed November 15, 2019]. Online at: https://neuroimage.usc.edu/neuro/Resources/BDPAddons?fbclid=IwAR3e5h9N-87T63tln9DSHh3LPsLLS_il12IB63Q1pnnoSZszRl0IpdDL7o4#affineReg.

[102] ZHANG, Y., M. BRADY and S. SMITH. Segmentation of Brain MR Images Through a Hidden Markov Random Field Model and the Expectation-Maximization Algorithm. *IEEE Transactions on Medical Imaging. Volume 20, Number 1.* 2001. p. 45-57. ISSN: 0278-0062. Online at: https://pubmed.ncbi.nlm.nih.gov/11293691/; accessed October 23, 2020.

[103] ANDERSSON, J.L.R., S. SKARE and J. ASHBURNER. How to correct susceptibility distortions in spin-echo echo-planar images: application to diffusion tensor imaging. *NeuroImage. Volume 20*, Number 2. 2003. p. 870-888. ISSN: 1053-8119. Online at: https://pubmed.ncbi.nlm.nih.gov/14568458/; accessed November 24, 2020.

[104] RUTHOTTO, L. et al. Hyperelastic Susceptibility Artifact Correction of DTI in SPM. *Bildverarbeitung für die Medizin*. 2013. p. 344-349. Online at: https://link.springer.com/chapter/10.1007/978-3-642-36480-8_60; accessed January 14, 2020.

[105] DWI Denoising Software. *DWIdenoisingPackage_r01*. [software]. [accessed March 24, 2020]. Online at: https://sites.google.com/site/pierrickcoupe/softwares/denoising-for-medical-imaging/dwi-denoising/dwi-denoising-software.

[106] MITK. *MITK Diffusion*. [software]. [accessed February 13, 2020]. Online at: https://github.com/MIC-DKFZ/MITK-Diffusion.

[107] BrainVoyager. *EPI distortion correction: echo spacing and bandwidth*. Online at: https://support.brainvoyager.com/brainvoyager/functional-analysis-preparation/29-pre-processing/78-epi-distortion-correction-echo-spacing-and-bandwidth; accessed February 09, 2020.

[108] LIN, Y. et al. Comparison of Intravoxel Incoherent Motion Diffusion-Weighted MR Imaging and Arterial Spin Labeling MR Imaging in Gliomas. *BioMed Research International*. 2015. ISSN: 2314-6133. Online at: https://www.ncbi.nlm.nih.gov/pmc/articles/PMC4402183/#!po=42.0000; accessed April 26, 2020.

[109] IBM SPSS Statistics. *IBM Corp. Released 2012. IBM SPSS Statistics for Windows, Version 21.0. Armonk, NY: IBM Corp*. [software]. [accessed March 28, 2020]. Online at: https://www.ibm.com/analytics/spss-statistics-software.

[110] MedCalc. *MedCalc Software*. [software]. [accessed March 28, 2020]. Online at: https://www.medcalc.org/.

[111] GURNEY-CHAMPION, O.J. et al. Comparison of six fit algorithms for the intra-voxel incoherent motion model of diffusion-weighted magnetic resonance imaging data of pancreatic cancer patients. *PLoS One. Volume 13, Number 4.* 2018. ISSN: 1932-6203. Online at: https://www.ncbi.nlm.nih.gov/pmc/articles/PMC5884505/#!po=21.4286; accessed March 28, 2020.

[112] LING, L. et al. Value of intravoxel incoherent motion magnetic resonance imaging for differentiating metastatic from nonmetastatic mesorectal lymph nodes with different short-axis diameters in rectal cancer. *Journal of Cancer Research and Therapeutics. Volume 15, Number 7*. 2019. p. 1508-1515. Online at: http://www.cancerjournal.net/article.asp?issn=0973-1482;year=2019;volume=15;issue=7;spage=1508;epage=1515;aulast=; accessed May 09, 2020.

[113] SONG, S. et al. Intravoxel incoherent motion diffusion weighted imaging of high-grade gliomas and brain metastases: Efficacy in preoperative differentiation. *International Journal of Clinical and Experimental Medicine. Volume 11, Number 7.* 2018. p. 7064-7071. Online at: http://www.ijcem.com/files/ijcem0065018.pdf; accessed April 03, 2020.

[114] HORTOBÁGYI, T. et al. Pathophysiology of meningioma growth in pregnancy. *Open medicine. Volume 12.* 2017. p. 195-200. Online at: https://www.degruyter.com/view/journals/med/12/1/article-p195.xml; accessed May 08, 2020.

14. APPENDICES

The list of appendices contains three following parts:

Appendix A: Mathematical description of IVIM fitting algorithms

Appendix B: Time duration of automated software tools for image analysis

Appendix C: Statistical analysis of IVIM parameters

Appendix D: Brain tissue and brain tumor types differentiation

14.1. Appendix A

This appendix part incorporates the mathematical description of two IVIM fitting algorithms groups; least squares algorithms (introduced in the section 4.3.3.1.1.) and algorithms based on probability theory (introduced in the section 4.3.3.1.2.).

A.I. Least squares algorithms

In general in the least square fitting problem, there is a set of independent and dependent variables $(x_{i,}\ y_i)$ and the aim is to find the parameters β of the model $f(x, \beta)$ in the way of minimizing the sum of the squares of deviations $S(\beta)$.

$$\hat{\beta} \in argmin_{\beta}\ S(\beta) = argmin_{\beta} \sum_{i=1}^{n} [y_i - f(x_i, \beta)]^2 \qquad (A.1)$$

Least squares algorithms minimize a difference between the real (acquired) and predicted (fitted) DWI signal and thus adjust the parameters of the bi-exponential model. The objective function of the minimization is:

$$min_{\beta} \sum_{i=1}^{n} [S_i - \hat{S}_i(\beta)]^2 \qquad (A.2)$$

- β: a set of parameters $f, D, D*$
- S_i: given signal strength
- $\hat{S}_i(\beta)$: predicted signal strength using a β set and is calculated for the i-th *b* value
- n: a total number of *b* values

The iterative *Levenberg-Marquardt* algorithm, a nonlinear least squares minimization algorithm, is often used. This technique is aiming to find a minimum of the $S(\beta)$ function. The minimization process starts with an initial starting point for the parameter vector β. After each iteration step, the β vector is updated to a new estimate $\beta_{k+1} = \beta_k + d$. To determine an additional term d, the relation A.3 can be used.

$$f(x_i, \beta + \mathrm{d}) \sim \mathrm{f}(x_i, \beta) + J_i \cdot d \qquad (A.3)$$

- $J_i = \frac{\partial \mathrm{f}(x_i, \beta)}{\partial \beta}$: Jacobian matrix

The sum of square of deviations is expressed with the following equation.

$$S(\mathrm{\beta}+\mathrm{d}) \sim \sum_{i=1}^{n}[y_i - f(x_i, \mathrm{\beta}) - J_i \cdot d]^2 \qquad (\mathrm{A}.4)$$

After taking the derivation of $S(\mathrm{\beta}+\mathrm{d})$ with respect to d and setting it to zero, there is a following equation.

$$(J^T \cdot J) \cdot d = J^T \cdot [y - f(\beta)] \qquad (\mathrm{A}.5)$$

In the *Levenberg-Marquardt* equation A.6 there is an additional term, the damping factor λ_i. This positive factor is adjusted at each iteration i to assure an error reduction.

$$(J_i^T \cdot \mathrm{J} + \lambda_i \cdot I) \cdot d_i \qquad (\mathrm{A}.6)$$

- I: an identity matrix

A.II. Algorithms based on probability theory

The principle of the Bayesian method stems from maximizing the posterior probability of IVIM parameters. Bayes´ theorem describes the probability of an event, in this case the MR signal level S, based on prior conditions that are used to describe properties of model parameters without seeing the data.

$$P(\Theta|S) = \frac{P(S\,|\,\Theta) \cdot \mathrm{P}(\Theta)}{P(S)} \qquad (\mathrm{A}.7)$$

- $P(\Theta|S)$: the posterior probability
- $P(S\,|\,\Theta)$: the likelihood function
- $P(S)$: a probability of the measurement called an evidence
- $P(\Theta)$: prior conditions

Maximization of the posterior probability does not depend on the evidence; thus, the equation A.7 might be simplified.

$$P(\Theta|S) = P(S|\Theta) \cdot \mathrm{P}(\Theta) \qquad (\mathrm{A}.8)$$

In a nutshell, a fundamental idea of the Bayesian method is to maximize the posterior probability of IVIM parameters given the observed signal. The Bayesian model enables to incorporate prior knowledge into the fitting technique.

Maximum likelihood estimation is a technique how to estimate model parameters by selecting model parameters values that maximize the likelihood function. The probability density P of observing a single data point x following a univariate normal distribution[74] with parameters μ as a mean value of the distribution and its standard deviation σ.

$$P(x|\mu, \sigma) = \frac{1}{\sigma\sqrt{2 \cdot \pi}} \cdot e^{\left(-\frac{(x-\mu)^2}{2 \cdot \sigma^2}\right)} \qquad (\mathrm{A}.9)$$

The likelihood function $L(\Theta|x)$ is equal to the probability density function[75] $P(x|\Theta)$ regarded as a function of Θ.

---

[74] There are two main reasons why the computation is based on the Gaussian distribution. Firstly, from the theoretical perspective due to the central limit theorem *„the distribution of the sum of N independently and identically distributed random variables becomes increasingly Gaussian as N grows."* Secondly, there is a practical reason that it is simple to compute with the normal distribution.

[75] The probability density function (PDF) specifies the probability of a variable falling within the particular range of values.

The maximum likelihood estimation:

$$\hat{\Theta}(x) = arg\, max_{\Theta} L(\Theta|x) \qquad (A.10)$$

To specify the likelihood function of IVIM DWI data, it is essential to determine the model of MR signal and noise. The signal model is expected to be the IVIM bi-exponential model and the noise model the Rician model. *„To simplify model fitting, the signal-to-noise ratio (SNR) is typically assumed to be high enough such that the Rician distribution can be approximated by a Gaussian one."* [31]

In this case the probability density function is described according to the following equation A.11. This equation specifies a deviation between the measured signal value $S(b)$ and the predicted value S_b given the IVIM signal model parameters.

$$P(S(b)|\Theta, \sigma) = \frac{1}{\sigma\sqrt{2 \cdot \pi}} \cdot e^{\left[-\frac{\left(S(b)-S_b(\Theta)\right)^2}{2 \cdot \sigma^2}\right]} \qquad (A.11)$$

The likelihood function $L(\Theta)$, where n is a number of measurements, is given A.12 The maximization[76] of this likelihood function is given by its derivation with respect to model parameters.

$$L(\Theta) = P(S|\Theta, \sigma) = \prod_{i=1}^{n} P(S(b_i|\Theta, \sigma) = (2 \cdot \pi \cdot \sigma^2)^{-\frac{n}{2}} \cdot e^{\left[-\frac{\sum_{i=1}^{n}\left(S(b_i)-S_{b_i}(\Theta)\right)^2}{2\sigma^2}\right]} \qquad (A.12)$$

14.2. Appendix B

This appendix part incorporates approximate duration of software tools performing image data analysis. These time data do not serve for any statistical analysis but just for rough comparison between different image analysis approaches and software tools. The time data were acquired as the average duration for three different subjects. This section includes time duration for skull stripping, image registration and for distortions correction in diffusion images. The description of these steps in different software tools is given in the chapter 8.

- **Skull stripping performed on 3D T_1 image**

Software tool	Duration [minutes]
FSL	0.5
SPM	19.0
ANTs	61.5
Freesurfer	16.0
BrainSuite	5.0

Table B.1: Time duration of automated skull stripping software tools; FSL, SPM, ANTs, Freesurfer and BrainSuite. Skull stripping performed on 3D T_1 image.

---

[76] It is more convenient to apply log $(P(S|\Theta, \sigma))$ since log () is a monotone function so it is easier to find the maximal value.

- **Image registration of 3D T_1 and FLAIR images**

Software tool	Duration [minutes]
FSL	5.0
ITK SNAP + ANTs	3.0
BrainSuite	26.0

Table B.2: Time duration of automated image registration software tools; FSL, ITK SNAP + ANTs and BrainSuite. Image registration of 3D T_1 and FLAIR image (a reference image: T_1 and a moving image: FLAIR).

- **Distortions correction in diffusion images**

Software tool	Duration [minutes]
FSL	50.0
SPM	9.0
BrainSuite	25.0

Table B.3: Time duration of automated software tools (FSL, SPM and BrainSuite) for distortions correction in diffusion images. Distortions correction performed on 4D IVIM image.

14.3. Appendix C

In this appendix part additional data derived from statistical analysis of IVIM parameters in different brain segments are given. The data for all subjects, for each IVIM parameter and for each brain segment are presented as mean value, standard deviation (std), median, first quartile, third quartile, IQR, maximum value, minimum value and range value. These statistical parameters for the data are shown in the tables. *n* represents a number of subjects. Moreover, the data are graphically represented by boxplots[77]. Furthermore, ROC curves for three IVIM parameters in different brain segments are graphically represented.

---

[77] On each box the central red line represents the median, the top and the bottom edges indicate third quartile and first quartile, respectively. Minimum and maximum points (the lowest and the largest point data point excluding any outliers) are visualized with a horizontal line under and above the box. The outliers are plotted using a red symbol „+“.

C.I. Different DWI correction tools

C.I.I. FSL

	parameter	**edema (n=15)**	**enhanced tumor (n=20)**	**non-enhanced tumor (n=15)**
f [-]	mean	0.118	0.155	0.160
	std	0.037	0.030	0.031
	median	0.108	0.153	0.164
	Q 25%	0.096	0.136	0.133
	Q 75%	0.130	0.170	0.172
	IQR	0.033	0.034	0.039
	maximum	0.235	0.235	0.223
	minimum	0.082	0.095	0.111
	range	0.153	0.140	0.112
D [x 10^{-4} mm^2/s]	mean	3.362	2.871	4.507
	std	1.119	1.046	2.249
	median	3.707	2.653	3.902
	Q 25%	2.495	1.954	3.148
	Q 75%	3.977	3.620	5.025
	IQR	1.481	1.665	1.877
	maximum	5.419	4.797	10.837
	minimum	1.240	1.394	1.785
	range	4.179	3.403	9.052
D* [x 10^{-3} mm^2/s]	mean	7.251	13.316	6.953
	std	6.140	9.270	4.313
	median	4.470	10.430	5.960
	Q 25%	2.980	7.450	4.470
	Q 75%	8.195	17.135	7.450
	IQR	5.215	9.685	2.980
	maximum	22.350	35.760	19.370
	minimum	2.980	2.980	1.490
	range	19.370	32.780	17.880

Table C.1: Calculated statistical parameters for IVIM parameters f, D and $D*$ in brain edema, contrast enhanced and contrast not enhanced part of a brain tumor. Diffusion images correction implemented in FSL, without denoising, fitting algorithm: Fit D and f (with high b), then fit D.*

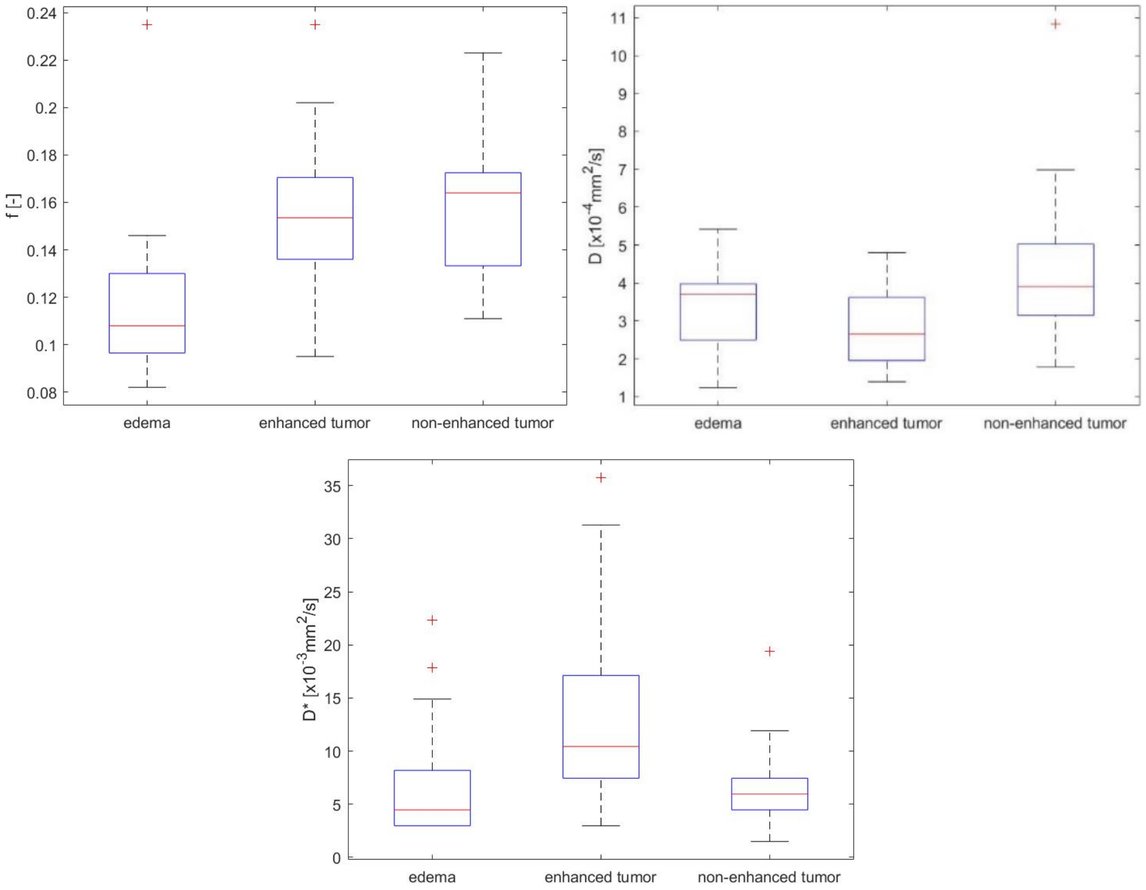

Figure C.1: Box plots of IVIM parameters f, D and $D*$ in brain edema (n=15), contrast enhanced (n=20) and contrast not enhanced (n=15) part of brain tumors.

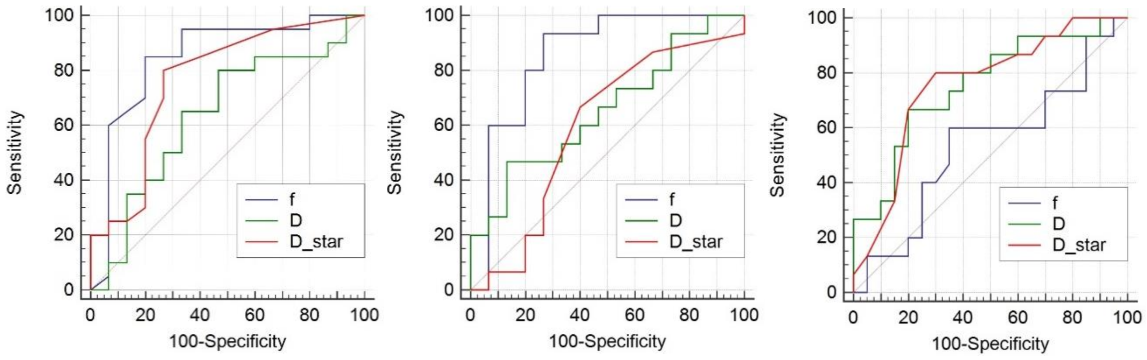

Figure C.2: ROC curves analysis for IVIM parameters f, D and $D*$ in brain edema, contrast enhanced and contrast not enhanced part of brain tumors. On the left: brain edema and contrast enhanced part, in the middle: brain edema and contrast not enhanced part, on the right: contrast enhanced and contrast not enhanced part of brain tumors.

	parameter	enhanced HGG (n=10)	enhanced metastasis (n=4)	enhanced meningioma (n=6)	edema HGG (n=10)	edema metastasis (n=4)	non-enhanced HGG (n=10)	non-enhanced metastasis (n=4)
f [-]	mean	0.136	0.184	0.168	0.119	0.114	0.150	0.181
	std	0.018	0.035	0.022	0.044	0.024	0.032	0.024
	median	0.140	0.172	0.170	0.103	0.113	0.139	0.173
	Q 25%	0.124	0.161	0.155	0.096	0.099	0.130	0.165
	Q 75%	0.147	0.207	0.178	0.131	0.130	0.165	0.196
	IQR	0.023	0.046	0.023	0.035	0.031	0.035	0.031
	maximum	0.159	0.235	0.202	0.235	0.146	0.223	0.216
	minimum	0.095	0.157	0.134	0.082	0.086	0.111	0.162
	range	0.064	0.078	0.068	0.153	0.060	0.112	0.054
D [x 10^{-4} mm^2/s]	mean	3.029	3.830	1.966	3.128	3.975	4.604	4.360
	std	1.009	0.705	0.509	1.279	0.491	2.592	1.831
	median	2.718	3.735	1.954	3.227	3.950	4.040	3.869
	Q 25%	2.409	3.335	1.470	2.303	3.615	3.022	3.277
	Q 75%	3.643	IV.60	2.274	3.945	4.336	5.186	5.443
	IQR	1.234	0.990	0.804	1.642	0.721	2.164	2.165
	maximum	4.797	4.766	2.754	5.419	4.587	10.837	6.984
	minimum	1.848	3.086	1.394	1.240	3.416	1.785	2.719
	range	2.949	1.680	1.360	4.179	1.171	9.052	4.265
D* [x 10^{-3} mm^2/s]	mean	8.604	8.195	24.585	7.748	4.097	5.662	7.077
	std	3.531	3.101	8.977	6.838	1.426	2.879	2.235
	median	8.940	8.195	25.330	4.470	3.725	5.215	5.960
	Q 25%	5.960	5.960	19.370	2.980	2.980	4.470	5.960
	Q 75%	10.430	10.430	31.290	8.940	5.215	7.450	8.195
	IQR	4.470	4.470	11.920	5.960	2.235	2.980	2.235
	maximum	14.900	11.920	35.760	22.350	5.960	11.920	10.430
	minimum	2.980	4.470	10.430	2.980	2.980	1.490	5.960
	range	11.920	7.450	25.330	19.370	2.980	10.430	4.470

Table C.2*: Calculated statistical parameters for IVIM parameters* f, D *and* $D*$ *in contrast enhanced part of brain tumors HGG, metastasis and meningioma, in brain edema of brain tumors HGG and metastasis, in contrast not enhanced part of brain tumors HGG and metastasis. Diffusion images correction implemented in FSL, without denoising, fitting algorithm: Fit D and f (with high b), then fit D*.*

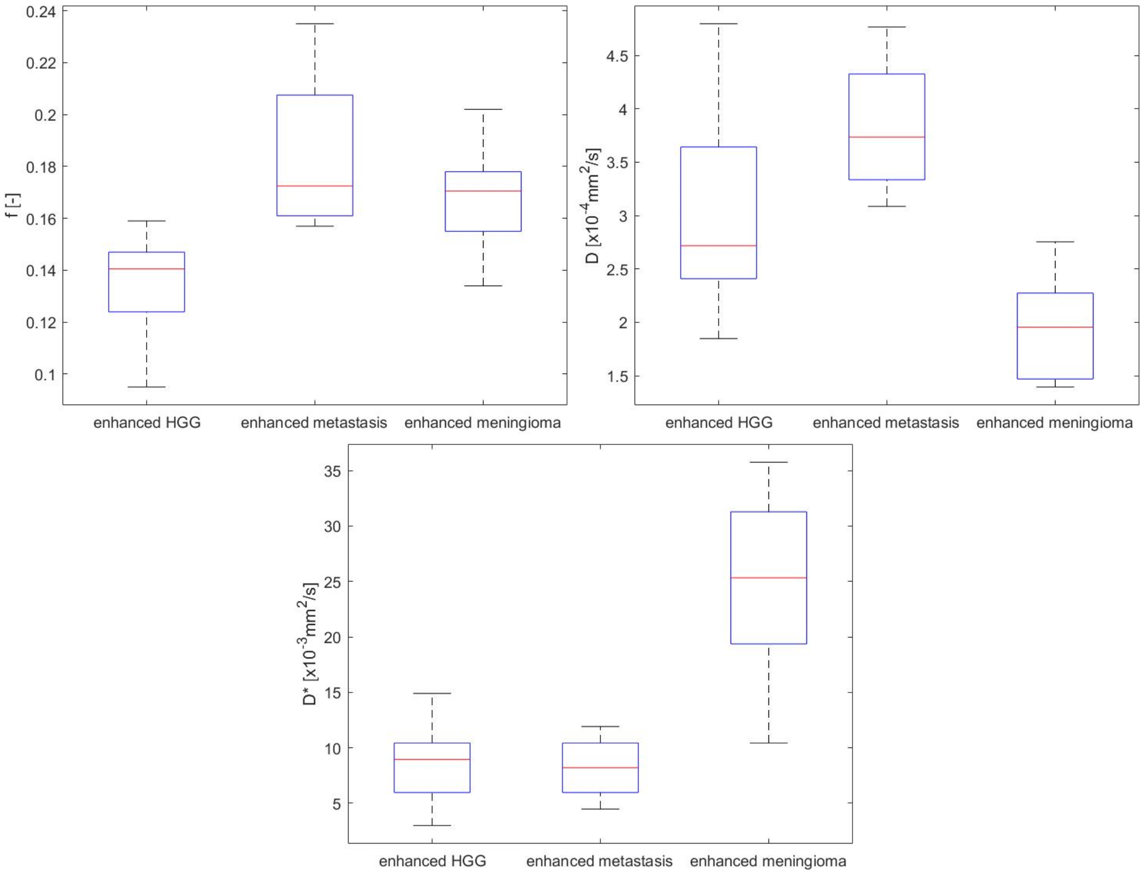

Figure C.3: Box plots of IVIM parameters f, D and $D*$ in contrast enhanced part of brain tumors HGG (n=10), metastasis (n=4) and meningioma (n=6).

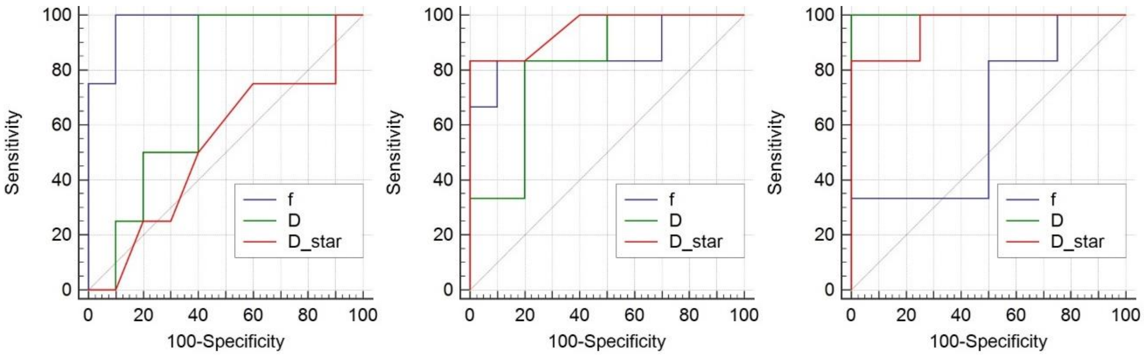

Figure C.4: ROC curves analysis for IVIM parameters f, D and $D*$ in contrast enhanced part of brain tumors HGG, metastasis and meningioma. On the left: HGG and metastasis, in the middle: HGG and meningioma, on the right: metastasis and meningioma.

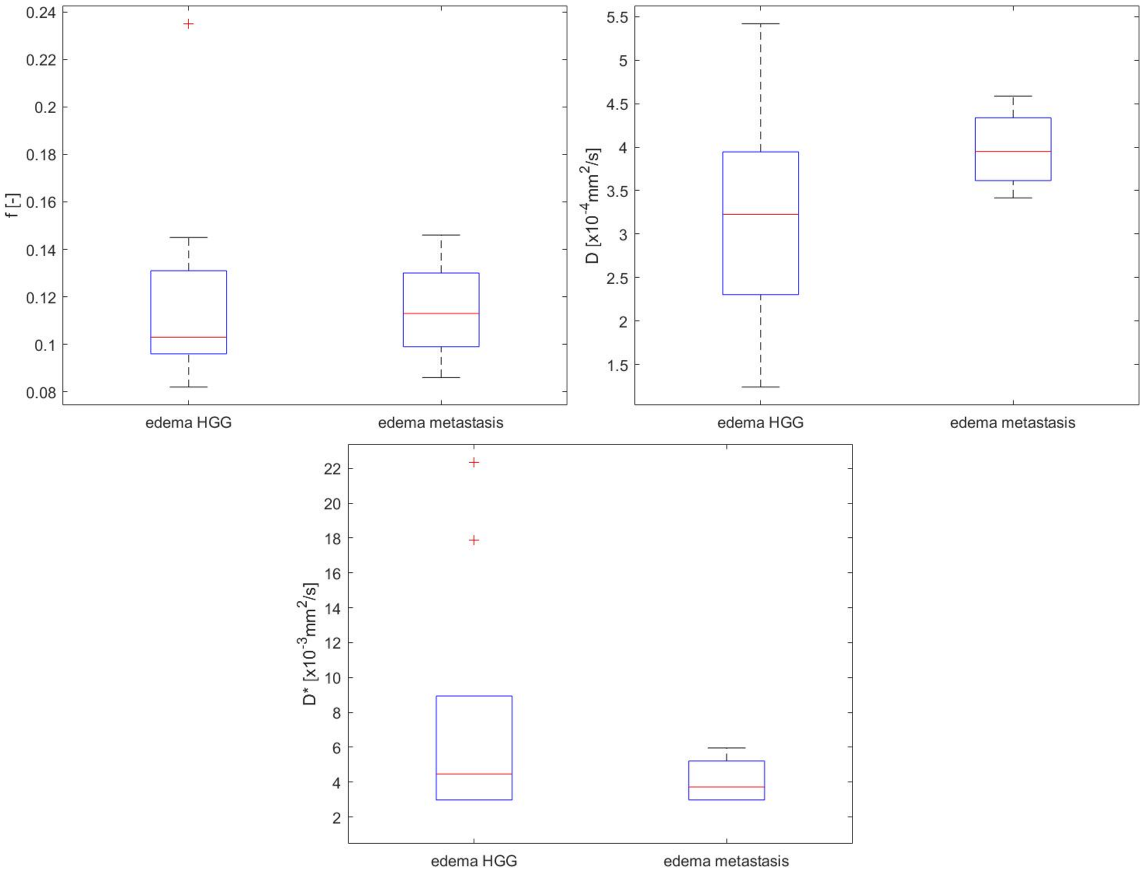

Figure C.5: Box plots of IVIM parameters f, D and $D*$ in brain edema of brain tumors HGG (n=10) and metastasis (n=4).

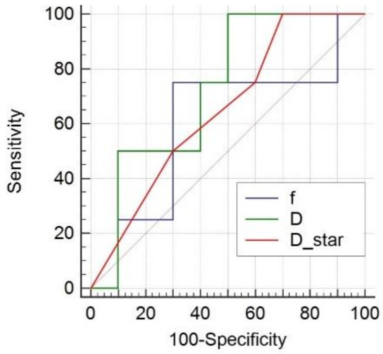

Figure C.6: ROC curves analysis for IVIM parameters f, D and $D*$ in edema of brain tumors HGG and metastasis.

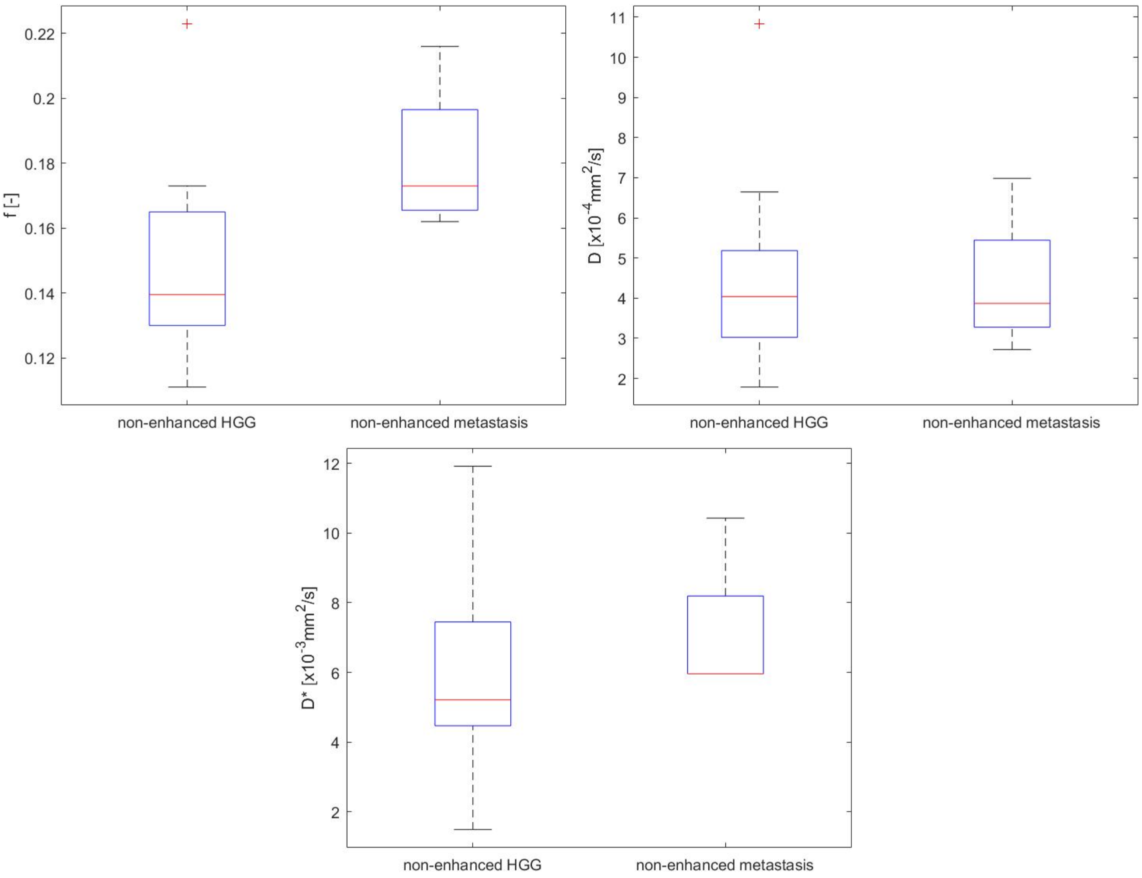

Figure C.7: Box plots of IVIM parameters f, D and $D*$ in non-enhanced part of brain tumors HGG (n=10) and metastasis (n=4).

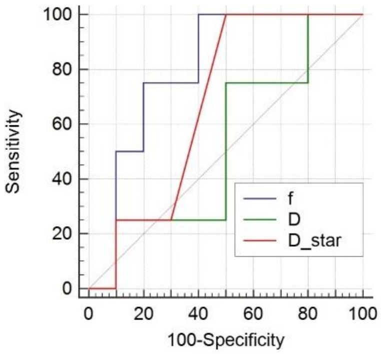

Figure C.8: ROC curves analysis for IVIM parameters f, D and $D*$ in contrast not enhanced part of brain tumors HGG and metastasis.

C.I.II. SPM

	parameter	edema (n=15)	enhanced tumor (n=20)	non-enhanced tumor (n=15)
f [-]	mean	0.111	0.155	0.154
	std	0.034	0.041	0.035
	median	0.102	0.146	0.151
	Q 25%	0.092	0.132	0.133
	Q 75%	0.124	0.166	0.170
	IQR	0.032	0.033	0.038
	maximum	0.193	0.263	0.221
	minimum	0.074	0.075	0.094
	range	0.119	0.188	0.127
D [x 10^{-4} mm^2/s]	mean	3.714	3.076	4.805
	std	1.287	1.145	2.436
	median	4.059	2.856	4.018
	Q 25%	2.702	2.115	3.270
	Q 75%	4.460	3.916	5.264
	IQR	1.758	1.801	1.995
	maximum	6.116	5.220	11.457
	minimum	1.499	1.149	2.010
	range	4.617	4.071	9.447
D* [x 10^{-3} mm^2/s]	mean	5.463	12.814	6.879
	std	3.635	9.379	4.286
	median	4.470	8.940	5.960
	Q 25%	2.980	7.450	4.470
	Q 75%	5.960	17.135	7.450
	IQR	2.980	9.685	2.980
	maximum	14.900	35.760	19.743
	minimum	2.980	2.980	1.490
	range	11.920	32.780	18.253

Table C.3: Calculated statistical parameters for IVIM parameters f, D and $D*$ in brain edema, contrast enhanced and contrast not enhanced part of a brain tumor. Diffusion images correction implemented in SPM, without denoising, fitting algorithm: Fit D and f (with high b), then fit D.*

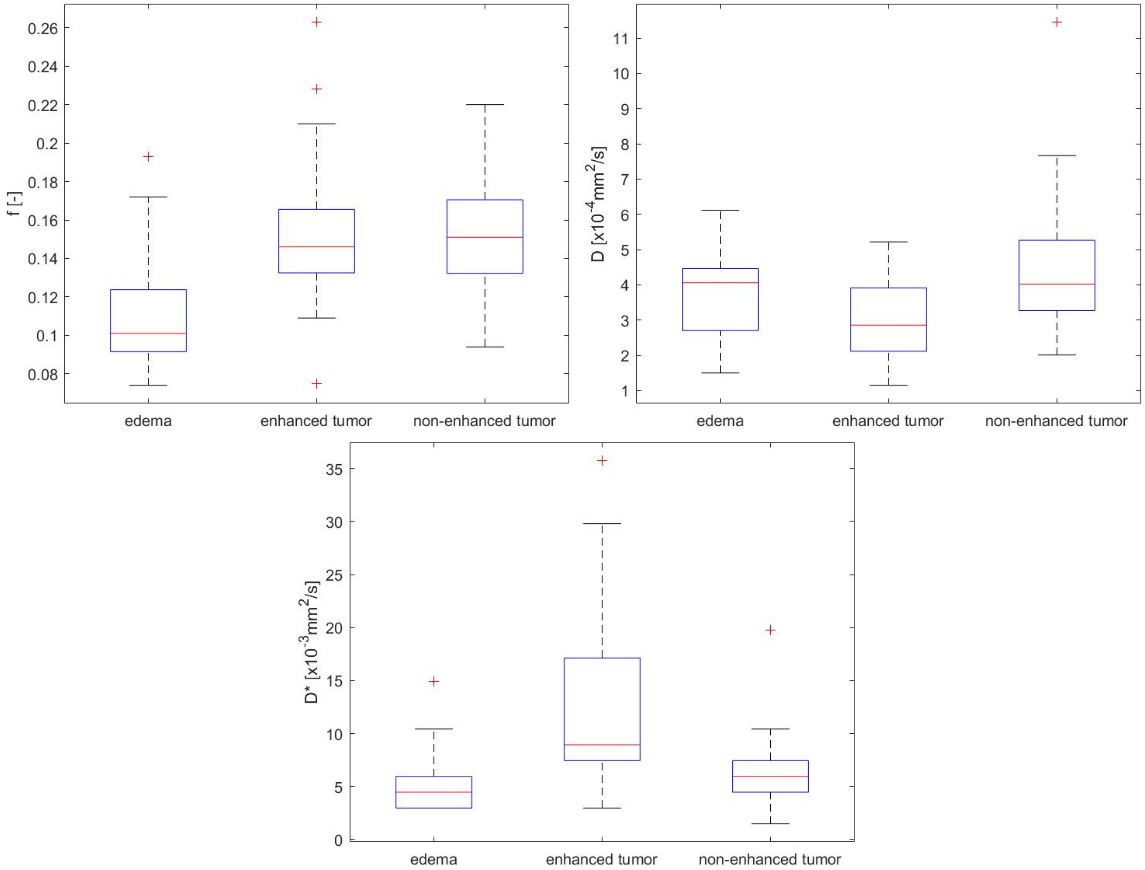

Figure C.9: Box plots of IVIM parameters f, D and $D*$ in brain edema (n=15), contrast enhanced (n=20) and contrast not enhanced (n=15) part of brain tumors.

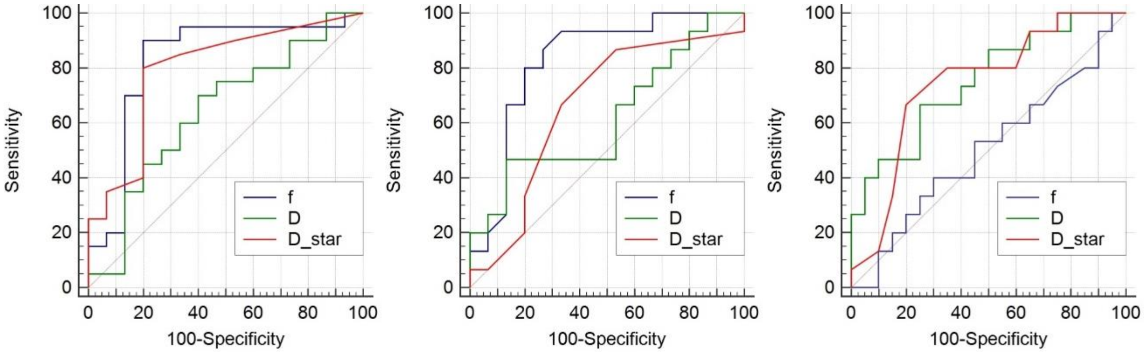

Figure C.10: ROC curves analysis for IVIM parameters f, D and $D*$ in brain edema, contrast enhanced and contrast not enhanced part of brain tumors. On the left: brain edema and contrast enhanced part, in the middle: brain edema and contrast not enhanced part, on the right: contrast enhanced and contrast not enhanced part.

	parameter	enhanced HGG (n=10)	enhanced metastasis (n=4)	enhanced meningioma (n=6)	edema HGG (n=10)	edema metastasis (n=10)	non-enhanced HGG (n=10)	non-enhanced metastasis (n=4)
f [-]	mean	0.135	0.164	0.184	0.117	0.094	0.146	0.159
	std	0.027	0.032	0.051	0.040	0.012	0.034	0.025
	median	0.135	0.152	0.169	0.104	0.100	0.146	0.158
	Q 25%	0.132	0.144	0.145	0.091	0.088	0.123	0.138
	Q 75%	0.157	0.184	0.228	0.135	0.101	0.161	0.180
	IQR	0.025	0.040	0.082	0.044	0.013	0.038	0.042
	maximum	0.168	0.210	0.263	0.193	0.101	0.220	0.187
	minimum	0.075	0.142	0.130	0.074	0.077	0.094	0.133
	range	0.093	0.069	0.133	0.119	0.024	0.126	0.054
D [x 10^{-4} mm^2/s]	mean	3.233	4.207	2.060	3.447	4.443	4.939	4.800
	std	1.085	0.614	0.566	1.445	0.707	2.751	2.086
	median	3.298	4.294	2.043	3.486	4.431	4.467	4.391
	Q 25%	2.419	3.768	1.848	2.444	3.874	3.196	3.370
	Q 75%	3.690	4.646	2.621	4.355	5.013	5.342	6.230
	IQR	1.272	0.878	0.773	1.911	1.139	2.146	2.860
	maximum	5.220	4.847	2.655	6.116	5.251	11.457	7.664
	minimum	1.814	3.394	1.149	1.499	3.661	2.010	2.754
	range	3.406	1.453	1.506	4.617	1.590	9.447	4.910
D* [x 10^{-3} mm^2/s]	mean	7.450	8.940	24.337	5.811	3.353	5.364	7.450
	std	3.369	2.107	9.071	3.939	0.745	2.453	2.107
	median	8.195	8.195	25.330	4.470	2.980	5.215	6.705
	Q 25%	4.470	7.450	20.860	2.980	2.980	4.470	5.960
	Q 75%	8.940	10.430	29.800	5.960	3.725	5.960	8.940
	IQR	4.470	2.980	8.940	2.980	0.745	1.490	2.980
	maximum	13.410	11.920	35.760	14.900	4.470	10.430	10.430
	minimum	2.980	7.450	8.940	2.980	2.980	1.490	5.960
	range	10.430	4.470	26.820	11.920	1.490	8.940	4.470

Table C.4: *Calculated statistical parameters for IVIM parameters f, D and $D*$ in contrast enhanced part of brain tumors HGG, metastasis and meningioma, in brain edema of brain tumors HGG and metastasis, in contrast not enhanced part of brain tumors HGG and metastasis. Diffusion images correction implemented in SPM, without denoising, fitting algorithm: Fit D and f (with high b), then fit D*.*

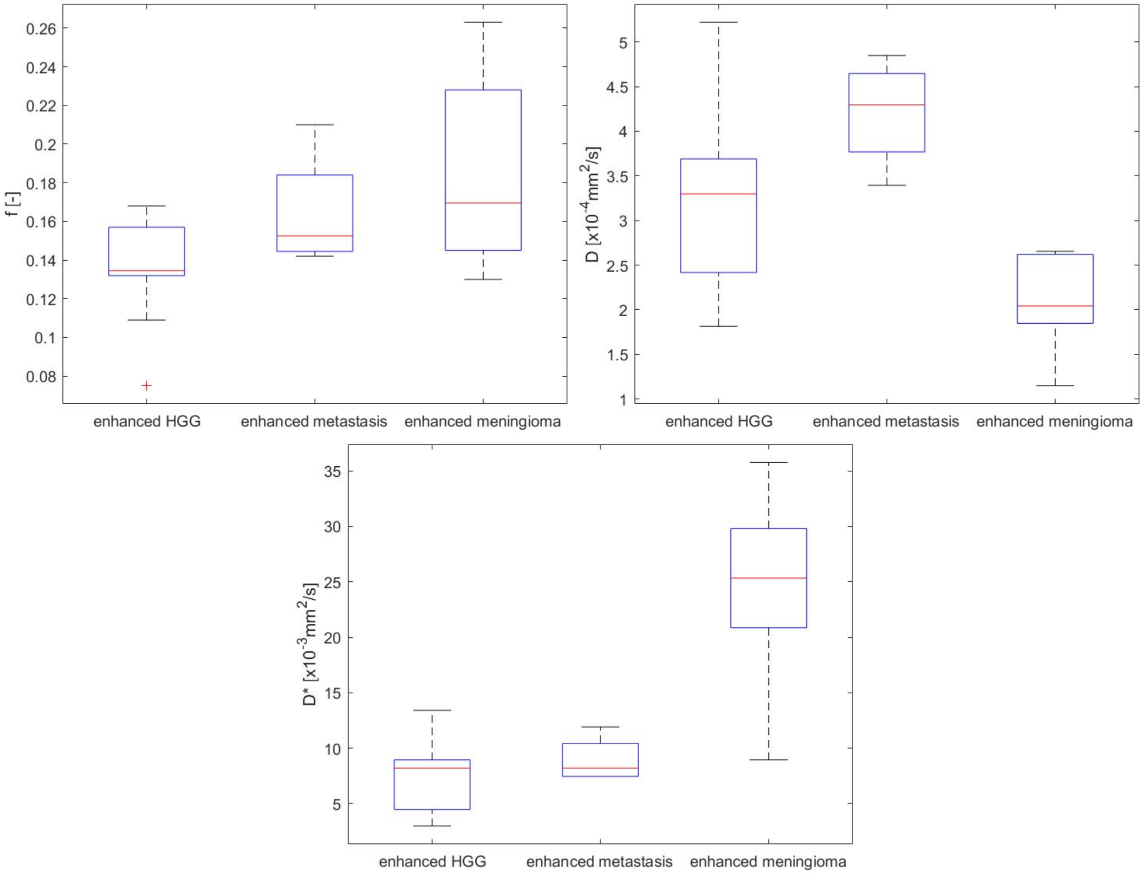

Figure C.11: Box plots of IVIM parameters f, D and $D*$ in contrast enhanced part of brain tumors HGG (n=10), metastasis (n=4) and meningioma (n=6).

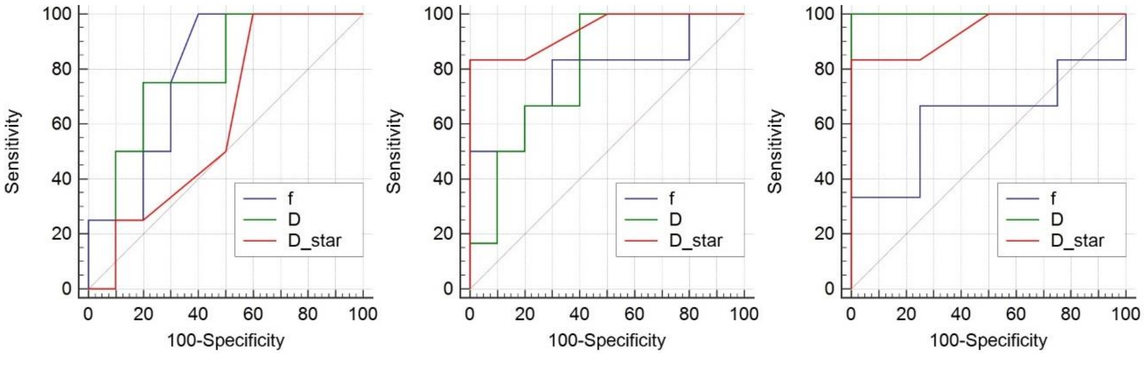

Figure C.12: ROC curves analysis for IVIM parameters f, D and $D*$ in contrast enhanced part of brain tumors HGG, metastasis and meningioma. On the left: HGG and metastasis, in the middle: HGG and meningioma, on the right: metastasis and meningioma.

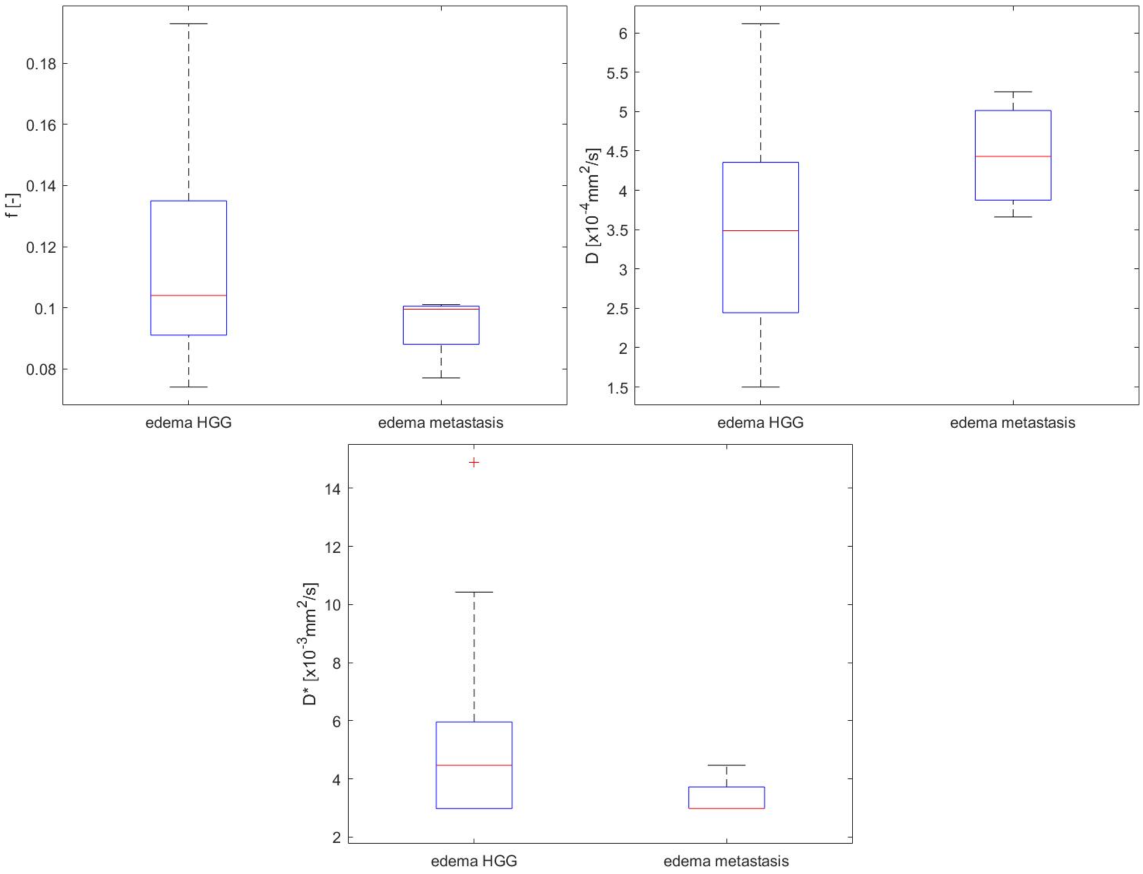

Figure C.13: Box plots of IVIM parameters f, D and $D*$ in brain edema of brain tumors HGG (n=10) and metastasis (n=4).

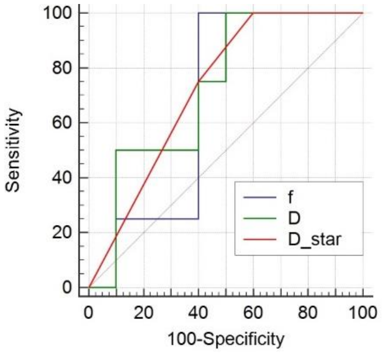

Figure C.14: ROC curves analysis for IVIM parameters f, D and $D*$ in edema of brain tumors HGG and metastasis.

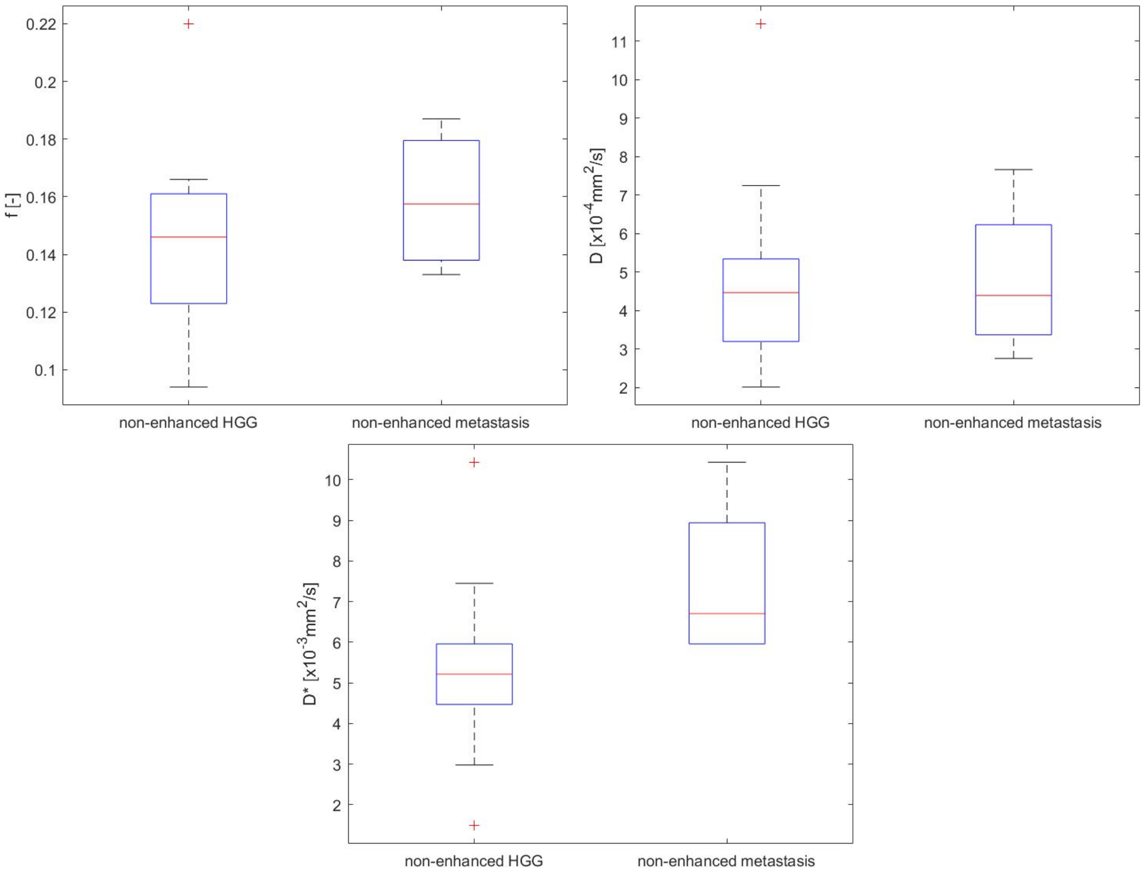

Figure C.15: Box plots of IVIM parameters f, D and $D*$ in non-enhanced part of brain tumors HGG (n=10) and metastasis (n=4).

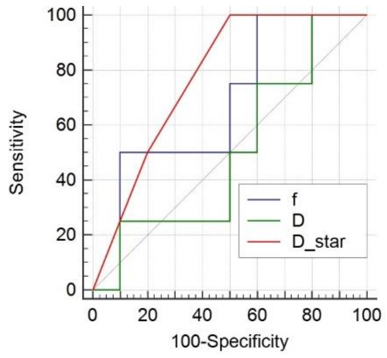

Figure C.16: ROC curves analysis for IVIM parameters f, D and $D*$ in contrast not enhanced part of brain tumors HGG and metastasis.

C.I.III. BrainSuite

	parameter	edema (n=15)	enhanced tumor (n=20)	non-enhanced tumor (n=15)
f [-]	mean	0.119	0.165	0.164
	std	0.042	0.038	0.033
	median	0.108	0.159	0.159
	Q 25%	0.094	0.139	0.140
	Q 75%	0.125	0.177	0.174
	IQR	0.031	0.037	0.034
	maximum	0.238	0.264	0.250
	minimum	0.077	0.111	0.125
	range	0.161	0.153	0.125
D [x 10^{-4} mm^2/s]	mean	3.809	3.207	4.841
	std	1.273	1.237	2.386
	median	4.075	3.151	3.987
	Q 25%	2.573	2.133	3.339
	Q 75%	4.533	3.911	5.672
	IQR	1.960	1.777	2.333
	maximum	5.895	5.704	10.863
	minimum	1.719	1.108	1.938
	range	4.176	4.596	8.925
D* [x 10^{-3} mm^2/s]	mean	7.130	17.801	8.727
	std	5.134	14.720	4.814
	median	4.470	13.410	5.960
	Q 25%	4.470	8.940	5.960
	Q 75%	8.940	23.840	11.920
	IQR	4.470	14.900	5.960
	maximum	20.860	58.110	20.860
	minimum	2.980	2.980	2.980
	range	17.880	55.130	17.880

Table C.5: Calculated statistical parameters for IVIM parameters f, D and $D*$ in brain edema, contrast enhanced and contrast not enhanced part of a brain tumor. Diffusion images correction implemented in BrainSuite, without denoising, fitting algorithm: Fit D and f (with high b), then fit D.*

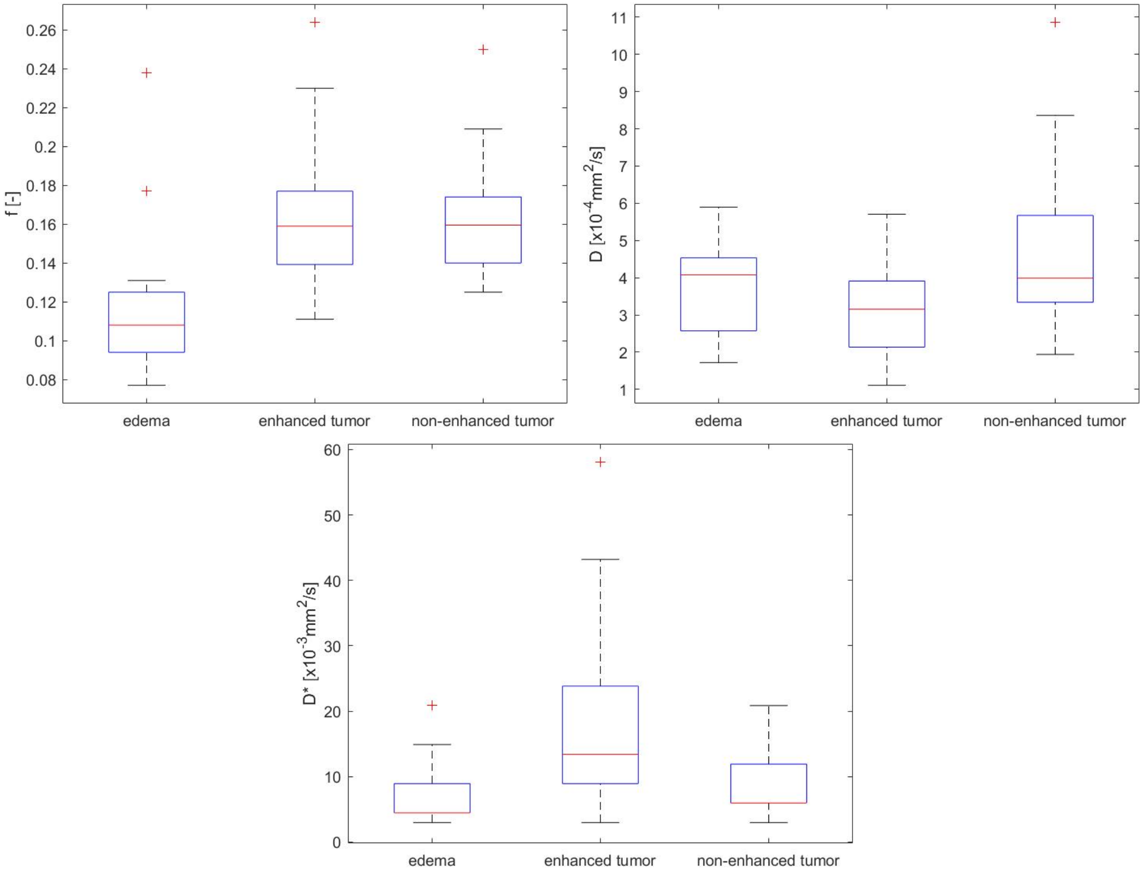

Figure C.17: Box plots of IVIM parameters f, D and $D*$ in brain edema (n=15), contrast enhanced (n=20) and contrast not enhanced (n=15) part of brain tumors.

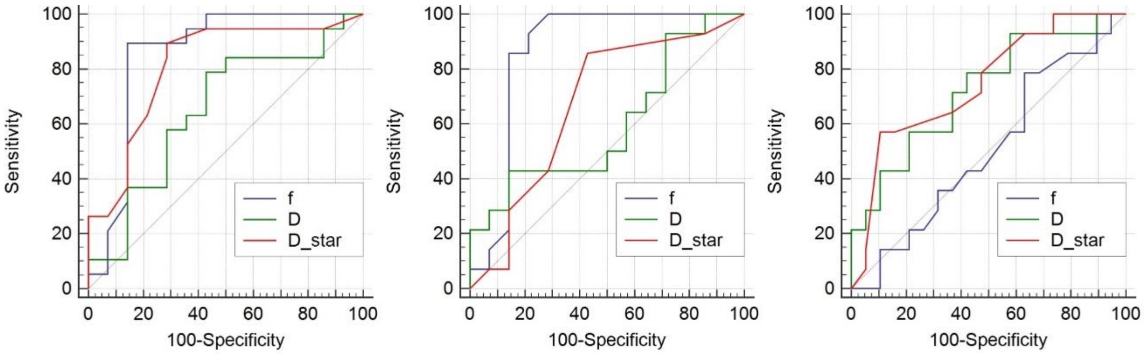

Figure C.18: ROC curves analysis for IVIM parameters f, D and $D*$ in brain edema, contrast enhanced and contrast not enhanced part of brain tumors. On the left: brain edema and contrast enhanced part, in the middle: brain edema and contrast not enhanced part, on the right: contrast enhanced and contrast not enhanced part of brain tumors.

	parameter	enhanced HGG (n=10)	enhanced metastasis (n=4)	enhanced meningioma (n=6)	edema HGG (n=10)	edema metastasis (n=4)	non-enhanced HGG (n=10)	non-enhanced metastasis (n=4)
f [-]	mean	0.144	0.172	0.193	0.128	0.100	0.155	0.161
	std	0.017	0.023	0.052	0.050	0.016	0.026	0.016
	median	0.140	0.163	0.190	0.110	0.105	0.152	0.165
	Q 25%	0.134	0.158	0.175	0.093	0.090	0.134	0.150
	Q 75%	0.154	0.187	0.230	0.142	0.110	0.171	0.173
	IQR	0.019	0.029	0.055	0.048	0.019	0.036	0.023
	maximum	0.177	0.208	0.264	0.238	0.114	0.209	0.177
	minimum	0.116	0.157	0.111	0.078	0.077	0.125	0.140
	range	0.061	0.051	0.153	0.160	0.037	0.084	0.037
D [x 10^{-4} mm^2/s]	mean	3.486	3.900	2.326	3.451	4.571	5.248	4.223
	std	1.325	0.696	0.974	1.422	0.680	2.789	1.567
	median	3.151	3.796	2.235	3.377	4.606	4.839	3.652
	Q 25%	2.325	3.340	1.694	2.329	4.120	3.512	3.210
	Q 75%	4.228	4.461	2.771	4.511	5.022	6.344	5.236
	IQR	1.903	1.120	1.077	2.181	0.902	2.831	2.026
	maximum	5.704	4.763	3.916	5.895	5.365	10.863	6.507
	minimum	1.969	3.247	1.108	1.719	3.708	1.938	3.081
	range	3.735	1.516	2.808	4.176	1.657	8.925	3.426
D* [x 10^{-3} mm^2/s]	mean	9.105	11.920	34.766	7.450	4.470	6.787	10.057
	std	3.607	2.720	15.674	5.575	1.216	3.170	3.303
	median	8.940	11.920	33.525	4.470	4.470	5.960	10.430
	Q 25%	7.077	9.685	26.820	4.470	3.725	5.587	7.450
	Q 75%	11.175	14.155	43.210	9.312	5.215	7.077	12.665
	IQR	4.097	4.470	16.390	4.842	1.490	1.490	5.215
	maximum	14.900	14.900	58.110	20.860	5.960	13.410	13.410
	minimum	2.980	8.940	13.410	2.980	2.980	2.980	5.960
	range	11.920	5.960	44.700	17.880	2.980	10.430	7.450

Table C.6: *Calculated statistical parameters for IVIM parameters* f*,* D *and* $D*$ *in contrast enhanced part of brain tumors HGG, metastasis and meningioma, in brain edema of brain tumors HGG and metastasis, in contrast not enhanced part of brain tumors HGG and metastasis. Diffusion images correction implemented in BrainSuite, without denoising, fitting algorithm: Fit D and f (with high b), then fit D*.*

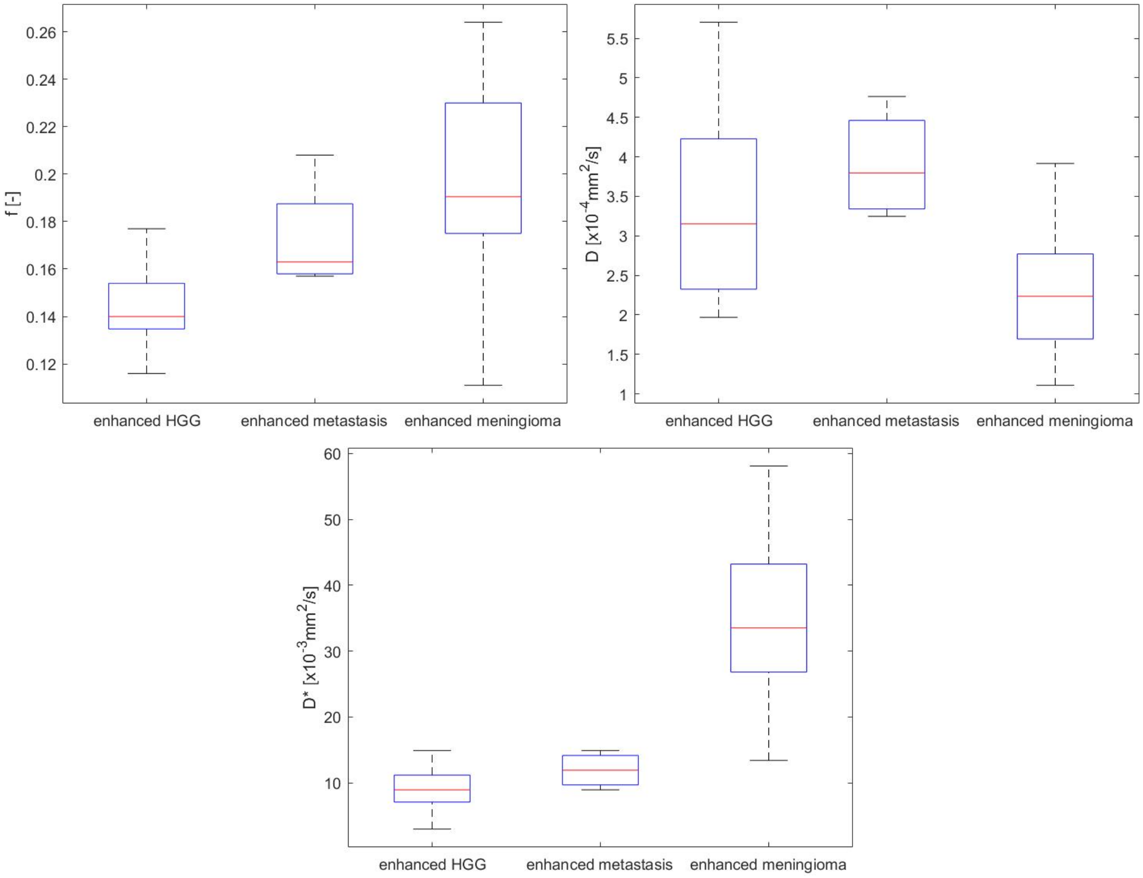

Figure C.19: Box plots of IVIM parameters f, D and $D*$ in contrast enhanced part of brain tumors HGG (n=10), metastasis (n=4) and meningioma (n=6).

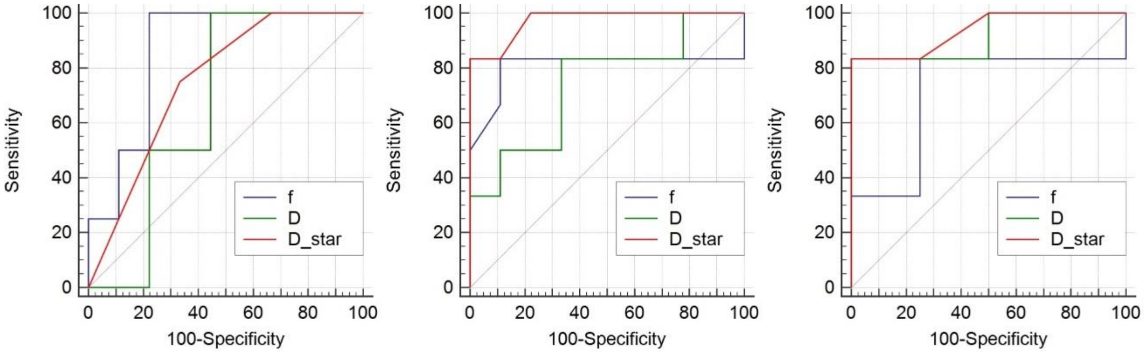

Figure C.20: ROC curves analysis for IVIM parameters f, D and $D*$ in contrast enhanced part of brain tumors HGG, metastasis and meningioma. On the left: HGG and metastasis, in the middle: HGG and meningioma, on the right: metastasis and meningioma.

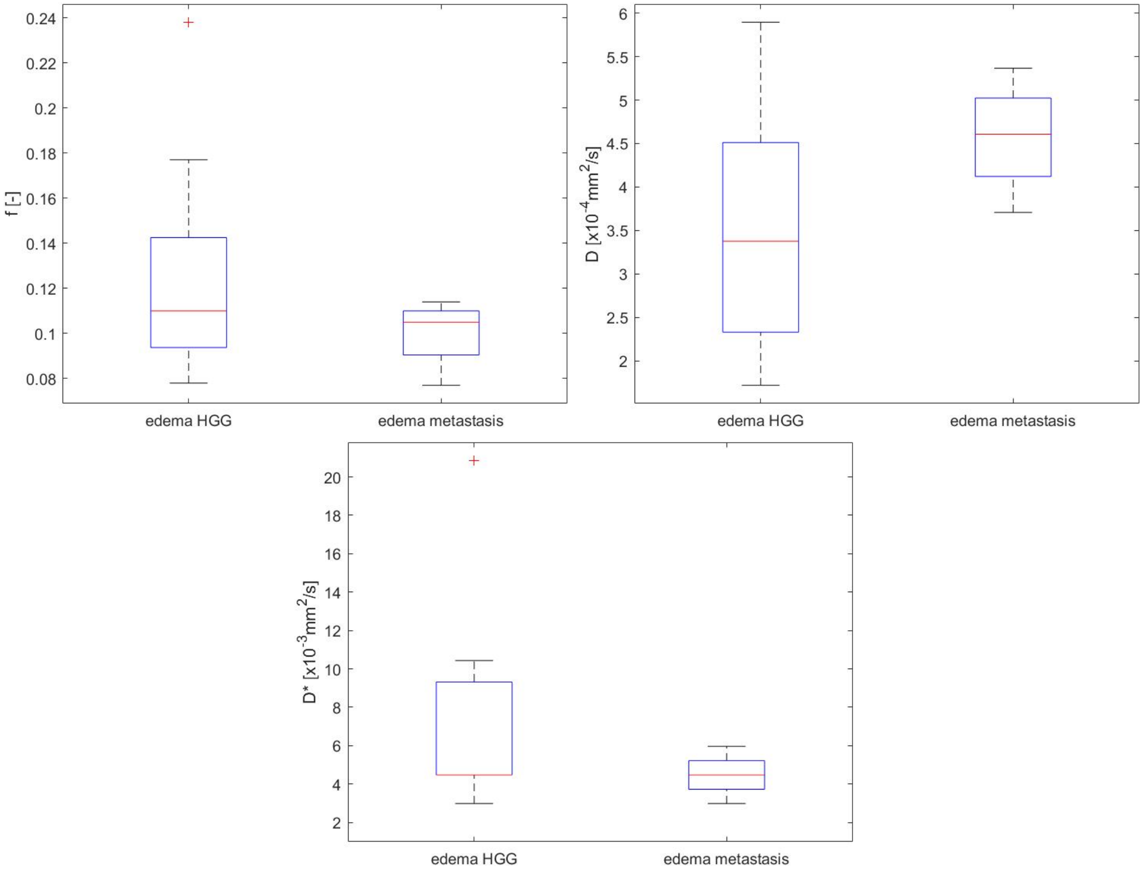

Figure C.21: Box plots of IVIM parameters f, D and $D*$ in brain edema of brain tumors HGG (n=10) and metastasis (n=4).

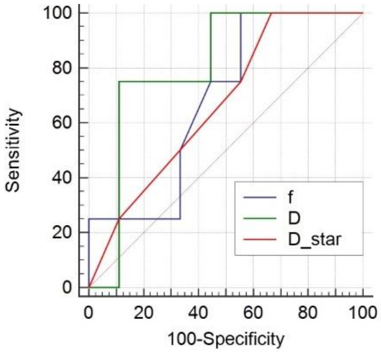

Figure C.22: ROC curves analysis for IVIM parameters f, D and $D*$ in edema of brain tumors HGG and metastasis.

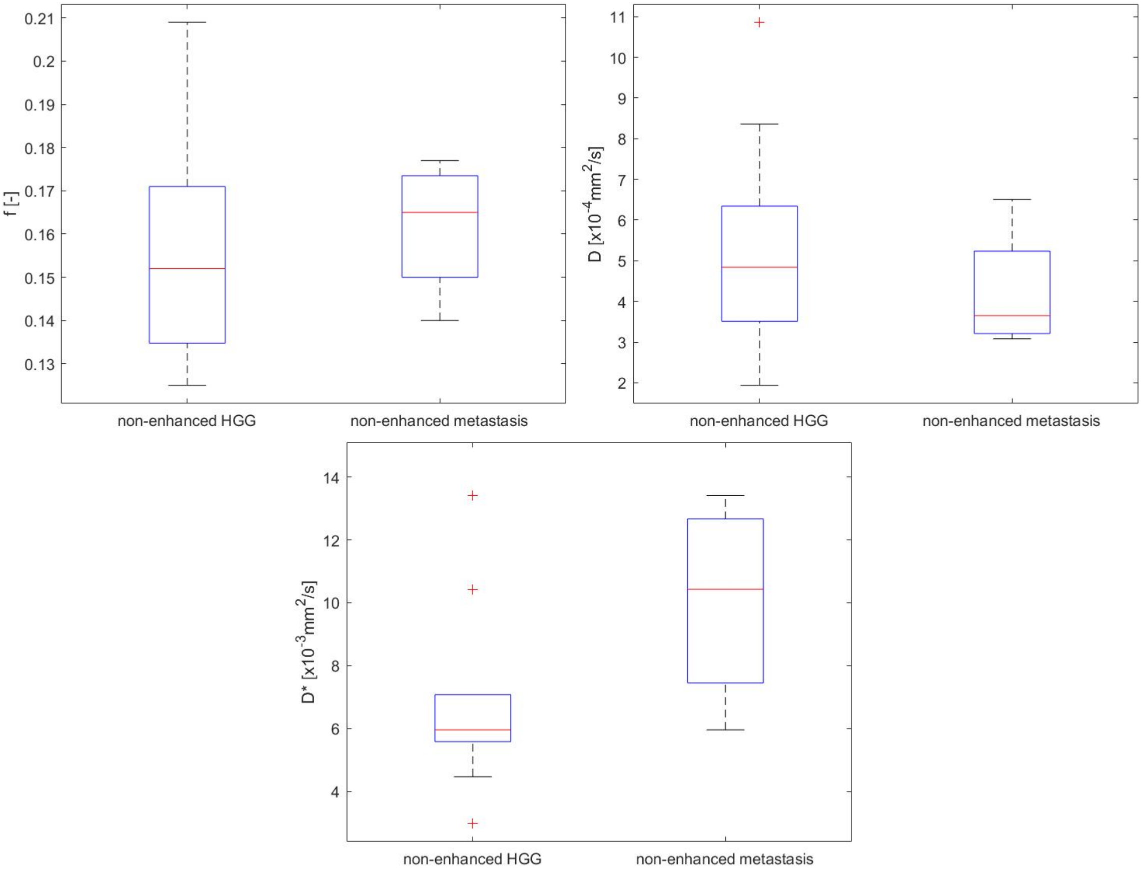

Figure C.23: Box plots of IVIM parameters f, D and $D*$ in non-enhanced part of brain tumors HGG (n=10) and metastasis (n=4).

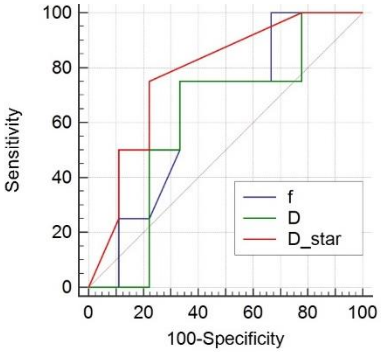

Figure C.24: ROC curves analysis for IVIM parameters f, D and $D*$ in contrast not enhanced part of brain tumors HGG and metastasis.

C.I.IV. Without correction

	parameter	edema (n=15)	enhanced tumor (n=20)	non-enhanced tumor (n=15)
f [-]	mean	0.117	0.157	0.162
	std	0.033	0.034	0.037
	median	0.108	0.158	0.163
	Q 25%	0.096	0.139	0.139
	Q 75%	0.129	0.169	0.175
	IQR	0.032	0.030	0.035
	maximum	0.198	0.224	0.242
	minimum	0.080	0.080	0.099
	range	0.118	0.144	0.143
D [x 10^{-4} mm^2/s]	mean	3.802	3.047	4.780
	std	1.310	1.153	2.312
	median	4.130	2.778	4.043
	Q 25%	2.719	2.182	3.278
	Q 75%	4.556	3.778	5.330
	IQR	1.837	1.596	2.052
	maximum	6.160	5.280	11.021
	minimum	1.553	1.407	2.042
	range	4.607	3.873	8.979
D* [x 10^{-3} mm^2/s]	mean	6.953	15.251	8.443
	std	5.120	10.600	4.931
	median	4.470	11.175	7.450
	Q 25%	4.470	8.940	5.960
	Q 75%	8.195	17.880	8.940
	IQR	3.725	8.940	2.980
	maximum	20.860	41.293	22.350
	minimum	2.980	2.980	2.980
	range	17.880	38.313	19.370

Table C.7: Calculated statistical parameters for IVIM parameters f, D *and* $D*$ *in brain edema, contrast enhanced and contrast not enhanced part of a brain tumor. No diffusion images correction, without denoising, fitting algorithm: Fit D and f (with high b), then fit D*.*

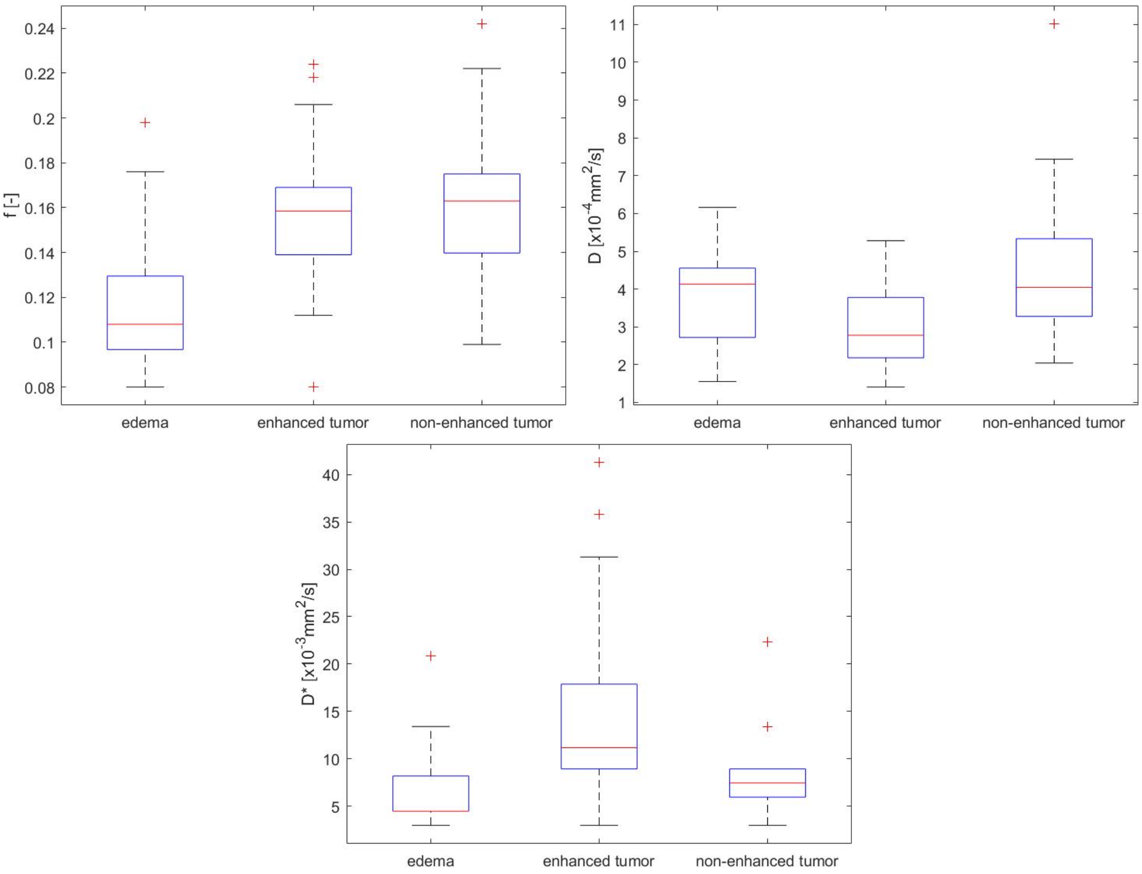

Figure C.25: Box plots of IVIM parameters f, D and $D*$ in brain edema (n=15), contrast enhanced (n=20) and contrast not enhanced (n=15) part of brain tumors.

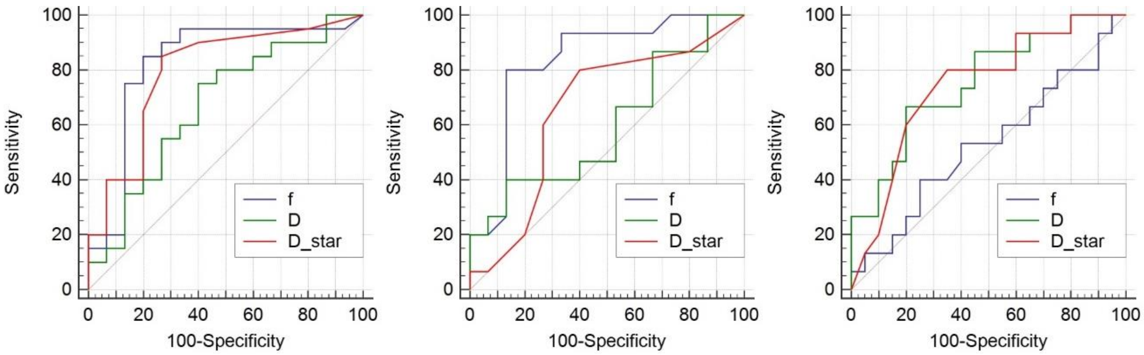

Figure C.26: ROC curves analysis for IVIM parameters f, D and $D*$ in brain edema, contrast enhanced and contrast not enhanced part of brain tumors. On the left: brain edema and contrast enhanced part, in the middle: brain edema and contrast not enhanced part, on the right: contrast enhanced and contrast not enhanced part of brain tumors.

	parameter	**enhanced HGG (n=10)**	**enhanced metastasis (n=4)**	**enhanced meningioma (n=6)**	**edema HGG (n=10)**	**edema metastasis (n=4)**	**non-enhanced HGG (n=10)**	**non-enhanced metastasis (n=4)**
f [-]	mean	0.138	0.176	0.177	0.122	0.101	0.151	0.170
	std	0.027	0.032	0.030	0.038	0.013	0.034	0.024
	median	0.140	0.162	0.173	0.109	0.108	0.150	0.169
	Q 25%	0.127	0.158	0.151	0.096	0.094	0.125	0.152
	Q 75%	0.162	0.194	0.206	0.138	0.109	0.168	0.188
	IQR	0.035	0.035	0.055	0.042	0.014	0.043	0.035
	maximum	0.173	0.224	0.218	0.198	0.110	0.222	0.200
	minimum	0.080	0.157	0.141	0.080	0.081	0.099	0.142
	range	0.093	0.067	0.077	0.118	0.029	0.123	0.058
D [x 10^{-4} mm^2/s]	mean	3.239	4.167	1.981	3.534	4.525	4.923	4.752
	std	1.081	0.617	0.534	1.479	0.704	2.633	1.873
	median	3.033	4.029	1.957	3.567	4.492	4.461	4.227
	Q 25%	2.490	3.709	1.499	2.466	3.953	3.216	3.560
	Q 75%	3.749	4.626	2.398	4.529	5.097	5.443	5.944
	IQR	1.259	0.917	0.899	2.063	1.144	2.227	2.384
	maximum	5.280	5.002	2.672	6.160	5.340	11.021	7.436
	minimum	1.846	3.610	1.407	1.553	3.777	2.042	3.118
	range	3.434	1.392	1.265	4.607	1.563	8.979	4.318
D* [x 10^{-3} mm^2/s]	mean	9.089	10.802	28.487	7.301	4.470	6.705	9.312
	std	4.001	2.820	9.560	5.725	1.216	3.081	3.071
	median	9.685	9.685	29.055	4.470	4.470	6.705	8.940
	Q 25%	5.960	8.940	19.370	4.470	3.725	4.470	7.450
	Q 75%	11.920	12.665	35.760	8.940	5.215	7.450	11.175
	IQR	5.960	3.725	16.390	4.470	1.490	2.980	3.725
	maximum	16.390	14.900	41.293	20.860	5.960	13.410	13.410
	minimum	2.980	8.940	16.390	2.980	2.980	2.980	5.960
	range	13.410	5.960	24.903	17.880	2.980	10.430	7.450

Table C.8: *Calculated statistical parameters for IVIM parameters* f, D *and* $D*$ *in contrast enhanced part of brain tumors HGG, metastasis and meningioma, in brain edema of brain tumors HGG and metastasis, in contrast not enhanced part of brain tumors HGG and metastasis. No diffusion images correction, without denoising, fitting algorithm: Fit D and f (with high b), then fit D*.*

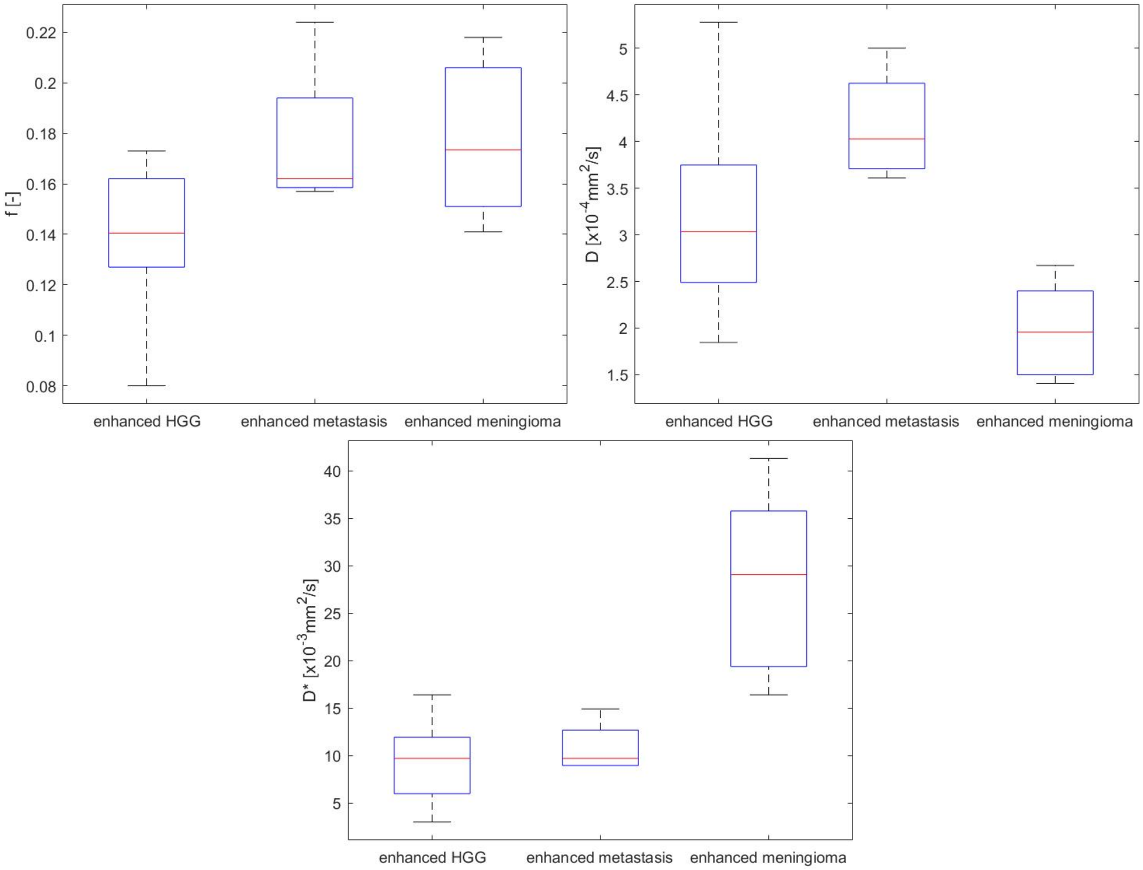

Figure C.27: Box plots of IVIM parameters f, D and $D*$ in contrast enhanced part of brain tumors HGG (n=10), metastasis (n=4) and meningioma (n=6).

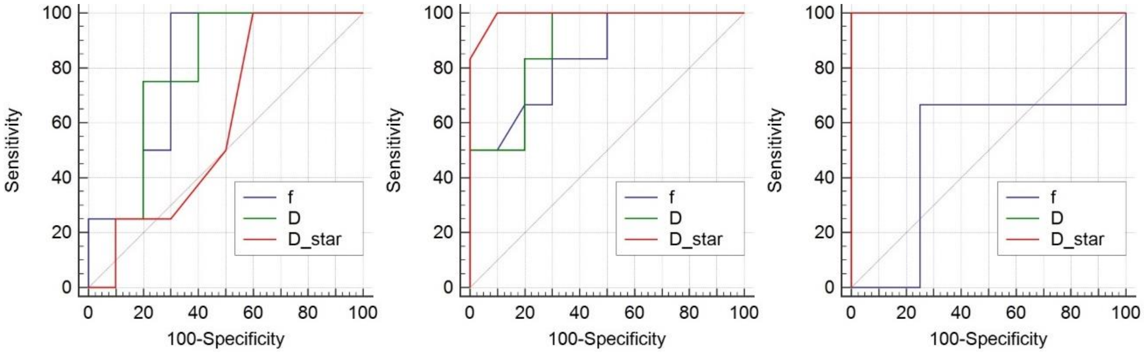

Figure C.28: ROC curves analysis for IVIM parameters f, D and $D*$ in contrast enhanced part of brain tumors HGG, metastasis and meningioma. On the left: HGG and metastasis, in the middle: HGG and meningioma, on the right: metastasis and meningioma.

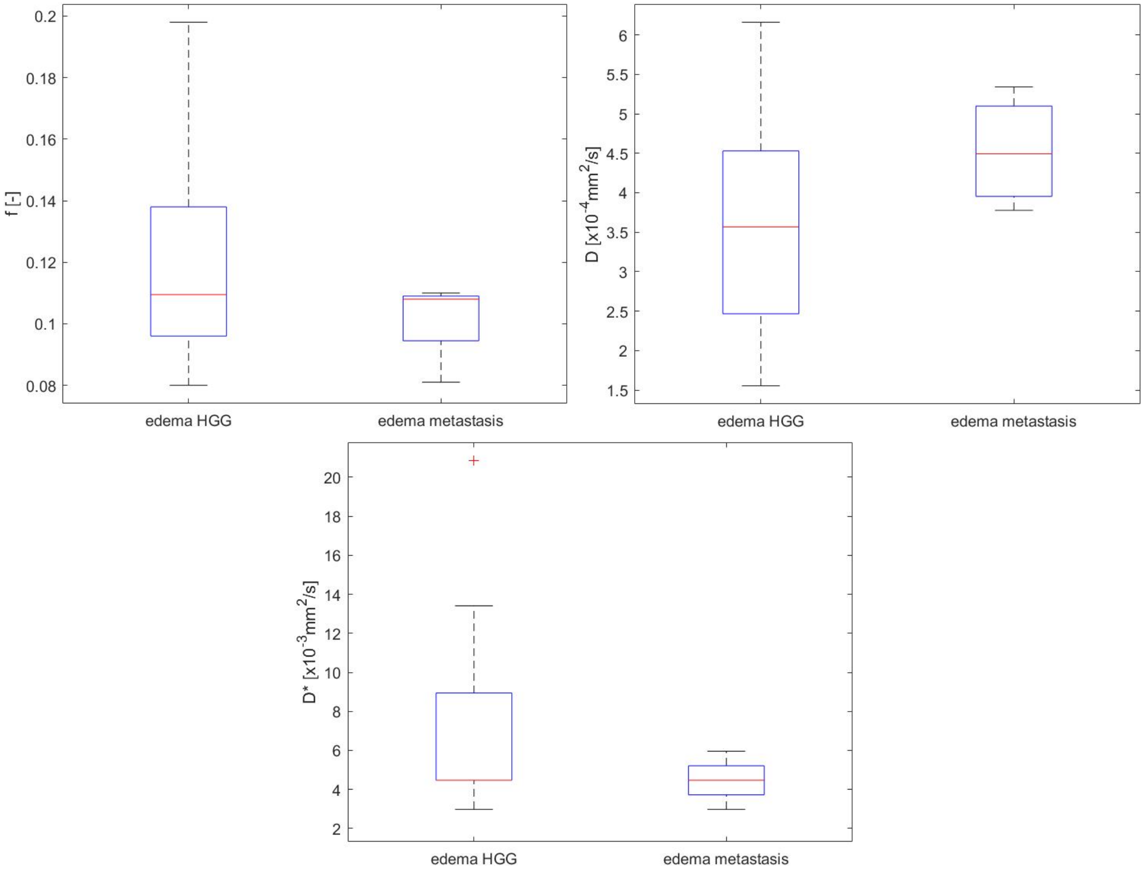

Figure C.29: Box plots of IVIM parameters f, D and $D*$ in brain edema of brain tumors HGG (n=10) and metastasis (n=4).

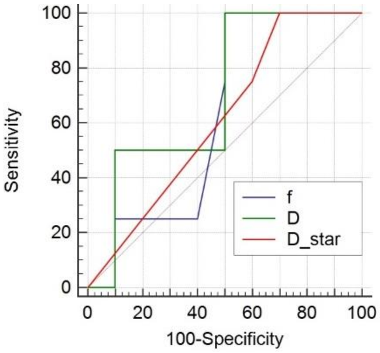

Figure C.30: ROC curves analysis for IVIM parameters f, D and $D*$ in edema of brain tumors HGG and metastasis.

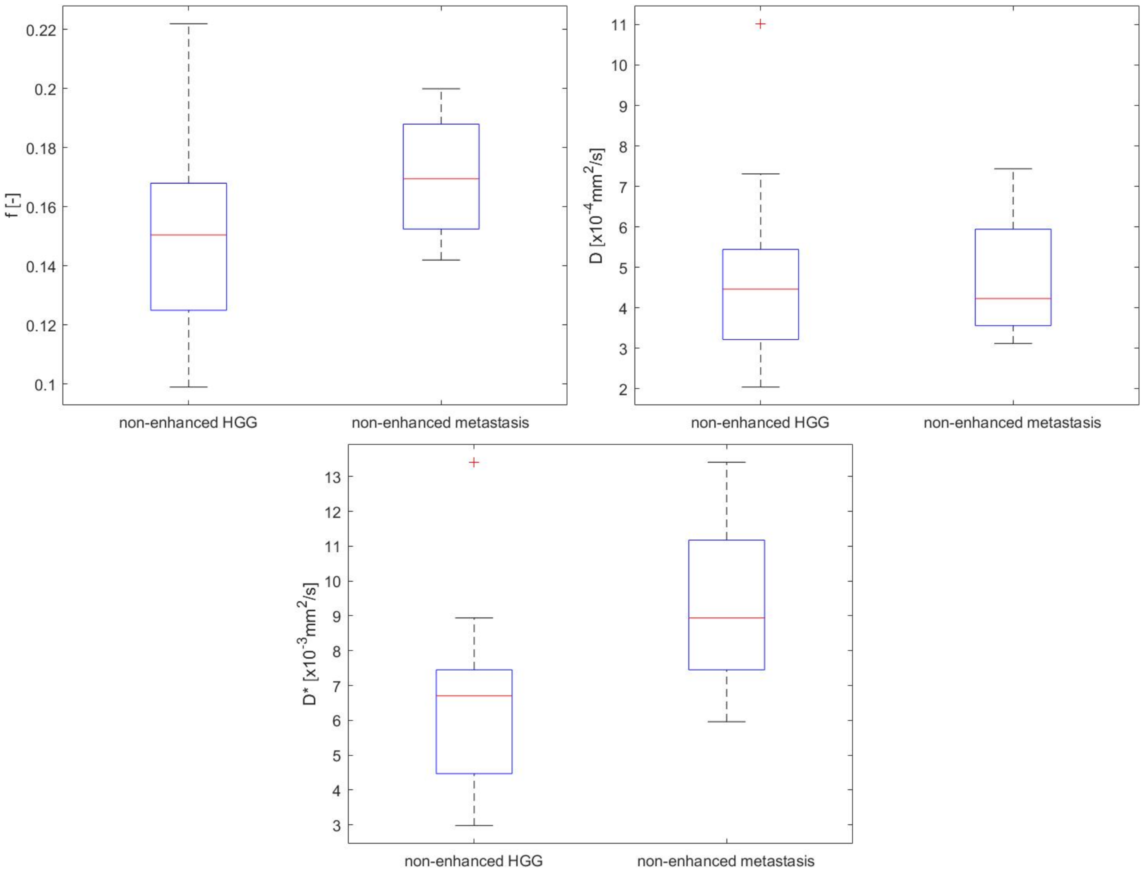

Figure C.31: Box plots of IVIM parameters f, D and $D*$ in non-enhanced part of brain tumors HGG (n=10) and metastasis (n=4).

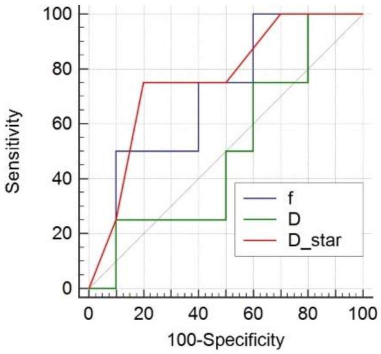

Figure C.32: ROC curves analysis for IVIM parameters f, D and $D*$ in contrast not enhanced part of brain tumors HGG and metastasis.

C.II. DWI Denoising

C.II.I. FSL

	parameter	edema (n=15)	enhanced tumor (n=20)	non-enhanced tumor (n=15)
f [-]	mean	0.090	0.129	0.135
	std	0.033	0.028	0.029
	median	0.085	0.129	0.136
	Q 25%	0.071	0.109	0.111
	Q 75%	0.098	0.149	0.150
	IQR	0.027	0.040	0.039
	maximum	0.192	0.184	0.196
	minimum	0.052	0.072	0.090
	range	0.140	0.112	0.106
D [x 10^{-4} mm^2/s]	mean	3.218	2.583	4.324
	std	1.227	1.022	2.491
	median	3.665	2.367	3.659
	Q 25%	2.174	1.722	2.787
	Q 75%	3.921	3.354	4.953
	IQR	1.746	1.632	2.165
	maximum	5.505	4.443	11.517
	minimum	0.950	1.024	1.479
	range	4.555	3.419	10.038
D* [x 10^{-3} mm^2/s]	mean	3.178	6.556	3.079
	std	2.633	5.889	3.004
	median	1.490	4.470	2.980
	Q 25%	1.490	2.980	1.490
	Q 75%	2.980	8.195	2.980
	IQR	1.490	5.215	1.490
	maximum	8.940	22.350	13.410
	minimum	1.490	1.490	1.490
	range	7.450	20.860	11.920

Table C.9: Calculated statistical parameters for IVIM parameters f, D and $D*$ in brain edema, contrast enhanced and contrast not enhanced part of a brain tumor. Diffusion images correction implemented in FSL, denoising included, fitting algorithm: Fit D and f (with high b), then fit D.*

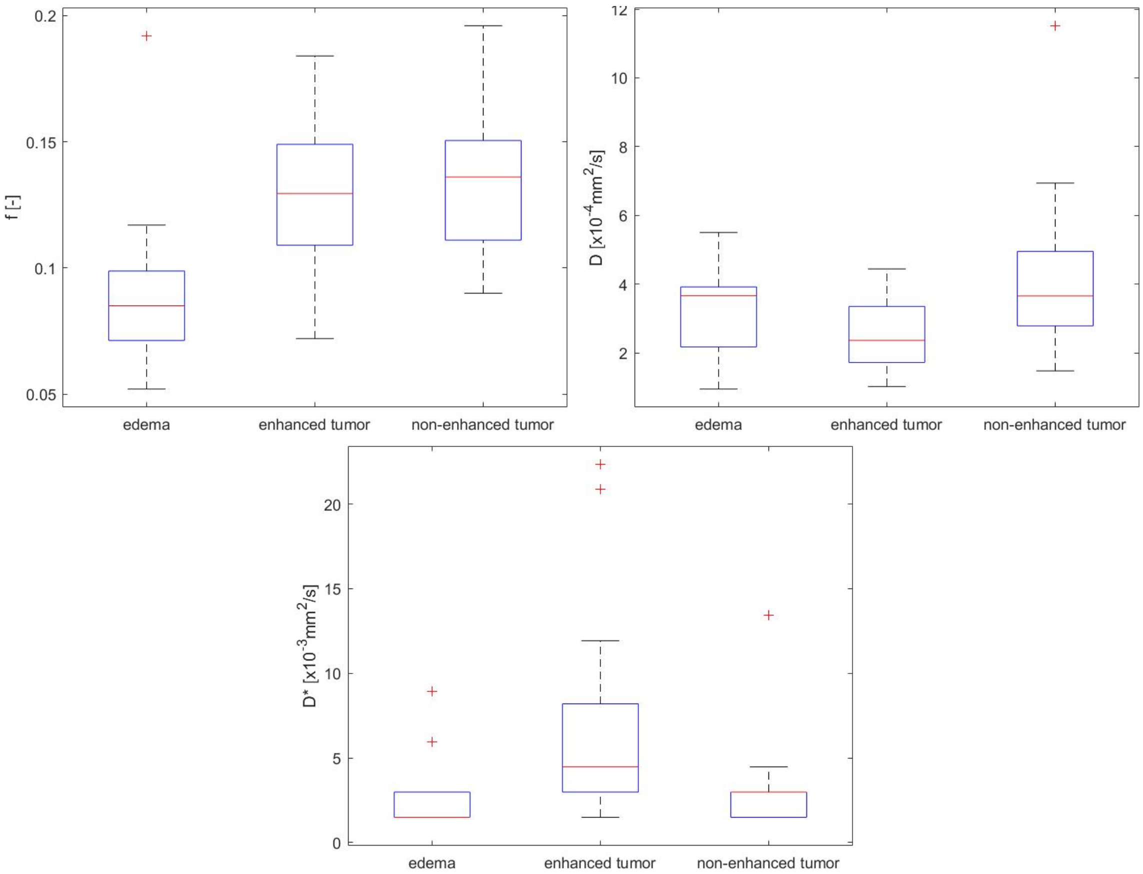

Figure C.33: Box plots of IVIM parameters f, D and $D*$ in brain edema (n=15), contrast enhanced (n=20) and contrast not enhanced (n=15) part of brain tumors.

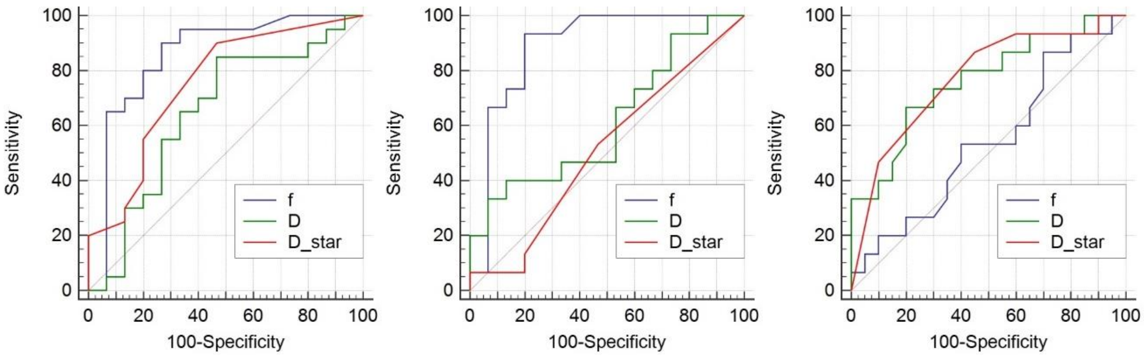

Figure C.34: ROC curves analysis for IVIM parameters f, D and $D*$ in brain edema, contrast enhanced and contrast not enhanced part of brain tumors. On the left: brain edema and contrast enhanced part, in the middle: brain edema and contrast not enhanced part, on the right: contrast enhanced and contrast not enhanced part of brain tumors.

	parameter	enhanced HGG (n=10)	enhanced metastasis (n=4)	enhanced meningioma (n=6)	edema HGG (n=10)	edema metastasis (n=4	non-enhanced HGG (n=10)	non-enhanced metastasis (n=4)
f [-]	mean	0.110	0.155	0.143	0.088	0.092	0.130	0.152
	std	0.020	0.021	0.023	0.040	0.018	0.032	0.019
	median	0.111	0.152	0.148	0.075	0.089	0.117	0.145
	Q 25%	0.097	0.140	0.124	0.066	0.080	0.110	0.141
	Q 75%	0.128	0.170	0.160	0.095	0.103	0.152	0.163
	IQR	0.031	0.030	0.036	0.029	0.023	0.042	0.022
	maximum	0.138	0.184	0.172	0.192	0.117	0.196	0.180
	minimum	0.072	0.134	0.109	0.052	0.072	0.090	0.138
	range	0.066	0.050	0.063	0.140	0.045	0.106	0.042
D [x 10^{-4} mm^2/s]	mean	2.762	3.428	1.721	2.968	3.874	4.473	4.075
	std	1.022	0.753	0.470	1.411	0.515	2.869	2.004
	median	2.549	3.397	1.722	3.066	3.964	3.921	3.550
	Q 25%	2.155	2.855	1.437	2.008	3.484	2.668	2.867
	Q 75%	3.457	4.001	2.069	3.902	4.264	5.117	5.282
	IQR	1.302	1.146	0.632	1.894	0.780	2.449	2.415
	maximum	4.443	4.343	2.354	5.505	4.372	11.517	6.939
	minimum	1.467	2.575	1.024	0.950	3.197	1.479	2.261
	range	2.976	1.768	1.330	4.555	1.175	10.038	4.678
D* [x 10^{-3} mm^2/s]	mean	3.427	4.097	13.410	3.278	1.490	2.235	2.607
	std	1.413	2.235	6.663	2.412	0.000	1.053	0.745
	median	2.980	2.980	11.175	2.980	1.490	1.490	2.980
	Q 25%	2.980	2.980	8.940	1.490	1.490	1.490	2.235
	Q 75%	4.470	5.215	20.860	2.980	1.490	2.980	2.980
	IQR	1.490	2.235	11.920	1.490	0.000	1.490	0.745
	maximum	5.960	7.450	22.350	8.940	1.490	4.470	2.980
	minimum	1.490	2.980	5.960	1.490	1.490	1.490	1.490
	range	4.470	4.470	16.390	7.450	0.000	2.980	1.490

Table C.10*: Calculated statistical parameters for IVIM parameters f, D and $D\ast$ in contrast enhanced part of brain tumors HGG, metastasis and meningioma, in brain edema of brain tumors HGG and metastasis, in contrast not enhanced part of brain tumors HGG and metastasis. Diffusion images correction implemented in FSL, denoising included, fitting algorithm: Fit D and f (with high b), then fit D*.*

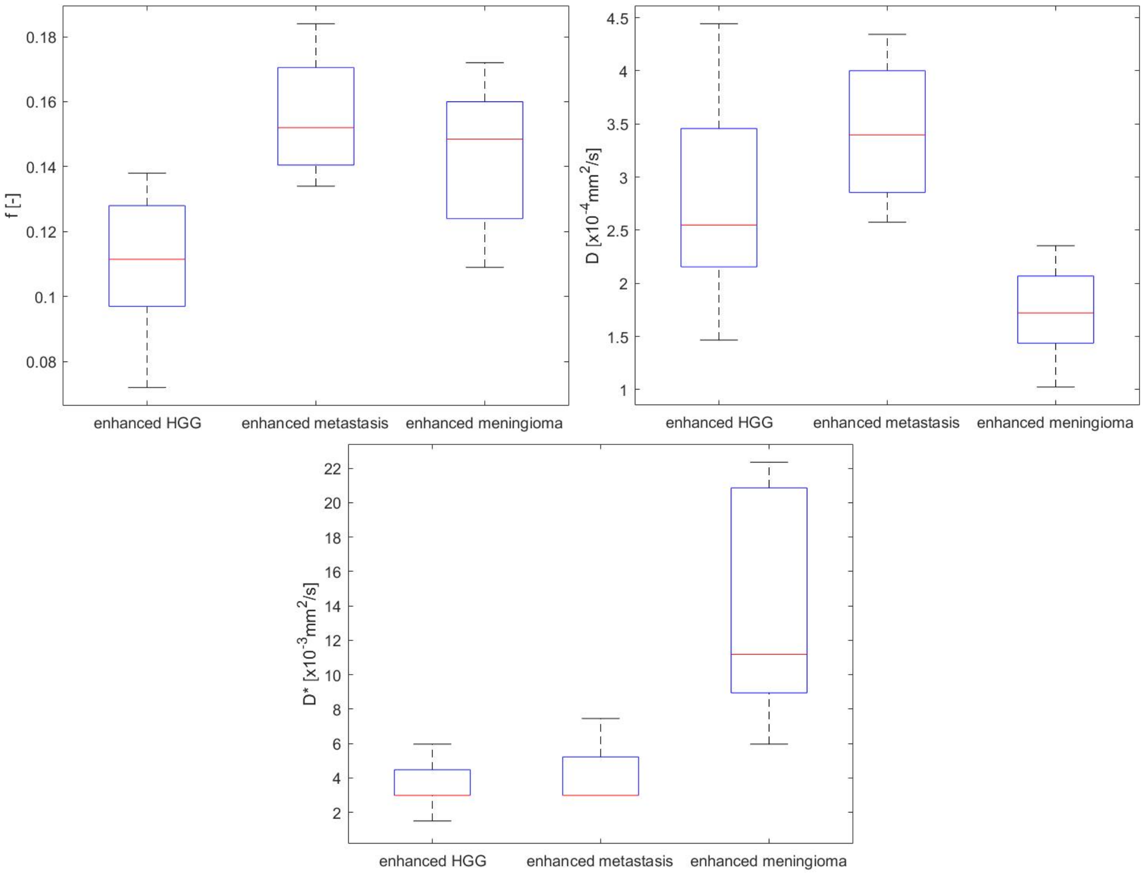

Figure C.35: Box plots of IVIM parameters f, D and $D*$ in contrast enhanced part of brain tumors HGG (n=10), metastasis (n=4) and meningioma (n=6).

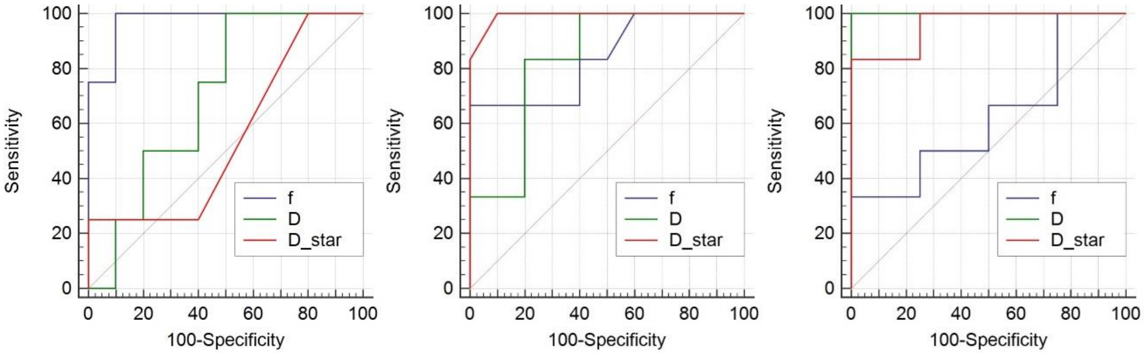

Figure C.36: ROC curves analysis for IVIM parameters f, D and $D*$ in contrast enhanced part of brain tumors HGG, metastasis and meningioma. On the left: HGG and metastasis, in the middle: HGG and meningioma, on the right: metastasis and meningioma.

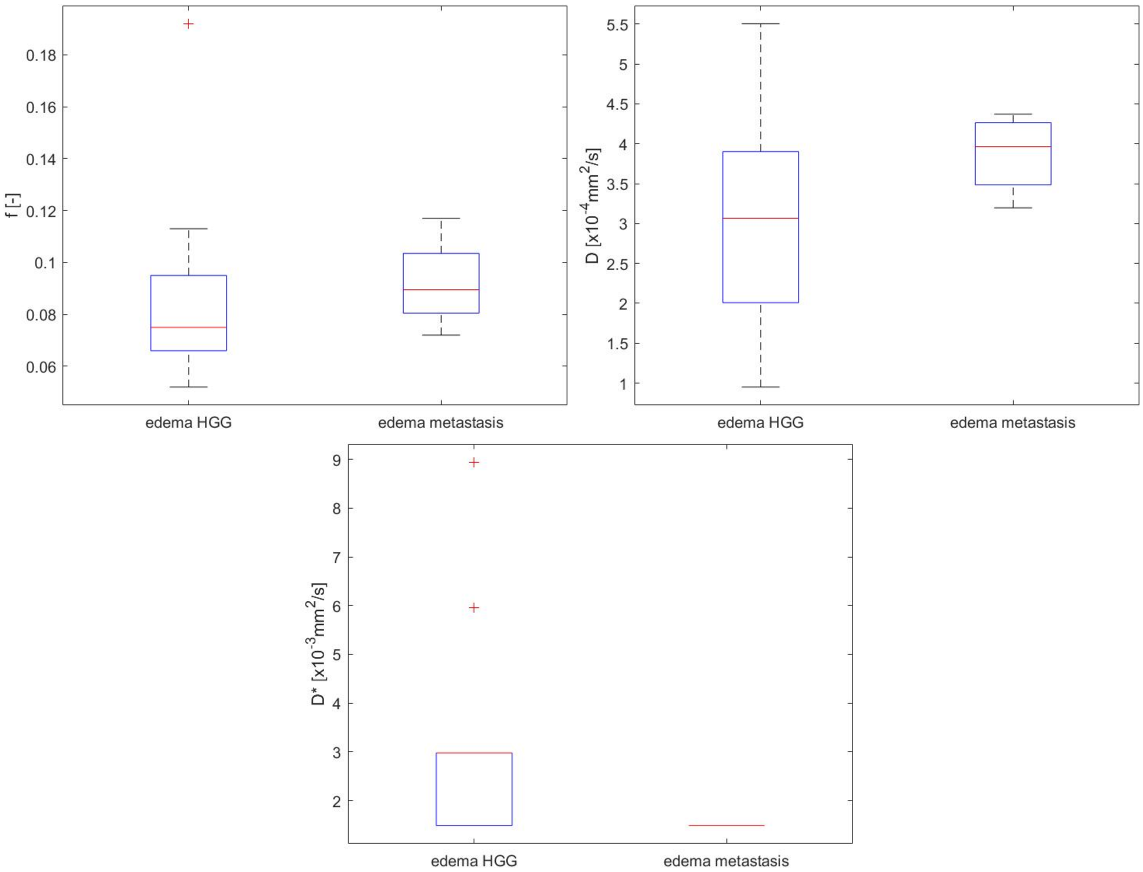

Figure C.37: Box plots of IVIM parameters f, D and $D*$ in brain edema of brain tumors HGG (n=10) and metastasis (n=4).

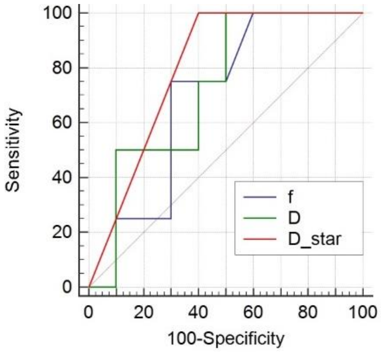

Figure C.38: ROC curves analysis for IVIM parameters f, D and $D*$ in edema of brain tumors HGG and metastasis.

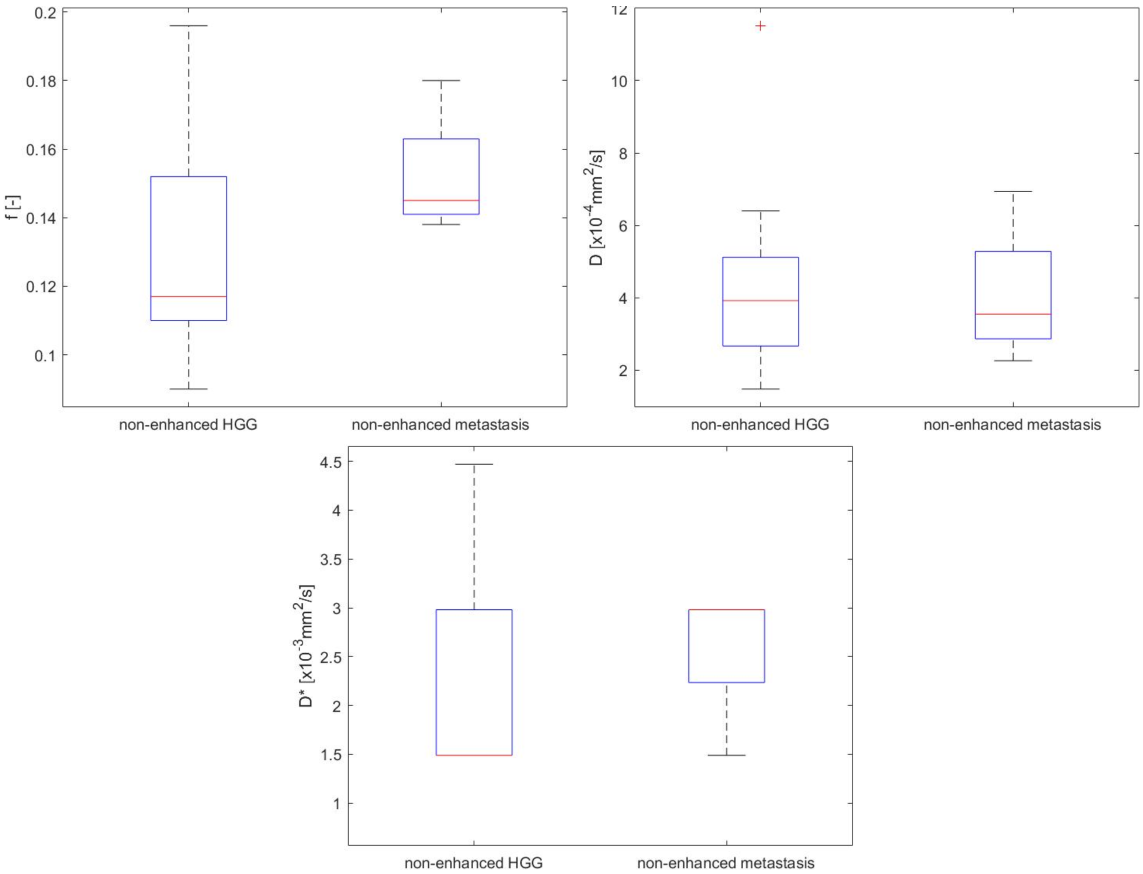

Figure C.39: Box plots of IVIM parameters f, D and $D*$ in non-enhanced part of brain tumors HGG (n=10) and metastasis (n=4).

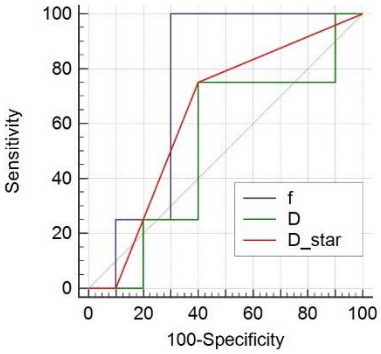

Figure C.40: ROC curves analysis for IVIM parameters f, D and $D*$ in contrast not enhanced part of brain tumors HGG and metastasis.

C.II.II. SPM

	parameter	edema (n=15)	enhanced tumor (n=20)	non-enhanced tumor (n=15)
f [-]	mean	0.075	0.131	0.127
	std	0.033	0.051	0.036
	median	0.069	0.119	0.125
	Q 25%	0.049	0.101	0.102
	Q 75%	0.079	0.143	0.135
	IQR	0.029	0.041	0.033
	maximum	0.153	0.292	0.205
	minimum	0.037	0.057	0.085
	range	0.116	0.235	0.120
D [x 10^{-4} mm^2/s]	mean	3.482	2.803	4.588
	std	1.439	1.126	2.649
	median	3.888	2.851	3.802
	Q 25%	2.301	2.025	3.085
	Q 75%	4.366	3.625	5.162
	IQR	2.065	1.600	2.077
	maximum	6.068	4.908	11.955
	minimum	0.919	0.650	1.612
	range	5.149	4.258	10.343
D* [x 10^{-3} mm^2/s]	mean	3.113	6.407	3.377
	std	1.854	4.884	2.547
	median	2.980	4.470	2.980
	Q 25%	1.490	2.980	1.862
	Q 75%	4.097	7.450	2.980
	IQR	2.607	4.470	1.117
	maximum	7.450	20.860	11.920
	minimum	1.490	1.490	1.490
	range	5.960	19.370	10.430

Table C.11: Calculated statistical parameters for IVIM parameters f, D and $D*$ in brain edema, contrast enhanced and contrast not enhanced part of a brain tumor. Diffusion images correction implemented in SPM, denoising included, fitting algorithm: Fit D and f (with high b), then fit D.*

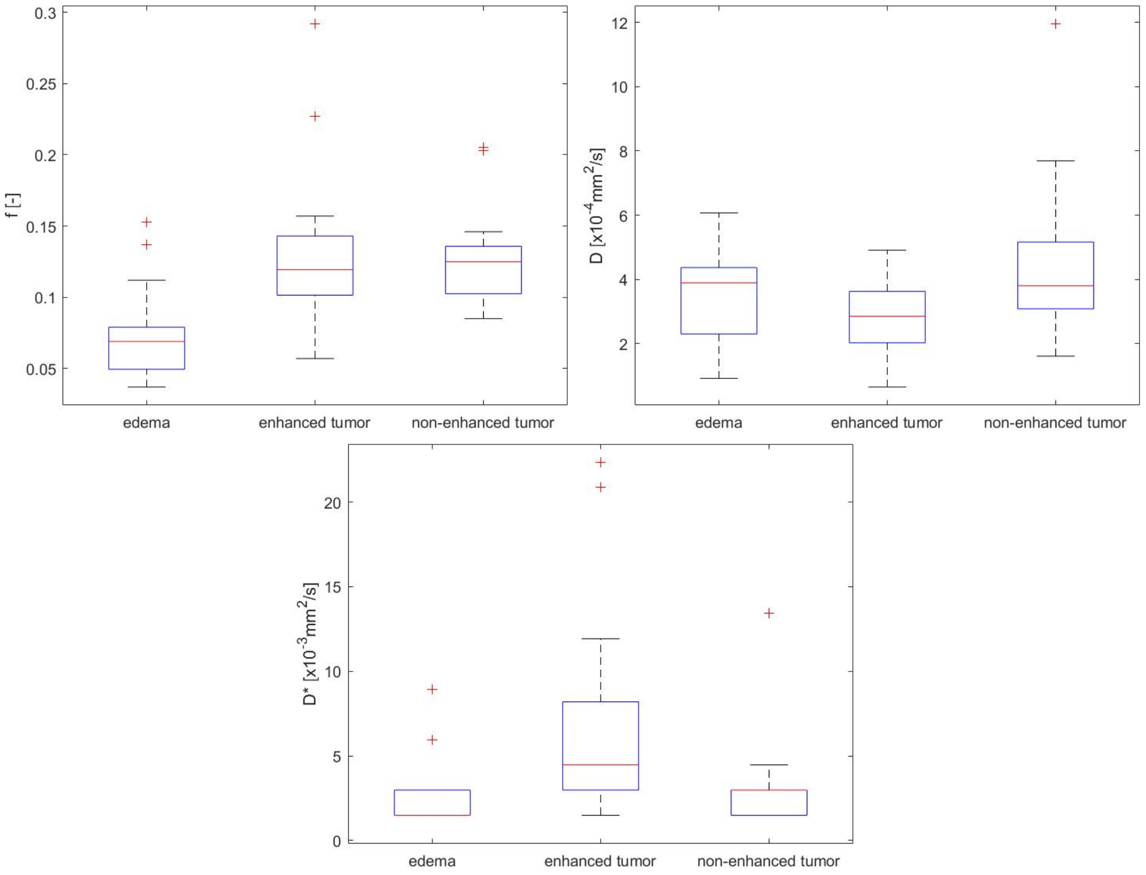

Figure C.41: Box plots of IVIM parameters f, D and $D*$ in brain edema (n=15), contrast enhanced (n=20) and contrast not enhanced (n=15) part of brain tumors.

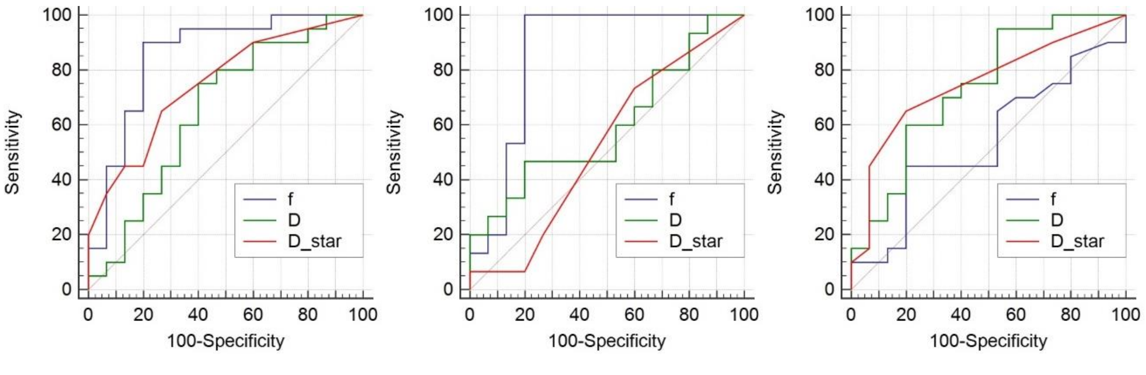

Figure C.42: ROC curves analysis for IVIM parameters f, D and $D*$ in brain edema, contrast enhanced and contrast not enhanced part of brain tumors. On the left: brain edema and contrast enhanced part, in the middle: brain edema and contrast not enhanced part, on the right: contrast enhanced and contrast not enhanced part of brain tumors.

	parameter	enhanced HGG (n=10)	enhanced metastasis (n=4)	enhanced meningioma (n=6)	edema HGG (n=10)	edema metastasis (n=4)	non-enhanced HGG (n=10)	non-enhanced metastasis (n=4)
f [-]	mean	0.108	0.135	0.168	0.080	0.060	0.121	0.124
	std	0.029	0.018	0.075	0.040	0.012	0.034	0.020
	median	0.110	0.132	0.141	0.069	0.064	0.117	0.123
	Q 25%	0.092	0.119	0.111	0.048	0.051	0.092	0.107
	Q 75%	0.142	0.151	0.227	0.112	0.069	0.135	0.141
	IQR	0.050	0.031	0.116	0.064	0.017	0.043	0.033
	maximum	0.143	0.157	0.292	0.153	0.069	0.203	0.146
	minimum	0.057	0.119	0.099	0.037	0.043	0.085	0.104
	range	0.086	0.038	0.193	0.116	0.026	0.118	0.042
D [x 10^{-4} mm^2/s]	mean	2.907	3.808	1.958	3.178	4.300	4.751	4.527
	std	1.115	0.674	0.785	1.624	0.737	2.982	2.310
	median	3.049	3.974	2.041	3.210	4.347	4.265	4.100
	Q 25%	2.164	3.349	1.658	1.950	3.699	3.048	2.955
	Q 75%	3.415	4.268	2.385	4.293	4.900	5.276	6.099
	IQR	1.251	0.919	0.727	2.343	1.201	2.228	3.143
	maximum	4.908	4.423	2.977	6.068	5.065	11.955	7.688
	minimum	1.311	2.863	0.650	0.919	3.440	1.612	2.220
	range	3.597	1.560	2.327	5.149	1.625	10.343	5.468
D* [x 10^{-3} mm^2/s]	mean	3.725	4.470	12.168	3.180	1.862	2.533	3.352
	std	1.609	2.107	5.111	1.540	0.745	1.005	0.745
	median	3.725	3.725	11.175	2.980	1.490	2.980	2.980
	Q 25%	2.980	2.980	7.450	1.490	1.490	1.490	2.980
	Q 75%	4.470	5.960	14.900	4.470	2.235	2.980	3.725
	IQR	1.490	2.980	7.450	2.980	0.745	1.490	0.745
	maximum	5.960	7.450	20.860	5.960	2.980	4.470	4.470
	minimum	1.490	2.980	7.450	1.490	1.490	1.490	2.980
	range	4.470	4.470	13.410	4.470	1.490	2.980	1.490

Table C.12*: Calculated statistical parameters for IVIM parameters f, D and $D*$ in contrast enhanced part of brain tumors HGG, metastasis and meningioma, in brain edema of brain tumors HGG and metastasis, in contrast not enhanced part of brain tumors HGG and metastasis. Diffusion images correction implemented in SPM, denoising included, fitting algorithm: Fit D and f (with high b), then fit D*.*

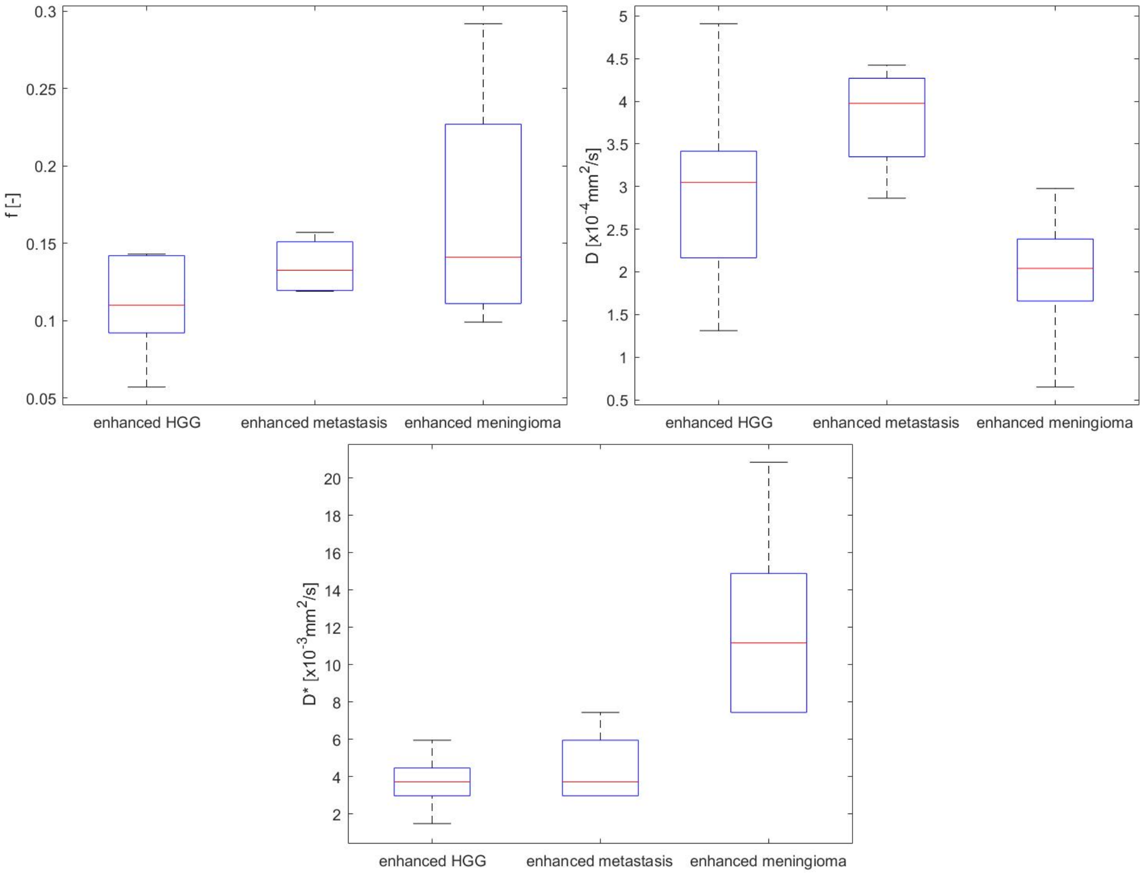

Figure C.43: Box plots of IVIM parameters f, D and $D*$ in contrast enhanced part of brain tumors HGG (n=10), metastasis (n=4) and meningioma (n=6).

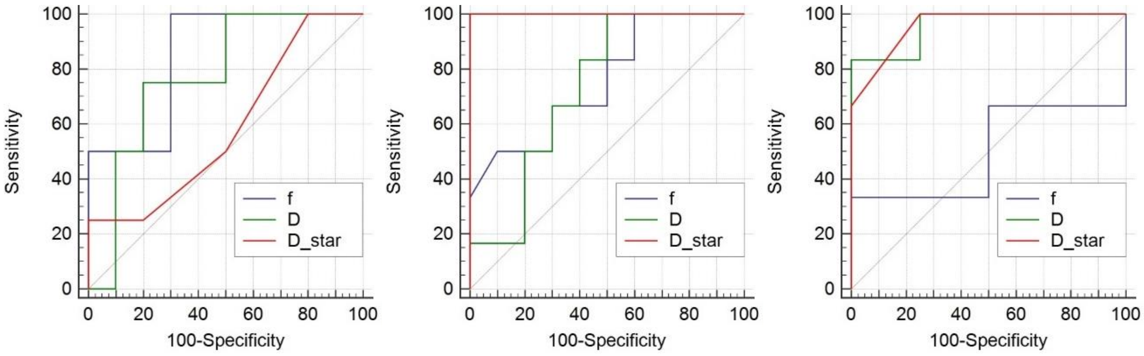

Figure C.44: ROC curves analysis for IVIM parameters f, D and $D*$ in contrast enhanced part of brain tumors HGG, metastasis and meningioma. On the left: HGG and metastasis, in the middle: HGG and meningioma, on the right: metastasis and meningioma.

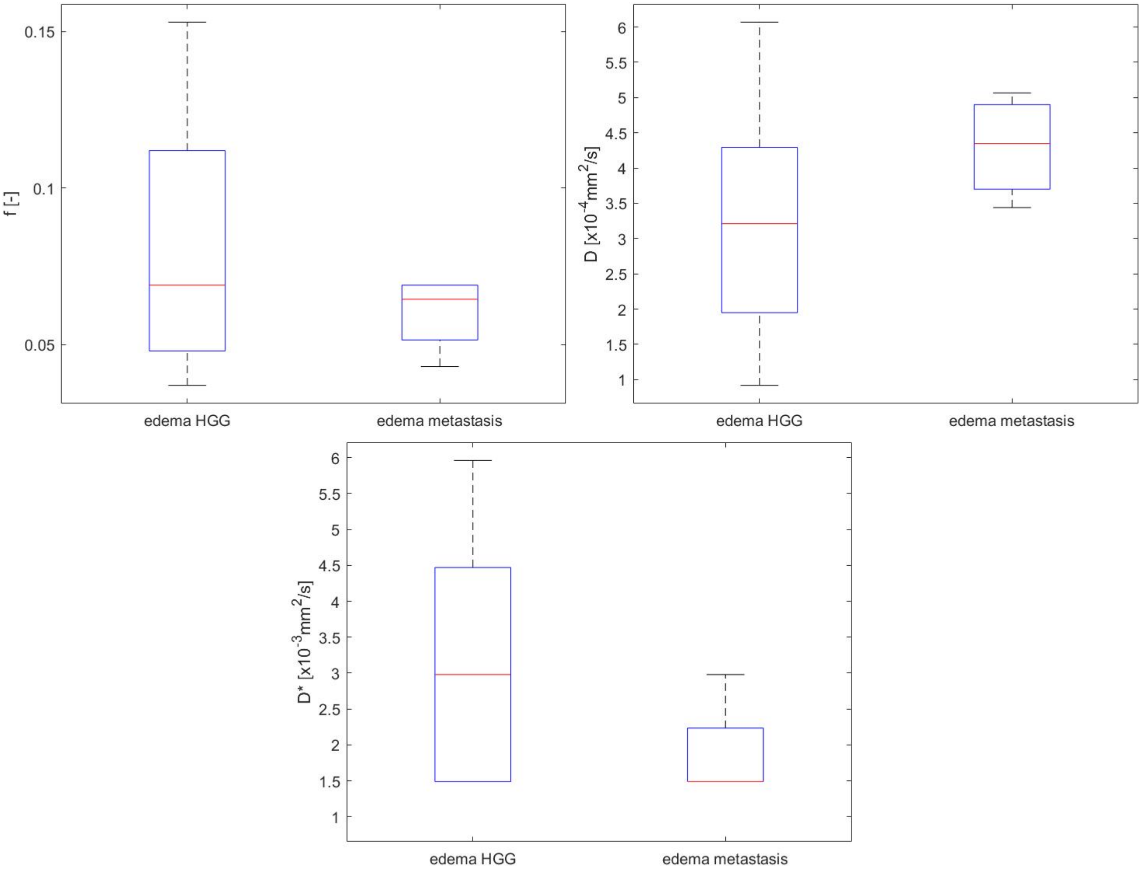

Figure C.45: Box plots of IVIM parameters f, D and $D*$ in brain edema of brain tumors HGG (n=10) and metastasis (n=4).

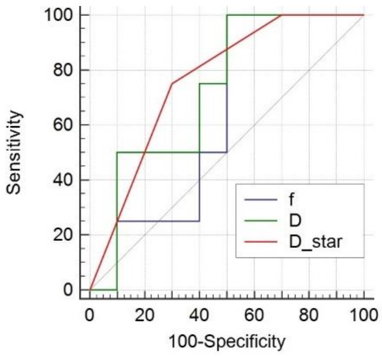

Figure C.46: ROC curves analysis for IVIM parameters f, D and $D*$ in edema of brain tumors HGG and metastasis.

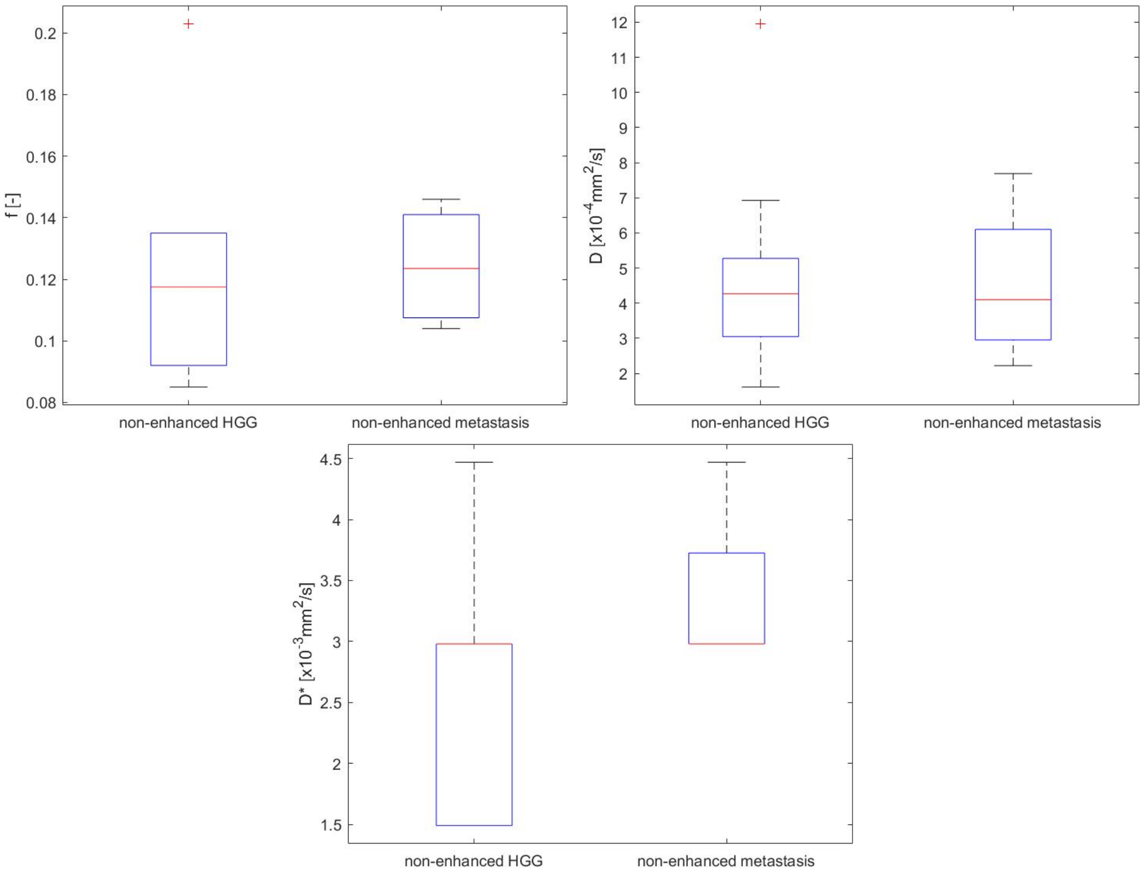

Figure C.47: Box plots of IVIM parameters f, D and $D*$ in non-enhanced part of brain tumors HGG (n=10) and metastasis (n=4).

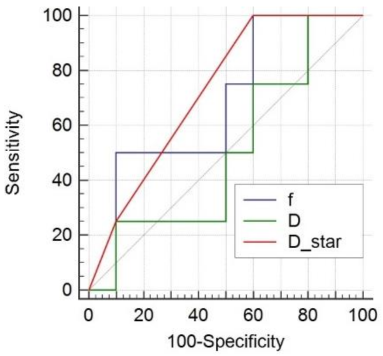

Figure C.48: ROC curves analysis for IVIM parameters f, D and $D*$ in contrast not enhanced part of brain tumors HGG and metastasis.

C.II.III. BrainSuite

	parameter	edema (n=15)	enhanced tumor (n=20)	non-enhanced tumor (n=15)
f [-]	mean	0.079	0.138	0.140
	std	0.043	0.051	0.050
	median	0.070	0.131	0.130
	Q 25%	0.049	0.111	0.105
	Q 75%	0.081	0.152	0.142
	IQR	0.032	0.041	0.037
	maximum	0.205	0.310	0.295
	minimum	0.036	0.076	0.095
	range	0.169	0.234	0.200
D [x 10^{-4} mm^2/s]	mean	3.563	3.110	4.744
	std	1.425	1.447	2.627
	median	3.905	2.832	4.289
	Q 25%	2.122	1.713	3.044
	Q 75%	4.520	4.364	5.594
	IQR	2.398	2.650	2.550
	maximum	5.859	5.374	11.523
	minimum	1.242	0.934	1.529
	range	4.617	4.440	9.994
D* [x 10^{-3} mm^2/s]	mean	3.192	9.018	4.576
	std	2.669	8.737	4.581
	median	2.235	5.960	2.980
	Q 25%	1.490	4.470	2.980
	Q 75%	2.980	10.430	4.470
	IQR	1.490	5.960	1.490
	maximum	10.430	38.740	19.370
	minimum	1.490	1.490	1.490
	range	8.940	37.250	17.880

Table C.13: Calculated statistical parameters for IVIM parameters f, D *and* $D*$ *in brain edema, contrast enhanced and contrast not enhanced part of a brain tumor. Diffusion images correction implemented in BrainSuite, denoising included, fitting algorithm: Fit D and f (with high b), then fit D*.*

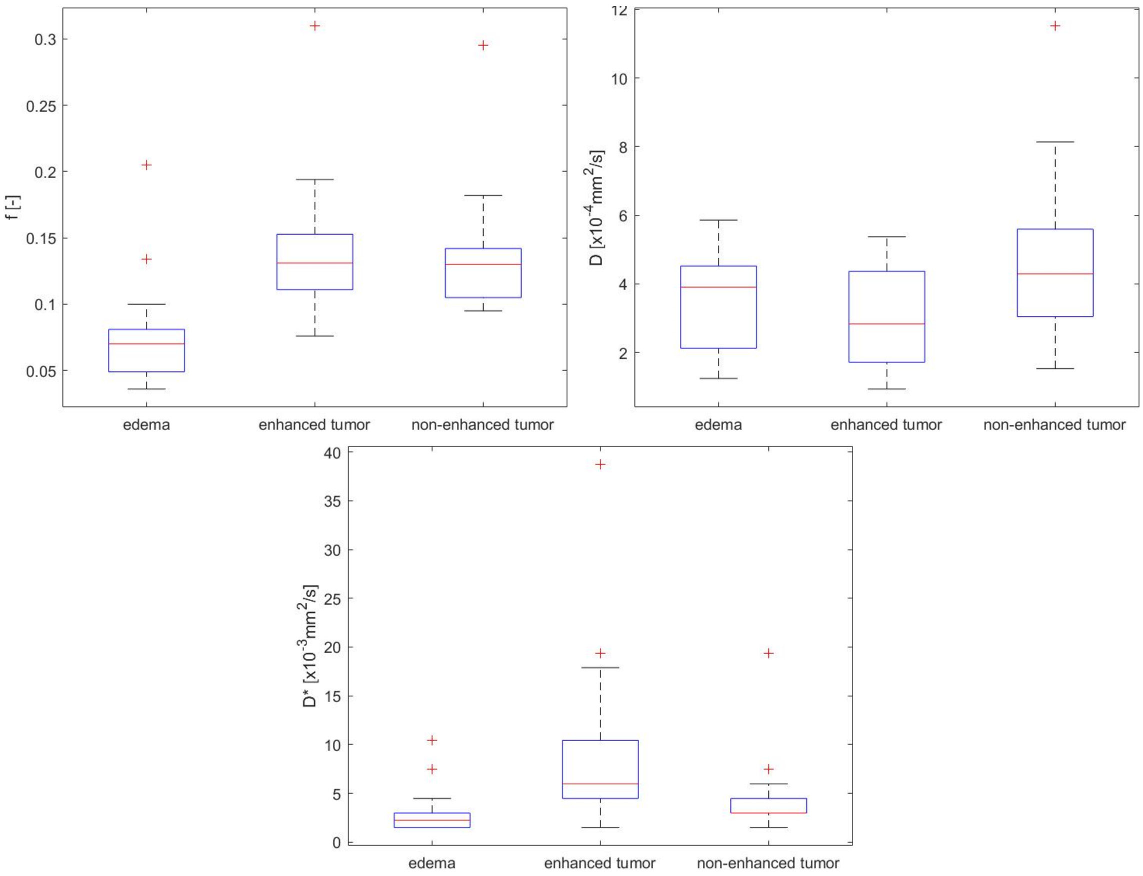

Figure C.49: Box plots of IVIM parameters f, D and $D*$ in brain edema (n=15), contrast enhanced (n=20) and contrast not enhanced (n=15) part of brain tumors.

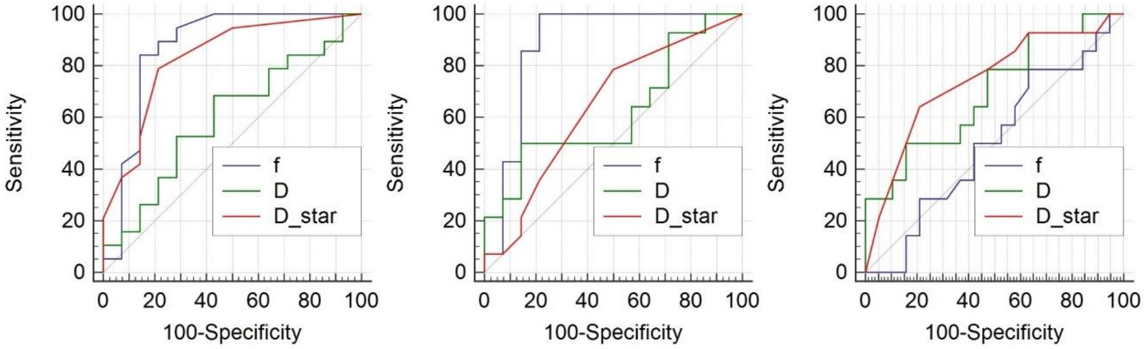

Figure C.50: ROC curves analysis for IVIM parameters f, D and $D*$ in brain edema, contrast enhanced and contrast not enhanced part of brain tumors. On the left: brain edema and contrast enhanced part, in the middle: brain edema and contrast not enhanced part, on the right: contrast enhanced and contrast not enhanced part of brain tumors.

	parameter	enhanced HGG (n=10)	enhanced metastasis (n=4)	enhanced meningioma (n=6)	edema HGG (n=10)	edema metastasis (n=4)	non-enhanced HGG (n=10)	non-enhanced metastasis (n=4)
f [-]	mean	0.114	0.141	0.171	0.087	0.063	0.127	0.129
	std	0.023	0.008	0.079	0.053	0.014	0.030	0.009
	median	0.118	0.142	0.166	0.070	0.067	0.126	0.130
	Q 25%	0.097	0.135	0.117	0.048	0.053	0.102	0.122
	Q 75%	0.129	0.148	0.194	0.108	0.073	0.147	0.136
	IQR	0.032	0.013	0.077	0.060	0.019	0.045	0.013
	maximum	0.153	0.152	0.310	0.205	0.076	0.182	0.139
	minimum	0.080	0.131	0.076	0.036	0.042	0.095	0.118
	range	0.073	0.021	0.234	0.169	0.034	0.087	0.021
D [x 10^{-4} mm^2/s]	mean	3.131	3.844	2.591	3.142	4.441	5.090	3.888
	std	1.390	0.775	1.825	1.582	0.735	3.087	1.769
	median	2.832	4.091	1.828	3.050	4.560	4.811	3.331
	Q 25%	1.959	3.289	1.238	1.812	3.979	3.069	2.745
	Q 75%	3.984	4.400	4.365	4.318	4.903	6.229	5.031
	IQR	2.024	1.111	3.127	2.505	0.924	3.159	2.285
	maximum	5.374	4.439	5.356	5.859	5.206	11.523	6.443
	minimum	1.405	2.756	0.934	1.242	3.438	1.529	2.447
	range	3.969	1.683	4.422	4.617	1.768	9.994	3.996
D* [x 10^{-3} mm^2/s]	mean	4.304	5.960	18.128	3.145	1.490	2.814	4.842
	std	1.738	3.218	10.802	1.891	0.000	1.382	1.874
	median	4.470	5.215	14.900	2.980	1.490	2.980	4.470
	Q 25%	2.980	3.725	10.430	1.490	1.490	1.490	3.725
	Q 75%	4.842	8.195	19.370	3.352	1.490	2.980	5.960
	IQR	1.862	4.470	8.940	1.862	0.000	1.490	2.235
	maximum	7.450	10.430	38.740	7.450	1.490	5.960	7.450
	minimum	1.490	2.980	10.430	1.490	1.490	1.490	2.980
	range	5.960	7.450	28.310	5.960	0.000	4.470	4.470

Table C.14: *Calculated statistical parameters for IVIM parameters f, D and $D*$ in contrast enhanced part of brain tumors HGG, metastasis and meningioma, in brain edema of brain tumors HGG and metastasis, in contrast not enhanced part of brain tumors HGG and metastasis. Diffusion images correction implemented in BrainSuite, denoising included, fitting algorithm: Fit D and f (with high b), then fit D*.*

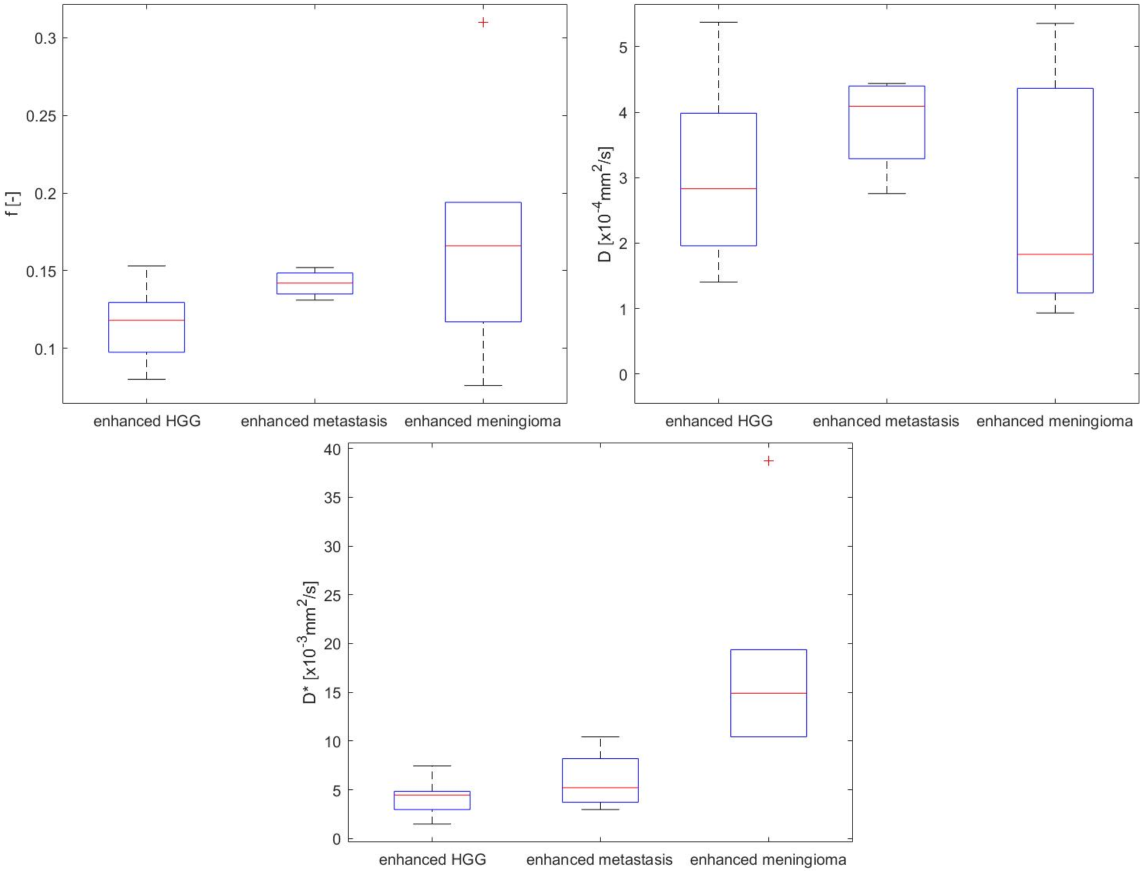

Figure C.51: Box plots of IVIM parameters f, D and $D*$ in contrast enhanced part of brain tumors HGG (n=10), metastasis (n=4) and meningioma (n=6).

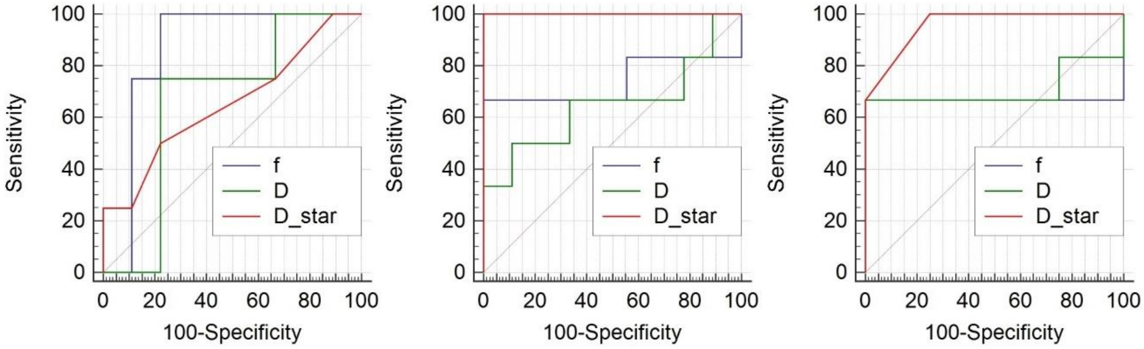

Figure C.52: ROC curves analysis for IVIM parameters f, D and $D*$ in contrast enhanced part of brain tumors HGG, metastasis and meningioma. On the left: HGG and metastasis, in the middle: HGG and meningioma, on the right: metastasis and meningioma.

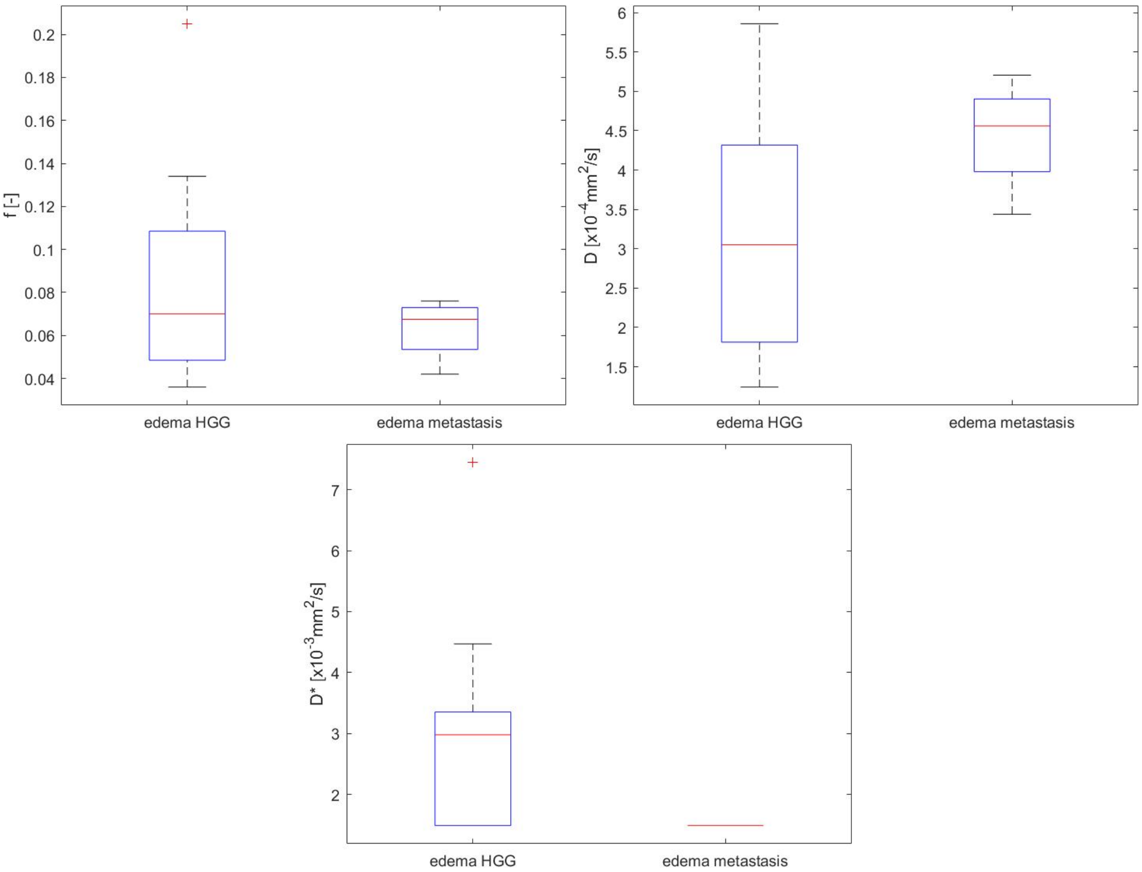

Figure C.53: Box plots of IVIM parameters f, D and $D*$ in brain edema of brain tumors HGG (n=10) and metastasis (n=4).

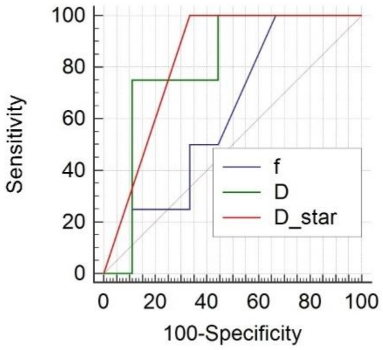

Figure C.54: ROC curves analysis for IVIM parameters f, D and $D*$ in edema of brain tumors HGG and metastasis.

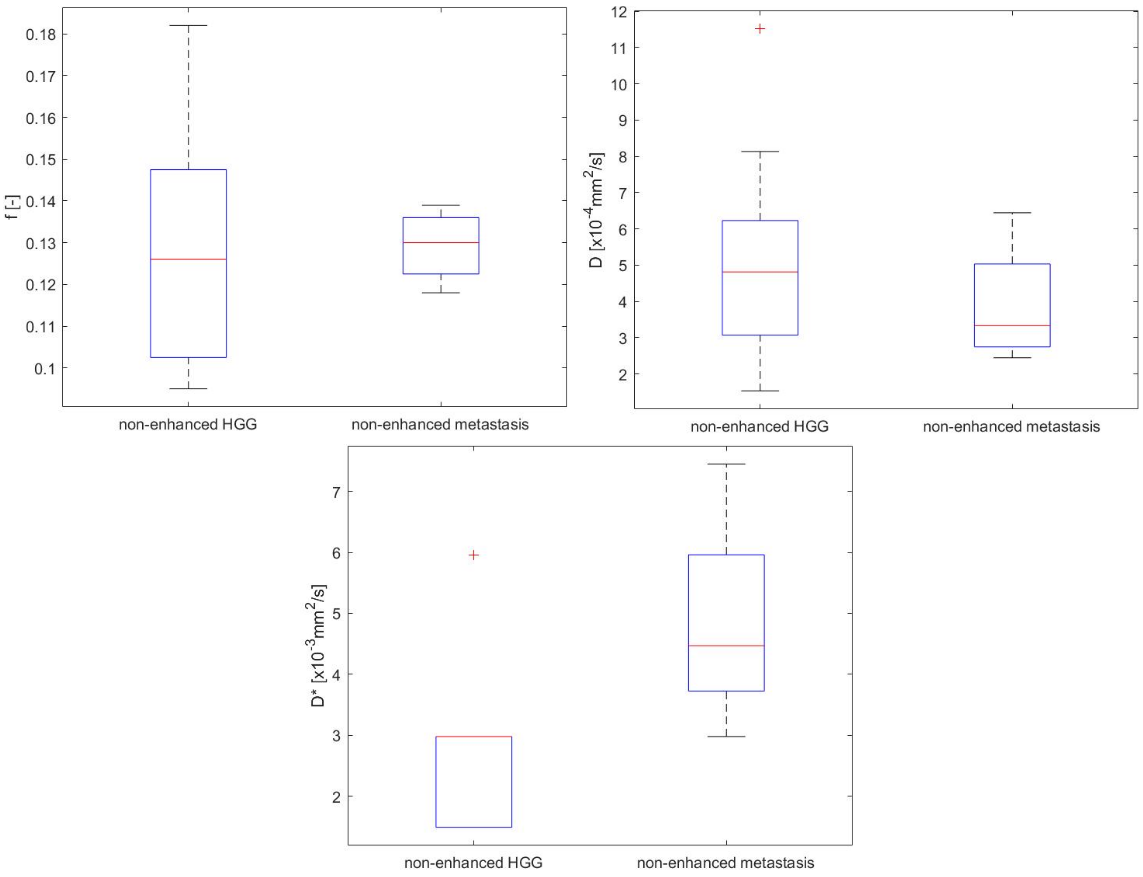

Figure C.55: Box plots of IVIM parameters f, D and $D*$ in contrast non-enhanced part of brain tumors HGG (n=10) and metastasis (n=4).

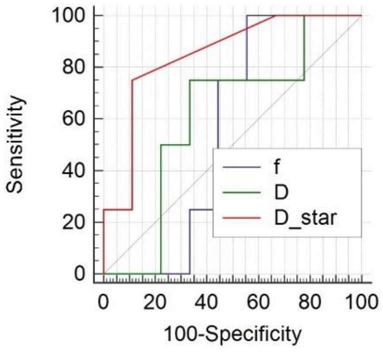

Figure C.56: ROC curves analysis for IVIM parameters f, D and $D*$ in contrast not enhanced part of brain tumors HGG and metastasis.

C.II.IV. Without correction

	parameter	**edema (n=15)**	**enhanced tumor (n=20)**	**non-enhanced tumor (n=15)**
f [-]	mean	0.074	0.128	0.132
	std	0.031	0.043	0.045
	median	0.069	0.133	0.128
	Q 25%	0.050	0.100	0.101
	Q 75%	0.078	0.145	0.140
	IQR	0.028	0.044	0.039
	maximum	0.144	0.257	0.251
	minimum	0.037	0.057	0.086
	range	0.107	0.200	0.165
D [x 10^{-4} mm^2/s]	mean	3.533	2.697	4.528
	std	1.470	1.110	2.600
	median	4.005	2.538	3.785
	Q 25%	2.268	1.886	3.054
	Q 75%	4.370	3.437	5.176
	IQR	2.101	1.551	2.121
	maximum	6.090	4.937	11.743
	minimum	0.969	0.833	1.540
	range	5.121	4.104	10.203
D* [x 10^{-3} mm^2/s]	mean	3.079	6.928	3.576
	std	1.988	5.453	2.915
	median	2.980	5.215	2.980
	Q 25%	1.490	2.980	1.862
	Q 75%	2.980	9.685	4.097
	IQR	1.490	6.705	2.235
	maximum	7.450	23.840	13.410
	minimum	1.490	1.490	1.490
	range	5.960	22.350	11.920

Table C.15: Calculated statistical parameters for IVIM parameters f, D and $D*$ in brain edema, contrast enhanced and contrast not enhanced part of a brain tumor. No diffusion images correction, denoising included, fitting algorithm: Fit D and f (with high b), then fit D.*

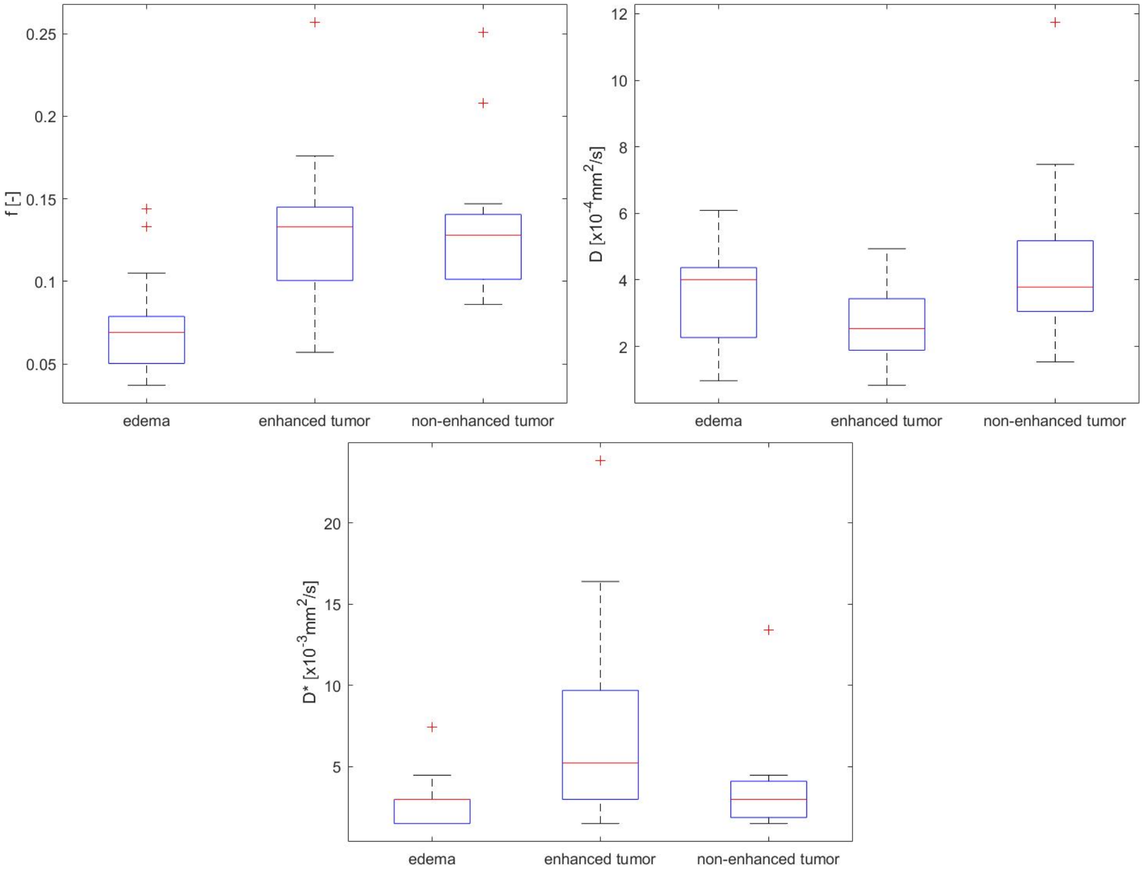

Figure C.57: Box plots of IVIM parameters f, D *and* $D*$ *in brain edema (n=15), contrast enhanced (n=20) and contrast not enhanced (n=15) part of brain tumors.*

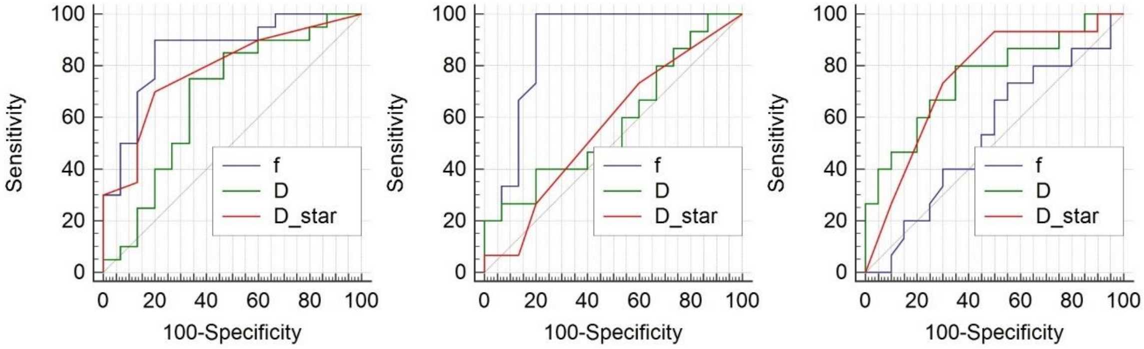

Figure C.58: ROC curves analysis for IVIM parameters f, D *and* $D*$ *in brain edema, contrast enhanced and contrast not enhanced part of brain tumors. On the left: brain edema and contrast enhanced part, in the middle: brain edema and contrast not enhanced part, on the right: contrast enhanced and contrast not enhanced part of brain tumors.*

	parameter	enhanced HGG (n=10)	enhanced metastasis (n=4)	enhanced meningioma (n=6)	edema HGG (n=10)	edema metastasis (n=4)	non-enhanced HGG (n=10)	non-enhanced metastasis (n=4)
f [-]	mean	0.105	0.140	0.159	0.078	0.063	0.121	0.130
	std	0.031	0.011	0.054	0.037	0.013	0.037	0.013
	median	0.106	0.137	0.150	0.068	0.067	0.115	0.130
	Q 25%	0.087	0.133	0.115	0.050	0.054	0.089	0.121
	Q 75%	0.137	0.148	0.176	0.105	0.072	0.136	0.139
	IQR	0.050	0.015	0.061	0.055	0.018	0.047	0.018
	maximum	0.145	0.156	0.257	0.144	0.073	0.208	0.147
	minimum	0.057	0.131	0.105	0.037	0.045	0.086	0.114
	range	0.088	0.025	0.152	0.107	0.028	0.122	0.033
D [x 10^{-4} mm^2/s]	mean	2.863	3.708	1.747	3.207	4.391	4.714	4.392
	std	1.106	0.623	0.537	1.653	0.739	2.950	2.174
	median	2.713	3.694	1.886	3.250	4.452	4.204	3.845
	Q 25%	2.120	3.251	1.446	1.905	3.791	3.000	2.993
	Q 75%	3.351	4.165	2.127	4.347	4.990	5.308	5.791
	IQR	1.231	0.914	0.681	2.442	1.199	2.308	2.798
	maximum	4.937	4.466	2.307	6.090	5.147	11.743	7.474
	minimum	1.326	2.979	0.833	0.969	3.513	1.540	2.404
	range	3.611	1.487	1.474	5.121	1.634	10.203	5.070
D* [x 10^{-3} mm^2/s]	mean	3.725	5.215	13.410	3.129	1.862	2.533	3.725
	std	1.609	1.923	5.732	1.783	0.745	1.005	0.860
	median	3.725	5.215	10.430	2.980	1.490	2.980	3.725
	Q 25%	2.980	3.725	10.430	1.490	1.490	1.490	2.980
	Q 75%	4.470	6.705	16.390	2.980	2.235	2.980	4.470
	IQR	1.490	2.980	5.960	1.490	0.745	1.490	1.490
	maximum	5.960	7.450	23.840	7.450	2.980	4.470	4.470
	minimum	1.490	2.980	8.940	1.490	1.490	1.490	2.980
	range	4.470	4.470	14.900	5.960	1.490	2.980	1.490

Table C.16*: Calculated statistical parameters for IVIM parameters f, D and $D*$ in contrast enhanced part of brain tumors HGG, metastasis and meningioma, in brain edema of brain tumors HGG and metastasis, in contrast not enhanced part of brain tumors HGG and metastasis. No diffusion images correction, denoising included, fitting algorithm: Fit D and f (with high b), then fit D*.*

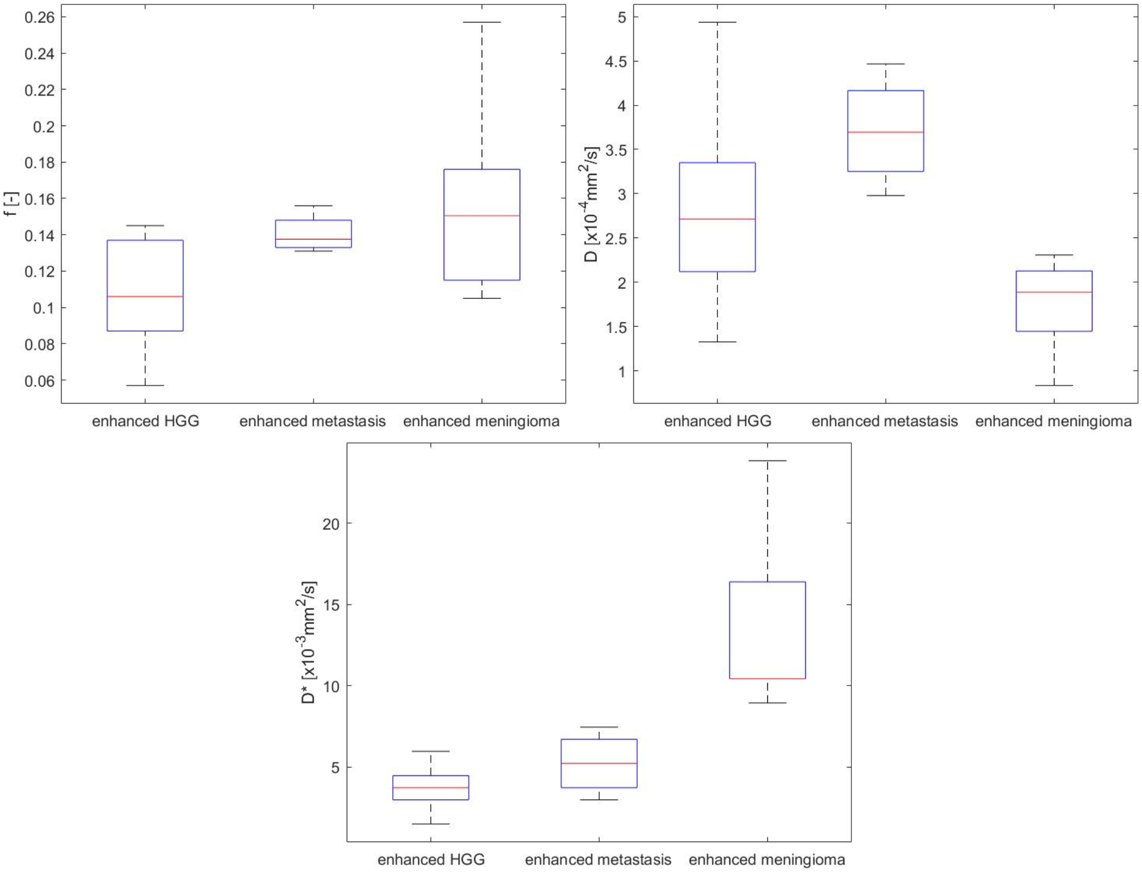

Figure C.59: Box plots of IVIM parameters f, D and $D*$ in contrast enhanced part of brain tumors HGG (n=10), metastasis (n=4) and meningioma (n=6).

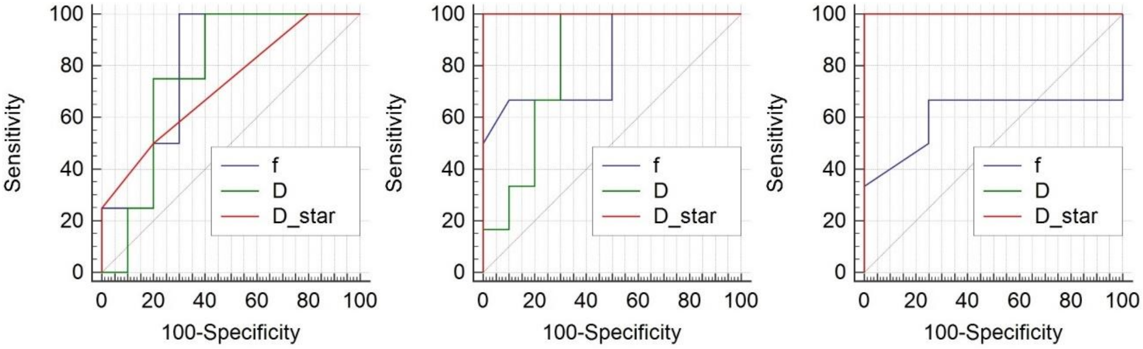

Figure C.60: ROC curves analysis for IVIM parameters f, D and $D*$ in contrast enhanced part of brain tumors HGG, metastasis and meningioma. On the left: HGG and metastasis, in the middle: HGG and meningioma, on the right: metastasis and meningioma.

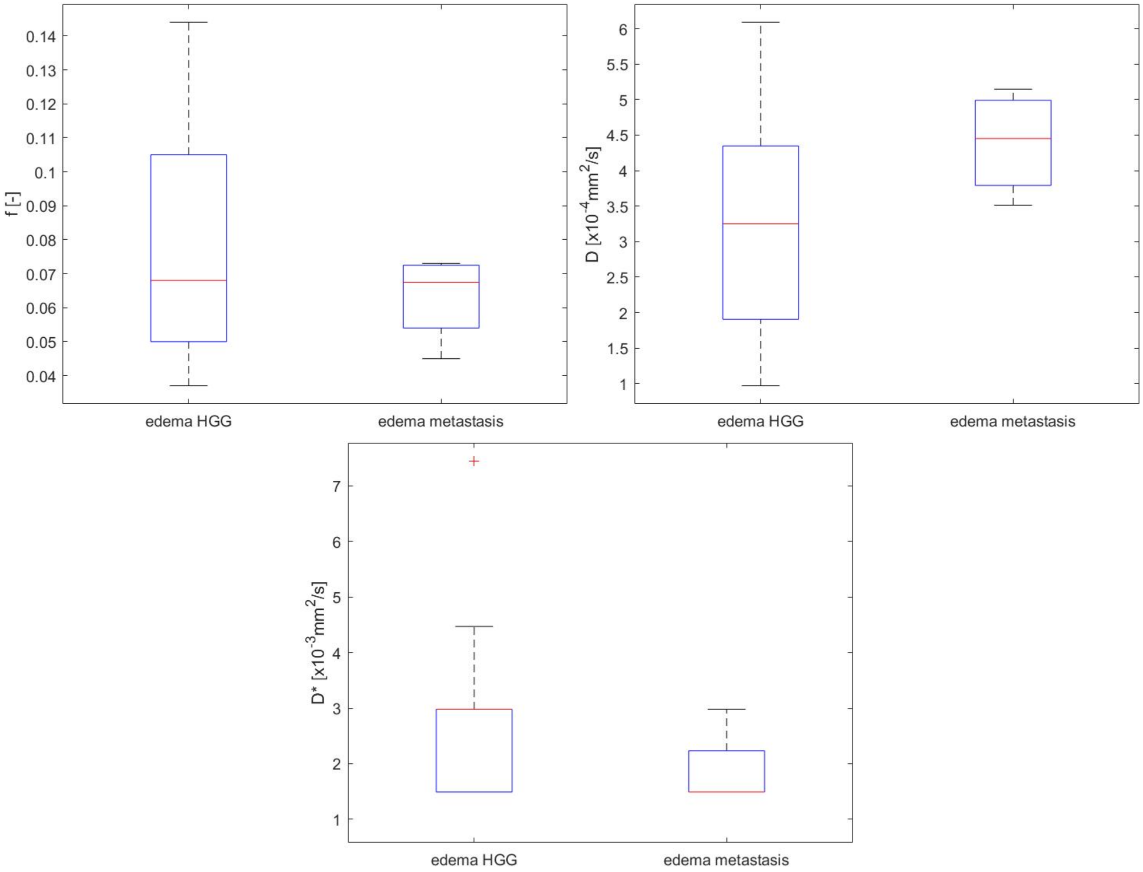

Figure C.61: Box plots of IVIM parameters f, D and $D*$ in brain edema of brain tumors HGG (n=10) and metastasis (n=4).

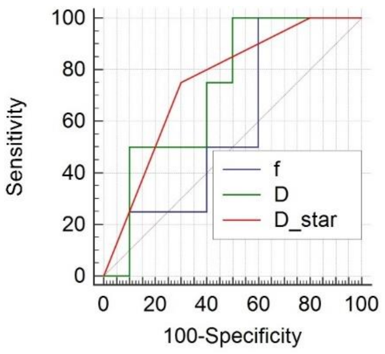

Figure C.62: ROC curves analysis for IVIM parameters f, D and $D*$ in edema of brain tumors HGG and metastasis.

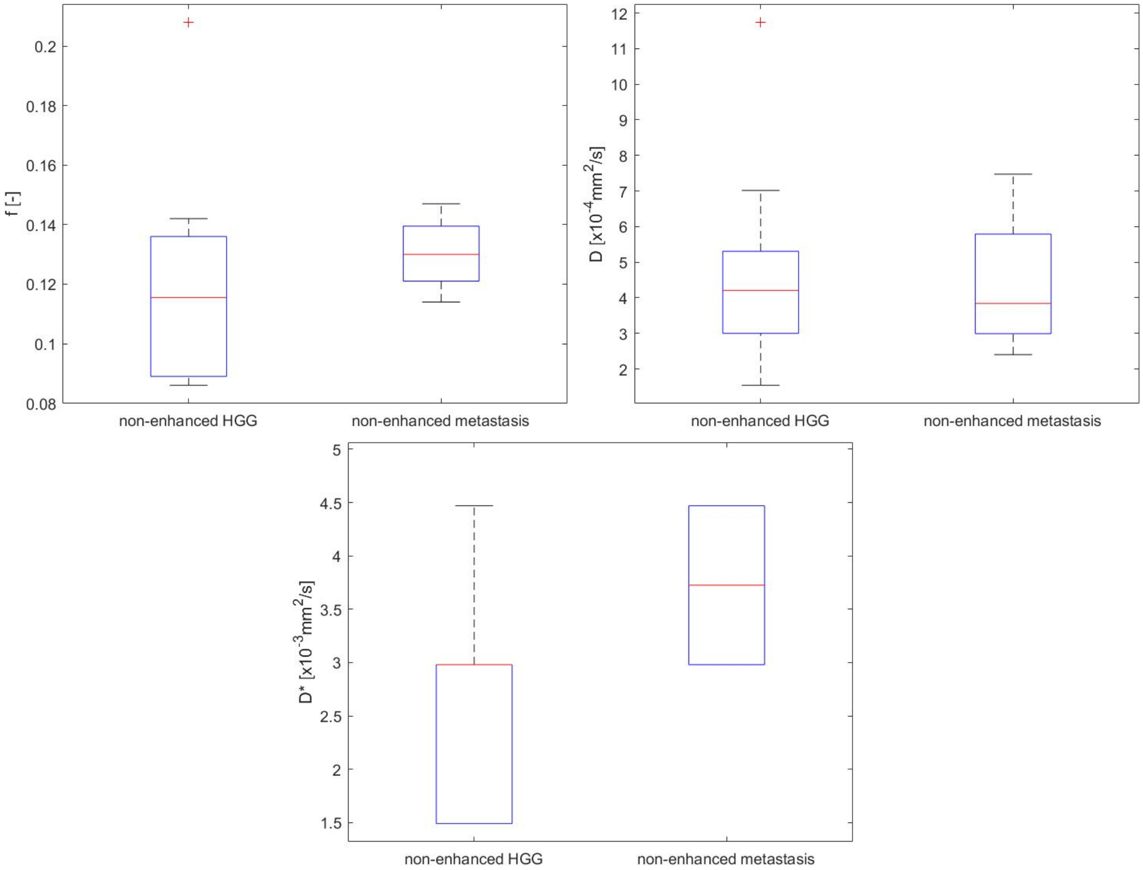

Figure C.63: Box plots of IVIM parameters f, D and $D*$ in non-enhanced part of brain tumors HGG (n=10) and metastasis (n=4).

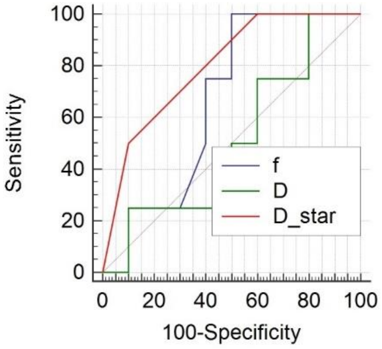

Figure C.64: ROC curves analysis for IVIM parameters f, D and $D*$ in contrast not enhanced part of brain tumors HGG and metastasis.

C.III. Different IVIM fitting algorithms

C.III.I. Jointly fit D, f and $D*$

	parameter	**edema (n=15)**	**enhanced tumor (n=20)**	**non-enhanced tumor (n=15)**
f [-]	mean	0.685	0.460	0.659
	std	0.130	0.163	0.116
	median	0.742	0.476	0.701
	Q 25%	0.644	0.378	0.629
	Q 75%	0.777	0.583	0.747
	IQR	0.132	0.205	0.117
	maximum	0.818	0.689	0.770
	minimum	0.400	0.193	0.353
	range	0.418	0.496	0.417
D [x 10^{-4} mm^2/s]	mean	7.476	4.754	6.841
	std	2.273	1.746	1.825
	median	7.635	4.330	6.517
	Q 25%	5.888	3.512	5.818
	Q 75%	9.472	5.395	7.791
	IQR	3.584	1.883	1.972
	maximum	10.720	8.295	11.359
	minimum	3.595	2.238	4.353
	range	7.125	6.057	7.006
D* [x 10^{-3} mm^2/s]	mean	29.919	66.978	37.261
	std	24.948	35.030	26.253
	median	20.469	53.426	25.501
	Q 25%	7.493	40.401	17.805
	Q 75%	47.196	89.897	55.771
	IQR	39.703	49.496	37.966
	maximum	78.894	134.132	103.456
	minimum	5.591	25.148	9.044
	range	73.303	108.984	94.412

Table C.17: Calculated statistical parameters for IVIM parameters f, D and $D*$ in brain edema, contrast enhanced and contrast not enhanced part of a brain tumor. Diffusion images correction implemented in SPM, without denoising, fitting algorithm: Jointly fit D, f and D.*

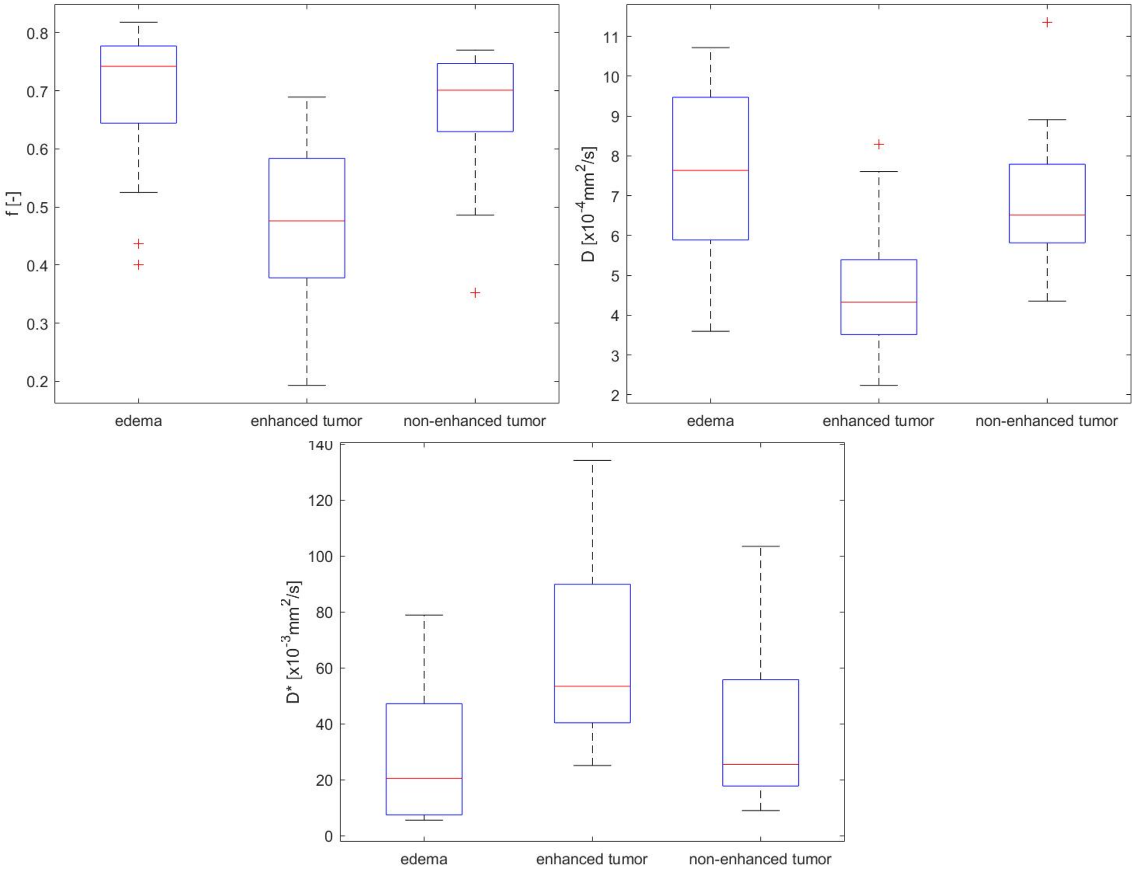

Figure C.65: Box plots of IVIM parameters f, D and $D*$ in brain edema (n=15), contrast enhanced (n=20) and contrast not enhanced (n=15) part of brain tumors.

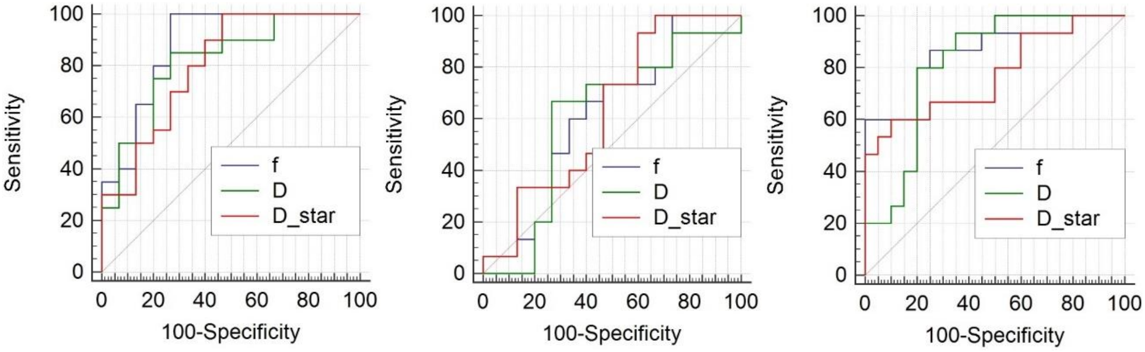

Figure C.66: ROC curves analysis for IVIM parameters f, D and $D*$ in brain edema, contrast enhanced and contrast not enhanced part of brain tumors. On the left: brain edema and contrast enhanced part, in the middle: brain edema and contrast not enhanced part, on the right: contrast enhanced and contrast not enhanced part of brain tumors.

	parameter	enhanced HGG (n=10)	enhanced metastasis (n=4)	enhanced meningioma (n=6)	edema HGG (n=10)	edema metastasis (n=4)	non-enhanced HGG (n=10)	non-enhanced metastasis (n=4)
f [-]	mean	0.562	0.474	0.281	0.677	0.747	0.708	0.612
	std	0.118	0.058	0.122	0.146	0.035	0.065	0.090
	median	0.576	0.472	0.221	0.738	0.744	0.725	0.632
	Q 25%	0.477	0.437	0.198	0.628	0.724	0.691	0.558
	Q 75%	0.683	0.512	0.360	0.785	0.770	0.757	0.667
	IQR	0.206	0.074	0.162	0.157	0.045	0.066	0.108
	maximum	0.689	0.549	0.497	0.818	0.793	0.770	0.701
	minimum	0.396	0.405	0.193	0.400	0.707	0.568	0.486
	range	0.293	0.144	0.304	0.418	0.086	0.202	0.215
D [x 10^{-4} mm^2/s]	mean	5.457	5.085	3.363	7.622	7.911	7.379	6.003
	std	1.931	1.186	0.794	2.577	0.668	1.974	0.758
	median	4.891	4.809	3.326	7.685	7.904	7.109	6.160
	Q 25%	3.901	4.307	2.958	5.469	7.390	6.088	5.410
	Q 75%	7.609	5.863	3.704	9.781	8.432	8.790	6.596
	IQR	3.708	1.556	0.746	4.312	1.042	2.702	1.186
	maximum	8.295	6.751	4.628	10.720	8.691	11.359	6.675
	minimum	3.382	3.973	2.238	3.595	7.145	4.353	5.017
	range	4.913	2.778	2.390	7.125	1.546	7.006	1.658
D* [x 10^{-3} mm^2/s]	mean	51.539	47.933	105.406	29.734	18.138	29.316	40.576
	std	20.493	21.007	33.215	24.022	13.741	19.595	19.463
	median	45.795	47.098	119.584	25.817	14.079	24.601	40.308
	Q 25%	38.776	31.058	81.572	7.158	8.422	12.023	23.758
	Q 75%	58.010	64.808	127.942	48.916	27.853	39.178	57.394
	IQR	19.234	33.750	46.370	41.758	19.431	27.155	33.636
	maximum	98.222	72.389	134.132	74.609	37.458	66.695	58.764
	minimum	29.034	25.148	49.625	5.591	6.935	9.044	22.924
	range	69.188	47.241	84.507	69.018	30.523	57.651	35.840

Table C.18: *Calculated statistical parameters for IVIM parameters f, D and $D*$ in contrast enhanced part of brain tumors HGG, metastasis and meningioma, in brain edema of brain tumors HGG and metastasis, in contrast not enhanced part of brain tumors HGG and metastasis. Diffusion images correction implemented in SPM, without denoising, fitting algorithm: Jointly fit D, f and D*.*

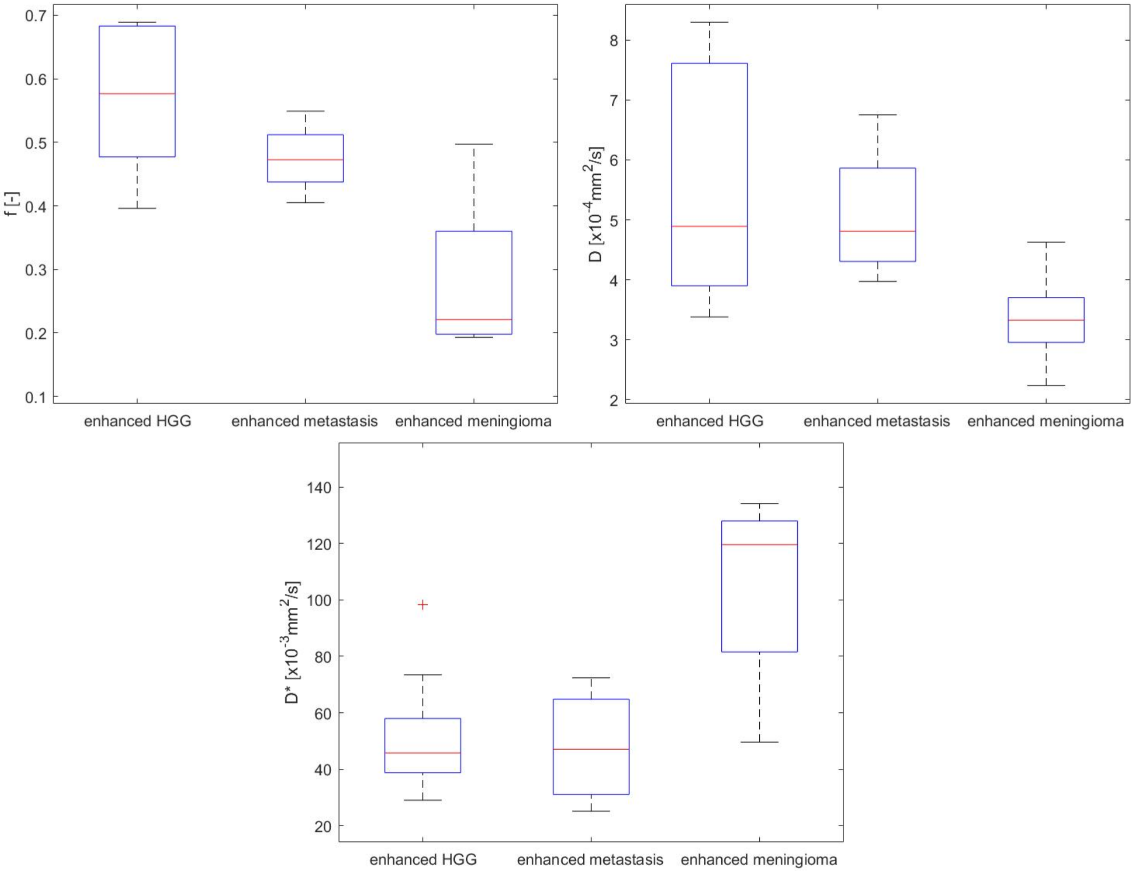

Figure C.67: Box plots of IVIM parameters f, D and $D*$ in contrast enhanced part of brain tumors HGG (n=10), metastasis (n=4) and meningioma (n=6).

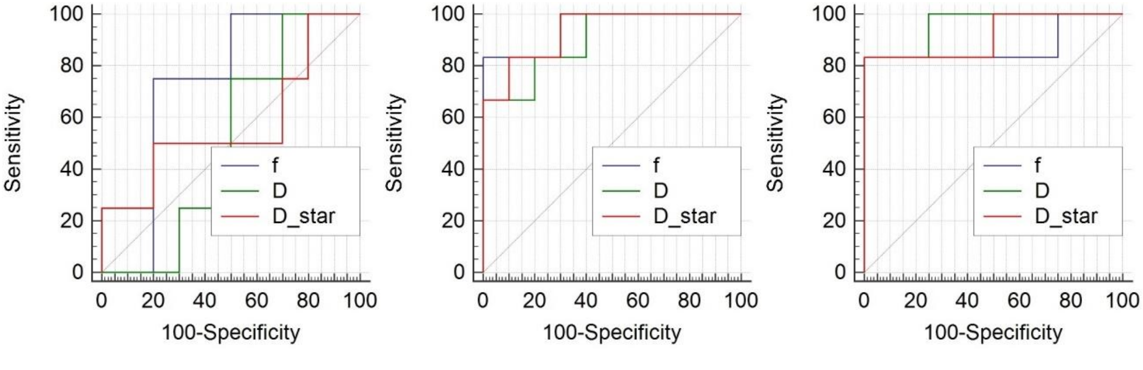

Figure C.68: ROC curves analysis for IVIM parameters f, D and $D*$ in contrast enhanced part of brain tumors HGG, metastasis and meningioma. On the left: HGG and metastasis, in the middle: HGG and meningioma, on the right: metastasis and meningioma.

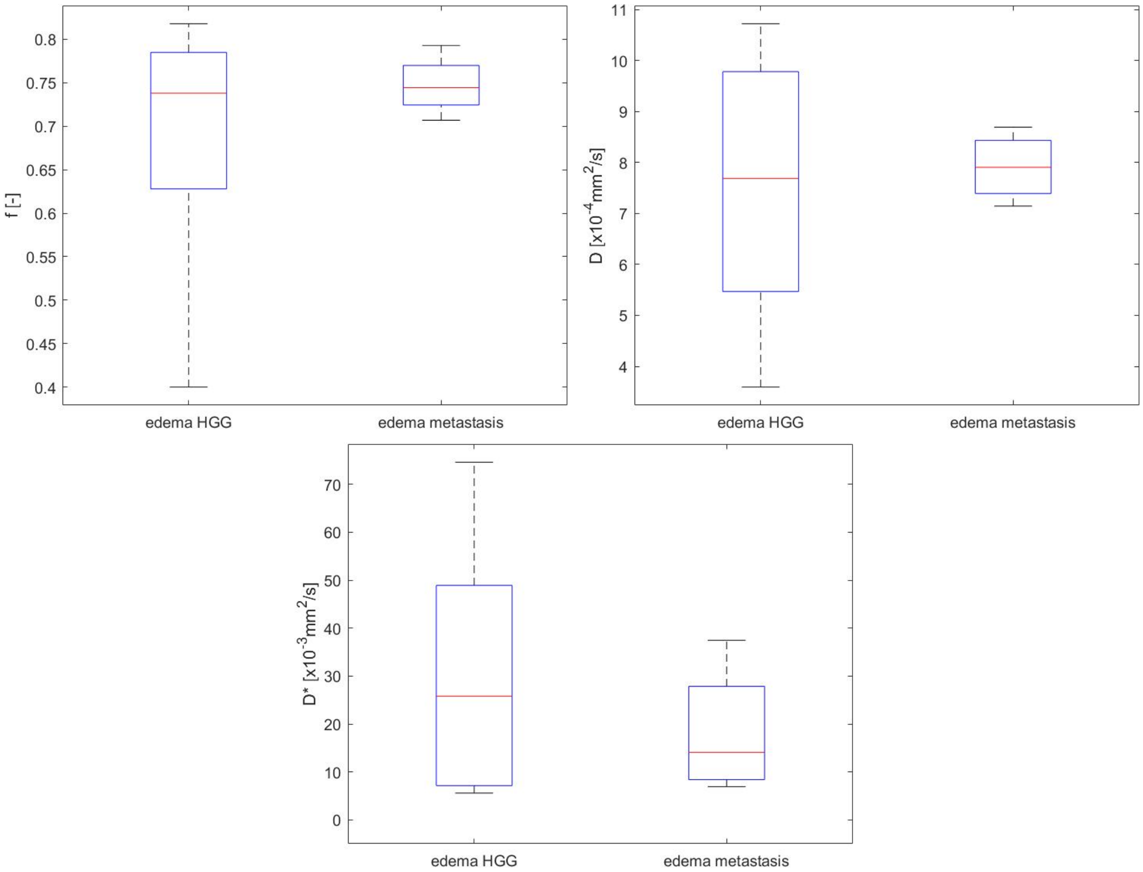

Figure C.69: Box plots of IVIM parameters f, D and $D*$ in brain edema of brain tumors HGG (n=10) and metastasis (n=4).

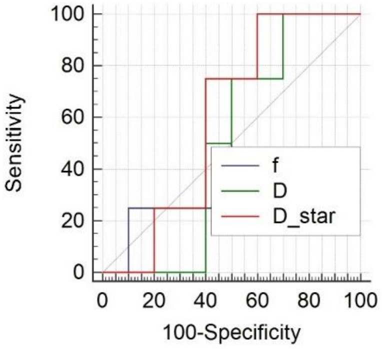

Figure C.70: ROC curves analysis for IVIM parameters f, D and $D*$ in edema of brain tumors HGG and metastasis.

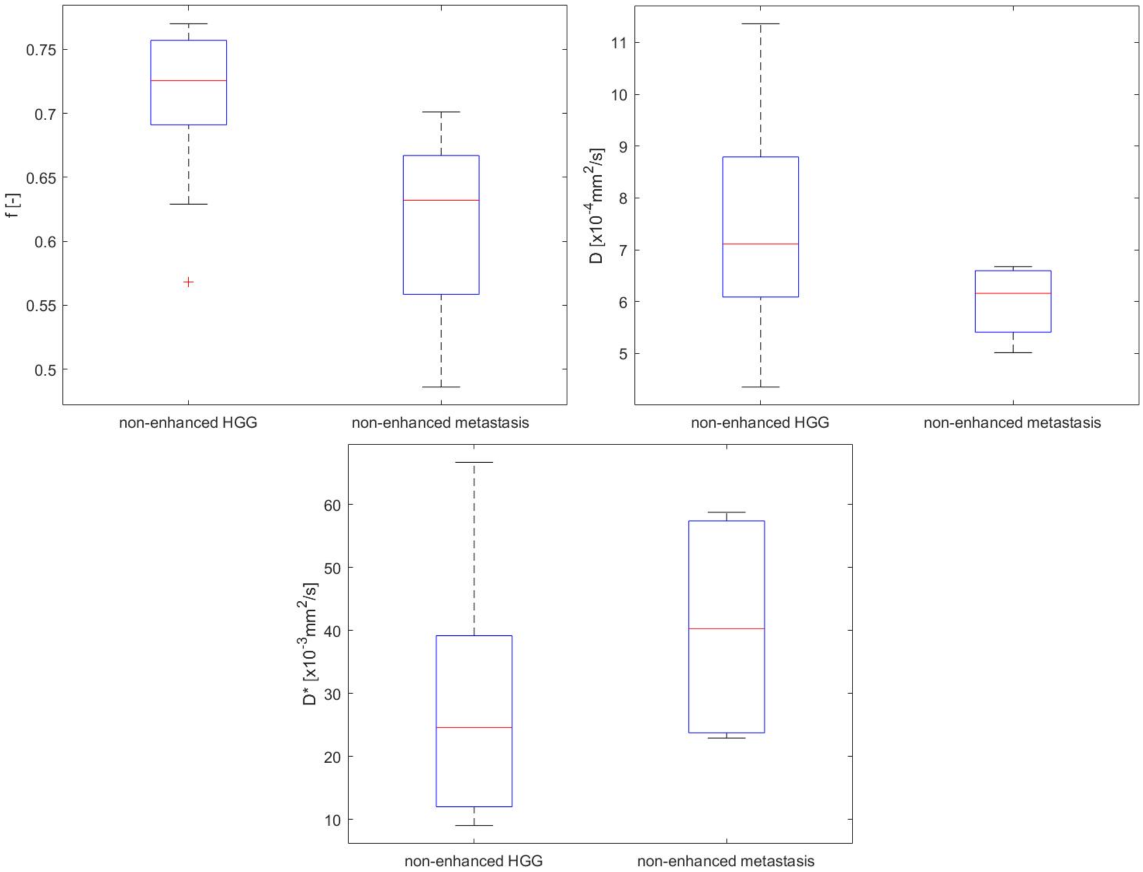

Figure C.71: Box plots of IVIM parameters f, D and $D*$ in non-enhanced part of brain tumors HGG (n=10) and metastasis (n=4).

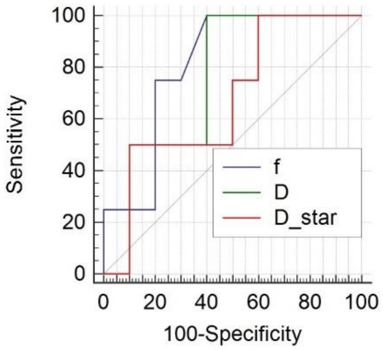

Figure C.72: ROC curves analysis for IVIM parameters f, D and $D*$ in contrast not enhanced part of brain tumors HGG and metastasis.

C.III.II. Fit D and f with fixed $D*$ value (0.07 $[\frac{s}{mm^2}]$)

	parameter	**edema (n=15)**	**enhanced tumor (n=20)**	**non-enhanced tumor (n=15)**
f [-]	mean	0.060	0.084	0.069
	std	0.023	0.029	0.021
	median	0.055	0.075	0.066
	Q 25%	0.045	0.068	0.058
	Q 75%	0.062	0.102	0.079
	IQR	0.017	0.034	0.020
	maximum	0.121	0.174	0.129
	minimum	0.039	0.045	0.038
	range	0.082	0.129	0.091
D [x 10^{-4} mm^2/s]	mean	4.842	4.680	7.514
	std	1.616	1.996	4.179
	median	5.268	4.660	6.875
	Q 25%	3.887	3.044	4.597
	Q 75%	5.544	5.899	9.144
	IQR	1.657	2.855	4.546
	maximum	7.657	8.446	16.681
	minimum	1.550	1.241	2.417
	range	6.107	7.205	14.264

Table C.19: Calculated statistical parameters for IVIM parameters f and D in brain edema, contrast enhanced and contrast not enhanced part of a brain tumor. Diffusion images correction implemented in SPM, without denoising, fitting algorithm: Fit D and f with fixed D value* (0.07 $[\frac{s}{mm^2}]$).

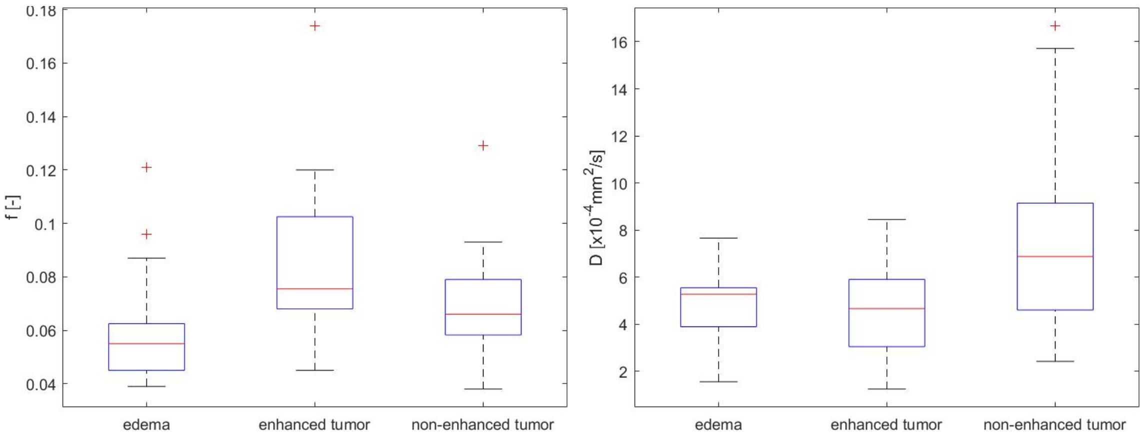

Figure C.73: Box plots of IVIM parameters f and D in brain edema (n=15), contrast enhanced (n=20) and contrast not enhanced (n=15) part of brain tumors.

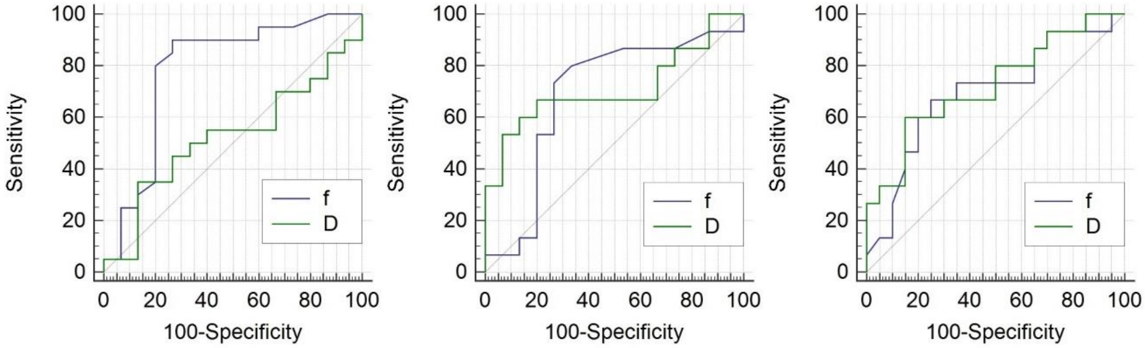

Figure C.74: ROC curves analysis for IVIM parameters f and D in brain edema, contrast enhanced and contrast not enhanced part of brain tumors. On the left: brain edema and contrast enhanced part, in the middle: brain edema and contrast not enhanced part, on the right: contrast enhanced and contrast not enhanced pat of brain tumors.

	parameter	enhanced HGG (n=10)	enhanced metastasis (n=4)	enhanced meningioma (n=6)	edema HGG (n=10)	edema metastasis (n=4)	non-enhanced HGG (n=10)	non-enhanced metastasis (n=4)
f [-]	mean	0.065	0.088	0.112	0.062	0.048	0.059	0.078
	std	0.011	0.018	0.036	0.026	0.006	0.012	0.012
	median	0.069	0.085	0.112	0.056	0.046	0.059	0.077
	Q 25%	0.059	0.074	0.087	0.045	0.044	0.057	0.068
	Q 75%	0.074	0.103	0.120	0.064	0.053	0.066	0.089
	IQR	0.015	0.029	0.033	0.019	0.009	0.009	0.021
	maximum	0.079	0.113	0.174	0.121	0.058	0.082	0.093
	minimum	0.045	0.071	0.067	0.039	0.043	0.038	0.066
	range	0.034	0.042	0.107	0.082	0.015	0.044	0.027
D [x 10^{-4} mm^2/s]	mean	4.754	6.736	3.186	4.431	5.764	7.456	8.117
	std	1.664	1.614	1.589	1.800	0.843	4.168	5.269
	median	4.981	6.853	2.995	4.829	5.734	7.065	6.594
	Q 25%	3.587	5.453	2.158	3.594	5.174	4.578	4.916
	Q 75%	5.448	8.019	3.986	5.362	6.355	9.529	11.318
	IQR	1.861	2.566	1.828	1.768	1.181	4.951	6.402
	maximum	7.862	8.446	5.744	7.657	6.815	16.681	15.714
	minimum	2.356	4.793	1.241	1.550	4.776	2.417	3.565
	range	5.506	3.653	4.503	6.107	2.039	14.264	12.149

Table C.20: *Calculated statistical parameters for IVIM parameters* f, D *and* $D*$ *in contrast enhanced part of brain tumors HGG, metastasis and meningioma, in brain edema of brain tumors HGG and metastasis, in contrast not enhanced part of brain tumors HGG and metastasis. Diffusion images correction implemented in SPM, without denoising, fitting algorithm: Fit D and f with fixed D* value* (0.07 $[\frac{s}{mm^2}]$).

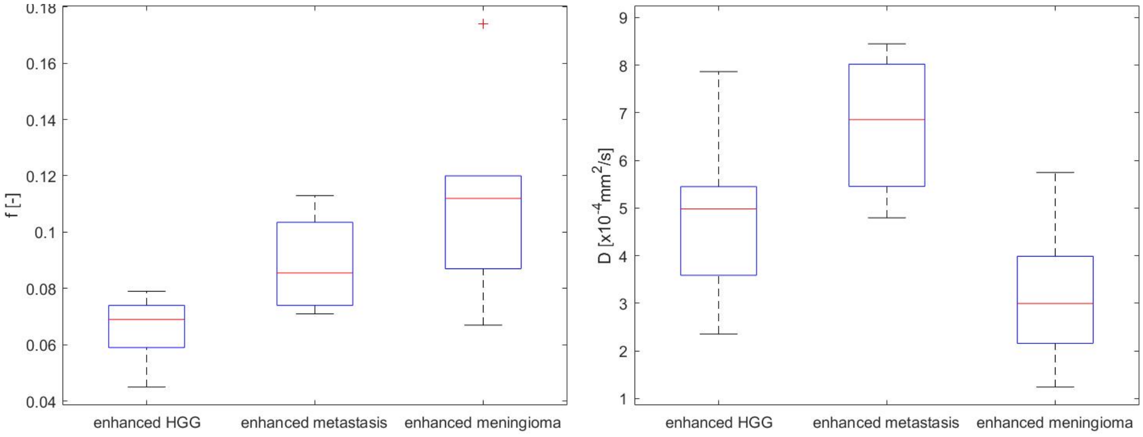

Figure C.75: Box plots of IVIM parameters f and D in contrast enhanced part of brain tumors HGG (n=10), metastasis (n=4) and meningioma (n=6).

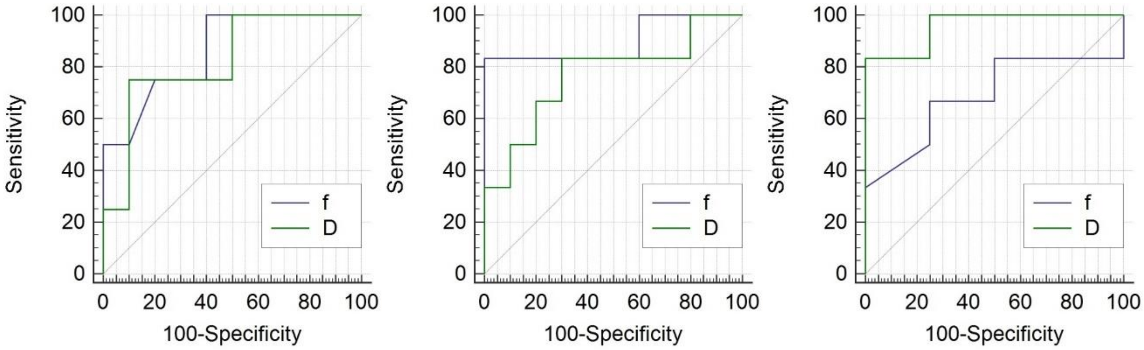

Figure C.76: ROC curves analysis for IVIM parameters f and D in contrast enhanced part of brain tumors HGG, metastasis and meningioma. On the left: HGG and metastasis, in the middle: HGG and meningioma, on the right: metastasis and meningioma.

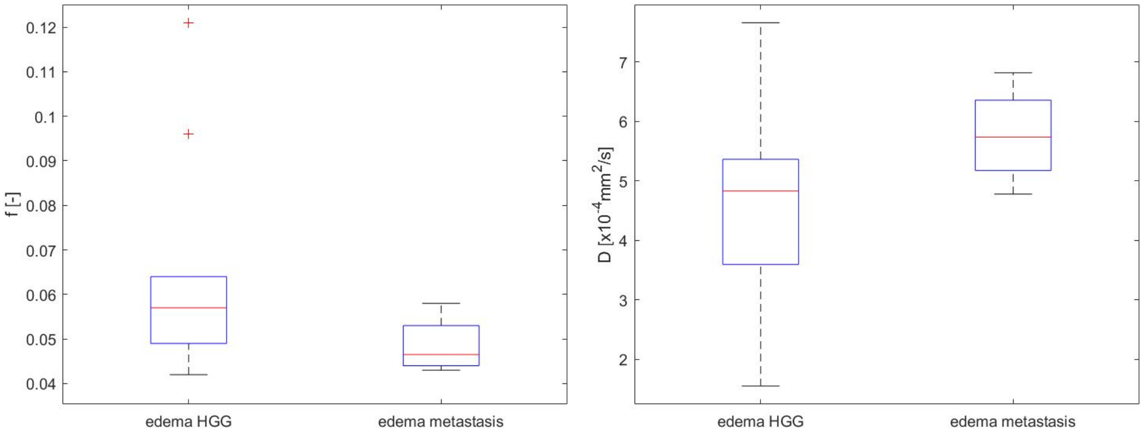

Figure C.77: Box plots of IVIM parameters f and D in brain edema of brain tumors HGG (n=10) and metastasis (n=4).

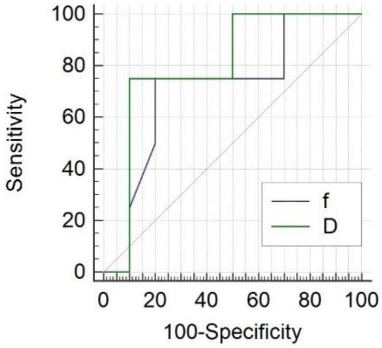

Figure C.78: ROC curves analysis for IVIM parameters f and D in edema of brain tumors HGG and metastasis.

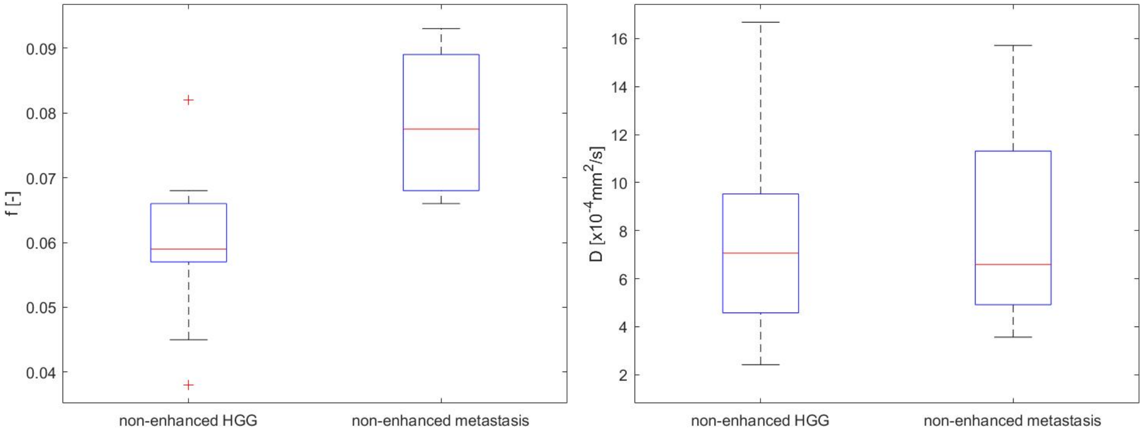

Figure C.79: Box plots of IVIM parameters f and D in non-enhanced part of brain tumors HGG (n=10) and metastasis (n=4).

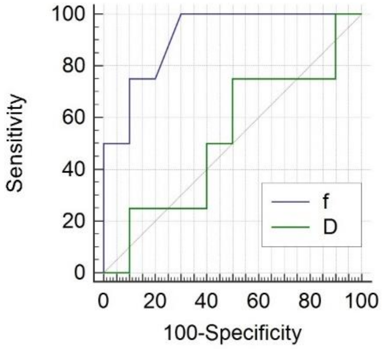

Figure C.80: ROC curves analysis for IVIM parameters f and D in contrast not enhanced part of brain tumors HGG and metastasis.

C.III.III. Fit D and f (with high b), then fit $D*$

The results acquired with the fitting algorithm *Fit D and f (with high b), then fit D** are the same as the results given in the section C.I.II.

14.4. Appendix D

In this appendix section the results acquired from constructing the ROC curves by applying FSL, BrainSuite and without any diffusion data correction approaches (without and after applying the denoising approach) are shown.

D.I. Different DWI correction tools

mean value (standard deviation)		**FSL**	**BrainSuite**	**Without correction**
enh. HGG (n=10)	f [-]	0.14 (0.02)	0.14 (0.02)	0.14 (0.03)
	D [x 10^{-4} mm^2/s]	3.03 (1.01)	3.49 (1.33)	3.24 (1.08)
	D^* [x 10^{-3} mm^2/s]	8.60 (3.53)	9.11 (3.61)	9.09 (4.00)
enh. meta (n=4)	f [-]	0.18 (0.04)	0.17 (0.02)	0.18 (0.03)
	D [x 10^{-4} mm^2/s]	3.83 (0.71)	3.90 (0.70)	4.17 (0.62)
	D^* [x 10^{-3} mm^2/s]	8.20 (3.10)	11.92 (2.72)	10.80 (2.82)
enh. meni. (n=6)	f [-]	0.17 (0.02)	0.19 (0.05)	0.18 (0.03)
	D [x 10^{-4} mm^2/s]	1.96 (0.51)	2.33 (0.97)	1.98 (0.53)
	D^* [x 10^{-3} mm^2/s]	24.59 (8.98)	34.77 (15.67)	28.49 (9.56)
edema HGG (n=10)	f [-]	0.12 (0.04)	0.13 (0.05)	0.12 (0.04)
	D [x 10^{-4} mm^2/s]	3.13 (1.28)	3.45 (1.42)	3.53 (1.48)
	D^* [x 10^{-3} mm^2/s]	7.75 (6.84)	7.45 (5.58)	7.30 (5.73)
edema meta. (n=4)	f [-]	0.11 (0.02)	0.10 (0.02)	0.10 (0.01)
	D [x 10^{-4} mm^2/s]	3.98 (0.49)	4.57 (0.68)	4.53 (0.70)
	D^* [x 10^{-3} mm^2/s]	4.10 (1.43)	4.47 (1.22)	4.47 (1.22)
non-enh HGG (n=10)	f [-]	0.15 (0.03)	0.16 (0.03)	0.15 (0.03)
	D [x 10^{-4} mm^2/s]	4.60 (2.59)	5.25 (2.79)	4.92 (2.63)
	D^* [x 10^{-3} mm^2/s]	5.66 (2.88)	6.79 (3.17)	6.71 (3.08)
non-enh meta (n=4)	f [-]	0.18 (0.02)	0.16 (0.02)	0.17 (0.02)
	D [x 10^{-4} mm^2/s]	4.36 (1.83)	4.22 (1.57)	4.75 (1.87)
	D^* [x 10^{-3} mm^2/s]	7.08 (2.24)	10.06 (3.30)	9.31 (3.07)

Table D.1: Comparison of IVIM parameters in contrast enhanced part of tumors HGG, metastasis and meningioma, in edema of tumors HGG and metastasis, in contrast non-enhanced part of tumors HGG and metastasis. Values expressed as mean value (standard deviation). Images correction implemented in FSL, BrainSuite and without diffusion correction. Without denoising. Fit D and f (with high b), then fit D.*

- **FSL DWI correction tool**

		p-value	AUC	*p* (AUC=0.5)	Youden index	Cut-off value	Sensit. [%]	Specific. [%]
edema × enhanced	f	0.004	0.85	<0.001	0.65	0.13 [-]	85.00	80.00
	D	0.197	0.64	0.172	0.33	3.64 [x 10^{-4} mm^2/s]	80.00	53.33
	$D*$	0.026	0.77	0.002	0.53	5.96 [x 10^{-3} mm^2/s]	80.00	73.33
edema × non-enhan.	f	0.003	0.85	<0.001	0.67	0.13 [-]	93.33	73.33
	D	0.111	0.65	0.135	0.33	4.09 [x 10^{-4} mm^2/s]	46.67	86.67
	$D*$	0.866	0.59	0.394	0.27	4.47 [x 10^{-3} mm^2/s]	66.67	60.00
enhanced × non-enhan.	f	0.671	0.54	0.736	0.24	0.16 [-]	60.00	65.00
	D	0.017	0.75	0.003	0.46	3.64 [x 10^{-4} mm^2/s]	66.67	80.00
	$D*$	0.011	0.76	0.003	0.50	7.45 [x 10^{-3} mm^2/s]	80.00	70.00
enhan. HGG × enh. meta.	f	0.066	0.98	<0.001	0.90	0.15 [-]	100.00	90.00
	D	0.130	0.73	0.113	0.60	2.88 [x 10^{-4} mm^2/s]	100.00	60.00
	$D*$	0.837	0.53	0.895	0.15	11.55 [x 10^{-3} mm^2/s]	75.00	10.00
enhan. HGG × enh. meni.	f	0.018	0.87	0.002	0.73	0.15 [-]	83.33	90.00
	D	0.015	0.82	0.005	0.63	2.27 [x 10^{-4} mm^2/s]	83.33	80.00
	$D*$	0.006	0.95	<0.001	0.83	14.90 [x 10^{-3} mm^2/s]	83.33	100.00
enh. meta × enh. meni	f	0.463	0.63	0.556	0.33	0.18 [-]	83.33	50.00
	D	0.006	1.00	<0.001	1.00	2.75 [x 10^{-4} mm^2/s]	100.00	100.00
	$D*$	0.005	0.96	<0.001	0.83	11.92 [x 10^{-3} mm^2/s]	83.33	100.00
edema HGG × edem. meta	f	0.799	0.60	0.617	0.45	0.11 [-]	75.00	70.00
	D	0.099	0.73	0.131	0.50	2.75 [x 10^{-4} mm^2/s]	100.00	50.00
	$D*$	0.138	0.65	0.342	0.30	5.96 [x 10^{-3} mm^2/s]	100.00	30.00
n-enh. HGG × n-enh. meta	f	0.092	0.80	0.017	0.60	0.14 [-]	100.00	60.00
	D	0.847	0.53	0.891	0.25	3.81 [x 10^{-4} mm^2/s]	75.00	50.00
	$D*$	0.358	0.68	0.223	0.50	4.47 [x 10^{-3} mm^2/s]	100.00	50.00

Table D.2: The p-value indicating the statistically significant difference, the values of AUC, p-value (AUC=0.5), Youden index, suggested cut-off, sensitivity and specificity values for IVIM parameters f, D and $D*$ derived from the ROC curve in different brain tissue types and different brain tumor types. Statistical difference $p<0.05$ highlighted with a gray color. Diffusion images correction implemented in FSL, without denoising, fitting algorithm: Fit D and f (with high b), then fit D.*

- **BrainSuite DWI correction tool**

		p-value	AUC	*p* (AUC=0.5)	Youden index	Cut-off value	Sensit. [%]	Specific. [%]
edema × enhanced	f	0.003	0.85	<0.001	0.75	0.13 [-]	89.47	85.71
	D	0.185	0.65	0.141	0.36	3.91 [x 10^{-4} mm^{2}/s]	78.95	57.14
	$D*$	0.007	0.81	<0.001	0.61	5.96 [x 10^{-3} mm^{2}/s]	89.47	71.43
edema × non-enhan.	f	0.011	0.86	<0.001	0.71	0.12 [-]	100.00	71.43
	D	0.188	0.60	0.389	0.29	4.68 [x 10^{-4} mm^{2}/s]	42.86	85.71
	$D*$	0.361	0.67	0.113	0.43	4.47 [x 10^{-3} mm^{2}/s]	85.71	57.14
enhanced × non-enhan.	f	0.884	0.50	0.971	0.15	0.17 [-]	78.57	36.84
	D	0.031	0.72	0.016	0.36	3.25 [x 10^{-4} mm^{2}/s]	78.57	57.89
	$D*$	0.020	0.75	0.005	0.47	5.96 [x 10^{-3} mm^{2}/s]	57.14	89.47
enhan. HGG × enh. meta.	f	0.092	0.86	<0.001	0.78	0.15 [-]	100.00	77.78
	D	0.478	0.67	0.291	0.56	3.15 [x 10^{-4} mm^{2}/s]	100.00	55.56
	$D*$	0.161	0.75	0.076	0.42	8.94 [x 10^{-3} mm^{2}/s]	75.00	66.67
enhan. HGG × enh. meni.	f	0.071	0.81	0.063	0.72	0.16 [-]	83.33	88.89
	D	0.073	0.74	0.095	0.50	2.77 [x 10^{-4} mm^{2}/s]	83.33	66.67
	$D*$	0.010	0.97	<0.001	0.83	14.9 [x 10^{-3} mm^{2}/s]	83.33	100.00
enh. meta × enh. meni	f	0.425	0.71	0.286	0.58	0.17 [-]	83.33	75.00
	D	0.018	0.92	<0.001	0.83	2.77 [x 10^{-4} mm^{2}/s]	83.33	100.00
	$D*$	0.015	0.94	<0.001	0.83	14.9 [x 10^{-3} mm^{2}/s]	83.33	100.00
edema HGG × edem. meta	f	0.165	0.68	0.273	0.44	0.11 [-]	100.00	44.44
	D	0.082	0.81	0.026	0.64	4.53 [x 10^{-4} mm^{2}/s]	75.00	88.89
	$D*$	0.160	0.67	0.279	0.33	5.96 [x 10^{-3} mm^{2}/s]	100.00	33.33
n.-enh. HGG × n-enh. meta	f	0.609	0.65	0.363	0.42	0.16 [-]	75.00	66.67
	D	0.419	0.61	0.543	0.42	3.97 [x 10^{-4} mm^{2}/s]	75.00	66.67
	$D*$	0.150	0.78	0.043	0.53	5.96 [x 10^{-3} mm^{2}/s]	75.00	77.78

Table D.3: The p-value indicating the statistically significant difference, the values of AUC, p-value (AUC=0.5), Youden index, suggested cut-off, sensitivity and specificity values for IVIM parameters f, D and $D*$ derived from the ROC curve in different brain tissue types and different brain tumor types. Statistical difference p<0.05 highlighted with a gray color. Diffusion images correction implemented in BrainSuite, without denoising, fitting algorithm: Fit D and f (with high b), then fit D.*

- **Without diffusion images correction**

		***p*-value**	**AUC**	***p* (AUC=0.5)**	**Youden index**	**Cut-off value**	**Sensit. [%]**	**Specific. [%]**
edema × enhanced	f	0.001	0.83	<0.001	0.65	0.13 [-]	85.00	80.00
	D	0.087	0.67	0.077	0.35	3.75 [x 10^{-4} mm^2/s]	75.00	60.00
	$D*$	0.005	0.80	<0.001	0.58	5.96 [x 10^{-3} mm^2/s]	85.00	73.33
edema × non-enhan.	f	0.003	0.83	<0.001	0.67	0.14 [-]	80.00	86.67
	D	0.181	0.60	0.376	0.27	4.86 [x 10^{-4} mm^2/s]	40.00	86.67
	$D*$	0.379	0.66	0.145	0.40	4.47 [x 10^{-3} mm^2/s]	80.00	60.00
enhanced × non-enhan.	f	0.713	0.53	0.784	0.15	0.17 [-]	40.00	75.00
	D	0.015	0.75	0.003	0.47	3.81 [x 10^{-4} mm^2/s]	66.67	80.00
	$D*$	0.017	0.74	0.005	0.45	8.94 [x 10^{-3} mm^2/s]	80.00	65.00
enhan. HGG × enh. meta.	f	0.093	0.80	0.017	0.70	0.15 [-]	100.00	70.00
	D	0.072	0.78	0.035	0.60	3.22 [x 10^{-4} mm^2/s]	100.00	60.00
	$D*$	0.392	0.60	0.539	0.40	7.45 [x 10^{-3} mm^2/s]	100.00	40.00
enhan. HGG × enh. meni.	f	0.029	0.84	0.001	0.53	0.15 [-]	83.33	70.00
	D	0.008	0.88	<0.001	0.70	2.67 [x 10^{-4} mm^2/s]	100.00	70.00
	$D*$	0.003	0.99	<0.001	0.90	11.92 [x 10^{-3} mm^2/s]	100.00	90.00
enh. meta × enh. meni	f	0.965	0.50	1.000	0.42	0.16 [-]	66.67	75.00
	D	0.001	1.00	<0.001	1.00	2.67 [x 10^{-4} mm^2/s]	100.00	100.00
	$D*$	0.005	1.00	<0.001	1.00	14.90 [x 10^{-3} mm^2/s]	100.00	100.00
edema HGG × edem. meta	f	0.163	0.63	0.434	0.50	0.11 [-]	100.00	50.00
	D	0.118	0.70	0.211	0.50	2.91 [x 10^{-4} mm^2/s]	100.00	50.00
	$D*$	0.167	0.61	0.470	0.30	5.96 [x 10^{-3} mm^2/s]	100.00	30.00
n.-enh. HGG × n-enh. meta	f	0.270	0.70	0.213	0.40	0.14 [-]	100.00	40.00
	D	0.894	0.50	1.00	0.25	4.45 [x 10^{-4} mm^2/s]	25.00	50.00
	$D*$	0.205	0.76	0.081	0.55	7.45 [x 10^{-3} mm^2/s]	75.00	80.00

Table D.4: The p-value indicating the statistically significant difference, the values of AUC, p-value (AUC=0.5), Youden index, suggested cut-off, sensitivity and specificity values for IVIM parameters f, D and $D*$ derived from the ROC curve in different brain tissue types and different brain tumor types. Statistical difference $p<0.05$ highlighted with a gray color. No diffusion images correction, without denoising, fitting algorithm: Fit D and f (with high b), then fit D.*

D.II. DWI denoising

mean value (standard deviation)		**FSL**	**BrainSuite**	**Without correction**
enh. HGG (n=10)	*f* [-]	0.11 (0.02)	0.11 (0.02)	0.11 (0.03)
	D [x 10^{-4} mm^2/s]	2.76 (1.02)	3.13 (1.39)	2.86 (1.11)
	*D** [x 10^{-3} mm^2/s]	3.43 (1.41)	4.30 (1.74)	3.73 (1.61)
enh. meta (n=4)	*f* [-]	0.16 (0.02)	0.14 (0.01)	0.14 (0.01)
	D [x 10^{-4} mm^2/s]	3.43 (0.75)	3.84 (0.78)	3.71 (0.62)
	*D** [x 10^{-3} mm^2/s]	4.10 (2.24)	5.96 (3.22)	5.22 (1.92)
enh. meni. (n=6)	*f* [-]	0.14 (0.02)	0.17 (0.08)	0.16 (0.05)
	D [x 10^{-4} mm^2/s]	1.72 (0.47)	2.59 (1.83)	1.75 (0.54)
	*D** [x 10^{-3} mm^2/s]	13.41 (6.66)	18.13 (10.80)	13.41 (5.73)
edema HGG (n=10)	*f* [-]	0.09 (0.04)	0.09 (0.05)	0.08 (0.04)
	D [x 10^{-4} mm^2/s]	2.97 (1.41)	3.14 (1.58)	3.21 (1.65)
	*D** [x 10^{-3} mm^2/s]	3.28 (2.41)	3.15 (1.89)	3.13 (1.78)
edema meta. (n=4)	*f* [-]	0.09 (0.02)	0.06 (0.01)	0.06 (0.01)
	D [x 10^{-4} mm^2/s]	3.87 (0.52)	4.44 (0.74)	4.39 (0.74)
	*D** [x 10^{-3} mm^2/s]	1.49 (0.00)	1.49 (0.00)	1.86 (0.75)
non-enh HGG (n=10)	*f* [-]	0.13 (0.03)	0.13 (0.03)	0.12 (0.04)
	D [x 10^{-4} mm^2/s]	4.47 (2.87)	5.09 (3.09)	4.71 (2.95)
	*D** [x 10^{-3} mm^2/s]	2.24 (1.05)	2.81 (1.38)	2.53 (1.01)
non-enh meta (n=4)	*f* [-]	0.15 (0.02)	0.13 (0.01)	0.13 (0.01)
	D [x 10^{-4} mm^2/s]	4.08 (2.01)	3.89 (1.77)	4.39 (2.17)
	*D** [x 10^{-3} mm^2/s]	2.61 (0.75)	4.84 (1.87)	3.73 (0.86)

Table D.5: Comparison of IVIM parameters f, D and $D*$ in contrast enhanced part of brain tumors HGG, metastasis and meningioma, in brain edema of brain tumors HGG and metastasis, in contrast non-enhanced part of brain tumors HGG and metastasis. Values expressed as mean value (standard deviation). Diffusion images correction implemented in FSL, BrainSuite and without diffusion correction. Denoising included. Fitting algorithm: Fit D and f (with high b), then fit D.*

- **FSL DWI correction tool**

		p-value	AUC	*p* (AUC=0.5)	Youden index	Cut-off value	Sensit. [%]	Specific. [%]
edema x enhanced	f	0.001	0.85	<0.001	0.63	0.10 [-]	90.00	73.33
	D	0.115	0.65	0.148	0.38	3.66 [x 10^{-4} mm^2/s]	85.00	53.33
	$D*$	0.031	0.75	0.003	0.43	1.49 [x 10^{-3} mm^2/s]	90.00	53.33
edema x non-enhan.	f	<0.001	0.89	<0.001	0.73	0.10 [-]	93.33	80.00
	D	0.158	0.61	0.288	0.27	4.16 [x 10^{-4} mm^2/s]	40.00	86.67
	$D*$	0.896	0.51	0.912	0.13	4.47 [x 10^{-3} mm^2/s]	6.67	80.00
enhanced x non-enhan.	f	0.554	0.54	0.681	0.17	0.11 [-]	86.67	30.00
	D	0.020	0.76	0.002	0.47	3.46 [x 10^{-4} mm^2/s]	66.67	80.00
	$D*$	0.030	0.77	<0.001	0.42	2.98 [x 10^{-3} mm^2/s]	86.67	55.00
enhan. HGG x enh. meta.	f	0.014	0.98	<0.001	0.90	0.13 [-]	100.00	90.00
	D	0.218	0.70	0.177	0.50	2.38 [x 10^{-4} mm^2/s]	100.00	50.00
	$D*$	0.607	0.55	0.777	0.25	5.96 [x 10^{-3} mm^2/s]	25.00	100.00
enhan. HGG x enh. meni.	f	0.018	0.84	0.003	0.66	0.14 [-]	66.67	100.00
	D	0.016	0.83	0.002	0.63	2.07 [x 10^{-4} mm^2/s]	83.33	80.00
	$D*$	0.014	0.99	<0.001	0.90	4.47 [x 10^{-3} mm^2/s]	100.00	90.00
enh. meta x enh. meni	f	0.433	0.63	0.532	0.33	0.12 [-]	33.33	100.00
	D	0.012	1.00	<0.001	1.00	2.35 [x 10^{-4} mm^2/s]	100.00	100.00
	$D*$	0.017	0.96	<0.001	0.83	7.45 [x 10^{-3} mm^2/s]	83.33	100.00
edema HGG x edem. meta	f	0.819	0.69	0.215	0.45	0.09 [-]	75.00	70.00
	D	0.104	0.73	0.132	0.50	2.47 [x 10^{-4} mm^2/s]	100.00	50.00
	$D*$	0.044	0.80	<0.001	0.60	1.49 [x 10^{-3} mm^2/s]	100.00	60.00
n.-enh. HGG x n-enh. meta	f	0.146	0.75	0.071	0.70	0.14 [-]	100.00	70.00
	D	0.776	0.53	0.894	0.35	3.63 [x 10^{-4} mm^2/s]	75.00	60.00
	$D*$	0.477	0.64	0.367	0.35	1.49 [x 10^{-3} mm^2/s]	75.00	60.00

Table D.6: The p-value indicating the statistically significant difference, the values of AUC, p-value (AUC=0.5), Youden index, suggested cut-off, sensitivity and specificity values for IVIM parameters f, D *and* $D*$ *derived from the ROC curve in different brain tissue types and different brain tumor types. Statistical difference p<0.05 highlighted with a gray color. Diffusion images correction implemented in FSL, denoising included, fitting algorithm: Fit D and f (with high b), then fit D*.*

- **BrainSuite DWI correction tool**

		p-value	AUC	p (AUC=0.5)	Youden index	Cut-off value	Sensit. [%]	Specific. [%]
edema × enhanced	f	0.001	0.87	<0.001	0.70	0.10 [-]	84.21	85.71
	D	0.379	0.60	0.341	0.26	3.82 [x 10^{-4} mm^2/s]	68.42	57.14
	$D*$	0.012	0.83	<0.001	0.58	2.98 [x 10^{-3} mm^2/s]	78.95	78.57
edema × non-enhan.	f	0.005	0.88	<0.001	0.79	0.08 [-]	100.00	78.57
	D	0.171	0.62	0.271	0.36	4.60 [x 10^{-4} mm^2/s]	50.00	85.71
	$D*$	0.155	0.64	0.169	0.29	1.49 [x 10^{-3} mm^2/s]	78.57	50.00
enhanced × non-enhan.	f	0.912	0.50	0.978	0.16	0.08 [-]	0.00	84.21
	D	0.049	0.70	0.039	0.34	4.44 [x 10^{-4} mm^2/s]	50.00	84.21
	$D*$	0.069	0.74	0.007	0.43	2.98 [x 10^{-3} mm^2/s]	64.29	78.95
enhan. HGG × enh. meta.	f	0.012	0.86	0.002	0.78	0.13 [-]	100.00	77.78
	D	0.265	0.67	0.334	0.53	3.65 [x 10^{-4} mm^2/s]	75.00	77.78
	$D*$	0.391	0.65	0.417	0.278	4.47 [x 10^{-3} mm^2/s]	50.00	77.78
enhan. HGG × enh. meni.	f	0.143	0.74	0.172	0.67	0.15 [-]	66.67	100.00
	D	0.554	0.65	0.393	0.39	1.57 [x 10^{-4} mm^2/s]	50.00	88.89
	$D*$	0.025	1.00	<0.001	1.00	7.45 [x 10^{-3} mm^2/s]	100.00	100.00
enh. meta × enh. meni	f	0.406	0.67	0.429	0.67	0.15 [-]	66.67	100.00
	D	0.178	0.71	0.278	0.67	2.09 [x 10^{-4} mm^2/s]	66.67	100.00
	$D*$	0.040	0.96	<0.001	0.75	5.96 [x 10^{-3} mm^2/s]	100.00	75.00
edema HGG × edem. meta	f	0.243	0.61	0.511	0.33	0.08 [-]	100.00	33.33
	D	0.069	0.81	0.026	0.64	4.38 [x 10^{-4} mm^2/s]	75.00	88.89
	$D*$	0.030	0.83	<0.001	0.67	1.49 [x 10^{-3} mm^2/s]	100.00	66.67
n.-enh. HGG × n-enh. meta	f	0.905	0.56	0.739	0.44	0.11 [-]	100.00	44.44
	D	0.397	0.61	0.543	0.42	3.62 [x 10^{-4} mm^2/s]	75.00	66.67
	$D*$	0.116	0.85	0.002	0.639	2.98 [x 10^{-3} mm^2/s]	75.00	88.89

Table D.7: The p-value indicating the statistically significant difference, the values of AUC, p-value (AUC=0.5), Youden index, suggested cut-off, sensitivity and specificity values for IVIM parameters f, D *and* $D*$ *derived from the ROC curve in different brain tissue types and different brain tumor types. Statistical difference p<0.05 highlighted with a gray color. Diffusion images correction implemented in BrainSuite, denoising included, fitting algorithm: Fit D and f (with high b), then fit D*.*

- **Without diffusion images correction**

		p-value	AUC	*p* (AUC=0.5)	Youden index	Cut-off value	Sensit. [%]	Specific. [%]
edema × enhanced	f	<0.001	0.86	<0.001	0.70	0.08 [-]	90.00	80.00
	D	0.077	0.68	0.074	0.42	3.35 [x 10^{-4} mm^2/s]	75.00	66.67
	$D*$	0.007	0.78	<0.001	0.50	2.98 [x 10^{-3} mm^2/s]	70.00	80.00
edema × non-enhan.	f	0.001	0.88	<0.001	0.80	0.08 [-]	100.00	80.00
	D	0.224	0.58	0.447	0.20	4.38 [x 10^{-4} mm^2/s]	40.00	80.00
	$D*$	0.465	0.57	0.512	0.13	1.49 [x 10^{-3} mm^2/s]	73.33	40.00
enhanced × non-enhan.	f	0.818	0.53	0.743	0.18	0.14 [-]	73.33	45.00
	D	0.020	0.75	0.003	0.45	2.98 [x 10^{-4} mm^2/s]	80.00	65.00
	$D*$	0.026	0.75	0.002	0.43	4.47 [x 10^{-3} mm^2/s]	93.33	50.00
enhan. HGG × enh. meta.	f	0.009	0.80	0.017	0.70	0.11 [-]	100.00	70.00
	D	0.101	0.78	0.035	0.60	2.84 [x 10^{-4} mm^2/s]	100.00	60.00
	$D*$	0.232	0.73	0.167	IV.47	4.47 [x 10^{-3} mm^2/s]	50.00	80.00
enhan. HGG × enh. meni.	f	0.066	0.83	0.006	0.57	0.14 [-]	66.67	90.00
	D	0.017	0.82	0.005	0.70	2.31 [x 10^{-4} mm^2/s]	100.00	70.00
	$D*$	0.008	1.00	<0.001	1.00	5.96 [x 10^{-3} mm^2/s]	100.00	100.00
enh. meta × enh. meni	f	0.454	0.60	0.611	0.42	0.14 [-]	66.67	75.00
	D	0.002	1.00	<0.001	1.00	2.31 [x 10^{-4} mm^2/s]	100.00	100.00
	$D*$	0.016	1.00	<0.001	1.00	7.45 [x 10^{-3} mm^2/s]	100.00	100.00
edema HGG × edem. meta	f	0.284	0.58	0.661	0.40	0.07 [-]	100.00	40.00
	D	0.090	0.73	0.132	0.50	2.50 [x 10^{-4} mm^2/s]	100.00	50.00
	$D*$	0.086	0.75	0.055	0.45	1.49 [x 10^{-3} mm^2/s]	75.00	70.00
n.-enh. HGG × n-enh. meta	f	0.514	0.66	0.286	0.50	0.11 [-]	100.00	50.00
	D	0.828	0.50	1.000	0.25	4.11 [x 10^{-4} mm^2/s]	25.00	50.00
	$D*$	0.064	0.80	0.008	0.40	1.49 [x 10^{-3} mm^2/s]	100.00	40.00

Table D.8: The p-value indicating the statistically significant difference, the values of AUC, p-value (AUC=0.5), Youden index, suggested cut-off, sensitivity and specificity values for IVIM parameters f, D and $D*$ derived from the ROC curve in different brain tissue types and different brain tumor types. Statistical difference p<0.05 highlighted with a gray color. No diffusion images correction, denoising included, fitting algorithm: Fit D and f (with high b), then fit D.*